

SIMULATIONS OF LIQUID TRANSPORT

**MOLECULAR DYNAMICS SIMULATIONS OF
LIQUID TRANSPORT THROUGH
NANOFILTRATION MEMBRANES**

by

LUYING WANG, B. Eng., M. Sc.

A Thesis

Submitted to the School of Graduate Studies

in Partial Fulfillment of the Requirements

for the Degree

Doctor of Philosophy

McMaster University

McMaster University © Copyright by Luying Wang, September 2012

DOCTOR OF PHILOSOPHY (2012)

McMaster University

(Chemical Engineering)

Hamilton, Ontario

TITLE: Simulations of Liquid Transport

AUTHOR: Luying Wang

B.Eng. (Beijing University of Chemical Technology)

M.Sc. (Tsinghua University)

SUPERVISOR: James M. Dickson

NUMBER OF PAGES: liv, 290

Abstract

Nanofiltration (NF) is a pressure-driven membrane separation process, which is often used for water purification, water softening, recovery of specific chemicals, concentration of products (such as proteins and dyes), and removal of organic molecules. NF process is a nonequilibrium process because of the pressure difference and concentration difference across the membrane. As one type of molecular dynamics (MD) simulations, nonequilibrium molecular dynamics (NEMD) simulations can provide the dynamics properties of NF transport on a molecular level description, which can serve as a complement to conventional experimental studies.

In the thesis, two kinds of membranes are modeled as NF membranes: (1) the carbon nanotube (CNT) membrane as an idealized membrane with smooth surfaces and a uniform straight pore; (2) the polyamide (PA) membrane as an amorphous polymeric membrane with complex and random free volume pores. CNT membranes are of interest because of the ability to support high throughput, as shown in previous experimental and simulation studies. The modeled PA membranes have a similar structure with the PA top layer of the FilmTec[®] NF 90 membrane, which is one of currently available, commercial NF membranes. Few NEMD simulation studies have been reported to show the pressure-driven liquid transport through a CNT membrane or a PA membrane at a low pressure difference (like at NF operating conditions).

The NEMD simulations are proposed in this thesis to study pressure-driven liquid

flows through the CNT and PA membranes at realistic NF conditions and to investigate the relationship between the membrane structures and the transport properties. Pure water flows passing through the membranes are studied primarily, and organic flows passing through the CNT membranes are also studied. The simulation results are analyzed to obtain the transport properties, such as flux, density and velocity distributions, and water permeability coefficient. The effects of the membrane structure (pore size, thickness, and electrical charge), pressure difference, and water–membrane interactions on the transport phenomena are investigated. The simulation transport properties of pressure-driven water flows and the membrane structures of the PA membranes are compared with traditional models and/or literature data. In summary, the studies in the thesis show that the liquid transport (especially water transport) through the CNT membrane is extremely fast and cannot be predicted by the continuum equations due to the special properties of the CNT, and the water transport of the PA membrane is strongly related to the free-volume properties of the amorphous polymeric membrane.

The MD simulation studies proposed in this thesis are feasible as a tool for describing and investigating pressure-drive liquid transport and can provide some fundamental basis for NF transport.

Acknowledgements

First and foremost, my sincere thanks are due to my supervisor, Dr. James M. Dickson, who has provided me a chance to pursue PhD at McMaster University. His continuous guidance, help, and support during my PhD study helped me to complete my study and research successfully. I am especially grateful for all his advice, patience, and encouragement, which were of great help to me as an international student for studying in my second language. Besides gaining the specialized knowledge of chemical engineering, I also benefited a lot from his dedication to work, teaching skills, and concern about students, which are all very helpful for my future career and life.

I also thank my committee members very much, Dr. Carlos Filipe and Dr. Randy Dumont, for their inspiring advice and discussions. I feel a great sense of gratitude to Dr. Shiping Zhu and Dr. Phillip Y. K. Choi (Department of Chemical and Materials Engineering, University of Alberta) who provided me valuable suggestions for my research project.

It has been my best experience to study in the department of Chemical Engineering, where I have been provided a wonderful environment for study and research. I especially thank Kathy Goodman, Lynn Falkiner, Nanci Cole, Doug Keller, Justyna Derkach, Dan Wright, Paul Gatt, and other staff members or students, who have helped me for the past four years.

I appreciate the financial support from Natural Sciences and Engineering Research

Council Canada and McMaster University. I am also grateful to the Shared Hierarchical Academic Research Computing Network (SHARCNET) and Compute Canada for providing high performance computing technology for my research.

Last but not least, I would like to express my heartfelt thanks to my parents for their love and encouragement throughout all these years. Without my parents' support, I would not keep to pursuit the PhD degree and not gain such a great achievement. I am also grateful to my friends for giving me support in my study and daily life.

Table of Contents

Abstract	iii
Acknowledgements	v
Table of Contents	vii
List of Figures	xiii
List of Tables	xlvi
List of Abbreviations and Symbols	1
Chapter 1 Introduction	1
1.1. Nanofiltration	1
1.1.1. Nanofiltration Membranes	2
1.1.2. Membrane Performance and Traditional Mathematical Modeling	4
1.1.3. Advantages and Applications of Nanofiltration	7
1.2. Molecular Dynamics Simulation	9
1.2.1. Force Field	10
1.2.2. Force Calculations and Algorithm	11
1.2.3. Periodic Boundary Conditions	13
1.2.4. Water Molecule Models	17
1.3. Carbon Nanotubes	17
1.4. Literature Review	20

1.4.1.	NEMD Simulations of Pressure-driven Transport	20
1.4.2.	Simulations of NF Polymeric Membranes	27
1.5.	Research Objectives	31
1.6.	Thesis Outline	32
	References	34
Chapter 2 Nonequilibrium Molecular Dynamics Simulation of Water Transport through Carbon Nanotube Membranes at Low Pressure		42
2.1.	Abstract	42
2.2.	Introduction	43
2.3.	Simulation Methods	48
2.4.	Results and Discussion	52
2.4.1.	The effect of pore size	57
2.4.2.	The effect of membrane thickness	73
2.5.	Conclusions	81
	References	83
Chapter 3 Comparison of Two Nonequilibrium Molecular Dynamics Simulation Systems for the Pressure-Driven Water Permeation through Carbon Nanotube Membranes		88
3.1.	Abstract	88

3.2.	Introduction	89
3.3.	Simulation Methods	93
3.4.	Results and Discussion	97
3.4.1.	Comparisons of the two systems	100
3.4.2.	The effect of pressure on flux	103
3.4.3.	Radial-direction distributions	110
3.4.4.	Flow-direction distributions	115
3.5.	Conclusions	118
	References	120

Chapter 4 Nonequilibrium Molecular Dynamics Simulation of Pressure-Driven Water Transport through Modified CNT Membranes123

4.1.	Abstract	123
4.2.	Introduction	124
4.3.	Simulation Methods	126
4.4.	Results and Discussion	129
4.4.1.	The modified Lennard-Jones parameters of the CNT membranes	131
4.4.2.	The polarized CNT membranes	137
4.5.	Conclusions	144
	References	146

Chapter 5 Nonequilibrium Molecular Dynamics Simulation of Pressure-Driven Water Transport through Charged CNT Membranes149

5.1.	Abstract	149
5.2.	Introduction	150
5.3.	Simulation Methods	152
5.4.	Results and Discussion	155
5.4.1.	The effect of charge distribution	158
5.4.2.	The effect of charge type	166
5.5.	Conclusions	171
	References	173

Chapter 6 Study of Pressure-Driven Organic Flows through CNT Membranes by Nonequilibrium Molecular Dynamics Simulations176

6.1.	Abstract	176
6.2.	Introduction	177
6.3.	Simulation Methods	179
6.4.	Results and Discussion	182
6.4.1.	The effect of liquid properties	184
6.4.2.	The effect of membrane pore Size	201
6.5.	Conclusions	210

References	211
------------------	-----

Chapter 7 Molecular Dynamics Simulations of Pressure-Driven Water Transport through Polyamide Membranes215

7.1. Abstract	215
7.2. Introduction	216
7.3. Simulation Methods	219
7.3.1. Modeling of PA membranes	219
7.3.2. Molecular dynamics simulations of water transport	224
7.4. Results and Discussion	227
7.4.1. PA membrane properties	227
7.4.2. Transport properties	237
7.5. Conclusions	246
References	248

Chapter 8 Molecular Dynamics Simulations of Water Transport through Cross-linked Polyamide Nanofiltration Membranes at Low Pressure252

8.1. Abstract	252
8.2. Introduction	253
8.3. Simulation Methods	256
8.3.1. Modeling of cross-linked PA membranes	256

8.3.2.	Molecular dynamics simulations of water transport	261
8.4.	Results and Discussion	263
8.4.1.	The effect of degree of cross-linking	264
8.4.2.	The effect of electrical charge	270
8.5.	Conclusions	277
	References	279
Chapter 9	General Conclusions, Contributions, and Future Work	282
9.1.	General Conclusions	282
9.2.	Contributions	285
9.3.	Future Work	288

List of Figures

Figure 1.1	Schematic representation of a cross-section view of the typical TFC membrane (adapted from Figure III-4. in reference [8]).	3
Figure 1.2	Schematic representation of a negatively charged NF membrane caused by deprotonated carboxylate groups.	4
Figure 1.3	Schematic representation of a NF separation process (adapted from Figure I-3. in reference [8]).	5
Figure 1.4	Periodic boundary conditions in a two-dimensional section.	15
Figure 1.5	A simulation system in a two-dimensional PBC for simulating a liquid flow through a slit between two solid walls: the liquid in light blue, and the walls in grey.	15
Figure 1.6	Cut-off radius in a two-dimensional section.	16
Figure 1.7	Schematic representation (in a two-dimensional section view) of a closed NEMD simulation system in 2D PBC (adapted from references [62] and [63]). The color drawing is the unit system, where external forces are applied on two solid movable walls (in black) located perpendicular along the flow direction. The dashed lines are periodic boundaries, and the grey drawing is the periodic copy of the unit system. The water molecules in the unit system leaving a boundary re-enter the unit system from the opposite boundary, and the periodic movement of	

water molecules does not exist in the flow direction due to 2D PBC.22

Figure 1.8 Schematic representation (in a two-dimensional section view) of an open NEMD simulation system in 2D PBC (adapted from references [54]). The color drawing is the unit system, where external forces are applied on two water control zones (in green) located near the boundaries along the flow direction. The dashed lines are periodic boundaries, and the grey drawing is the periodic copy of the unit system. The water molecules in the unit system leaving a boundary re-enter the unit system from the opposite boundary, and the periodic movement of water molecules does not exist in the flow direction due to 2D PBC.23

Figure 1.9 Schematic representation (in a two-dimensional section view) of the PBC along the flow direction for a unit system in 3D PBC. The dashed lines are periodic boundaries. The PBC along other two directions are not shown in this figure.25

Figure 1.10 Schematic representation (in a two-dimensional section view) of one type of the NEMD simulation system in 3D PBC. The color drawing is the unit system, where external forces are applied on two water control layers (in green) located near the boundaries along the flow direction. The dashed lines are periodic boundaries, and the grey drawings are the periodic copies of the unit system. The water molecules in the unit system leaving any boundary re-enter the unit system from the opposite boundary, due to 3D PBC.26

Figure 1.11	The reaction formula of the PA active layer of the NF 90 membrane. The cross-linking degree, n , is defined by the percentage of the cross-linked repeat units to the total repeat units.	29
Figure 2.1	Orthographic snapshots of the CNT membrane model produced by the VMD package for the MD simulation: (a) Top view down through the CNT membrane model; (b) Side view of the CNT membrane model. Two graphene sheets are located at the ends of the CNT and each sheet has an approximated hole in the center to match the pore size of the CNT.....	48
Figure 2.2	Perspective snapshots of the simulation systems produced by VMD package at the beginning status of MD simulations. Shown are the two graphene sheets which act as the movable walls, the CNT membrane model shown in Figure 2.1, and the two water reservoirs connected by the membrane. Forces f_i and f_b are applied on the movable walls. Carbon atoms in green, hydrogen atoms in white, and oxygen atoms in red.....	51
Figure 2.3	Pressure produced in each water reservoir as a function of the simulation time (10 ns as an example shown here, real simulation time is longer and dependent on each case). Each pressure value is averaged in 10 ps after the pressure difference stabilizes in the NEMD simulation. The error about the mean value of the pressure is less than 0.2% for the high pressure on the top reservoir, and is less than 10% for	

the low pressure on the bottom reservoir. The standard deviation for the pressure differences over all seven simulations is about 0.2 MPa.....56

Figure 2.4 Number flow rate of #4 CNT membranes in a 30 ns simulation, shown as the slope of the linear trend in the net number of water molecules passing through the membrane as a function of the simulation time. The data shown are for membrane simulations of CNT #4 (Table 2.1): (12, 12) CNT: $L_z = 6.0$ nm; $\Delta P = 5.0$ MPa; $T = 300$ K. The standard error of the slope is ± 0.05 molecules/nm.....59

Figure 2.5 Flux (rate per membrane area), shown both as molecular flux and conventional flux (in m/s), as a function of the membrane pore size as represented by the pore area. The points are based on membrane simulations on CNT #1 to #4 (Table 2.1): #1 (8, 8), #2 (10, 10), #3 (11, 11), and #4 (12, 12) CNT, respectively: $L_z = 6.0$ nm; $\Delta P = 5.0$ MPa; $T = 300$ K. H-P Equation refers to the Hagen-Poiseuille Equation (Eqn. (2.1)), and solid line is the trend based on the simulation results. The statistical error for each data point is evaluated and less than 0.5% (see Figure 2.4 for the case of the #4 membrane).60

Figure 2.6 Effect of pore size as represented by the pore radius on the density distributions along radial direction for the four membrane models: density as a function of r ; values are averaged over a thin annular section in the pore at r (excluding the entrance and exit regions). The points are based on membrane simulations on CNT #1 to #4 (Table 2.1):

#1 (8, 8), #2 (10, 10), #3 (11, 11), and #4 (12, 12) CNT, respectively: $L_z = 6.0$ nm; $\Delta P = 5.0$ MPa; $T = 300$ K. Solid lines are the trend curves based on the simulation results, dotted lines are the pore surfaces represented by the effective pore radii (Table 2.1). The statistical error for each data point is less than 1%.....65

Figure 2.7 Orthographic snapshots of water molecules in the different CNT membranes. Atoms are shown by balls with the van der Waals volumes: carbon atoms in green, hydrogen atoms in white, and oxygen atoms in red.....66

Figure 2.8 Effect of pore size as represented by the pore radius on the velocity (in z direction) distributions along the radial direction for the four membrane models: velocity as a function of r ; values are averaged over a thin annular section in the pore at r (excluding the entrance and exit regions). The points are based on membrane simulations on CNT #1 to #4 (Table 2.1): #1 (8, 8), #2 (10, 10), #3 (11, 11), and #4 (12, 12) CNT, respectively: $L_z = 6.0$ nm; $\Delta P = 5.0$ MPa; $T = 300$ K. N-S equation refers to the Navier-Stokes Equation (Eqn. (2.2)). Dashed lines are the trends based on the Navier-Stokes Equation, solid lines are the trend curves based on the simulation results, and dotted lines are the pore surfaces represented by the effective pore radii (Table 2.1). The statistical errors for most data points are less than 10%.....67

Figure 2.9 Effect of pore size on the density distributions along the flow direction

for the four membrane models: density as a function of z ; values are averaged over a thin section at z (cylindrical sections in the pore and cuboid sections in the water reservoirs). The points are based on membrane simulations on CNT #1 to #4 (Table 2.1): #1 (8, 8), #2 (10, 10), #3 (11, 11), and #4 (12, 12) CNT, respectively: $L_z = 6.0$ nm; $\Delta P = 5.0$ MPa; $T = 300$ K. Dashed lines are the membrane boundaries along z direction separating the system in three parts from left to right: the water reservoir at high pressure side, the pore of the CNT membrane, and the water reservoir at low pressure side. Solid lines are the trend curves based on the simulation results. The statistical error for each data point is less than 1%.....72

Figure 2.10 Effect of pore size on the velocity (in z direction) distributions along the flow direction for the four membrane models: velocity as a function of z ; values are averaged over a thin section at z (cylindrical sections in the pore and square cuboids sections in the water reservoirs). The points are based on membrane simulations on CNT #1 to #4 (Table 2.1): #1 (8, 8), #2 (10, 10), #3 (11, 11), and #4 (12, 12) CNT, respectively: $L_z = 6.0$ nm; $\Delta P = 5.0$ MPa; $T = 300$ K. Dashed lines are the membrane boundaries along z direction separating the system in three parts from left to right: the water reservoir at high pressure side, the pore of the CNT membrane, and the water reservoir at low pressure side. Solid lines are the trend curves based on the simulation results. The

statistical error for each data point is less than 15%.....74

Figure 2.11 Flux (rate per membrane area), shown both as molecular flux and conventional flux (in m/s), as a function of the inverse membrane thickness. The points are based on membrane simulations on CNT #5, #4, #6, and #7 (Table 2.1) corresponding to different lengths of 3.0 nm, 6.0 nm, 9.0 nm, and 15.0 nm, respectively: $r_p = 0.643$ nm; $\Delta P = 5.0$ MPa; $T = 300$ K. H-P Equation refers to the Hagen-Poiseuille Equation (Eqn. (2.1)), and the solid line is the trend based on the simulation results. The statistical error for each data point is less than 0.5% (see Figure 2.4 for the case of #4 membrane).75

Figure 2.12 Effect of membrane thickness on the distributions along the radial direction for the four membrane models; values are averaged over a thin annular section in the pore at r (excluding the entrance and exit regions): (a) Density as a function of r ; (b) Velocity, in z direction, as a function of r . The points are based on membrane simulations on CNT #5, #4, #6, and #7 (Table 2.1) corresponding to (12, 12) CNT with different lengths of 3.0 nm, 6.0 nm, 9.0 nm, and 15.0 nm, respectively: $r_p = 0.643$ nm; $\Delta P = 5.0$ MPa; $T = 300$ K. N-S equation refers to the Navier-Stokes Equation (Eqn. (2.2)). Dashed lines are the trends based on the Navier-Stokes Equation, solid lines are the trend curves based on the simulation results, and dotted lines are the pore surface represented by the effective pore radius (0.643 nm) The statistical

error for each density data point is less than 1% and the statistical errors for most data points are less than 10%.79

Figure 2.13 Effect of membrane thickness on the distributions along flow direction for the four membrane models; values are averaged over a thin section at z (cylindrical sections in the pore and square cuboids sections in the water reservoirs): (a) Density distributions as a function of z ; (b) Velocity, in z direction, as a function of z . The points are based on membrane simulations on CNT #5, #4, #6, and #7 (Table 2.1) corresponding to (12, 12) CNT with different length of 3.0 nm, 6.0 nm, 9.0 nm, and 15.0 nm, respectively: $r_p = 0.643$ nm; $\Delta P = 5.0$ MPa; $T = 300$ K. Dashed lines are the membrane boundaries along the z direction separating the system in three parts, from left to right: the water reservoir at high pressure side, the pore of the CNT membrane, and the water reservoir at low pressure side. Solid lines are the trend curves based on the simulation results. The statistical error for each density data point and each velocity data point are less than 1%, and less than 15%, respectively.80

Figure 3.1 Orthographic snapshots of the CNT membrane model produced by the VMD package for the MD simulation. (a) Top view down through the CNT membrane model: the graphene sheet, with an approximated hole in the center, to match the pore size of the CNT. (b) Side view of the CNT membrane model: two graphene sheets are located at the

ends of the CNT. Used, with permission from reference [5]..... 95

Figure 3.2 Perspective snapshots of the simulation systems produced by the VMD package at the beginning state of the MD simulations. Carbon atoms are green, hydrogen atoms white, and oxygen atoms red. (a) 2D PBC System (adapted from the figure in reference [5]): two water reservoirs connected by the CNT membrane model shown in Figure 3.1; and the two graphene sheets acted as the movable walls where the force f_t or f_b is applied on each carbon atom of the top or bottom wall. (b) 3D PBC System: two water reservoirs connected by the CNT membrane model shown in Figure 3.1; forces f is applied on each oxygen atom of the water control layers located near the top and bottom boundaries within 0.25 nm.96

Figure 3.3 Flux (rate per membrane area), shown both as molecular flux and conventional flux (in m/s), as a function of the pressure difference (ΔP) for the two kinds of simulations systems. The statistical error for each data point is less than 0.5%. The points are based on membrane simulations modeled by (12, 12) CNT: $r_p = 0.643$ nm, $L_z = 6.0$ nm, $T = 300$ K. H-P Equation refers to the Hagen-Poiseuille equation (Eqn. (3.1)) represented by the dashed line. The solid line is the linear trend through origin based on the simulation fluxes estimated by 2D PBC system, while the dotted line is the curve trend through origin based on the simulation fluxes estimated by 3D PBC system.107

Figure 3.4 Forward and backward fluxes (rate per membrane area), shown both as molecular flux and conventional flux (in m/s), as a function of the pressure difference (ΔP) for the 2D PBC and 3D PBC systems: (a) Forward flux vs. ΔP ; (b) Backward flux vs. ΔP . The statistical error for each data point is less than 0.5%. The points are based on membrane simulations modeled by (12, 12) CNT: $r_p = 0.643$ nm, $L_z = 6.0$ nm, $T = 300$ K. The solid line and dotted line are trend lines based on the simulation results.108

Figure 3.5 Effect of pressure difference on the density distributions along the radial direction for the 2D PBC and 3D PBC systems; values are averaged over a thin annular section in the pore at r (excluding the entrance and exit regions): (a) 2D PBC system; (b) 3D PBC system. The statistical error for each data point is less than 1%. The points are based on membrane simulations on (12, 12) CNT: $r_p = 0.643$ nm, $L_z = 6.0$ nm, $T = 300$ K. The solid lines are the trend curves based on the simulation results, and the dotted lines are the pore surface represented by the effective pore radius (0.643 nm). 111

Figure 3.6 Comparison of the radial density distributions of the 2D PBC and 3D PBC systems at 1.0 MPa pressure difference: the solid line for the 2D PBC system, from Figure 3.5(a); the dashed lines for the 3D PBC system, from Figure 3.5(b). The statistical error for each data point is less than 1%. The dotted lines are the pore surface represented by the

effective pore radius (0.643 nm)..... 112

Figure 3.7 Effect of pressure difference on the velocity (in z direction) distributions along the radial direction for the 2D PBC and 3D PBC systems; values are averaged over a thin annular section in the pore at r (excluding the entrance and exit regions): (a) 2D PBC system; (b) 3D PBC system. The statistical errors for most data points are less than 20%. The points are based on membrane simulations on (12, 12) CNT: $r_p = 0.643$ nm, $L_z = 6.0$ nm, $T = 300$ K. N-S equation refers to the Navier-Stokes Equation (Eqn. (3.2)). The dashed lines are the trends based on the Navier-Stokes Equation, the solid lines are the trend curves based on the simulation results, and the dotted lines are the pore surface represented by the effective pore radius (0.643 nm)..... 113

Figure 3.8 Comparison of the 2D PBC and 3D PBC systems of the velocity (in z direction) distributions along the radial direction at different pressure difference: (a) 1.0 MPa, (b) 3.0 MPa, (c) 5.0 MPa, and (d) 8.0 MPa. The statistical errors for most data points are less than 20%. Each solid/dashed line is the trend curve of the radial distribution of the velocity values: the solid lines for the 2D PBC system, from Figure 3.7(a); the dashed lines for the 3D PBC system, from Figure 3.7(b). The dotted lines are the pore surface represented by the effective pore radius (0.643 nm)..... 114

Figure 3.9 Effect of pressure difference on the density distributions along flow

direction for the 2D PBC and 3D PBC systems; values are averaged over a thin section at z (cylindrical sections in the pore and square cuboids sections in the water reservoirs): (a) 2D PBC system; (b) 3D PBC system. The statistical error for each data point is less than 1%. The points are based on membrane simulations on (12, 12) CNT: $r_p = 0.643$ nm, $L_z = 6.0$ nm, $T = 300$ K. The dashed lines are the membrane boundaries along z direction separating the system in three parts from left to right: the water reservoir at high pressure side, the pore of the CNT membrane, and the water reservoir at low pressure side. The solid lines are the trend curves based on the simulation results. 116

Figure 3.10 Effect of pressure difference on the velocity (in z direction) distributions along flow direction for the 2D PBC and 3D PBC systems; values are averaged over a thin section at z (cylindrical sections in the pore and square cuboids sections in the water reservoirs): (a) 2D PBC system; (b) 3D PBC system. The statistical error are less than 15% for data points at 3.0 – 8.0 MPa and are about 25% for data points at 1.0 MPa. The points are based on membrane simulations on (12, 12) CNT: $r_p = 0.643$ nm, $L_z = 6.0$ nm, $T = 300$ K. The dashed lines are the membrane boundaries along z direction separating the system in three parts from left to right: the water reservoir at high pressure side, the pore of the CNT membrane, and the water reservoir at low pressure side. The solid lines are the trend curves based on the simulation results. 117

Figure 4.1 Perspective snapshots of the simulation systems produced by VMD package at the beginning status of MD simulations (adapted from the figure in reference [12]). Shown is the beginning empty CNT membrane model connecting two liquid filled reservoirs, and the two graphene sheets acted as the movable walls where the force f_i or f_b is applied on each carbon atom of the top or bottom wall. Carbon atoms in green, hydrogen atoms in white, and oxygen atoms in red. 127

Figure 4.2 Bar chart of simulation and theoretical flow rates (molecules/ns) of unmodified and modified CNT membranes. The results are based on membrane simulations using the (12, 12) CNT, $L_z = 6.0$ nm; $\Delta P = 8.0$ MPa; $T = 300$ K . The statistical error for each flow rate data is less than 0.5%. H-P equation refers to the Hagen-Poiseuille equation (Eqn. (4.5)), and the values of the well-depth parameters ($\epsilon_{(CC)}$, $\epsilon_{(HH)}$, and $\epsilon_{(OO)}$) are shown in Table 4.1. 132

Figure 4.3 Simulation flow rate (molecules/ns) as a function of the square root of the well-depth parameter. The data points are based on membrane simulations using the (12, 12) CNT, $L_z = 6.0$ nm; $\Delta P = 8.0$ MPa; $T = 300$ K. The statistical error for each data point is less than 0.5%. The solid line is the linear trends based on the simulation results..... 133

Figure 4.4 Effect of van der Waals interactions between water and membrane, represented by the well-depth parameter of the Lennard-Jones potential, on the density distributions along the radial direction: density values

are averaged over thin annular sections in the pore at the indicated r values over the entire NEMD simulation. The data points are based on membrane simulations using the (12, 12) CNT, $L_z = 6.0$ nm; $\Delta P = 8.0$ MPa; $T = 300$ K. The statistical error for each data point is less than 1%. The values of the well-depth parameters ($\epsilon_{(CC)}$, $\epsilon_{(HH)}$, and $\epsilon_{(OO)}$) are shown in Table 4.1. The solid lines are the trend curves based on the simulation results, and the dotted lines are the pore surface represented by the effective pore radius (0.643 nm).134

Figure 4.5 Effect of van der Waals interactions between water and membrane, represented by the well-depth parameter of the Lennard-Jones potential, on the density distributions along the flow direction: density values are averaged over thin sections about the indicated z values (cylindrical sections in the pore and cuboid sections in the water reservoirs) over the entire NEMD simulation. The data points are based on membrane simulations using the (12, 12) CNT, $L_z = 6.0$ nm; $\Delta P = 8.0$ MPa; $T = 300$ K. The statistical error for each data point is less than 1%. The values of the well-depth parameters ($\epsilon_{(CC)}$, $\epsilon_{(HH)}$, and $\epsilon_{(OO)}$) are shown in Table 4.1. The solid lines are the trend curves based on the simulation results. The dashed lines are the membrane boundaries along z direction separating the system in three parts from left to right: the water reservoir at high pressure side, the pore of the CNT membrane, and the water reservoir at low pressure side.135

Figure 4.6 Effect of van der Waals interactions between water and membrane, represented by the well-depth parameter of the Lennard-Jones potential, on the velocity distributions (in z direction) as a function of radial position: velocity (in z direction) values are averaged over thin annular sections in the pore at the indicated r values over the entire NEMD simulation. The data points are based on membrane simulations using the (12, 12) CNT, $L_z = 6.0$ nm; $\Delta P = 8.0$ MPa; $T = 300$ K. The statistical errors for most data points are less than 10%. N-S equation refers to the Navier-Stokes Equation (Eqn. (4.6)), and the values of the well-depth parameters ($\epsilon_{(CC)}$, $\epsilon_{(HH)}$, and $\epsilon_{(OO)}$) are shown in Table 4.1. The solid lines are the trend curves based on the simulation results, the dashed lines are the trends based on the Navier-Stokes Equation, and the dotted lines are the pore surface represented by the effective pore radius (0.643 nm).....136

Figure 4.7 Effect of van der Waals interactions between water and membrane, represented by the well-depth parameter of the Lennard-Jones potential, on the velocity distributions (in z direction) along the flow direction: velocity (in z direction) values are averaged over thin sections about the indicated z values (cylindrical sections in the pore and cuboid sections in the water reservoirs) over the entire NEMD simulation. The data points are based on membrane simulations using the (12, 12) CNT, $L_z = 6.0$ nm; $\Delta P = 8.0$ MPa; $T = 300$ K. The statistical error for each data

point is less than 10%. The values of the well-depth parameters ($\varepsilon_{(CC)}$, $\varepsilon_{(HH)}$, and $\varepsilon_{(OO)}$) are shown in Table 4.1. The solid lines are the trend curves based on the simulation results. The dashed lines are the membrane boundaries along the z direction separating the system in three parts from left to right: the water reservoir at high pressure side, the pore of the CNT membrane, and the water reservoir at low pressure side.137

Figure 4.8 Charge patterns of the unmodified and modified CNTs: (a) unmodified CNT, (b) unwrapped CNT of the ring polarized model, and (c) unwrapped CNT of the band polarized model. This figure illustrates the bonds between neutral atoms in black, between positive atoms in red, and between negative atoms in blue.138

Figure 4.9 Bar chart of simulation and theoretical flow rates (molecules/ns) of unmodified and modified polarized CNT membranes. The results are based on membrane simulations using the (12, 12) CNT, $L_z = 6.0$ nm; $\Delta P = 8.0$ MPa; $T = 300$ K. The statistical error for each flow rate data is less than 0.5%. H-P equation refers to the Hagen-Poiseuille equation (Eqn. (4.5)), and the charge patterns of the modified polarized CNTs are shown in Figures 4.8(b) and 4.8(c).140

Figure 4.10 Effect of electrostatic interactions between water and membrane, caused by the charge patterns within the CNT, on the density distributions along the radial direction: density values are averaged

over thin annular sections in the pore at the indicated r values over the entire NEMD simulation. The data points are based on membrane simulations using the (12, 12) CNT, $L_z = 6.0$ nm; $\Delta P = 8.0$ MPa; $T = 300$ K. The statistical error for each data point is less than 1%. The charge patterns of the modified polarized CNTs are shown in Figures 4.8(b) and 4.8(c). The solid lines are the trend curves based on the simulation results, and the dotted lines are the pore surface represented by the effective pore radius (0.643 nm).141

Figure 4.11 Effect of electrostatic interactions between water and membrane, caused by the charge patterns within the CNT, on the density distributions along the flow direction: density values are averaged over thin sections about the indicated z values (cylindrical sections in the pore and cuboid sections in the water reservoirs) over the entire NEMD simulation. The data points are based on membrane simulations using the (12, 12) CNT, $L_z = 6.0$ nm; $\Delta P = 8.0$ MPa; $T = 300$ K. The statistical error for each data point is less than 1%. The charge patterns of the modified polarized CNTs are shown in Figures 4.8(b) and 4.8(c). The solid lines are the trend curves based on the simulation results. The dashed lines are the membrane boundaries along the z direction separating the system in three parts from left to right: the water reservoir at high pressure side, the pore of the CNT membrane, and the water reservoir at low pressure side.142

Figure 4.12 Effect of electrostatic interactions between water and membrane, caused by the charge patterns of the CNT, on the velocity (in z direction) distributions along the radial direction: velocity (in z direction) values are averaged over thin annular sections in the pore at the indicated r values, over the entire NEMD simulation. The data points are based on membrane simulations using the (12, 12) CNT, $L_z = 6.0$ nm; $\Delta P = 8.0$ MPa; $T = 300$ K. The statistical errors for most data points are less than 10%. N-S equation refers to the Navier-Stokes Equation (Eqn. (4.6)), and the charge patterns of the modified polarized CNTs are shown in Figures 4.8(b) and 4.8(c). The solid lines are the trend curves based on the simulation results, the dashed lines are the trends based on the Navier-Stokes Equation, and the dotted lines are the pore surface represented by the effective pore radius (0.643 nm).143

Figure 4.13 Effect of electrostatic interactions between water and membrane, caused by the charge patterns of the CNT, on the velocity (in z direction) distributions along the flow direction: velocity (in z direction) values are averaged over thin sections about the indicated z values (cylindrical sections in the pore and cuboid sections in the water reservoirs) over the entire NEMD simulation. The data points are based on membrane simulations using the (12, 12) CNT, $L_z = 6.0$ nm; $\Delta P = 8.0$ MPa; $T = 300$ K. The statistical error for each data point is less than 10%. The charge patterns of the modified polarized CNTs are shown in Figures

4.8(b) and 4.8(c). The solid lines are the trend curves based on the simulation results. The dashed lines are the membrane boundaries along the z direction separating the system in three parts from left to right: the water reservoir at high pressure side, the pore of the CNT membrane, and the water reservoir at low pressure side. 144

Figure 5.1 Perspective snapshots of the simulation systems produced by VMD package at the beginning status of MD simulations (adapted from the figure in reference [16]). Shown is the beginning empty CNT membrane model connecting two liquid filled reservoirs, and the two graphene sheets acted as the movable walls where the force f_i or f_b is applied on each carbon atom of the top or bottom wall. Carbon atoms in green, hydrogen atoms in white, and oxygen atoms in red. 154

Figure 5.2 Bar chart of simulation and theoretical flow rates (molecules/ns) of uncharged and negatively charged (#1 – 3) CNT membranes. The results are based on membrane simulations using the (12, 12) CNT, $L_z = 6.0$ nm; $\Delta P = 8.0$ MPa; $T = 300$ K. The statistical error for each flow rate data is less than 0.5%. H-P equation refers to the Hagen-Poiseuille equation (Eqn. (6.2)). The charges are on the pore surface, the two membrane surfaces, and the whole membrane for the #1, #2, and #3 membranes, respectively (Table 5.1). 159

Figure 5.3 Effect of electrostatic interactions between water and membrane, caused by the negative charges on the CNT membrane, on the density

distributions along the radial direction: density as a function of r ; values are averaged over a thin annular section in the pore at r (excluding the entrance and exit regions). The data points are based on membrane simulations using the (12, 12) CNT, $L_z = 6.0$ nm; $\Delta P = 8.0$ MPa; $T = 300$ K. The statistical error for each data point is less than 1%. The charged types are shown in Table 5.1. The solid lines are the trend curves based on the simulation results, and the dotted lines are the pore surface represented by the effective pore radius (0.643 nm). ...162

Figure 5.4 Effect of electrostatic interactions between water and membrane, caused by the negative charges of the CNT membrane, on the density distributions along the flow direction: density as a function of z ; values are averaged over a thin section at z (cylindrical sections in the pore and cuboid sections in the water reservoirs). The data points are based on membrane simulations using the (12, 12) CNT, $L_z = 6.0$ nm; $\Delta P = 8.0$ MPa; $T = 300$ K. The statistical error for each data point is less than 1%. The charged types are shown in Table 5.1. The solid lines are the trend curves based on the simulation results. The dashed lines are the membrane boundaries along z direction separating the system in three parts from left to right: the water reservoir at high pressure side, the pore of the CNT membrane, and the water reservoir at low pressure side.....162

Figure 5.5 Effect of electrostatic interactions between water and membrane,

caused by the negative charges of the CNT membrane, on the velocity (in z direction) distributions along the radial direction: velocity (in z direction) values are averaged over a thin annular section in the pore at r (excluding the entrance and exit regions). The data points are based on membrane simulations using the (12, 12) CNT, $L_z = 6.0$ nm; $\Delta P = 8.0$ MPa; $T = 300$ K. The statistical errors for most data points are less than 15%. N-S equation refers to the Navier-Stokes Equation (Eq. (2)), and the charged types are shown in Table 5.1. The solid lines are the trend curves based on the simulation results, the dashed lines are the trends based on the Navier-Stokes Equation, and the dotted lines are the pore surface represented by the effective pore radius (0.643 nm). 163

Figure 5.6 Effect of electrostatic interactions between water and membrane, caused by the negative charges of the CNT membrane, on the velocity (in z direction) distributions along the flow direction: velocity (in z direction) values are averaged over thin sections about the indicated z values (cylindrical sections in the pore and cuboid sections in the water reservoirs) over the entire NEMD simulation. The data points are based on membrane simulations using the (12, 12) CNT, $L_z = 6.0$ nm; $\Delta P = 8.0$ MPa; $T = 300$ K. The statistical error for each data point is less than 10%. The charged types are shown in Table 5.1. The solid lines are the trend curves based on the simulation results. The dashed lines are the membrane boundaries along z direction separating the

system in three parts from left to right: the water reservoir at high pressure side, the pore of the CNT membrane, and the water reservoir at low pressure side.....164

Figure 5.7 Bar chart of simulation and theoretical flow rates (molecules/ns) of uncharged and charged (#3 and #4) CNT membranes. The results are based on membrane simulations using the (12, 12) CNT, $L_z = 6.0$ nm; $\Delta P = 8.0$ MPa; $T = 300$ K. The statistical error for each data point is less than 0.5%. H-P equation refers to the Hagen-Poiseuille equation (Eqn. (6.2)). The charges are on the whole membrane for the #3 or #4 membranes (Table 5.1): the #3 membrane is negatively charged and the #4 membrane is positively charged.....167

Figure 5.8 Effect of electrostatic interactions between water and membrane, caused by the positive or negative charges of the CNT membrane, on the density distributions along the radial direction: density as a function of r ; values are averaged over a thin annular section in the pore at r (excluding the entrance and exit regions). The data points are based on membrane simulations using the (12, 12) CNT, $L_z = 6.0$ nm; $\Delta P = 8.0$ MPa; $T = 300$ K. The statistical error for each data point is less than 1%. The charged types are shown in Table 5.1. The solid lines are the trend curves based on the simulation results, and the dotted lines are the pore surface represented by the effective pore radius (0.643 nm).....167

Figure 5.10 Effect of electrostatic interactions between water and membrane, caused by the positive or negative charges of the CNT membrane, on the velocity (in z direction) distributions along the radial direction: velocity (in z direction) values are averaged over a thin annular section in the pore at r (excluding the entrance and exit regions). The data points are based on membrane simulations using the (12, 12) CNT, $L_z = 6.0$ nm; $\Delta P = 8.0$ MPa; $T = 300$ K. The statistical errors for most data points are less than 15%. N-S equation refers to the Navier-Stokes Equation (Eq. (2)), and the charged types are shown in Table 5.1. The solid lines are the trend curves based on the simulation results, the dashed lines are the trends based on the Navier-Stokes Equation, and the dotted lines are the pore surface represented by the effective pore radius (0.643 nm).....168

Figure 5.11 Effect of electrostatic interactions between water and membrane, caused by the positive or negative charges of the CNT membrane, on the velocity (in z direction) distributions along the flow direction: velocity (in z direction) values are averaged over thin sections about the indicated z values (cylindrical sections in the pore and cuboid sections in the water reservoirs) over the entire NEMD simulation. The data points are based on membrane simulations using the (12, 12) CNT, $L_z = 6.0$ nm; $\Delta P = 8.0$ MPa; $T = 300$ K. The statistical error for each data point is less than 10%. The charged types are shown in Table 5.1.

The solid lines are the trend curves based on the simulation results. The dashed lines are the membrane boundaries along z direction separating the system in three parts from left to right: the water reservoir at high pressure side, the pore of the CNT membrane, and the water reservoir at low pressure side.....169

Figure 5. 12 Orthographic snapshots of water molecules in the #3 (a) and #4 (b) CNT membranes. Atoms are shown by balls with the van der Waals volumes: carbon atoms in green, hydrogen atoms in white, and oxygen atoms in red.....170

Figure 6.1 Perspective snapshots of the simulation at the beginning status for simulating ethanol transport (adapted from the figure in reference [16]). Shown is the beginning empty CNT membrane model connecting two liquid filled reservoirs (ethanol molecules as an example shown here, other liquid molecules listed in Table 6.2 can compose different liquid reservoirs), and the two graphene sheets acted as the movable walls where the force f_t or f_b is applied on each carbon atom of the top or bottom wall. Carbon atoms in green, hydrogen atoms in white, and oxygen atoms in red..... 181

Figure 6.2 Bar chart of simulation and theoretical volume fluxes (m/s) for the six liquids through the (12, 12) CNT membrane; $L_z = 6.0$ nm; $\Delta P = 8.0$ MPa; $T = 300$ K. The statistical error for each flux data is less than 10%. The theoretical flux is calculated from the Hagen-Poiseuille

	equation (Eqn. (6.1)).....	186
Figure 6.3	Simulation volume flux (m/s) as a function of the molecular mass the six liquids through the (12, 12) CNT membrane; $L_z = 6.0$ nm; $\Delta P = 8.0$ MPa; $T = 300$ K. The statistical error for each data point is less than 10%. The solid line is the linear trend based on the simulation results.....	187
Figure 6.4	Simulation and theoretical volume fluxes (m/s) as a function of the inverse liquid viscosity, for the six liquids through the (12, 12) CNT membrane; $L_z = 6.0$ nm; $\Delta P = 8.0$ MPa; $T = 300$ K. The statistical error for each flux data is less than 10%. H-P Equation refers to the Hagen-Poiseuille Equation (Eqn. (6.1)) represented by the dashed line, and the solid line is the trend based on the simulation results.....	187
Figure 6.5	The ratio of the simulation flux to the theoretical flux as a function of the inverse liquid viscosity, for the six liquids through the (12, 12) CNT membrane; $L_z = 6.0$ nm; $\Delta P = 8.0$ MPa; $T = 300$ K. The statistical error for each flux data is less than 10%. The theoretical flux is calculated from the Hagen-Poiseuille equation (Eqn. (6.1)), and the solid line is the trend, for 5 carbon molecules, based on the simulation results.....	188
Figure 6.6	Density distributions, (a) molecule number density and (b) mass density, along the radial direction for the six liquids: density as a function of r ; values are averaged over a thin annular section in the pore at r (excluding the entrance and exit regions). The CNT membrane is	

modeled by the (12, 12) CNT, $L_z = 6.0$ nm; $\Delta P = 8.0$ MPa; $T = 300$ K. The statistical error for each data point is less than 1%. The solid lines are the trend curves based on the simulation results, and the dotted lines are the pore surface represented by the effective pore radius (0.643 nm). ...193

Figure 6.7 Orthographic snapshots (stick figures) of liquid molecules in the CNT membrane modeled by (12, 12) CNT: (a) water, (b) ethanol, (c) pentane, (d) 1-pentanol, (e) 1,5-pentanediol, and (f) benzene flows, as shown in Table 6.1. Molecules are represented by bonds and in different color: carbon atoms in green, hydrogen atoms in white, and oxygen atoms in red.195

Figure 6.8 Density distributions, (a) molecule number density and (b) mass density, along the flow direction for the water, ethanol, and 1-pentanol flows: density as a function of z ; values are averaged over a thin section at z (cylindrical sections in the pore and cuboid sections in the water reservoirs). The CNT membrane is modeled by the (12, 12) CNT, $L_z = 6.0$ nm; $\Delta P = 8.0$ MPa; $T = 300$ K. The statistical error for each data point is less than 1%. The solid lines are the trend curves based on the simulation results. The dashed lines are the membrane boundaries along z direction separating the system in three parts from left to right: the top reservoir, the pore of the CNT membrane, and the bottom reservoir.200

Figure 6.9 Simulation flux (m/s) as a function of the membrane pore size as

represented by the pore area for the ethanol, 1-Pentanol, and benzene flows. The points are based on three CNT membranes modeled by (8, 8) CNT, (10, 10) CNT, and (12, 12) CNT, shown in Table 6.2; $L_z = 6.0$ nm; $\Delta P = 8.0$ MPa; $T = 300$ K. The statistical error for each data point is less than 10%. The solid line is the trend based on the simulation results. H-P Equation refers to the Hagen-Poiseuille Equation (Eqn. (6.1)), and the dashed line is the trend based on the Hagen-Poiseuille Equation.204

Figure 6.10 Effect of pore size on mass density distributions along the radial direction for the (a) ethanol, (b) 1-Pentanol, and (c) benzene flows, respectively: density as a function of r ; values are averaged over a thin annular section in the pore at r (excluding the entrance and exit regions). The points are based on three CNT membranes modeled by (8, 8) CNT, (10, 10) CNT, and (12, 12) CNT, shown in Table 6.2; $L_z = 6.0$ nm; $\Delta P = 8.0$ MPa; $T = 300$ K. The statistical errors for most data points are less than 1%, and the larger errors ($< 10\%$) are found for some data points in the pore center sections. The solid lines are the trend curves based on the simulation results, and the dotted lines are the pore surfaces represented by the effective pore radii (Table 6.2).205

Figure 6.11 Orthographic snapshots (stick figures) of (a) ethanol, (b) 1-Pentanol, and (c) benzene molecules in the different CNT membranes: three CNT membranes are modeled by (8, 8) CNT, (10, 10) CNT, and (12, 12)

CNT, shown in Table 6.2. Molecules are shown by bonds and in different color: carbon atoms in green, hydrogen atoms in white, and oxygen atoms in red.206

Figure 6.12 Effect of pore size on mass density distributions along the radial direction for the (a) ethanol, (b) 1-Pentanol, and (c) benzene flows, respectively: density as a function of r ; values are averaged over a thin annular section in the pore at r (excluding the entrance and exit regions). The points are based on three CNT membranes modeled by (8, 8) CNT, (10, 10) CNT, and (12, 12) CNT, shown in Table 6.2; $L_z = 6.0$ nm; $\Delta P = 8.0$ MPa; $T = 300$ K. The statistical error for each data point is less than 1%. The solid lines are the trend curves based on the simulation results. The dashed lines are the membrane boundaries along z direction separating the system in three parts from left to right: the top reservoir, the pore of the CNT membrane, and the bottom reservoir.209

Figure 7.1 Chemical structure of the PA active layer of the NF 90 membrane (adapted from reference [42]): the symbol n denotes the degree of cross-linking with value in between 0–1 ($n=1$ for a fully cross-linking structure, and $n=0$ for a fully linear structure).220

Figure 7.2 Chemical structure of the linear PA polymer used to begin the modeling of the PA membranes. The 10 non-carboxylated units and 30 carboxylated units are arranged randomly with carboxyl acid groups

as end groups.	221
Figure 7.3 A snapshot of the dry (prehydrated) #2 membrane (a cubic PA membrane model composed of 21 PA polymers). Molecules are shown by bonds: carbon atoms in green, hydrogen atoms in white, oxygen atoms in red, and nitrogen atoms in blue.	223
Figure 7.4 The snapshot of the NEMD simulation system including the PA membrane model and two water reservoirs to simulate pressure-driven water flow along the $z+$ direction. The PA membrane shown by bonds in blue; the hydrogen atoms and oxygen atoms of water molecule showed by van der waals atoms in white and red, respectively. The external force (f) is applied on each water molecule of the two water layers near the top and bottom boundaries along the $z+$ direction.	226
Figure 7.5 Average water density distributions along the $x+$, $y+$, and $z+$ directions for the #1–4 PA membranes (see Table 7.1). The points of each membrane are based on the equilibrated status of the NEMD system at 300 K and 0.1 MPa. Each data point is the average of three density values from the cuboid sections at the same position along the $x+$, $y+$, and $z+$ directions; and the standard error of the three densities is less than 10% for most average density values. The solid lines are the trend curves based on the simulation results, and the dotted lines represent the average density values from -2.6 nm to +2.6 nm. The dashed lines are the membrane boundaries along the flow direction	

separating the system in to three parts from left to right: the water reservoir at the high pressure side, the PA membrane, and the water reservoir at the low pressure side.228

Figure 7.6 Average FFV distributions along the $x+$, $y+$, and $z+$ directions for the #1–4 PA membranes (see Table 7.1). The points of each membrane are based on the equilibrated status of the NEMD system at 300 K and 0.1 MPa. Each data point is the average of three FFV values from the cuboid sections at the same position along the $x+$, $y+$, and $z+$ directions; and the standard error of the three densities is less than 10% for most FFV values. The solid lines are the trend curves based on the simulation results, and the dotted lines represent the average FFV values from -2.6 nm to +2.6 nm. The dashed lines are the membrane boundaries along the flow direction separating the system in to three parts from left to right: the water reservoir at the high pressure side, the PA membrane, and the water reservoir at the low pressure side.231

Figure 7.7 Free volume hole distributions of the #1–4 PA membranes: the hole number as a function of the hole radius. The results are based on the equilibrated state of the system at 300 K and 0.1 MPa, and the properties of the #1–4 PA membranes are shown in Table 7.1. The solid curved is the log-normal distribution trend based on the free volume hole distribution for each PA membrane.233

Figure 7.8 FFV distributions of the #1–4 PA membranes: the FFV value as a

function of the hole radius. The results are based on the equilibrated state of the system at 300 K and 0.1 MPa, and the properties of the #1–4 PA membranes are shown in Table 7.1.234

Figure 7.9 Flux (rate per membrane area) at each pressure difference, shown both as molecular flux and conventional flux (in m/s), as a function of the mean free volume radius. The points are based on the NEMD simulations on the #1–4 membranes (Table 7.2): $L = 7.0$ nm; and $T = 300$ K. The solid curves are the trends through the origin based on the simulation results. The statistical error for each data point is evaluated and less than 10%.239

Figure 7.10 Flux (rate per membrane area) of each PA membrane, shown both as molecular flux and conventional flux (in m/s), as a function of the pressure difference. The points are based on the NEMD simulations on the #1–3 membranes (Table 7.2): $L = 7.0$ nm; and $T = 300$ K. The solid lines are the linear trends through the origin based on the simulation results. The statistical error for each data point is evaluated and less than 10%.241

Figure 7.11 Flux (rate per membrane area) of each PA membrane, shown both as molecular flux and conventional flux (in m/s), as a function of the pressure difference (as expected from Eqn. (7.1)). The points are based on the NEMD simulations on the three membranes (Table 7.4) at 300 K. The solid lines are the linear trends through the origin based

on the simulation results. The statistical error for each data point is evaluated and is less than 10%.	245
Figure 7.12 Water permeability coefficient as a function of the reciprocal of the membrane thickness. The water permeability coefficients and membrane thicknesses of the membranes are shown in Table 7.2 and Table 7.3. The standard error of each water permeability coefficient for the membrane model is evaluated from the linear regression of the linear trend (through the origin) in Figure 7.11, and is less than 10%.	246
Figure 8.1 The reaction formula of the PA active layer of the NF 90 membrane (adapted from reference [3]): the degree of cross-linking, n , is with value in between 0–1 ($n=1$ for a fully cross-linking structure, and $n=0$ for a fully linear cross-linking structure).	254
Figure 8.2 Inserting MPD cross-linkers between carboxylic acid groups of different PA reactants to form a cross-linked structure. The degree of cross-linking, n , is decided by the number of MPD cross-linkers inserted in the uncross-linked membrane model.	257
Figure 8.3 A snapshot of the dry (prehydrated) #3 PA membrane with the degree of cross-linking of 25% (Table 8.1). Molecules are shown by bonds: carbon atoms in green, hydrogen atoms in white, oxygen atoms in red, and nitrogen atoms in blue.	260
Figure 8.4 The snapshot of the NEMD simulation system including the PA membrane model and two water reservoirs to simulate pressure-driven	

water flow along the $z+$ direction. The PA membrane shown by bonds in blue; the hydrogen atoms and oxygen atoms of water molecule showed by van der waals atoms in white and red, respectively. The external force (f) is applied on each water molecule of the two water control layers near the top and bottom boundaries along the $z+$ direction.262

Figure 8.5 Flux (rate per membrane area) at each pressure difference, shown both as molecular flux and conventional flux (in m/s), as a function of the cross-link degree. The statistical error for each data point is evaluated and less than 10%. The points are based on the NEMD simulations on the #1–4 membranes (Table 8.1): $L = 7.0$ nm; and $T = 300$ K. The solid curves are the trends based on the simulation results.266

Figure 8.6 Flux (rate per membrane area) of each PA membrane, shown both as molecular flux and conventional flux (in m/s), as a function of the pressure difference. The statistical error for each data point is evaluated and less than 10%. The points are based on the NEMD simulations on the #1–4 membranes (Table 8.1): $L = 7.0$ nm; and $T = 300$ K. The solid lines are the linear trends through the origin based on the simulation results.267

Figure 8.7 Water permeability coefficient as a function of the free volume radius. The solid curve is the trend through the origin based on the simulation results. The radii of the #1–4 PA membrane are shown in Table 8.2;

and the standard error of each water permeability coefficient is evaluated from the linear regression of the linear trend (through the origin) in Figure 8.6 and is less than 10%.268

Figure 8.8 Average water density distributions along the $x+$, $y+$, and $z+$ directions for the #3, #5, and #6 PA membranes (see Table 8.1). The points of each membrane are based on the equilibrated status of the NEMD system at 300 K and 0.1 MPa. Each data point is the average of three density values from the cuboid sections at the same position along the $x+$, $y+$, and $z+$ directions; and the standard error of the three densities is less than 10% for most average density values. The solid lines are the trend curves based on the simulation results, and the dotted lines are the average densities from -2.6 nm to 2.6 nm. The dashed lines are the membrane boundaries along the flow direction separating the system in to three parts from left to right: the water reservoir at the high pressure side, the PA membrane, and the water reservoir at the low pressure side.273

Figure 8.9 Average ion density distributions along the $x+$, $y+$, and $z+$ directions for the #3, #5, and #6 PA membranes (see Table 8.1). The points of each membrane are based on the equilibrated status of the NEMD system at 300 K and 0.1 MPa. Each data point is the average of three density values from the cuboid sections at the same position along the $x+$, $y+$, and $z+$ directions; and the standard error of the three densities

is less than 10% for most average density values. The solid lines are the trend curves based on the simulation results, and the dotted lines are the average densities from -2.6 nm to 2.6 nm. The dashed lines are the membrane boundaries along the flow direction separating the system in to three parts from left to right: the water reservoir at the high pressure side, the PA membrane, and the water reservoir at the low pressure side.274

Figure 8.10 Bar chart of the water fluxes, shown both as molecular flux and conventional flux (in m/s), of the neutral (#3) and negatively charged membranes (#5, #6). The statistical error for each data point is evaluated and less than 10%. The results are based on the NEMD simulations: $L = 7.0$ nm; $T = 300$ K; and $\Delta P = 10$ MPa.276

List of Tables

Table 2.1	Specifications of different CNT membrane physical parameters used in the simulations.	53
Table 2.2	Comparison of the enhancement factors ^a between our NEMD simulation and the experimental data of Qin ^[45]	63
Table 2.3	Enhancement factors ^a of the #4–7 CNT membranes at 5.0 MPa pressure difference.	76
Table 3.1	Comparison of the two systems	102
Table 4.1	The Lennard-Jones parameters of the unmodified and modified CNT membranes	132
Table 5.1	Specifications (charged parts and charge densities) of the #1–4 membranes.	158
Table 6.1	Physical properties of liquid molecules.	182
Table 6.2	Effective radii of the three CNTs.	202
Table 7.1	Membrane properties of the #1–4 membranes. ^{a, b}	230
Table 7.2	FFV values and free volume radii of the #1–4 PA membranes. ^a	236
Table 7.3	Comparisons of the PA membranes and the NF 90 membrane.	242
Table 7.4	Water permeability coefficients of the modeled PA membranes with different membrane thicknesses.	244
Table 8.1	Parameters in the membrane modeling and NEMD simulations.	259

Table 8.2	Properties of #1–4 membranes with different degrees of cross-linking. ^{a,b}	265
Table 8.3	Comparisons of the PA membranes and the NF 90 membrane.	269
Table 8.4	Properties of the neutral and negatively charged membranes. ^a	272

List of Abbreviations and Symbols

\vec{a}_i	the acceleration of particle i
A_K	the membrane porosity
AMBER	Assisted Model Building and Energy Refinement
CHARMM	Chemistry at HARvard Molecular Mechanics
$C_{i,f}$	the concentration of solute i in the bulk feed
$C_{i,p}$	the concentration of solute i in the permeate
CNT	carbon nanotube
CVD	chemical vapor deposition
DCV-GCMD	dual control volume grand canonical molecular dynamics
E	the potential energy
E_{bend}	the bond-bend potential energy
E_{bonded}	the internal or bonded potential energy
E_{elect}	the electrostatic interaction potential energy
$E_{non-bonded}$	the external or non-bonded potential energy
$E_{rotation}$	the bond-rotation potential energy
$E_{stretch}$	the bond-stretch potential energy
E_v	the velocity error
E_{vw}	the van der Waals interaction potential energy

f	the force applied on each oxygen atom of the water molecules
f_b	the force applied on each carbon atom by the bottom movable wall
FFV	fractional free volume (%)
\vec{F}_i	the force exerted on particle i
f_t	the force applied on each carbon atom by the top movable wall
GROMOS	GRoningen MOlecular Simulation
H-P	Hagen-Poiseuille
IT	irreversible thermodynamics
J	the simulation flux (molecules/ns/nm ² , m ³ /(m ² s), m/s)
J_V	the volumetric solution flux (m/s)
J_W	the pure water flux (m/s)
J_{theor}	the theoretical flux (molecules/ns, molecules/ns/nm ² , m/s)
k_B	the Boltzmann constant
L	the thickness of the cubic PA membrane model (nm)
L_P	the pure water permeability coefficient (m/s/MPa)
L_x	the length of the CNT membrane model in x axis (nm)
L_y	the length of the CNT membrane model in y axis (nm)
L_z	The tube length of the CNT or the thickness of the CNT membrane model (nm)
MD	molecular dynamics
m_i	the mass of particle i
MPD	m-phenylenediamine

M_w	weight average molecular weight (g/mol)
n	the degree of cross-linking
N	the total number of atoms in the system or the number of time correlated samples
NAMD	NAnoscale Molecular Dynamics
NEMD	nonequilibrium molecular dynamics
NF	nanofiltration
N-S	Navier-Stokes
PA	polyamide
PBC	periodic boundary condition
PME	Particle Mesh Ewald
r	the radial position in the pore
R	the rejection of an NF membrane or the gas constant
r_c	the cut-off radius (nm)
\vec{r}_i	the atomic coordinate of particle i
r_{ij}	the distance between atoms i and j
$R_{min(ij)}$	the Lennard-Jones minimum interaction energy between atoms i and j (nm)
\vec{r}_N	the complete set of $3N$ atomic coordinates
RO	reverse osmosis
R_{obs}	the observed rejection of NF membrane

r_p	the pore radius of the membrane (nm)
SPC	simple point charge
SPC/E	extended simple point charge
t	the simulation time (fs, ps, ns)
T	the temperature (K)
TFC	thin-film composite
TIP3P	transferable intermolecular potential three-point
TMC	trimesoylchloride
UF	ultrafiltration
V	the volume of a sample section,
\vec{v}_i	the velocity of particle i
$\vec{v}_{i,0}$	the initial velocity of particle i
v_z	the average velocity along z direction
$v_z(r)$	the z -direction velocity at radial position r
VMD	Visual Molecular Dynamics
ΔP	the pressure difference (MPa)
Δx	the membrane effective thickness (nm)
$\Delta \pi$	the difference of osmotic pressure
$\varepsilon_{(ij)}$	the Lennard-Jones well-depth between atoms i and j (kJ/mol, kcal/mol)
η	the liquid viscosity (Pa · s)

ρ the liquid density (kg/m³)
 τ the pore tortuosity or the integrated autocorrelation time

Chapter 1 Introduction

In recent years, considerable attention has focused on liquid flows through nanoscale channels driven by external fields, because this transport process is a key constituent in various fields, such as biological channels, drug delivery, membrane separation, fuel cells, and novel nanofluidic applications (nanopumps, nanosyringes, nanosensors, etc.). Molecular dynamics (MD) simulations can be used to study an external field-induced liquid passing through a nanochannel and can directly give a molecular scale analysis and visualization of the liquid fluid, in order to help in understanding the transport mechanism and controlling the liquid flow.

This research focuses on studying pressure-driven liquid flows passing through nanofiltration (NF) membranes by using nonequilibrium molecular dynamics (NEMD) simulations.

1.1. Nanofiltration

Nanofiltration is a type of pressure-driven membrane process with properties between reverse osmosis (RO) and ultrafiltration (UF) membranes. The history of NF dates back to the late 1970s when RO membranes with a reasonable water flux operating at relatively low pressures were developed for water filtration and purification.^[1] The low-pressure RO membranes was given the name “nanofiltration” at the end of the 1980s.^[2, 3] By the

second half of the 1980s, NF had become established and the first applications had been reported. Starting in the early 1990s, journal publications and issued patents on NF have increased rapidly, and NF applications have been developed from a small scale to a large scale in industry.^[4]

The key difference between NF and RO is that NF allows monovalent salts and rejects multivalent salts to pass, while RO highly rejects monovalent salts. For example, NF does not exhibit a very high NaCl rejection but is well capable of removing divalent salts ($MgCl_2$, $CaCl_2$, etc.) and small organic molecules (like sucrose) at considerably lower pressures and higher fluxes, whereas RO is used where the high salt (NaCl) rejection is required but at high pressures. Since NF operates at a lower pressure than RO, energy costs of NF are lower than a comparable RO treatment system. Due to effectively removing hardness elements (such as calcium or magnesium) from water and leaving dissolved salts in water, NF is attractive to be applied in water softening and a NF membrane is often referred as the “softening membrane”.

1.1.1. Nanofiltration Membranes

NF processes usually have an operating pressure range of 0.5 – 2 MPa, and NF membranes have a pore size about 1 – 10 nm and molecular weight cutoffs of 200 – 1000 g/mol.^[5, 6] NF membranes can be categorized by the membrane materials into organic polymeric membranes, inorganic ceramic membranes, and organic/inorganic hybrid membranes; by the morphology into symmetric and asymmetric membranes; also by the structure into homogeneous (dense) and heterogeneous (porous) membranes.

Commercial NF membranes are generally made from synthetic polymers and fabricated as thin-film composite (TFC) membranes. The TFC membranes belong to the family of asymmetric membranes and are fabricated in a three-layer structure (shown in Figure 1.1): a non-woven polyester fabric as the substrate, a porous layer as the supporting base, and an ultra-thin, denser polymer coating as the active skin layer. The porous base acts as a mechanical support for the top layer and has a thickness of approximately 100 μm . The coating layer is the active layer that provides the selectivity of the NF TFC membrane. Common polymers used to produce the active layer include cellulose acetate, polyamide (PA), sulfonated polyethersulfone, sulfonated polysulfone, polyvinyl alcohol, polyphenylene oxide, polyethylenimine, and others.^[7-9]

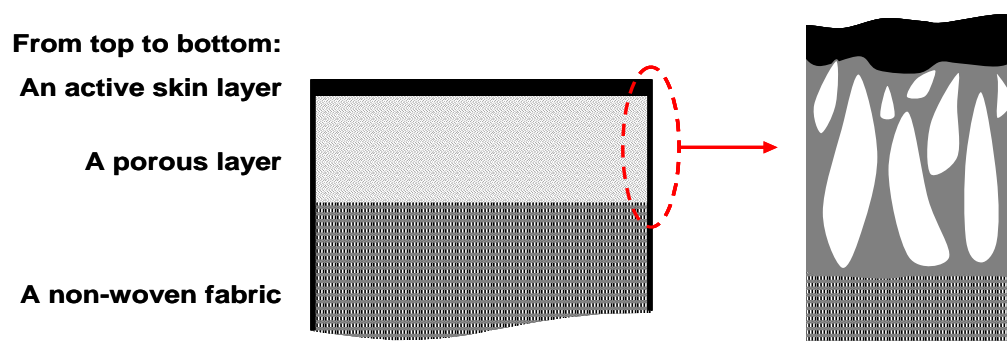


Figure 1.1 Schematic representation of a cross-section view of the typical TFC membrane (adapted from Figure III-4. in reference [8]).

Most NF membranes are charged, usually with negative charges. The charge may result from the dissociation of functional groups in the membrane matrix and/or the adsorption of ions on the membrane. Figure 1.2 shows a polymeric membrane with negative groups from deprotonated carboxylates. The charges affect the solution–membrane interactions and the electrical potential developed across the

membrane, and consequently have a significant effect on the membrane separation performance.

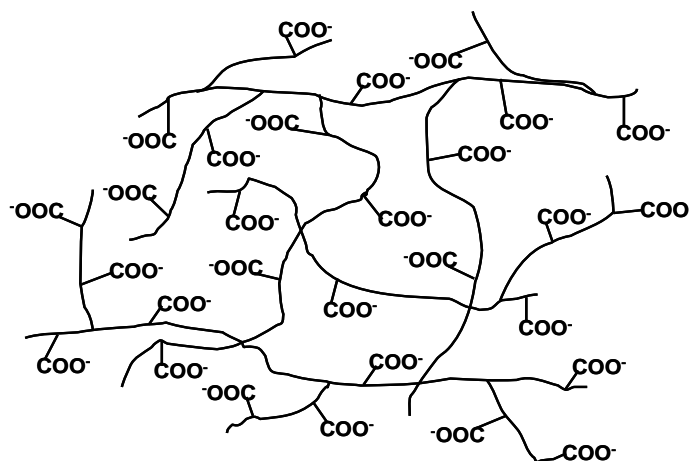


Figure 1.2 Schematic representation of a negatively charged NF membrane caused by deprotonated carboxylate groups.

The membrane performance is affected by membrane design factors and operation factors. The membrane design factors include pore size, membrane thickness, porosity, charges on the membrane, and surface area. The operation factors include solute concentration, pressure difference, operation temperature, pH value of the fluid, module design, feed pretreatment and configuration such as multiple-pass membranes.

1.1.2. Membrane Performance and Traditional Mathematical Modeling

The feed to a NF membrane is separated into a concentrated stream called the retentate and a purified stream called the permeate, as shown in Figure 1.3. The performance of the NF membrane is typically described by some measurements, such as pure water flux,

solute rejection, and solution flux.

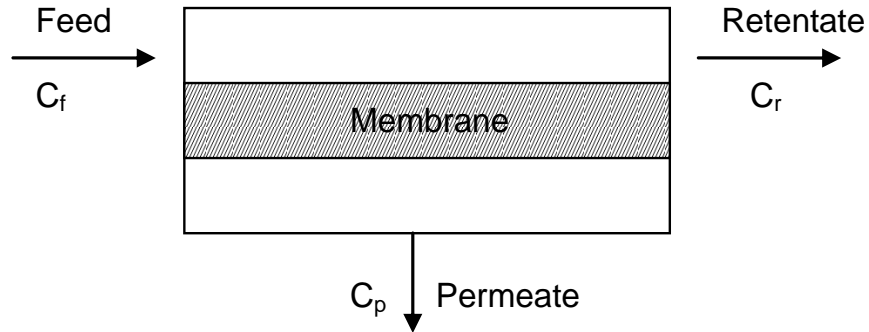


Figure 1.3 Schematic representation of a NF separation process (adapted from Figure I-3. in reference [8]).

The pure water flux (J_w) is a basic measurement for the NF membrane, which is related to the membrane structure and the applied pressure difference (ΔP) across the membrane. The Hagen-Poiseuille equation derived from the Navier-Stokes equations is used to calculate the pure water flux (J_w), as given by Equation (1.1):

$$J_w = L_p \Delta P = \frac{r_p^2}{8\eta\tau(\Delta x/A_K)} \Delta P \quad (1.1)$$

where L_p is the pure water permeability coefficient, r_p is the pore radius of the membrane, η is the viscosity of the solution at the operating temperature, τ is the pore tortuosity, and $\Delta x/A_K$ is the ratio of the membrane effective thickness to the membrane porosity.

Another important factor for describing the membrane performance is the membrane rejection, R . The rejection characteristic of a membrane for a solute i is through the observed rejection (R_{obs}), which is defined as:

$$R_{obs} = \frac{C_{i,f} - C_{i,p}}{C_{i,f}} \quad (1.2)$$

where $C_{i,f}$ and $C_{i,p}$ are the concentrations of the solute i in the bulk feed and in the permeate.

The volumetric solution flux (J_V), which is the permeate rate per membrane area, is related to the applied pressure (ΔP) and osmotic pressure ($\Delta\pi$) by Equation (1.3):

$$J_V = L_p (\Delta P - \Delta\pi) \quad (1.3)$$

The Eqn. (1.3) works with solute permeating as is evidenced by having a concentration ($C_{i,p}$) defined. For single non-dissociating solutes, the osmotic pressure ($\Delta\pi$) can be estimated using an adaptation of the van't Hoff Equation as,

$$\Delta\pi = RT \sum_i (C_{i,f} - C_{i,p}) \quad (1.4)$$

where R is the gas constant and T is the solution temperature (the operation temperature).

Various traditional mathematical models have been proposed to predict membrane transport performance. Generally, these models are based either on a non-mechanistic model such as irreversible thermodynamics (IT) or a mechanistic transport model.

In the IT theory, the NF membrane is assumed as a 'black box' separating the solutions on the two sides of the membrane. The basic assumption is that the system is divided into some subsystems where 'local equilibrium' can exist. The models based on the IT theory can relate fluxes to driving forces and can be set up with no assumption on the membrane structure nor the transport mechanism. Examples of IT membrane models are the Kedem-Katchalsky equations,^[10] Spiegler-Kedem equations,^[11] and Teorell-Meyers-Sievers model,^[12, 13] and so forth.

Mechanistic models assume a membrane structure and also relate fluxes to driving forces, and account for the physical and chemical characteristics of the membrane and

solution. The Solution-diffusion mechanism is usually used to explain the transport mechanism for nonporous membranes. Models based on the solution-diffusion mechanism are often applied to homogeneous NF membranes and are usually not used for transport in porous membranes. The Extended Nernst-Planck equation^[14, 15] with the inclusion of the Donnan exclusion effect is often applied to NF membranes, and the Donnan-steric pore model^[16] and space charge pore model^[17] are two main models based on the extended Nernst-Planck equation.

1.1.3. Advantages and Applications of Nanofiltration

A major advantage of membrane processes over other separation techniques, such as distillation, adsorption, or extraction, is that the products (solutions of metal ions, proteins, or other organics) are not destroyed or altered in membrane separation processes and are allowed to be recycled or reused. NF can offer other advantages, including low operation pressure, high flux, high rejection, relatively low investment, and low operation and maintenance costs.

Because of these advantages, the NF applications have increased worldwide, especially in water treatment field, such as water softening, organics removal, radium and heavy metal removal from wastewater, and sulfate removal from seawater.^[3, 18, 19] Other applications include pulp and paper effluent treatment in the papermaking industry, removal of dyes and other coloring agents in the textile industry, and concentration of intermediates and antibiotics in the pharmaceutical industry.^[4] Since the past few decades, using NF technology to remove organic micropollutants from water has grown

significantly, especially for removal of organic substances in drinking water treatment.^[20]

^{21]} The organic micropollutants can be found in a wide range of man-made chemicals used in industry and our daily life, including pesticides, hormones, endocrine disrupting compounds, pharmaceutically active compounds, personal care products, and so forth. The occurrence of the organic micropollutants in the water system has become an environmental problem and raises human-health concerns due to the toxicity or potential health effects.

The traditional models, as mentioned above, have only been partially successful in predicting the NF transport performance. A deep understanding in the transport of small compounds or ions through NF membranes is still a challenging issue, since solute transport depends on the physico-chemical properties of the solutes and the interaction between solutes and the NF membrane.

Using molecular dynamics (MD) simulations to study NF process is the approach investigated in this thesis. For traditional models the parameters are either phenomenological coefficients or parameters that have to be obtained from fitting experimental data. Sometimes the parameters are from independent data (like obtaining a pore size distribution by one method and using this distribution in the model) but most often from experimental NF data itself. Unlike using adjustable parameters in the traditional models, the method in this thesis will require no fitting parameters at all but are based on approximations of known physics. The MD studies in this thesis can show the dynamics of NF transport on the molecular scale and can be expected to verify the

assumptions in the traditional mathematical models and to provide a complete picture of the transport mechanism.

1.2. Molecular Dynamics Simulation

Molecular dynamics simulation is a form of computer simulation in which atoms and molecules are allowed to interact for a period of time by approximations of known physics, giving a view of the motion of the atoms. MD simulations can calculate the time-dependent behavior (trajectory information) and the time-dependent movement of particles in a system during a MD simulation can be visualized. MD simulation serves as a complement to conventional experiments in the hope of understanding the dynamic properties of molecules in terms of the structure and the microscopic interactions between them.

In the late 1950s, Alder and Wainwright first used MD simulations to study the interactions of hard spheres,^[22, 23] and then their studies invoke many important works about the dynamics behavior of simple liquids. In 1964, a realistic potential was first used to study liquid argon,^[24] and later a realistic water system was first simulated in 1974.^[25] In 1977, the MD simulation of the bovine pancreatic trypsin inhibitor was reported first for the protein study.^[26] Today, MD simulations have been applied widely in studying phase transitions, collective behaviors, complex fluids, fluid dynamics, polymers, biomolecules, and so forth.^[27] Next we will examine the major components of MD simulations.

1.2.1. Force Field

A MD simulation requires an empirical potential function for describing the particles interactions in the simulation. The empirical potential function is frequently called the force field. Some force fields have been developed for MD simulations, such as AMBER (Assisted Model Building and Energy Refinement) force field,^[28] CHARMM (Chemistry at HARvard Molecular Mechanics) force field,^[29] and GROMOS (GRONingen MOlecular Simulation) force field.^[30]

A force field consists of a summation of internal bonded forces and non-bonded forces,^[31] as shown in Equation (1.5). The bonded potential energy function includes several energy terms for describing the deviations of bond lengths, bond angles, and torsion angles away from equilibrium values; the non-bonded potentials are other external interactions such as the van der Waals and electrostatic interactions.^[31]

$$\begin{aligned}
 E &= E_{bonded} + E_{non-bonded} \\
 E_{bonded} &= E_{stretch} + E_{bend} + E_{rotation} \\
 E_{non-bonded} &= E_{vw} + E_{elect}
 \end{aligned}
 \tag{1.5}$$

where E is the total potential energy; E_{bonded} is the internal or bonded term composed by the bond-stretch energy ($E_{stretch}$), the bond-bend energy (E_{bend}), and the bond-rotation energy ($E_{rotation}$); and $E_{non-bonded}$ is the external or non-bonded term including the van der Waals interaction energy (E_{vw}) and the electrostatic interaction energy (E_{elect}).

The 6-12 type Lennard-Jones potential is commonly used to describe the van der Waals interaction. The Lennard-Jones potential expresses the interaction energy using the distance between two particles (r_{ij}) and the atom-type dependent constants ($\epsilon_{(ij)}$ and $R_{min(ij)}$):^[31]

$$E_{\text{VW}} = \sum_{\text{nonbondedatom pairs}} \varepsilon_{(ij)} \left[\left(\frac{R_{\text{min}(ij)}}{r_{ij}} \right)^{12} - 2 \left(\frac{R_{\text{min}(ij)}}{r_{ij}} \right)^6 \right] \quad (1.6)$$

where $\varepsilon_{(ij)}$ is the Lennard-Jones well-depth between atoms i and j ; and $R_{\text{min}(ij)}$ is the distance at the Lennard-Jones minimum interaction energy between atoms i and j .

The electrostatic interaction between a pair of atoms is usually represented by the Coulomb potential.^[31]

$$E_{\text{elect}} = \sum_{\text{nonbondedatom pairs}} \frac{q_i q_j}{4\pi\varepsilon_0 r_{ij}} \quad (1.7)$$

where ε_0 is the electric constant with a value of $8.854 \times 10^{-12} \text{ C}^2/(\text{N m}^2)$; q_i and q_j is the partial atomic charges of atoms i and j , respectively.

The set of parameters in the mathematical expression of a force field, such as equilibrium bond lengths, bond angles, force constants, van der Waals parameters, partial charge values, and so forth, are collectively known based on the implementation of molecular mechanics.^[32] Different force fields may have slightly different parameters in the potential functions to describe the same molecule. Therefore, the appropriate force field should be used in the MD simulation for a desired simulation system.

1.2.2. Force Calculations and Algorithm

A MD simulation consists of the numerical, step-by-step, solution of the classical equations of motion, which is based on Newton's second law or the equation of motion for a simple atomic system.^[31] The force on an atom is defined as:

$$\vec{F}_i = m_i \vec{a}_i \quad (1.8)$$

where \vec{F}_i is the force exerted on particle i , m_i is the mass of particle i , and \vec{a}_i is the acceleration of particle i .

The \vec{F}_i can be derived from the potential energy $E(\vec{r}_N)$, where the $\vec{r}_N = (\vec{r}_1; \vec{r}_2; \vec{r}_3; \dots; \vec{r}_N)$ represents the complete set of $3N$ atomic coordinates and N is the total number of atoms in the system:^[31]

$$\vec{F}_i = -\nabla_i E(\vec{r}_N) = -\left(\vec{i} \frac{\partial}{\partial x_i} + \vec{j} \frac{\partial}{\partial y_i} + \vec{k} \frac{\partial}{\partial z_i}\right)E \quad (1.9)$$

Take the simple case where the acceleration is constant and follows Newton's Second law. According to Eqns. (1.8) and (1.10), Newton's equation of motion can relate the derivative of the potential energy to the changes in velocity/position as a function of time, as:^[31]

$$\vec{a}_i = \frac{d\vec{v}_i}{dt} = \frac{d^2}{dt^2} \vec{r}_i = -\frac{1}{m_i} \nabla_i E(\vec{r}_N) \quad (1.10)$$

where \vec{a}_i is the acceleration of particle i , \vec{v}_i is the velocity of particle i at time t , and \vec{r}_i is the coordinate of particle i .

Integration of the equations of motion can yield a trajectory that describes the position and velocity of the particle:^[31]

$$\vec{v}_i = \vec{a}_i t + \vec{v}_{i,0} \quad (1.11)$$

$$\vec{r}_i = \frac{1}{2} \vec{a}_i t^2 + \vec{v}_{i,0} t + \vec{r}_{i,0} \quad (1.12)$$

where the above equation gives the values of \vec{v}_i and \vec{r}_i at time t as a function of \vec{a}_i and the initial velocity ($\vec{v}_{i,0}$).

From the knowledge of the force on each atom, it is possible to determine the acceleration of each atom in the system. Once the position and velocity of each atom are known, the state of the system can be predicted at any time in the future or the past. Thus positions and the velocities at an initial time determine the positions and velocities at all other times, t .

The MD algorithms used to solve the Newton's equations of motion in the system are commonly based on a Taylor series expansion.^[31] The trajectory information (the positions, velocities and accelerations) can be approximated by the integration algorithms. Numerous numerical algorithms have been developed for integrating the equations of motion, such as Verlet algorithm,^[33] Leap-frog algorithm,^[34] Beeman's algorithm,^[35] and Velocity Verlet algorithm;^[36] and these algorithms all have different advantages and disadvantages. In choosing which algorithm to be used, some criteria should be considered: for example, the algorithm should be computationally efficient and should permit a long time step for integration.

1.2.3. Periodic Boundary Conditions

The "periodic boundary conditions" (PBC) are a set of boundary conditions that are often used to simulate a system with a large size by modeling a small part that is far from the edge of the system.^[31] The PBC is particularly useful for simulating a part of a bulk

system with no surfaces present, such as bulk gasses, liquids, crystals or mixtures. Using PBC is usually required that the unit cell of the simulation system should be a three-dimensional shape, and a cube or cuboid prism is the most common choice for the unit cell.

All atoms in the simulation system are put into a unit cell, which is a geometrically suitable space-filling box and is surrounded by some translated copies (called “images”) of the unit cell. A large system can be view as periodically repeated perfect tiles of the unit cell, and then there is no edge effect on the unit cell. During the simulation, only the properties of the unit cell need to be recorded and propagated. When an atom passes through one face of the unit cell, it reappears on the opposite face with the same velocity and other properties. Figure 1.4 shows an example of a two-dimensional section through a small portion of a periodically repeated system: the center cell containing grey particles is the unit cell; the copies surround the unit cell, and the positions of the particles (images) in a copy are the same as in the unit cell. For instance, as the red particle in the unit cell leaves the left boundary, its image (the blue particle) enters from an adjoining copy, shown by the vector displacement. For a 3D rectangular system, for instance, particles leaving from any of the six sides reappear in the diametrically opposite cell; for instance, particles exiting the back of the cell reenter at the front. The PBC allows each particle in the unit cell to be influenced by every other particle in the unit cell.

In addition to applying PBC in a three-dimensional system, a two-dimensional PBC is often used in a slab boundary condition or a planar surface condition. Figure 1.5 shows

an example of a slab boundary condition with two-dimensional PBC for simulating a liquid flow in a slit: the unit cell has two solid walls in the z direction and liquid between the walls. The x and y directions are set with periodic boundaries, so there is no edge effect in the x and y direction. The two-dimensional PBC for a planar surface condition is usually used to study surface properties, such as surface tension, surface absorption, and so forth.

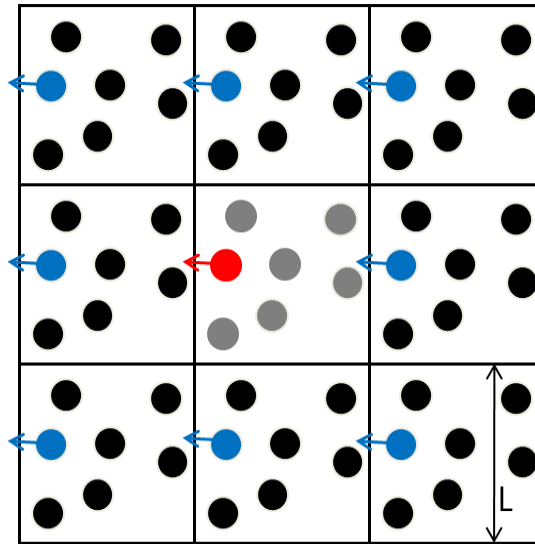


Figure 1.4 Periodic boundary conditions in a two-dimensional section.

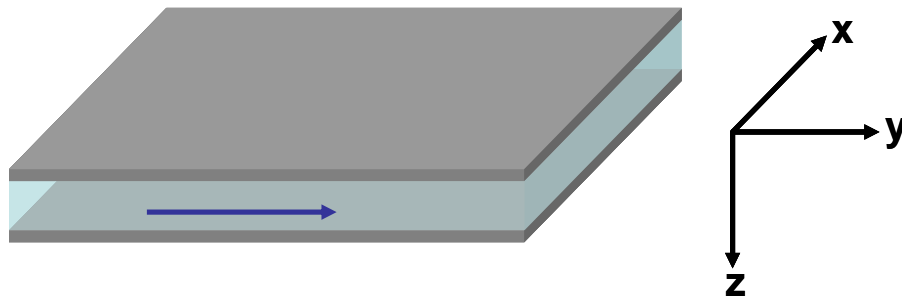


Figure 1.5 A simulation system in a two-dimensional PBC for simulating a liquid flow through a slit between two solid walls: the liquid in light blue, and the walls in grey.

In MD simulations, the minimum-image convention is a common method for calculating the potentials among atoms in the simulation system: each atom only interacts with the closest atom/image of the remaining atoms. A distance parameter, named cut-off radius, r_c , is introduced for calculating the potentials based on the minimum-image convention, in order to avoid the inaccuracy results by repeating calculations. As shown in Figure 1.6, the red particle in the unit cell only interacts with the particles/images, which are at a distance smaller than the r_c . The potential between any particle/image pair is negligible, if the distance between the particle/image pair is not within the certain value of r_c . Using a small r_c typically gives rise to significant errors, while using a large r_c is computationally expensive. Generally, the value of r_c cannot exceed half of the cell length (cell length is L as in Figure 1.4), and r_c is usually chosen as 1.0-1.5 nm.

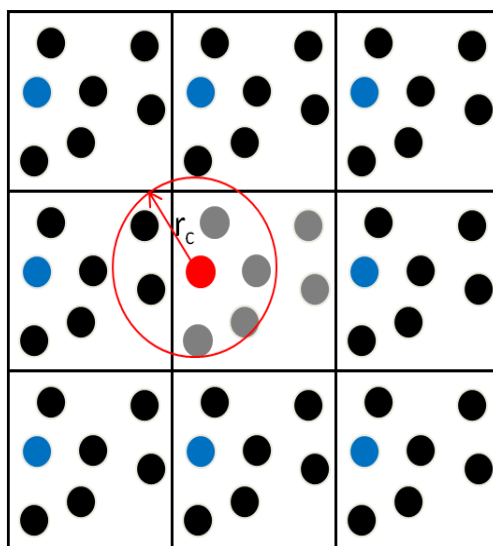


Figure 1.6 Cut-off radius in a two-dimensional section.

1.2.4. Water Molecule Models

Water is composed of two hydrogen atoms and one oxygen atom. Because of the higher electronegativity of the oxygen atom compared to that of the hydrogen atom, the oxygen site in a water molecule model has a “partial negative charge,” and the hydrogen sites has a “partial positive charge.” Many molecular models have been proposed for describing water in MD simulation. These models can be classified according to the number of sites (from 2-site to 6-site models), the structure (rigid or flexible), and the polarization effects (with or without).

The 3-site models are popular for MD simulations because of the simplicity and computational efficiency. These kinds of models have three interaction sites, corresponding to the three atoms of the water molecule. Each atom gets assigned a point charge, and only the oxygen atom has Lennard-Jones parameters. The 3-site models include transferable intermolecular potential three-point (TIP3P) model,^[37] simple point charge (SPC) model,^[38] extended simple point charge (SPC/E) model,^[39] etc. Most 3-site models use a rigid geometry matching the known geometry of the water molecule. An exception is the SPC model, which assumes an ideal tetrahedral shape (H-O-H angle of 109.47 °) instead of the observed angle of 104.5 °. The 4-site models set the negative charge on a dummy atom placed near the oxygen along the bisector of the H-O-H angle, such as Bernal-Fowler model and potential four-point (TIP4P) model^[40]. In the 5-site models, two dummy atoms with negative charges are set to represent the lone electron pair on the oxygen atom; while the 6-site model contains both structures of the 4-site and 5-site models.

The simulations in this thesis are carried out by using NAMD (NANoscale Molecular Dynamics) package^[41] based on the CHARMM (Chemistry at HARvard Molecular Mechanics)^[42] force field. NAMD only supports the TIP3P model^[37] and the TIP4P model^[40]. Unlike the original TIP3P model in which the van der Waals force is only set on the oxygen atom, the TIP3P water model in NAMD package is a flexible model and includes the Lennard-Jones parameters for the hydrogen atoms. The TIP3P model used in simulations is specified as follow: “a predominance of positive charge on each hydrogen atom (0.417e) and excess negative charge on the oxygen atom (-0.834 e); the O-H bond length (r_{OH}) and H-O-H bond angle (θ_{HOH}) are set to equal to experimental gas-phase values (0.9572 Å and 104.52 °), respectively;^[37] and the Lennard-Jones parameters in CHARMM force field are $R_{min(HH)} = 0.04490$ nm, $\epsilon_{(HH)} = 0.19255$ kJ/mol (0.0460 kcal/mol), $R_{min(OO)} = 0.35364$ nm, and $\epsilon_{(OO)} = 0.63666$ kJ/mol (0.1521 kcal/mol)”.^[41] The use of a flexible water model with Lennard-Jones parameters for both the oxygen and hydrogen atoms requires more calculations during a MD simulation compared to a rigid water model with only Lennard-Jones parameters for the oxygen atom but produces a more accurate representation of the water molecule needed in this work.

1.3. Carbon Nanotubes

Carbon nanotubes (CNTs) are allotropes of carbon with a cylindrical nanostructure, and can be seen as a member of the fullerene family. CNTs are categorized based on the structure as single-walled carbon nanotubes (SWNTs), multi-walled carbon nanotubes

(MWNTs), torus, nanobud, and cup stacked CNTs. Most SWNTs have a diameter of close to 1-2 nm, with a tube length that can be many millions of times longer. Different forms of SWNTs depend on atomic arrangement to be classified as zigzag, armchair, and chiral SWNTs. The zig-zag SWNT is (n, 0) type, the armchair SWNT is (n, n) type, and the chiral SWNT is (n, m) type.

The chemical bonds of CNTs are composed entirely of C-C sp^2 bonds, similar to bonds of graphite; the all sp^2 bonds of the CNT can build a layered structure with strong in-plane bonds. The bond structure makes the CNT exhibit extraordinary mechanical properties, such as high tensile strength,^[43,44] elastic modulus,^[45, 46] and bulk modulus.^[47] In addition to the distinguishing mechanical properties, CNTs also show some other important properties: good thermal properties,^[48, 49] either metallic or semiconductor properties^[50] and chemical reactivity.^[51]

The remarkable properties of CNTs and the nanoscale pore size make the CNT attractive for studying water transport of nanochannels. Through MD simulation studies of water in CNTs, some different transport properties with in bulk fluid are found: the single-file formation of water in CNT,^[52, 53] the extraordinarily fast water flow,^[54, 55] the gating phenomenon of water permeation,^[56] and so forth.^[57] In addition to the results of the MD studies, the fast water transport of CNTs or CNT membranes has been found through experimental studies.^[58-61] Due to the exceptional materials properties and the enhanced water transport, CNTs are the great choice to be applied in membrane transport.

It can be expected that the potential for application of CNTs to NF could be large and show greater separation performance. Partial studies in this thesis are to study the water

transport through CNT membranes at realistic NF conditions through MD simulations.

1.4. Literature Review

In this section, studies that have used molecular dynamics (MD) simulations to model pressure-driven liquid transport and to model polyamide (PA) membranes are reviewed.

1.4.1. NEMD Simulations of Pressure-driven Transport

Some simulation works using MD have been published for studying liquid flows through membranes or CNTs, and the driven force for the flow can be pressure difference,^[62-66] osmotic pressure difference,^[67, 68] and electric field.^[69] The transport in a NF process is driven by the pressure difference and the concentration difference to carry solvent and solute across the membrane. Therefore, the pressure-driven flow through NF membrane is not an equilibrium condition and cannot be studied by equilibrium MD simulations. To understand the microscopic dynamic properties of the NF transport by using MD studies, we turn to nonequilibrium molecular dynamics (NEMD) simulations. NEMD is a valuable tool for studying the liquid flow through nanoscale channels, such as the pores in an NF membrane, induced by pressure difference.

The key point of a NEMD methodology for simulating a NF process is to design a simulation system, in which the constant pressure difference across the NF membrane can be produced to drive the flow through the NF membrane. In general, the pressure difference across the membrane is achieved by applying external forces on the simulation system. Two kinds of NEMD simulation systems are commonly used to study

pressure-driven liquid flows passing through nanoporous membranes. The major differences between the two system kinds are the PBC along the flow direction and the methodology to produce the pressure difference across the membrane.

A. NEMD simulation systems with two-dimensional PBC

This kind of simulation system is modified from the dual control volume grand canonical molecular dynamics (DCV-GCMD) method.^[70-72] The PBC is not applied along the flow direction, and a two-dimensional PBC is used in this kind of system. Two different pressures at the two sides of the nanoporous membrane can be generated from the different external forces applied on the two sides, in order to drive the liquid flow passing through the membrane. The NEMD simulation system, used in the previous works^[54, 62, 63] for studying pressure-driven liquid flows, is either a closed system or an open system.

Figure 1.7 shows a closed NEMD system, where external forces are applied on two solid movable walls located perpendicular along the flow direction at the front and back boundaries resulting in a closed system in terms of the flow direction. The two movable walls can automatically maintain the pressures to be constant in the two liquid reservoirs, and steady-state permeation through the nanopore can be achieved by using this closed system. Using this kind of system, Huang^[62, 73-75] examined liquid argon transport through a straight cylindrical nanopore by performing NEMD simulations. Takaba^[63] also investigated the transport properties of liquid argon flows through slit and cylindrical nanopores driven by a constant pressure difference. These published works all chose

argon as the liquid flow, so the simulation temperature must be quite low in order to keep argon in the liquid state. However, the operation temperature in a NF process is typically at room temperature, generally about 300 K.

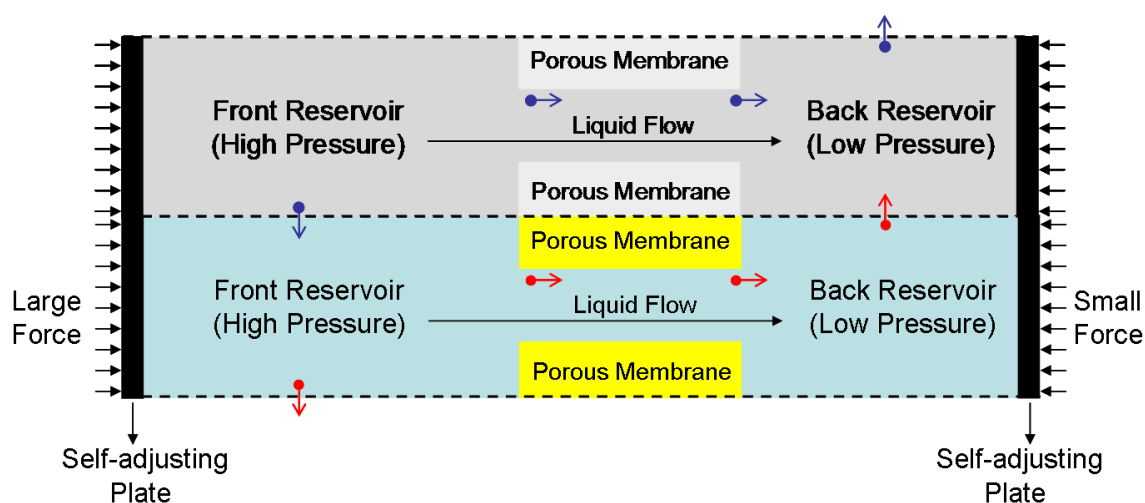


Figure 1.7 Schematic representation (in a two-dimensional section view) of a closed NEMD simulation system in 2D PBC (adapted from references [62] and [63]). The color drawing is the unit system, where external forces are applied on two solid movable walls (in black) located perpendicular along the flow direction. The dashed lines are periodic boundaries, and the grey drawing is the periodic copy of the unit system. The water molecules in the unit system leaving a boundary re-enter the unit system from the opposite boundary, and the periodic movement of water molecules does not exist in the flow direction due to 2D PBC.

Figure 1.8 shows an open system introduced by Nicholls^[54] for investigating pressure-driven water transport through CNTs. In this open system, the movable walls of the closed system are replaced by two water control zones, and external forces are applied on two water zones. The water control zones play similar roles as the movable walls in the closed system to control the pressures in the water reservoirs. However, water molecules in the water zones are continually inserted to the front control zone and

removed from the back control zone, as the water flow passes the CNT from the front water reservoir to the back water reservoir. The inserting and removing molecules in the control zones results in an open system in terms of the flow direction, and requires the USHER algorithm^[76] to maintain material balance and the dynamics steady for the system.

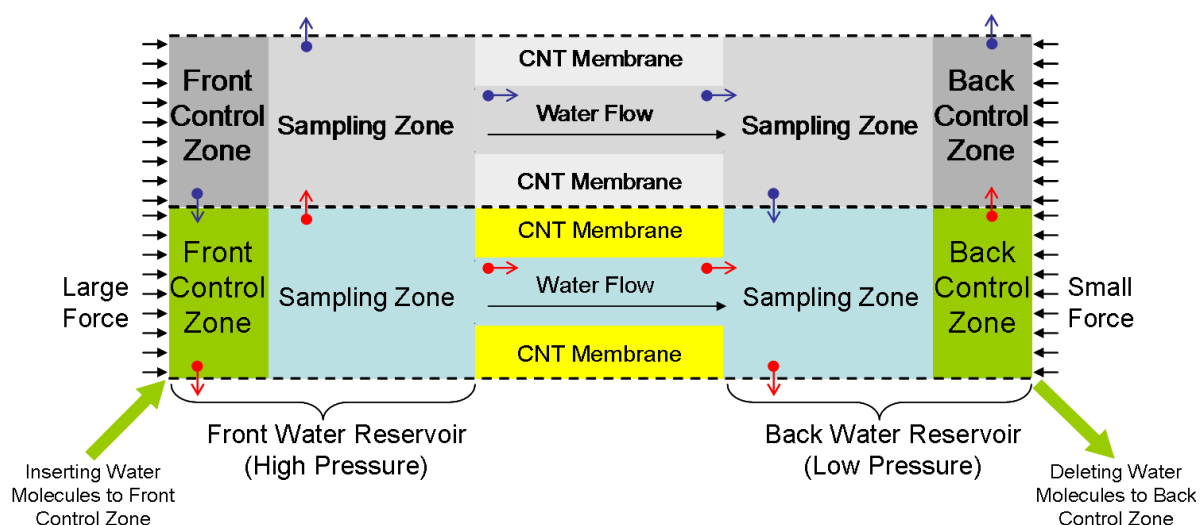


Figure 1.8 Schematic representation (in a two-dimensional section view) of an open NEMD simulation system in 2D PBC (adapted from references [54]). The color drawing is the unit system, where external forces are applied on two water control zones (in green) located near the boundaries along the flow direction. The dashed lines are periodic boundaries, and the grey drawing is the periodic copy of the unit system. The water molecules in the unit system leaving a boundary re-enter the unit system from the opposite boundary, and the periodic movement of water molecules does not exist in the flow direction due to 2D PBC.

The closed and open NEMD simulation systems both produce two pressure sides across the membrane to form a pressure-driven liquid flow: the external forces are applied on two movable walls in the closed system but on two water zones in the open system. For the closed system, the argon molecules in each liquid reservoir vary as the

argon flow passes through the membrane. For the open system, the water molecules in each reservoir are constant with water molecules passing through the CNT, due to water molecules continually being inserted in the upper reservoir and deleted from the bottom reservoir. The inserting/deleting liquid molecules and the external forces directly applied on the liquid molecules suggest that the open system is suitable for studying a liquid flow with a smaller molecular size, such as water, ions, and argon. However, the closed system can be used to study different kinds of liquid flows, for example, an organic flow with larger molecular size or a mixed-liquid flow containing multi-components.

B. NEMD simulation systems with three-dimensional PBC

The NEMD simulation systems with three-dimensional PBC usually contains a membrane model connecting top and bottom liquid reservoirs, and the system is periodically repeated along the flow direction, as shown in Figure 1.9. The PBC along the flow direction requires that the water molecules leaving the bottom boundary immediately appear at the top boundary.

This NEMD simulation system is often used to investigate aqueous flows passing through different membranes, which can be CNT membranes,^[52, 64] palmitoyloleoyl phosphatidyl- ethanolamine membranes,^[66] and other modeled membranes.^[65, 77] The pressure difference across the membrane is generated by applying external forces along the flow direction on all or parts of liquid molecules (water molecules or other liquids and/or ions) in the system. Figure 1.10 shows a more reasonable method to produce the

pressure difference by applying external forces on parts of water molecules in the system. A constant external force is applied on each molecule of the two water control layers, which have the same thickness and are located near the top and bottom boundaries along the flow direction, respectively.

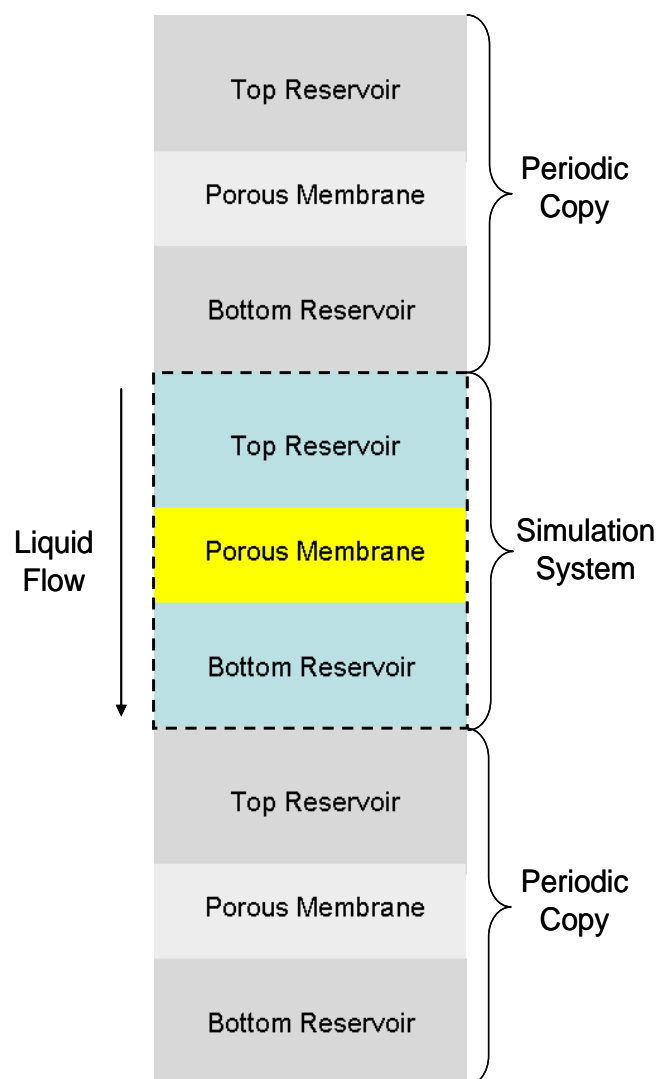


Figure 1.9 Schematic representation (in a two-dimensional section view) of the PBC along the flow direction for a unit system in 3D PBC. The dashed lines are periodic boundaries. The PBC along other two directions are not shown in this figure.

Some previous works already used this kind of system and the open system (as introduced above) to study pressure-drive water flows through membranes. The pressure-driven flows in these published works are simulated at similar temperatures to real NF processes, but are driven by very high pressure differences, even hundreds of that in a real NF process (usually 100 MPa or more). Little research, that we are aware of, has been done at realistic NF operating conditions to show the NF transport properties, which is one of the objectives in this thesis.

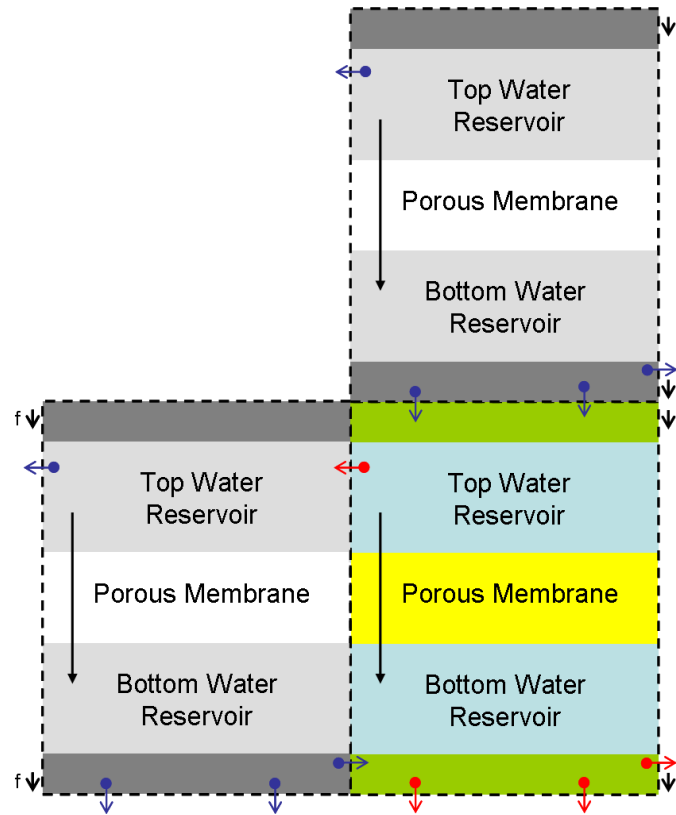


Figure 1.10 Schematic representation (in a two-dimensional section view) of one type of the NEMD simulation system in 3D PBC. The color drawing is the unit system, where external forces are applied on two water control layers (in green) located near the boundaries along the flow direction. The dashed lines are periodic boundaries, and the grey drawings are the periodic copies of the unit system. The water molecules in the unit system leaving any boundary re-enter the unit system from the opposite boundary, due to 3D PBC.

1.4.2. Simulations of NF Polymeric Membranes

Before simulating transport phenomenon of a real polymeric NF membrane, the polymeric membrane should be modeled first through MD simulations. For modeling polymers by MD simulations, two different methods, the full atomistic simulation method and the coarse-graining simulation method, are generally used. In the full atomistic simulation method, a molecule is described by a full atoms model containing atomistic information for every atom of the molecule.

In the coarse-graining simulation method, a molecule is represented by several rigid groups of atoms and each group as a coarse-graining site connected with another group (site) by an atomic bond. Clearly, the full atomistic simulation requires many more calculations than the coarse-graining MD simulation, due to the larger number of intramolecular or intermolecular potential energies in the system. The major advantages of the coarse-graining MD simulation method are a longer timescale or time-step allowed in MD simulations and less high-computational resource resulting in less computational cost. The difficulty of the coarse-graining MD simulation method is to determine the empirical parameters of the small molecules or the modeled coarse-grained polymers for describing the molecules or polymers to well match the appropriate experimental data or the full atomistic simulation results. The full atomistic MD simulation can model molecules or polymers with a better accuracy and reliability but requires a higher computational cost than the coarse-graining MD simulation.

MD simulations of some permeable polymers for gas transport (permeants such as H₂, O₂, N₂, CO₂, CH₄, or other gases/vapors) have been published for many years. For

example, polycarbonate,^[78-80] poly(2,6-dimethyl-1,4-phenylene oxide),^[81] polyimide,^[82, 83, 84] and polydimethylsiloxane^[85, 86, 87] have been studied for gas/vapour transport. Recently, some works have focused on study liquid transport properties of polymeric membranes through MD simulations, such as water-ethanol mixtures through a polydimethylsiloxane membrane by pervaporation,^[88] ionic conduction of nanoscale porous polyethylene terephthalate,^[89] the solubility of drugs in block copolymers,^[90, 91] and aqueous solution through cross-linked PA membranes by RO.^[92-96]

As introduced above, most commercial NF membranes are polymeric membranes with thin-film composite (TFC) structure. The FilmTec[®] NF 90 membrane manufactured by DOW Company is one of several commercially successful NF membranes. The top layer of the NF 90 membrane is a cross-linked aromatic PA fabricated through interfacial polymerization. In a real operation, the NF 90 membrane becomes a negatively charged membrane at pH=7, because the unreacted carboxylic acid groups are deprotonated to negatively charged carboxylate anions (as shown in Figure 1.2).^[97]

Figure 1.11 shows the polymerization reaction formula for the PA top layer of the NF 90 membrane, where the two monomers, trimesoyl chloride (TMC) and m-phenylene diamine (MPD), react to form a cross-linked PA. Some TMC monomer reacts incompletely to form linear chains (with the MPD) and some are left unreacted resulting in a cross-linked structure with pendent acid chloride groups that form carboxylates in aqueous solution. Kwon^[98] investigated the degree of cross-linking, n , (as in Figure 1.11) of the aromatic PA for the NF 90 membrane experimentally and found cross-linking degrees up to 25.6%.

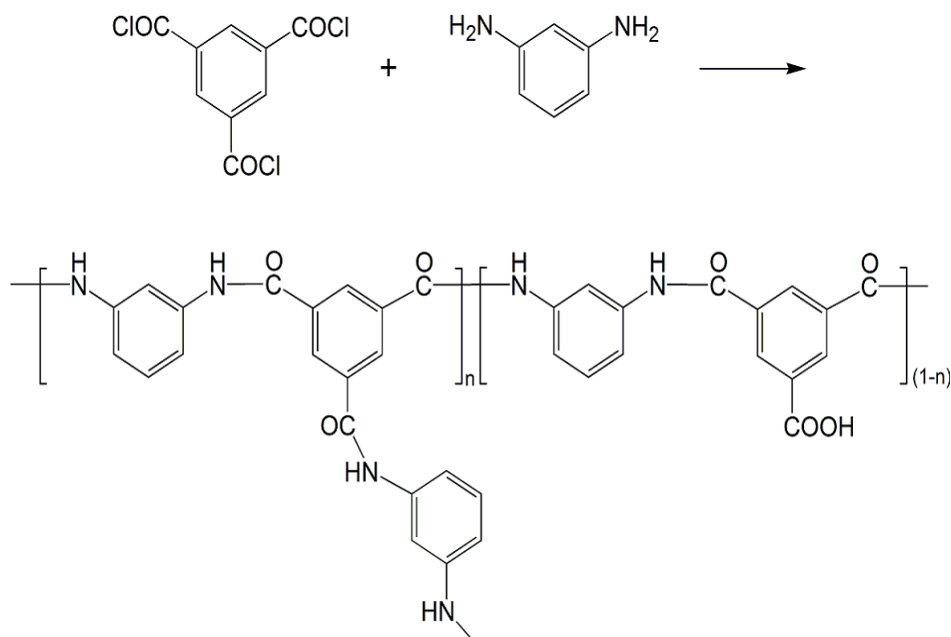


Figure 1.11 The reaction formula of the PA active layer of the NF 90 membrane. The cross-linking degree, n , is defined by the percentage of the cross-linked repeat units to the total repeat units.

No matter, using the full atomistic simulation method or using the coarse-graining simulation method, it is important to model the cross-linked bonds in the PA polymer. The cross-linked PA membranes have been modeled as the PA top layer of the FT 30 membrane by using full atomistic MD simulations or coarse-graining MD simulations in some previous works to study liquid transport of RO membranes through MD simulations.^[92, 94, 95, 96, 99-101] The FT 30 membrane, manufactured by Dow Company, is an RO membrane and has a quite similar chemical structure of the top PA layer of the NF 90 membrane (the cross-linked aromatic PA polymer shown in Figure 1.11).

Based on the simulation studies for the FT 30 membrane, there are three simulation approaches to model the cross-linked structures in the PA membrane: (1) to simulate interfacial polymerization between two monomer cells of TMC and MPD respectively,^{[96,}

^{99, 100]} (2) to simulate traditional polymerization in a TMC-MPD mixture,^[94, 101] (3) to simulate cross-links between linear PA polymers by inserting MPD monomers.^[92, 95] The simulation of a polymerization (the first or second approach) are close to the real membrane fabrication but need a reasonable force field to define the molecules/polymers continually formed in the polymerization simulation. The cross-linking simulation (the third approach) only needs to parameterize the linear PA polymer and the cross-linker (MPD), which is usually easier and faster than the polymerization simulation. Moreover, the cross-linking degree is hard to be controlled in the polymerization simulation, while the cross-linking simulation can control the cross-linking degree which is decided by the number of the cross-linkers inserted in PA polymers.

In the previous simulation works of FT 30 membranes, the pressure-driven liquid transport through the membrane is studied at a much higher pressure difference (> 100 MPa) than the NF operating condition by using the NEMD simulation, and the diffusivity or solubility of small molecules in the membrane is studied by using the equilibrium MD simulation. So far, few works have been focused on modeling a polymeric NF membrane and then studying a pressure-driven liquid transport at realistic NF conditions through NEMD simulations.

In this research, NEMD simulation systems are constructed based on the literature works to investigate the transport properties of pure pressure-driven liquid flows through CNT or PA membranes under realistic NF operating conditions for the first time.

1.5. Research Objectives

This research treats liquid flows passing through approximate NF membranes under reasonable NF operating conditions; few such works have been published previously.

The major challenge of this research is to build a NEMD simulation system and methodology to well represent a real NF processes. The overall objectives of this research are to deeply understand transport phenomena of the NF process on the molecular scale and to provide potential in helping to better design NF membranes.

The specific objectives of this research are:

1. To design a NEMD simulation method.

A NEMD simulation system is constructed to simulate the NF process, such as pressure control, membrane structure, simulation size, and so forth; and the simulation methodology should be chose appropriately, such as force field, molecule models, integration algorithm, PBC, and so forth. The simulation method should well present a real NF process, so that reliable simulation results can be obtained.

2. To analyze the transport phenomena.

The transport phenomenon can be described by the flux, and the density and velocity distributions of liquid fluids, which are obtained from analyzing simulation results. The effects of the membrane structure (pores size, membrane thickness, and electrical charge) and pressure difference on the transport phenomena are investigated.

3. To compare simulation results with literature data or theoretical results by traditional models.

A comparison of the simulations with some literatures or traditional models is helpful

to evaluate the NEMD simulations method, to verify the assumptions in traditional models, and to test the accuracy of the traditional models.

1.6. Thesis Outline

The research provides a valuable tool, NEMD simulations, for describing the pure liquid transport through NF membranes and providing the fundamental basis for the NF process.

In this Chapter, the basic knowledge about NF, MD, and NEMD are introduced and some recent literatures related to this research are reviewed. Also the objectives of this research are clarified and the thesis outline is provided. The thesis is of the sandwich style and is based on the materials in Chapters 2-8 (as introduced below).

Chapter 2 is to construct a NEMD simulation system derived from previous works for simulating liquid argon flows. The constructed NEMD system is used to study pressure-driven water flows passing through well defined carbon nanotube (CNT) membranes under NF operating conditions (low pressure differences). The CNT membranes having different pore size and membrane thickness are modeled to study the effects of the membrane structure (pores size, membrane thickness) on the transport phenomenon. The simulation results of the water transport are compared with the experimental results evaluated by using the experimentally manufactured CNT membranes and with traditional models based on the Navier-Stokes equations. Chapter 2 is reproduced with permission from the reference [102].

Chapter 3 gives two NEMD simulation systems which are constructed by using

different methodologies to produce the pressure difference across the membrane. The two systems use the same CNT membrane model and are used to simulation the pressure-driven water flow at the same pressure difference. The effect of pressure difference on the pure water transport is studied and the simulation results of the two systems are compared.

In Chapter 4, the CNT membrane model used in the previous chapters are modified to still be neutral membranes but with different Lennard-Jones parameters or with positive and negative charges on the carbon atoms in the CNT membrane. The influence of the water –CNT interactions, including the van der Waals interactions and the electrostatic interactions, on the transport properties are investigated by simulating pressure-driven water flows through unmodified CNT membrane and modified CNT membranes.

In Chapter 5, the pressure-driven water transports through charged CNT membranes are studied. The unmodified CNT membrane is set with positive or negative charges on the carbon atoms of the CNT membrane to model positively or negatively charged membranes. The electrostatic interactions between water molecules and the charged CNT membranes on the transport properties are investigated by using NEMD simulations.

Chapter 6 is the NEMD simulations of pressure-driven organic liquid flowing through the CNT membrane instead of water. To investigate the effects of molecular structure and physical properties on the transport phenomenon, the pressure-driven liquid flows are modeled using five different organic molecules and water molecule for comparison.

Chapter 7 presents a full atomistic MD simulation method (derived from a previous

work for modeling a porous polymeric membrane) to model an amorphous uncross-linked PA membrane composed of linear PA polymers. The free volume properties of the amorphous PA membranes composed of PA polymers in different numbers are evaluated, such as the fractional free volume and free volume radius of each membrane. The effects of membrane structure and pressure difference on the pressure-driven water transport properties are investigated through NEMD simulations.

In Chapter 8, a series of cross-linked PA membranes are modeled as the aromatic PA active layer of a commercial NF 90 membrane through MD simulations (based on the previous works for modeling RO membranes) and pressure-driven water flows through the membranes are simulated at NF operating conditions (low pressure differences) through NEMD simulations. The membrane structures and water transport properties of the membranes are analyzed to investigate the effects of cross-linking degree and electrical charges on the membrane structure and water transport.

Chapter 9 summarizes the major conclusions of the thesis and proposes some recommendations for future work.

References

- [1] B. Van der Bruggen and C. Vandecasteele, *Environ. Pollut.* **122** 435 (2003).
- [2] W. J. Conlon and S. A. McClellan, *J. Am. Water Works Ass.* **81** 47 (1989).
- [3] J. Schaep, B. Van der Bruggen, S. Uytterhoeven, R. Croux, C. Vandecasteele, D. Wilms, E. Van Houtte and F. Vanlerberghe, *Desalination* **119** 295 (1998).
- [4] A. I. Schäfer, A. G. Fane, T. D. Waite, *Nanofiltration: Principles and Applications*,

(Elsevier Advanced Technology, Oxford, 2005).

- [5] L. E. Applegate, Chem. Eng. (New York) **91** 64 (1984).
- [6] S. Ramakrishna, Z. Ma, and T. Matsuura, *Polymer Membranes in Biotechnology: Preparation, Functionalization and Application*, (Imperial College, London, 2011).
- [7] W. Ho and K. Sirkar, *Membrane Handbook*, (Van Nostrand Reinhold, New York, 1992).
- [8] M. Mulder, *Basic Principles of Membrane Technology*, (Kluwer Academic Publisher, London, 1996).
- [9] R. Petersen, J. Membr. Sci. **83** 81 (1993).
- [10] O. Kedem and A. Katchalsky, Biochim. Biophys. Acta. **27** 229 (1958).
- [11] K. Spiegler and O. Kedem, Desalination **1** 311 (1966).
- [12] T. Tsuru, S. Nakao, and S. Kimura, J. Chem. Eng. Jpn. **24** 511 (1991).
- [13] X. Wang, T. Tsuru, M. Togoh, S. Nakao, and S. Kimura, J. Chem. Eng. Jpn. **28** 186 (1995).
- [14] R. Schogl, Ber. Bunseng. Physik. Chem. **70** 400 (1966).
- [15] L. Dresner, Desalination **10** 27 (1972).
- [16] W. Bowen, A. Mohammad, and N. Hilal, J. Membr. Sci. **126** 91 (1997).
- [17] X. Wang, T. Tsuru, S. Nakao, and S. Kimura, J. Membr. Sci. **103** 117 (1995).
- [18] N. Hilal, H. Al-Zoubi, N. A. Darwish, A. W. Mohammad, and M. Abu Arabi, Desalination **170** 281 (2004).
- [19] X. Lu, X. Bian, and Shi, L. J. Membr. Sci. **210** 3 (2002).

- [20] S. A. Snyder, S. Adham, A. M. Redding, F. S. Cannon, J. DeCarolis, J. Oppenheimer, E. C. Wert, and Y. Yoon, *Desalination* **202** 156 (2006).
- [21] C. H. Huang and D. L. Sedlak, *Environ. Toxicol. Chem.* **20** 133 (2001).
- [22] B. J. Alder and T. E. Wainwright, *J. Chem. Phys.* **27** 1208 (1957).
- [23] B. J. Alder and T. E. Wainwright, *J. Chem. Phys.* **31** 459 (1959).
- [24] A. Rahman, *Phys. Rev. A* **136** 405 (1964).
- [25] F. H. Stillinger and A. Rahman, *J. Chem. Phys.* **60** 1545 (1974).
- [26] J. A. McCammon, B. R. Gelin, and M. Karplus, *Nature* **267** 585 (1977).
- [27] D. C. Rapaport, *The Art of Molecular Dynamics Simulation (Second Edition)*, (Cambridge University Press, Cambridge, 2004).
- [28] W. D. Cornell, P. Cieplak, C. I. Bayly, I. R. Gould, K. M. Jr. Merz, D. M. Ferguson, D. C. Spellmeyer, T. Fox, J. W. Caldwell, and P. A. Kollman, *J. Am. Chem. Soc.* **117** 5179 (1995).
- [29] A. D. MacKerell, N. Banavali, and N. Foloppe, *Biopolymers* **56** 257 (2001).
- [30] N. Schmid, A. Eichenberger, A. Choutko, S. Riniker, M. Winger, A. Mark, and W. van Gunsteren, *Eur. Biophys. J.* **40** 843 (2011).
- [31] M. P. Allen, *Introduction to Molecular Dynamics Simulation*, in: N. Attig, K. Binder, H. Grubmüller, K. Kremer (Eds.), *Computational Soft Matter: From Synthetic Polymers to Proteins, Lecture Notes*, (John von Neumann Institute for Computing, Jülich, 2004).
- [32] U. Burkert and N. L. Allinger, *Molecular Mechanics*, (American Chemical Society,

Washington, DC, 1982).

- [33] L. Verlet, Phys. Rev. **165** 201 (1968).
- [34] R. W. Hockney and J. W. Eastwood, *Computer Simulations Using Particles*, (Adam Hilger, Bristol, 1988).
- [35] D. Beeman, J. Computat. Phys. **20** 130 (1976).
- [36] W. C. Swope, H. C. Andersen, P. H. Berens, and K. R. Wilson, J. Chem. Phys. **76** 637 (1982).
- [37] W. L. Jorgensen, J. Chandrasekhar, J. D. Madura, R. W. Impey, and M. L. Klein, J. Chem. Phys. **79** 926 (1983).
- [38] H. J. C. Berendsen, J. P. M. Postma, W. F. van Gunsteren, and J. Hermans Interaction models for water in relation to protein hydration, in *Intermolecular Forces*, edited by B. Pullman (Reidel, Dordrecht, 1981).
- [39] H. J. C. Berendsen, J. R. Grigera, and T. P. Straatsma, J. Phys. Chem. **91** 6269 (1987).
- [40] W. L. Jorgensen and J. D. Madura, Mol. Phys. **56** 1381 (1985).
- [41] J. Phillips, R. Braun, W. Wang, J. Gumbart, E. Tajkhorshid, E. Villa, C. Chipot, R. D. Skeel, L. Kalé and K. Schulten, J. Comput. Chem. **26** 1781 (2005).
- [42] A. D. MacKerell, N. Banavali, and N. Foloppe, Biopolymers **56** 257 (2001).
- [43] R. S. Ruoff and D. C. Lorents, Carbon **33** 925(1995).
- [44] M. F. Yu, O. Lourie, M. Dyer, K. Moloni, T. Kelly, and R. S. Ruoff, Science **287** 637 (2000).

- [45] B. T. Kelly, *Physics of Graphite*, (Applied Science Publisher, London, 1981).
- [46] M. M. J. Treacy, T. W. Ebbesen, T. M. and Gibson. *Nature* **381** 678 (1996).
- [47] M. Popov, M. Kyotani, R. J. Nemanich, and Y. Koga, *Phys. Rev. B* **65** 033408 (2002).
- [48] E. Thostenson, C. Li, and T. Chou, *Compos. Sci. Technol.* **65** 491 (2005).
- [49] E. Pop, D. Mann, Q. Wang, K. Goodson, and H. Dai. *Nano Lett.* **6** 96 (2006).
- [50] P. G. Collins and P. Avouris, *Sci. Am.* **283** 62 (2000).
- [51] S. Niyogi, M. A. Hamon, H. Hu, B. Zhao, P. Bhowmik, R. Sen, M. E. Itkis, and R. C. Haddon, *Acc. Chem. Res.* **35** 1105 (2002).
- [52] B. Corry, *J. Phys. Chem. B* **112** 1427 (2008).
- [53] G. Hummer, J. C. Rasaiah, and J. P. Noworyta, *Nature* **414** 188 (2001).
- [54] W. D. Nicholls, M. K. Borg, D. A. Lockerby, and J. M. Reese, *Microfluid. Nanofluid.* **12** 257 (2012).
- [55] M. E. Suk and N. R. Aluru, *J. Phys. Chem. Lett.* **1** 1590 (2010).
- [56] H. Fang, R. Wan, X. Gong, H. Lu, and S. Li, *J. Phys. D: Appl. Phys.* **41** 103002 (2008).
- [57] A. Alexiadis and S. Kassinos, *Chem. Rev.* **108** 5014 (2008).
- [58] J. K. Holt, H. G. Park, Y. Wang, M. Stadermann, A. B. Artyukhin, C. P. Grigoropoulos, A. Noy, and O. Bakajin, *Science* **312** 1034 (2006).
- [59] M. Majumder, N. Chopra, R. Andrew, and B. J. Hinds, *Nature* **438** 44 (2005).
- [60] M. Majumder, N. Chopra, and B. J. Hinds, *ACS Nano* **5** 3867 (2011).

- [61] X. Qin, Q. Yuan, Y. Zhao, S. Xie, and Z. Liu, *Nano Lett.* **11** 2173 (2011).
- [62] C. Huang, K. Nandakumar, P. Choi, and L. W. Kostiuk, *J. Chem. Phys.* **124** 234701 (2006).
- [63] H. Takaba, Y. Onumata, and S. Nakao, *J. Chem. Phys.* **127** 054703 (2007).
- [64] J. Goldsmith and C. C. Martens, *J. Phys. Chem. Lett.* **1** 528 (2010).
- [65] K. Leung and S. B. Rempe, *J. Comput. Theor. Nanosci.* **6** 1948 (2009).
- [66] F. Zhu, E. Tajkhorshid, and K. Schulten, *Biophys. J.* **83** 154 (2002).
- [67] A. Kalra, S. Garde, and G. Hummer, *Proc. Natl. Acad. Sci. U.S.A.* **100** 10175 (2003).
- [68] A. N. Raghunathan and N. R. Aluru, *Phys. Rev. Lett.* **97** 024501 (2006).
- [69] J. Su and H. Guo, *ACS Nano* **5** 351 (2011).
- [70] J. M. D. Macelroy, *J. Chem. Phys.* **101** 5274 (1994).
- [71] R. F. Cracknell, D. Nicholson, and N. Quirke, *Phys. Rev. Lett.* **74** 2463 (1995).
- [72] H. Takaba, E. Matsuda, and S. Nakao, *J. Phys. Chem. B* **108** 14142 (2004).
- [73] C. Huang, P. Choi, K. Nandakumar, and L. W. Kostiuk, *J. Chem. Phys.* **126** 224702 (2007).
- [74] C. Huang, P. Choi, K. Nandakumar, and L. W. Kostiuk, *Phys. Chem. Chem. Phys.* **10** 186 (2008).
- [75] C. Huang, P. Choi, K. Nandakumar, and L. W. Kostiuk, *J. Nanosci. Nanotechnol.* **9** 793 (2009).
- [76] R. Delgado-Buscalioni and P. V. Coveney, *J. Chem. Phys.* **119** 978 (2003).

- [77] J. Goldsmith and C. C. Martens, *Phys. Chem. Chem. Phys.* **11** 528 (2009).
- [78] A. A. Gusev and U. W. Suter, *J. Chem. Phys.* **99** 2228 (1993).
- [79] M. Lopez-Gonzalez, E. Saiz, J. Guzman, and E. Riande, *J. Chem. Phys.* **115** 6728 (2001).
- [80] A. A. Gusev, U. W. Suter, and D. J. Moll, *Macromolecules* **28** 2582 (1995). [81] J. R. Fried, M. Sadat-Akhavi, and J. E. Mark, *J. Membr. Sci.* **149** 115 (1998).
- [82] M. Heuchel and D. Hofmann, *Desalination* **144** 67 (2002).
- [83] M. Heuchel, D. Hofmann, and P. Pullumibi, *Macromolecules* **37** 201 (2004).
- [84] S. Neyertz and D. Brown, *Macromolecules* **37** 10109 (2004).
- [85] D. Hofmann, L. Fritz, J. Ulbrich, and D. Paul, *Polymer* **38** 6148 (1997).
- [86] D. Hofmann, L. Fritz, J. Ulbrich and D. Paul, *Comput. Theor. Polym. Sci.* **10** 419 (2000).
- [87] J. S. Yang, K. Choi, and W. H. Jo, *MacroMol. Theor. Simul.* **9** 287 (2000).
- [88] L. Fritz and D. Hofmann, *Polymer* **38** 1035 (1997).
- [89] E. R. Cruz-Chu, T. Ritz, Z. S. Siwy, and K. Schulten, *Faraday Discuss.* **143** 47 (2009).
- [90] S. K. Patel, A. Lavasanifar, P. Choi, *Biomaterials* **31** 345 (2010).
- [91] S. K. Patel, A. Lavasanifar, P. Choi, *Biomacromolecules* **9** 3014 (2008).
- [92] M. J. Kotelyanskii, N. J. Wagner, and M. E. Paulaitis, *J. Membr. Sci.* **139** 1 (1998).
- [93] M. J. Kotelyanskii, N. J. Wagner, and M. E. Paulaitis, *Comput. Theor. Polym. Sci.* **9** 301 (1999).

- [94] E. Harder, D. E. Walters, Y. D. Bodnar, R. S. Faibish, and B. Roux, *J. Phys. Chem. B* **113** 10177 (2009).
- [95] Z. E. Hughes and J. D. Gale, *J. Mater. Chem.* **20** 7788 (2010).
- [96] R. Oizerovich-Honig, V. Raim, and S. Srebnik, *Langmuir* **26** 299 (2010).
- [97] C. Bellona and J. E. Drewes, *J. Membr. Sci.* **249** 227 (2005).
- [98] Y. Kwon, C. Y. Tang, and J. O. Leckie, *J. Appl. Polym. Sci.* **108** 2061 (2008).
- [99] J. Pitera, T. Chen, Y. Na, R. Sooriyakumaran, A. Vora, and G. Dubois. Computational modeling of reverse osmosis membrane active layers: structure and transport, (NAMS Annual Meeting, Las Vegas, USA, 2011).
- [100] R. Nadler and S. Srebnik, *J. Membr. Sci.* **315** 100 (2008).
- [101] Y. Luo, E. Harder, R. S. Faibish, B. Roux, *J. Membr. Sci.* **384** 1 (2011).
- [102] L. Wang, R. S. Dumont, and J. M. Dickson, *J. Chem. Phys.* **134** 044102 (2012).

Chapter 2 Nonequilibrium Molecular Dynamics Simulation of Water Transport through Carbon Nanotube Membranes at Low Pressure

This chapter is reproduced based on the article by L. Wang, R. S. Dumont, and J. M. Dickson, Nonequilibrium Molecular Dynamics Simulation of Water Transport through Carbon Nanotube Membranes at Low Pressure. Reprinted with permission from L. Wang, R. S. Dumont, J. M. Dickson, *Journal of Chemical Physics* **134** 044102. Copyright © 2012 American Institute of Physics.

Author contributions: Luying Wang performed all research studies and the manuscript preparation. Dr. Dumont participated in some discussion and provided helpful suggestions. Dr. Dickson supervised this work and revised the manuscript.

2.1. Abstract

Nonequilibrium molecular dynamics (NEMD) simulations are used to investigate pressure-driven water flow passing through carbon nanotube (CNT) membranes at low pressures (5.0 MPa) typical of real nanofiltration (NF) systems. The CNT membrane is modeled as a simplified NF membrane with smooth surfaces, and uniform straight pores of typical NF pore sizes. A NEMD simulation system is constructed to study the effects of the membrane structure (pores size and membrane thickness) on the pure water transport properties. All simulations are run under conditions (temperature and pressure

difference) similar to the operating condition of a real NF processes. Simulation results are analyzed to obtain water flux, density and velocity distributions along both the flow and radial directions. Results show that water flow through a CNT membrane under a pressure difference has the unique transport properties of very fast flow and a non-parabolic radial distribution of velocities, which cannot be represented by the Hagen-Poiseuille or Navier-Stokes equations. Density distributions along radial and flow directions show that water molecules in the CNT form layers with an oscillatory density profile, and have a lower average density than in the bulk flow. The NEMD simulations provide direct access to dynamic aspects of water flow through a CNT membrane, and give a view of the pressure-driven transport phenomena on a molecular scale.

2.2. Introduction

Carbon nanotubes (CNTs) are allotropes of carbon with a cylindrical nanostructure, and are members of the fullerene family. Most CNTs have nanoscale channels, extremely nonstick tube surfaces, and extraordinary mechanical properties - on length scales up to several millimeters.^[1] These remarkable properties make them attractive candidates for pores in membranes used in membrane separation. Currently, the experimentally produced CNT membranes typically consist of an aligned array of CNTs growing on a template by chemical vapor deposition (CVD) process^[2-5] or CNTs immobilized in a polymer membrane.^[6, 7] Application of these membranes in gas separation^[4, 7] and water desalination^[6] are also studied experimentally and exhibit fast gas and water flux.

Because of the quite narrow pore size and the high water flux, the potential for application of CNT membranes to nanofiltration (NF) is large; with greater separation performance, low-cost, and energy-savings.

NF is a pressure-driven membrane separation process that has several advantages over other membrane separation processes, such as low operation pressure, high flux, high rejection, relatively low investment, and low operation/maintenance costs. Because of these advantages, NF technology has been applied worldwide in different fields since the late 1980s, especially in water treatment,^[8-10] such as water purification, water softening, recovery of specific chemicals, concentration of products (such as proteins and dyes), and removal of organic solutes. Most commercial NF membranes are operated at room temperature and low pressure.^[11] Membranes are typically made from synthetic polymers; and are often fabricated as thin-film composite (TFC) membranes. The top layer of a TFC membrane is an ultra-thin, dense polymeric coating with a pore diameter about 1 to 10 nm. It provides the selectivity, while the remaining two porous layers act to support the surface layer.^[12]

In a molecular dynamics (MD) simulation, atom positions and momenta are evolved for a period of time according to classical mechanics and well-known approximate interactions between atoms. This provides an atomic-level dynamic picture of the process being simulated. Today, MD simulations have been applied widely in studying phase transitions, collective behavior, complex fluids, fluid dynamics, polymers, biomolecules, etc.^[13] The pressure-controlled methods to maintain a constant pressure were reported in the 1980s^[14, 15] and continue to be used as reported in recent works.^[16-18]

However, these methods are intended for equilibrium conditions - there is no driving force across the membrane if the pressure is constant. They are not strictly applicable to the real nonequilibrium conditions in a membrane process. An actual NF process is naturally a nonequilibrium process due to the pressure and concentration differences across the membrane, and the resulting transport of material through the membrane. Nonequilibrium molecular dynamics (NEMD) simulations provide direct access to the molecular motions induced by external fields; in this case, the liquid flow through the membrane driven by the pressure difference.

In this study, all NEMD simulations are carried out at 5.0 MPa pressure difference across the CNT membranes; this pressure difference value is at the high end of pressure differences used for real NF processes. In previous simulation works studying the water flow through CNTs or CNT membranes, the pressure difference is usually set at about 100 – 200 MPa or even much higher, so that low statistical errors of simulation results (e.g. flux and stream velocity) can be achieved with trajectory data collected within a few nanoseconds.^[19-22] To simulate at such high pressure differences is interesting but those pressure difference are not relevant to practical NF transport. The simulations done here at the pressure difference of 5.0 MPa require long simulation times to collect enough data (up to hundreds of millions of samples) to get statistically significant data.

A key point of the NEMD simulation for studying a pure liquid flow passing through a NF membrane is to design a simulation system in which two different external pressures across the membrane can be maintained in a nonequilibrium condition. Recently, Nicholls^[22] reported a NEMD simulation methodology to investigate water transport

through CNTs with different tube lengths driven by a pressure difference of 200 MPa. The pressures of the upstream and downstream sides are controlled by applying external forces on a control zone, which is composed by water molecules located near the upstream or downstream boundary of the system. The NEMD simulation system is an open system similar to the dual control volume grand canonical molecular dynamics (DCV-GCMD) method.^[23-25] Water molecules are continually inserted to the upstream control zone and removed from the downstream while water molecules are transported from the upstream to downstream zones during the NEMD simulation. This method can maintain two constant pressures in a nonequilibrium condition, but the method of inserting and removing molecules during the simulation requires the liquid molecule should be small and have a simple chemical structure.

Besides the open NEMD system, two similar NEMD simulation systems are presented by Huang^[26-29] and by Takaba,^[30] respectively, to study pressure-driven liquid argon fluid transport through a slit or cylindrical nanoporous membrane. In their simulation system, two liquid reservoirs are connected by a single straight nanopore and are sealed by two moveable walls. The moveable walls are located perpendicular to the nanopore to cause the liquid to flow through the nanopore. The model includes interactions of the walls with liquid molecules or the membrane. The pressure difference is achieved by applying large and small external forces on the movable walls to produce high and low pressures sides of the membrane. It has been shown that this closed NEMD simulation system has a constant number of liquid molecules and achieves two constant pressure sides inducing a steady flow through the membrane.^[26, 30] This NEMD simulation method is

theoretically suitable to study different liquid flows, but so far is only published to study transport properties of liquid argon fluids. The simulation temperatures in the published works are quite low (about 133 K or 85 K)^[26-30] in order to keep argon as a liquid phase. However, real NF processes operate with water near room temperature, about 300 K.

In this work, a CNT membrane with a single straight pore is modeled as the selective layer of the NF membrane. The CNT membrane is a simplified membrane with smooth surfaces and uniform straight pores of typical NF pore sizes. Based on the NEMD systems reported by Huang^[26] and Takaba,^[30] a simulation system is constructed to study pure water liquid through CNT membranes under NF operating conditions by using NEMD simulations. The effects of the membrane pores size and the membrane thickness, on the transport properties are investigated. The transport properties of pure water, including the flux, density and velocity distributions along both the radial and flow directions, are obtained through the NEMD simulation results. The flux results are compared with theoretical values calculated by the Hagen-Poiseuille equation, and the velocity distributions in the nanopore are compared with the appropriate solution to the Navier-Stokes equation.

The effect of pressure difference across the CNT membrane on water transport is shown elsewhere,^[31] and therefore not repeated here, where we compare the method of simulation used in this current paper to others shown in previous literature. That paper shows that the simulation method used here is more consistent with real system than previous simulation systems. Overall, the effect of pressure is consistent with the results in this paper with similar oscillatory density and velocity profiles and enhanced water

flux over conventional transport theory.

2.3. Simulation Methods

A CNT membrane model (shown in Figure 2.1) is modeled by an armchair single-walled CNT (the membrane pore) perpendicularly embedded in two graphene sheets (the membrane surfaces). The Cartesian coordinates are defined with the direction of flow through the CNT along the z direction and the surface of the membrane in the x and y directions (4.0 nm by 4.0 nm). Two water reservoirs are connected by the CNT membrane model to form the high-pressure (top) and low-pressure (bottom) sides to simulate a pressure-driven water flow through the CNT membrane.

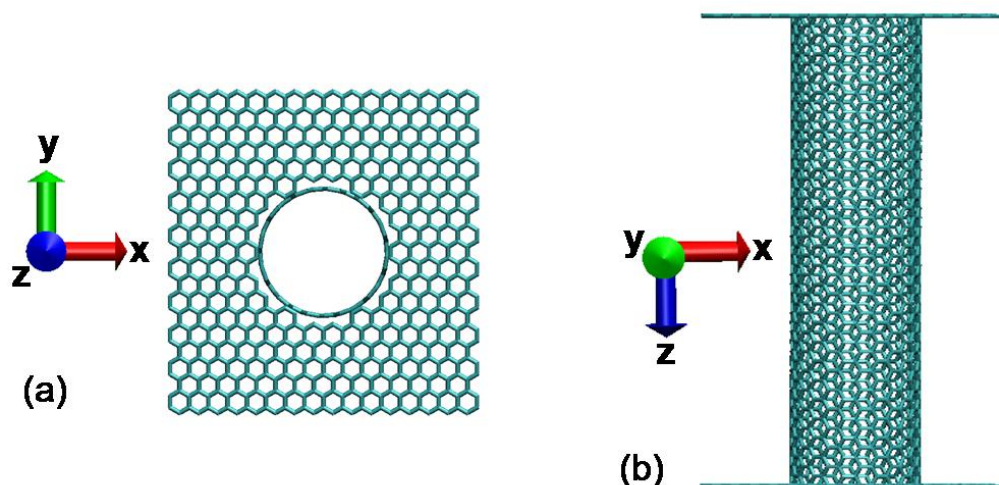


Figure 2.1 Orthographic snapshots of the CNT membrane model produced by the VMD package for the MD simulation: (a) Top view down through the CNT membrane model; (b) Side view of the CNT membrane model. Two graphene sheets are located at the ends of the CNT and each sheet has an approximated hole in the center to match the pore size of the CNT.

The system model, shown in Figure 2.2, has two additional graphene sheet moveable

walls for creating the pressure difference across the CNT membrane. An external force along $+z$ is applied on each carbon atom of top wall to produce a pressure of 5.1 MPa, while an external force along $-z$ is applied on each carbon atom of the bottom wall to produce a pressure of 0.1 MPa (close to the atmospheric pressure). During the simulations, water molecules can interact with the movable walls and the CNT membrane. The walls must therefore be started far from the membrane surfaces to avoid interactions between walls and membrane surface or between walls and water molecules near the membrane, which would affect the simulation results. The number of water molecules in each simulation is 10 000 or larger depending on the membrane pore size and thickness. For some representative cases, simulations were run with different simulation times and/or different numbers of molecules to insure that the results were representative and not anomalies of the choices for system simulation conditions.

NAMD (NANoscale Molecular Dynamics) package^[32] is used to run NEMD simulations based on the CHARMM (Chemistry at HARvard Molecular Mechanics)^[33] force field. The VMD (Visual Molecular Dynamics) package^[34] is used to construct simulation models and analyze simulation results. In the CHARMM force field, the nonbonded term, also called the long-range potential energy, is modeled by the Lennard-Jones 6-12 type potential and the Coulomb potential, for describing van der Waals interactions and electrostatic interactions, respectively. To describe the water molecules the modified flexible TIP3P (transferable intermolecular potential three-point) water model^[35] in CHARMM force field is used: a positive charge of 0.417e is set on each hydrogen atom and a negative charge of -0.834e on the oxygen atom. The original

TIP3P water model as a typical 3-site model specifies a rigid water molecule matching with the known geometry and physics of the water molecule, while the TIP3P model in CHARMM force field is modified to include Lennard-Jones parameters of hydrogen atoms to represent a flexible water molecule. The Lennard-Jones parameters of the water model are $R_{min(HH)} = 0.04490$ nm, $\epsilon_{(HH)} = 0.19255$ kJ/mol (0.0460 kcal/mol), $R_{min(OO)} = 0.35364$ nm, and $\epsilon_{(OO)} = 0.63666$ kJ/mol (0.1521 kcal/mol). The movable walls and the CNT membrane model are composed of neutral carbon atoms with the Lennard-Jones parameters of $R_{min(CC)} = 0.39848$ nm and $\epsilon_{(CC)} = 0.29301$ kJ/mol (0.0700 kcal/mol).^[33] The interactions between different water molecules include van der Waals interactions and electrostatic interactions, while interactions between water and solids (which can be the movable walls or the CNT membrane) are only van der Waals interactions. The Lennard-Jones parameters for describing van der Waals interactions between different two species of atoms are based on the Lorentz-Berthelot combining rules^[36], in which the R_{min} and ϵ are calculated by an arithmetic mean and a geometric mean of the Lennard-Jones parameters of two atoms, respectively.

In all simulations, the CNT membrane model is fixed in position, and periodic boundary conditions (PBC) are applied only in the x and y directions. The membrane interacts with the water through intermolecular interactions – though only the water molecules experience the resulting forces. This is a good approximation since the membrane is extraordinarily rigid. Constant temperature (300 K) is achieved via Langevin dynamics.^[18] The equation of motion is integrated with the Velocity Verlet algorithm.^[37] The cut-off radius of van der Waals interaction is set to 1.2 nm with a

switching function starting at 1.0 nm. PME (Particle Mesh Ewald) electrostatics calculations^[38] are used to take into account the electrostatic interaction. Note that a three-dimensional PBC is required by the PME method. The PBC size in the z direction is set to be at least ten times the system size in z direction. Although the PBC is actually applied in all three directions, the distance between the unit system and any replication along the z direction is large enough to render the influence of the PBC in the z direction negligible.

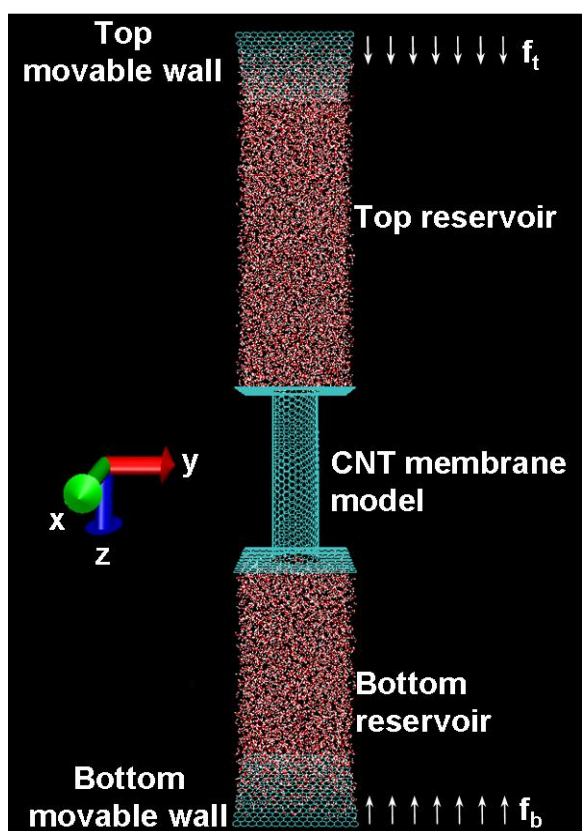


Figure 2.2 Perspective snapshots of the simulation systems produced by VMD package at the beginning status of MD simulations. Shown are the two graphene sheets which act as the movable walls, the CNT membrane model shown in Figure 2.1, and the two water reservoirs connected by the membrane. Forces f_t and f_b are applied on the movable walls. Carbon atoms in green, hydrogen atoms in white, and oxygen atoms in red.

Initially the water molecules, which are only in the reservoirs (the CNT is empty), are placed randomly and are not yet temperature and atmospheric pressure equilibrated. Therefore, the first 2.0 ns of simulation time (equilibrium simulation with 0.5 fs time step) are to let the system reach the desired temperature and pressure, without the pressure driving force. At this stage, the Langevin Nosé-Hoover piston method is used to achieve constant pressure in addition to constant temperature.^[18] For the simulation condition of 300 K and 0.1 MPa, the water reservoir should match the known density of water (1000 kg/m³); if not then this means the simulation system has not reached the desired equilibrium and additional equilibrium simulation time is provided. During the equilibrium simulations, the water molecules fill the CNT membrane, but cannot pass through it.

After the equilibrium simulation, the resulting status of the system provides initial conditions for the following NEMD simulation wherein only temperature is kept constant. The NEMD simulation is started by applying the external force field (pressure difference) and is carried out using 1.0 fs time steps at 300 K. During the first 1.0 ns (or longer) of simulation the pressure difference stabilizes and the data collected in this period are not used. The subsequent results of NEMD simulations are analyzed every time step to calculate the time average values of the flux, and the density and velocity distributions along both radial and flow directions.

2.4. Results and Discussion

Physical parameters for seven CNT membranes used in the simulations are listed in

Table 2.1 including the different pore radii and lengths. These membranes are used to investigate the effect of the membrane structure (pore size and membrane thickness) on the pure water transport properties through NEMD simulations.

Table 2.1 Specifications of different CNT membrane physical parameters used in the simulations.

Membrane model	CNT Type	Effective length^a (L_z) nm	Tube radius^b nm	Effective radius^b (r_p) nm	Porosity^c (A_K) %
1	(8, 8)	6.0	0.546	0.372	2.71
2	(10, 10)	6.0	0.677	0.507	5.05
3	(11, 11)	6.0	0.745	0.575	6.49
4	(12, 12)	6.0	0.813	0.643	8.11
5	(12, 12)	3.0	0.813	0.643	8.11
6	(12, 12)	9.0	0.813	0.643	8.11
7	(12, 12)	15.0	0.813	0.643	8.11

^aThe length of a CNT is the thickness of the CNT membrane in the model.

^bThe tube radii are defined as the distance measured between the centers of carbon atoms and the pore center, while that the effective radius is the tube radius minus van der Waals radius of carbon atom.^[39, 40]

^cThe porosity values of the CNT membranes are calculated by using the effective radii of the CNTs and the total membrane area in the model.

The effective radius of the CNT (i.e. accounting for the van der Waals radius of the carbon atoms and the water molecules) is used as the appropriate pore size of the

membrane model for analyzing simulation results, to obtain water flux, and density and velocity (all velocities in this work are in z direction) distributions along both radial and flow directions. The stream velocity of water flow in the water reservoirs is quite low because of the reservoir cross-sectional area and the low pressure driving force in the NEMD simulation. Since the water density is shown to be constant (below) in the reservoirs then the water velocity in each reservoir is determined by the velocity of each movable wall, which can be calculated from the linear relationship between the wall position and the simulation time.

When the pressure-driven water flow passes through the CNT membrane, the number of water molecules in the top/bottom reservoir gradually decreases/increases with increasing the simulation time. The number flow rate, the number of water molecules passing through the membrane model in unit simulation time (molecule/ns), is given by the slope of the linear profile obtained by plotting the increasing number of water molecules in the bottom reservoir as a function of the simulation time. The water flux is defined as the number flow rate per membrane area (not pore area), and calculated in the units of both 'molecules/(ns nm²)' and 'm³/(m² s)' or equivalently 'm/s'. The CNT is divided equally into several sections along the radial and flow directions to get the water density and velocity distributions. The time average values of density and velocity in each section are then calculated by averaging all data collected in a unit simulation time.

From the Navier-Stokes equations for describing flow in a cylindrical channel, both the flux and z velocity component at different radial positions can be derived. Equations (2.1) and (2.2) are for a porous membrane with a single straight pore: Equations (2.1) is

the Hagen-Poiseuille equation for calculating water flux as ‘rate per membrane area’. We will simply refer to Equation (2.2) as the Navier-Stokes Equation. The flux is given by

$$J_W = L_P \Delta P = \frac{r_p^2}{8 \eta (L_z / A_K)} \Delta P \quad (2.1)$$

$$A_K = \frac{\pi \cdot r_p^2}{A_{mem}} = \frac{\pi \cdot r_p^2}{L_x \cdot L_y}$$

while

$$v_z(r) = \frac{\Delta P}{4 \eta L_z} (r_p^2 - r^2) \quad (2.2)$$

gives the radial distribution of the axial velocity. L_P is the pure water permeability coefficient, r_p is the pore radius of the membrane, η is the viscosity of the liquid fluid at the operating temperature, and L_z/A_K is the ratio of the membrane effective thickness to the membrane porosity, ΔP is the pressure difference, and r is the radial position of the fluid. The theoretical flux (rate per membrane area), J_W , is calculated by the Hagen-Poiseuille equation, and is converted to units of molecules/ns/nm² using the density (1000 kg/m³) and viscosity (8.54×10⁻⁴ Pa · s) of water at 300 K and 1 atm.^[41]

The pressure in each water reservoir is calculated by the total force applied on each movable wall, including the external forces as shown in the Figure 2.2 and the z -direction van der Waals forces applied by the water molecules to the wall for each reservoir; the instantaneous pressure equals the total force divided by the cross-sectional area (the membrane area). Figure 2.3 shows the pressures produced in the top and bottom reservoirs as a function of the simulation time, where each pressure value is averaged

every 10 ps and the van der Waals forces are calculated by accounting for the PBC along x and y direction. The pressure profiles fluctuate around the target pressure values, and the maximum fluctuation is about 1 MPa. The fluctuations of the pressure profile are caused by the changing van der Waals forces between the wall and water molecules with the wall moving along the flow direction. Pressure fluctuating in such a small time (every 10 ps) has little influence on the water transport in a nanosecond-scale (sometimes up to hundreds of nanoseconds) simulation.

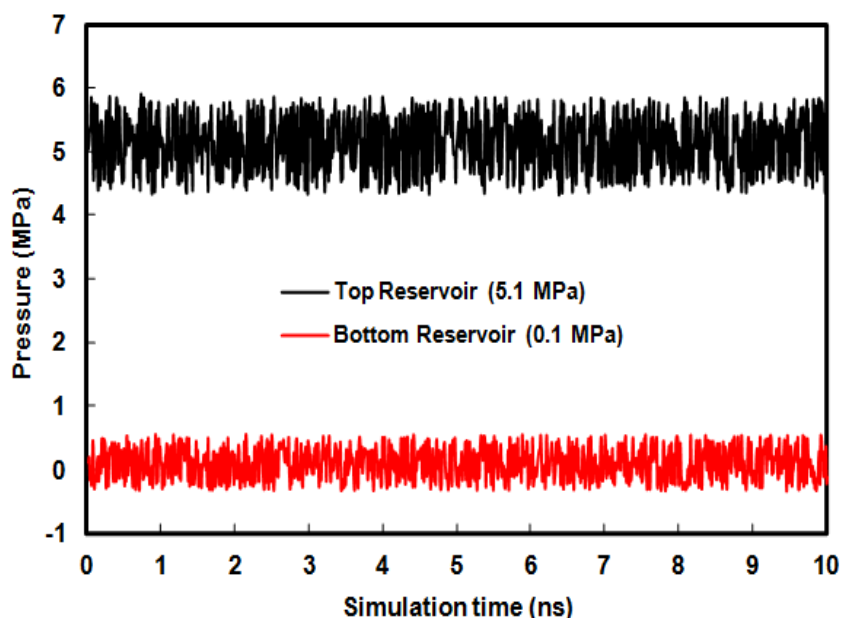


Figure 2.3 Pressure produced in each water reservoir as a function of the simulation time (10 ns as an example shown here, real simulation time is longer and dependent on each case). Each pressure value is averaged in 10 ps after the pressure difference stabilizes in the NEMD simulation. The error about the mean value of the pressure is less than 0.2% for the high pressure on the top reservoir, and is less than 10% for the low pressure on the bottom reservoir. The standard deviation for the pressure differences over all seven simulations is about 0.2 MPa.

During the NEMD simulation, the number of water molecules passing through the CNT membrane has a steady increasing rate as a function of the simulation time (shown

in Figure 2.4) and the water densities in the reservoirs and the CNT are all constant. The constant wall pressure and the steady water transport indicate that the pressure in each reservoir is constant with time. Using two movable walls to control pressures in the liquid reservoirs is derived from the NEMD systems presented by Huang^[26-29] and by Takaba.^[30] They both used the Irving–Kirkwood method^[42] to estimate the pressures near the inlet and outlet regions in the reservoirs (liquid argon fluids), and the results showed that the pressures in the reservoirs corresponded to the targeted values at the walls.^[28, 30] Other methods for producing a constant pressure difference have been reported and confirmed for pressure-driven water flow through CNTs or CNT membranes.^[19, 22]

The pressure difference is calculated from the values as above. With the assumption of uncorrelated pressure values the statistical error of the average pressure is estimated by using the standard deviation of the sampled mean. The statistical error is less than 0.01 MPa, corresponding to 0.2% for the high pressure reservoir and 10% for the low pressure reservoir. Therefore, the statistical error of the pressure difference is less than 0.2%. The standard deviation of the calculated pressure differences in all NEMD simulations is about 0.2 MPa, which is an acceptable variation.

2.4.1. The effect of pore size

Four CNT membrane models with difference pore size (#1–4 membranes in Table 2.1) are used to construct simulation systems to study the effect of membrane pore size on the transport properties of water flow passing through the CNT membranes.

A. Flux

As mentioned above, the flux is calculated as the number flow rate divided by the membrane area. The plot of the number of water molecules passing through the membrane as a function of simulation time, for #4 membrane (30 ns simulation as an example), is shown in Figure 2.4. In this case, the number flow rate obtained from the slope of the linear trend through the origin is 28.55 ± 0.05 (standard error) molecules/ns, which gives a water flux of 1.784 ± 0.003 molecules/ns/nm². The uncertainty given here is the standard error on the slope based upon the assumption of uncorrelated data – i.e. a correlation time shorter than 50 ps. For the other six membranes the relative standard error of the water flux data are all smaller than 0.5%. Similar analysis for the distance moved by each wall, as a function of simulation time, is used to calculate both the velocity of the movable wall and the water velocity in the reservoirs.

Figure 2.5 shows the water fluxes of #1–4 CNT membranes. As shown in Figure 2.5, the water flux (rate per membrane area) increases with pore size and the increasing flux is (qualitatively) consistent with the Hagen-Poiseuille equation (Eqn. (2.1)). The Hagen-Poiseuille equation predicts the flux to be proportional to the fourth power of the pore radius; for instance, the effective radius of the #4 membrane model is about twice of that of the #1 membrane model which is consistent with the flux of the #4 membrane model being about ten times higher than that for #1 membrane model. The simulation flux as a function of pore area curves upwards faster than the theoretical curved line based on the Hagen-Poiseuille equation, however. Thus, the pressure-driven water flux

through the simulated CNT membrane not only has a higher flux overall, but also a flux rate that increases faster with pore size than is predicted from the Hagen-Poiseuille equation.

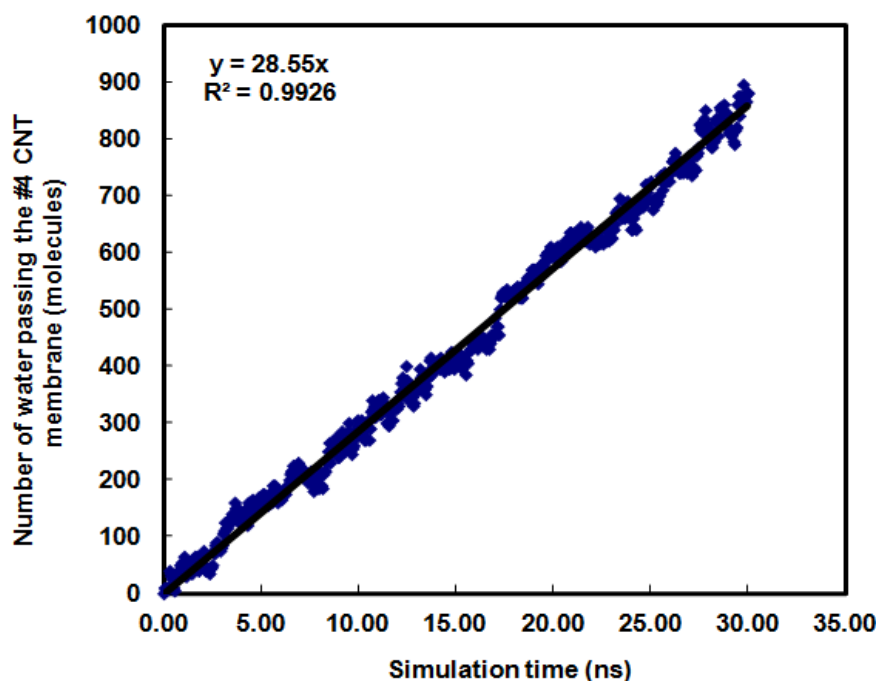


Figure 2.4 Number flow rate of #4 CNT membranes in a 30 ns simulation, shown as the slope of the linear trend in the net number of water molecules passing through the membrane as a function of the simulation time. The data shown are for membrane simulations of CNT #4 (Table 2.1): (12, 12) CNT: $L_z = 6.0$ nm; $\Delta P = 5.0$ MPa; $T = 300$ K. The standard error of the slope is ± 0.05 molecules/nm.

The exceptional high simulation flux compared with theoretical flux (Figure 2.5) is caused by a combination of the smooth and frictionless CNT surface, the quite narrow pore size, and the weak interactions between the water molecules and the CNT surface. The continuum flow of liquid in a cylinder dominated by the bulk properties can be described by the Hagen-Poiseuille equation. However water passing through the CNT membrane forms a nanoscale flow in which water molecules in the CNT are quite near to the CNT pore surface within a fraction of an nm and the water molecules align with each

other in a regular pattern. The narrow pore size of the CNT restricts the movement of water molecules in the x or y direction, so natural kinetic movement of the water molecules is directed along the flow direction. The nearly frictionless surface of CNT applies negligible resistance to the water flow. In normal Hagen-Poiseuille flow the velocity of the liquid is zero at the pore wall – the no-slip condition. In the CNT, weak interactions between water and the CNT membrane render the no-slip condition invalid - water near the pore wall moves rapidly. In summary, under pressure difference, water molecules are driven to transport through the CNT membrane with high flow rate, not governed by the Hagen-Poiseuille equation.

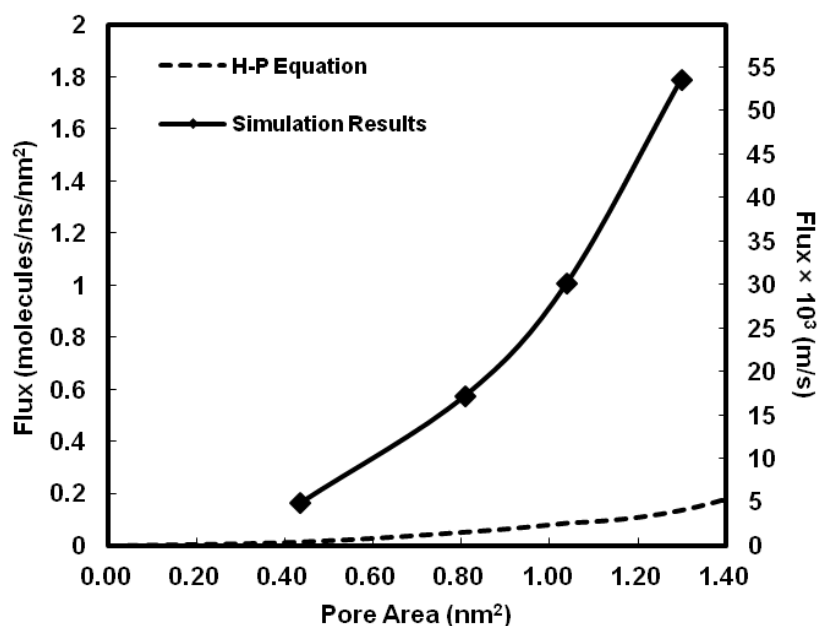


Figure 2.5 Flux (rate per membrane area), shown both as molecular flux and conventional flux (in m/s), as a function of the membrane pore size as represented by the pore area. The points are based on membrane simulations on CNT #1 to #4 (Table 2.1): #1 (8, 8), #2 (10, 10), #3 (11, 11), and #4 (12, 12) CNT, respectively: $L_z = 6.0$ nm; $\Delta P = 5.0$ MPa; $T = 300$ K. H-P Equation refers to the Hagen-Poiseuille Equation (Eqn. (2.1)), and solid line is the trend based on the simulation results. The statistical error for each data point is evaluated and less than 0.5% (see Figure 2.4 for the case of the #4 membrane).

Recently, enhanced pressure-driven liquid flow through CNTs has been measured experimentally.^[4, 43-45] Majumder^[43] fabricated CNT membranes with aligned arrays of multi-walled CNTs with a pore diameter of 7 nm and a length of 34–126 μm to experimentally investigate water transport through the CNT membranes. The experimental water flow rates obtained were four to five orders of magnitude faster than the theoretical water flow rate calculated by using Eqn. (2.1). Similarly, Holt^[4] found CNT membranes, fabricated from aligned arrays of double-walled CNTs with a pore diameter of 1.3–2.0 nm and a length of 2.0–3.0 μm , exhibit an experimental water flux three orders of magnitude faster than the theoretical value. While the CNT membrane modeled in this study shows faster than theoretical flux (Figure 2.5), the simulation cannot account for such a large change as the 3 to 5 orders of magnitude enhancement observed experimentally by Majumder^[43] and Holt.^[4] Possible reasons for the difference between simulation results and the experimental results relate to the CNT membrane configurations; the model CNT membrane is simulated based on a single CNT with a nanoscale length, while the fabricated CNT membranes are multiwalled or double walled in an array of CNTs with much longer lengths – roughly 6000 to 20 000 times longer. It is not practical to study a water flow passing through such a thick CNT membrane with MD simulations, even at extremely high pressure difference, because of computational limitations. However, the membrane thickness dependence of enhanced water flow was investigated experimentally by Thomas.^[21] The results presented there, for long CNTs (75 and 150 nm), were compared with Corry's results^[46] for short CNTs (1.3 and 2.6 nm) of similar diameter. The comparison shows the long CNTs have an

enhanced water flow much greater than (by about 100 times) the short CNTs, and it is concluded that the water transport in a short CNT (shorter than 10 nm) is more like a coordinated diffusion rather than like flow in a long pipe resulting in less flux enhancement.^[21]

Another experimental approach is reported by Qin to measure the water flow rate through individual ultralong CNTs with a length of 1050 μm .^[45] Qin experimentally studied seven single-walled CNTs with different tube diameters from 0.81 nm to 1.59 nm. These results are compared with our results for CNT membranes (#1–4) – ranging from (8, 8) to (12, 12) - in Table 2.2. Table 2.2 shows the enhancement factor, defined as the ratio of the simulation flux to that predicted by the Hagen-Poiseuille theory (Eqn. (2.1)). The enhancement factors of the #1–4 membranes increase very slowly from 10.7 to 13.2 with increasing the pore size; essentially about one order of magnitude enhanced. The experimental enhancement factors of the seven CNTs decrease with increasing pore size (with one exception between the 0.98 nm and 1.10 nm diameters). A decreasing enhancement factor with increasing pore size is as one might expect. As pore size increases, water molecules are less restricted and more likely to behave like bulk water and be better described by Eqn. (2.1).

The enhancement factors we obtained are much smaller than the experimental values. Besides the difference between the nanoscale length (6.0 nm) we used and the ultralong scale (1050 μm) used in Qin's experiments, the pressure driving forces (listed in Table 2.2) are also different. For the (12, 12) type CNT with a 1.63 nm tube diameter which is close to the 1.59 nm tube diameter in Qin's work, the pressure difference in the

experimental measurement is about 3 times that of our simulation, while the experimental enhancement factor is about 4 times the simulation enhancement factor.

Table 2.2 Comparison of the enhancement factors^a between our NEMD simulation and the experimental data of Qin^[45].

NEMD simulation ^b			Experimental data ^{[45],c}		
Membrane model	Pressure difference (MPa)	Enhancement factor	Tube diameter (nm)	Pressure difference (MPa)	Enhancement factor
			0.81	117.6	882
			0.87	89.57	662
			0.98	52.09	354
1	5.0	10.7	1.10	31.37	580
2	5.0	10.9	1.42	16.21	103
3	5.0	11.6	1.52	15.43	59
4	5.0	13.2	1.59	15.09	51

^aThe enhancement factor is the ratio of the flux to that predicted by the Hagen-Poiseuille theory (Eqn. (2.1))

^bThe thicknesses of the #1–4 CNT membranes (the lengths of the CNTs) are 6.0 nm.

^cThe lengths of CNTs measured by Qin are about 1050 μm , and the calculations of the enhancement factors use a water viscosity of $1 \times 10^{-3} \text{ Pa} \cdot \text{s}$ and the effective radius of each CNTs.

B. Radial-direction distributions

The pore of the CNT membrane is divided into nine or ten annular sections of equal space in the radial direction to investigate the radial density and velocity distributions.

Radial density and velocity distributions, in the pore, are obtained by averaging over water molecules within a thin annular section in the pore (excluding the entrance and exit regions) at radius, r .

Figure 2.6 shows the density distributions along the radial direction of the CNT membrane models with different pore sizes. Note that the density distributions in Figure 2.6 are all in the form of oscillatory waves and are center symmetric (as they must be). For all the membrane pore sizes there is a ring of water molecules adjacent to the pore wall. Moving inward either additional rings of water molecules are present or not, depending on the available room – i.e. if there is enough room for another water layer (or ring). For the largest pore size (#4, (12, 12) CNT) a full second layer is present but with no room for a third layer near the center; hence the center density is near zero. At the other end of the pore sizes, the smallest membrane pore size (#1, (8, 8) CNT), only one layer is able to fit and the center density is essentially zero. For the second smallest pore size (#2, (10, 10) CNT) a single column of water molecules exists at the center. Finally, for the second largest pore size (#3, (11, 11) CNT), the central column of water is partially expanded into an inner ring of water molecules – the density is lower at the center of the pore.

The above patterns can be interpreted as the water molecules arranging themselves in a well-ordered manner in the CNT under the effect of hydrogen bond interactions between water molecules and intermolecular interactions between water and the CNT pore surface. As the pore size of the four membrane models increases, the number of rings in the density distributions increases from 1 to 2 - there is one hydration layer for

the #1 membrane model and two hydration layers for other models. Figure 2.7 shows the snapshots of the cross section view of the water flow in the CNT of each membrane model. A single ring of about 4 water molecules is observed in the #1 membrane model. A similar water ring near the CNT surface appears in other models, but with increasing number of water molecules in this outer ring reaching about 10 water molecules in the #4 membrane. For the largest membrane (#4) a full inner ring of about 4 water molecules exists in center part of the CNT. The middle two membrane pore sizes show an outer ring of water molecules, plus a single column of water in the #2 pore and a partial inner ring in the #3 pore; i.e. as concluded from the density profiles in Figure 2.6.

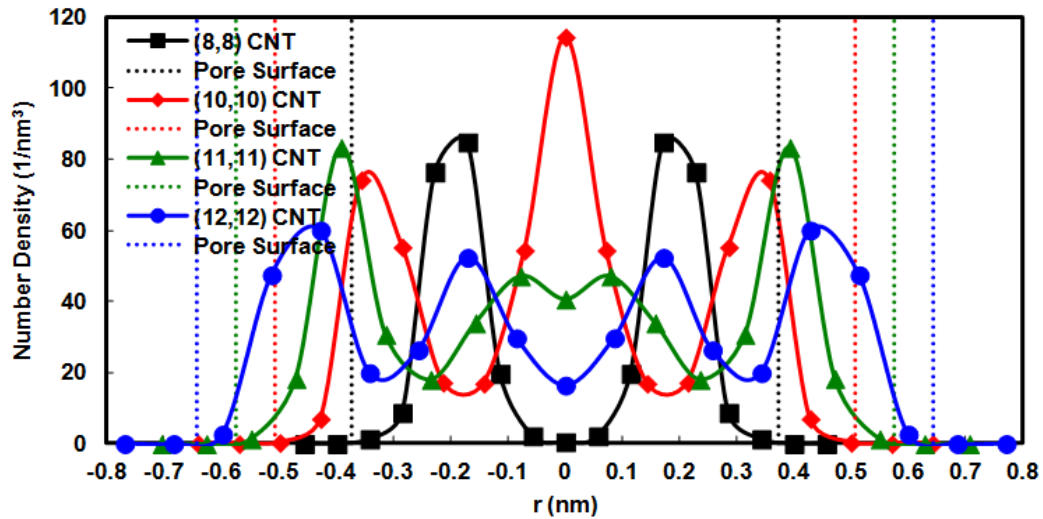


Figure 2.6 Effect of pore size as represented by the pore radius on the density distributions along radial direction for the four membrane models: density as a function of r ; values are averaged over a thin annular section in the pore at r (excluding the entrance and exit regions). The points are based on membrane simulations on CNT #1 to #4 (Table 2.1): #1 (8, 8), #2 (10, 10), #3 (11, 11), and #4 (12, 12) CNT, respectively: $L_z = 6.0$ nm; $\Delta P = 5.0$ MPa; $T = 300$ K. Solid lines are the trend curves based on the simulation results, dotted lines are the pore surfaces represented by the effective pore radii (Table 2.1). The statistical error for each data point is less than 1%.

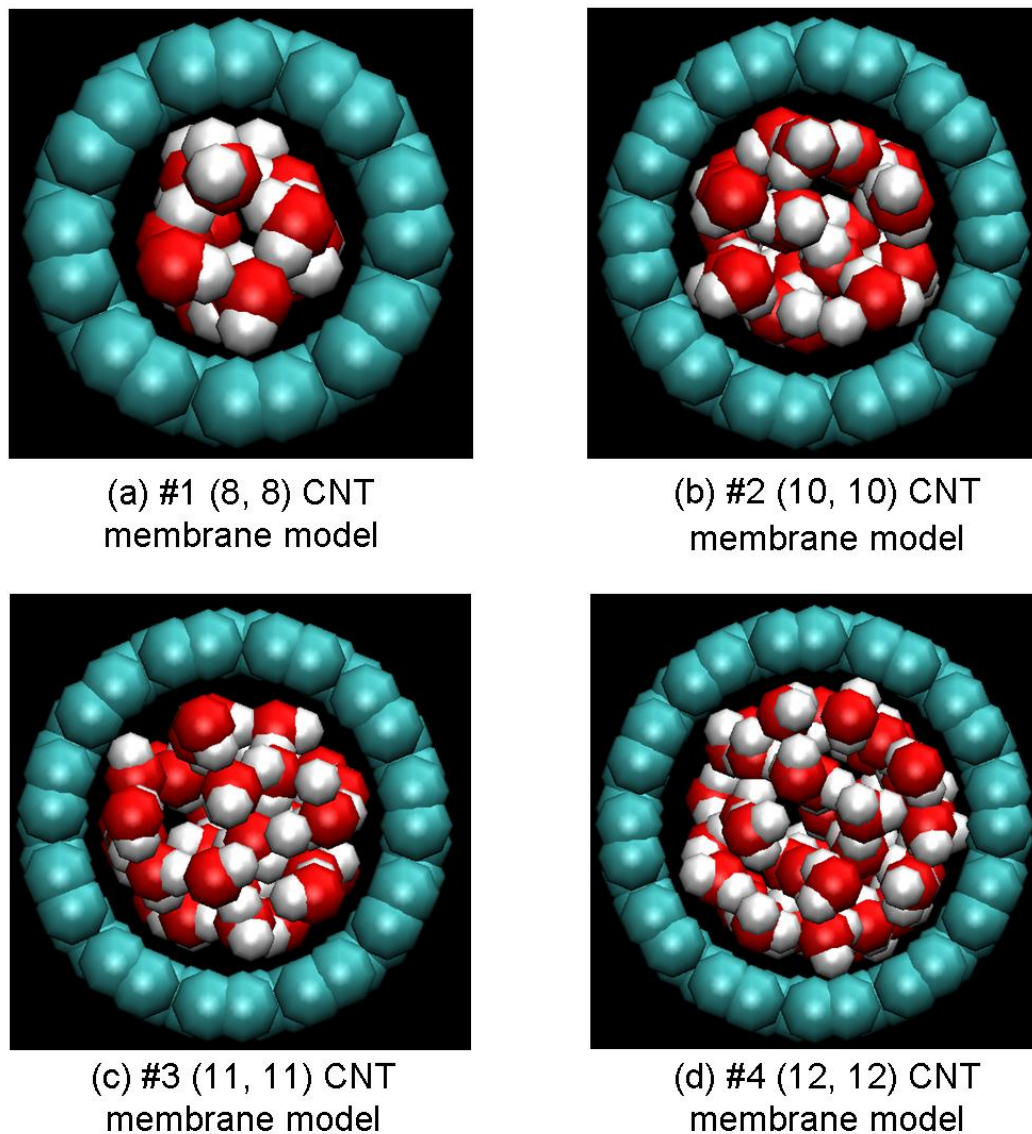


Figure 2.7 Orthographic snapshots of water molecules in the different CNT membranes. Atoms are shown by balls with the van der Waals volumes: carbon atoms in green, hydrogen atoms in white, and oxygen atoms in red.

The outer radial positions corresponding to zero density (in Figure 2.6) is determined by the effective radius of the CNT carbon material (see Table 2.1) which sets the distance of closest approach that a water molecule center can make to the CNT membrane.

The radial distributions of velocity for the different CNT membranes are shown in

Figure 2.8. These velocity distributions are oscillatory like the density distributions seen in Figure 2.6. They are not parabolic as predicted by the Navier-Stokes equation. As well, the velocity profiles from the NEMD simulations are much higher than the theoretical values predicted by the Navier-Stokes equation, also shown in Figure 2.8.

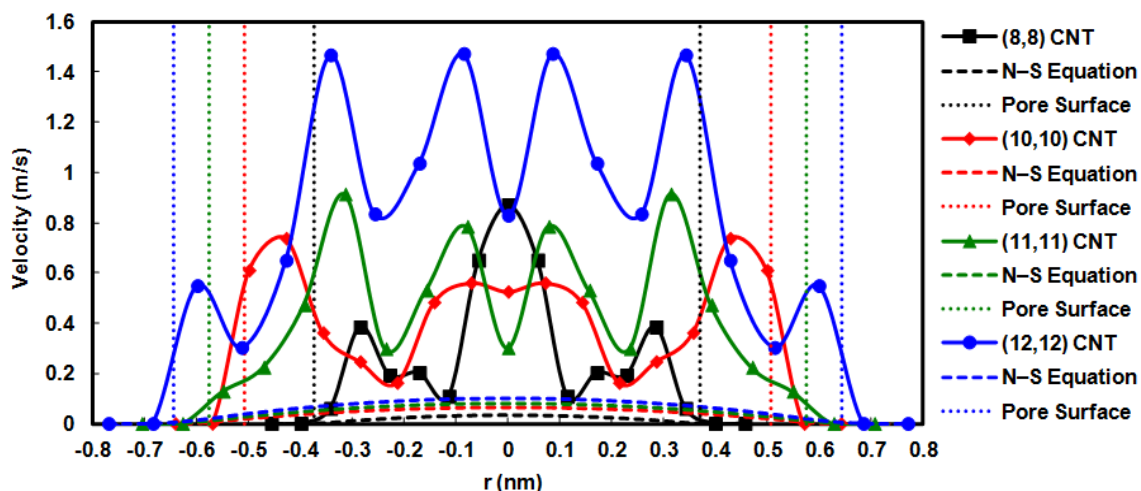


Figure 2.8 Effect of pore size as represented by the pore radius on the velocity (in z direction) distributions along the radial direction for the four membrane models: velocity as a function of r ; values are averaged over a thin annular section in the pore at r (excluding the entrance and exit regions). The points are based on membrane simulations on CNT #1 to #4 (Table 2.1): #1 (8, 8), #2 (10, 10), #3 (11, 11), and #4 (12, 12) CNT, respectively: $L_z = 6.0$ nm; $\Delta P = 5.0$ MPa; $T = 300$ K. N-S equation refers to the Navier-Stokes Equation (Eqn. (2.2)). Dashed lines are the trends based on the Navier-Stokes Equation, solid lines are the trend curves based on the simulation results, and dotted lines are the pore surfaces represented by the effective pore radii (Table 2.1). The statistical errors for most data points are less than 10%.

A non-parabolic distribution of water velocity in nanotubes has been seen in other literature,^[47] but not exactly the same as seen here. On a macroscopic scale, a continuum flow has a parabolic velocity profile with the position along the radial direction described by the Navier-Stokes equation. When the pore size of a CNT is comparable to the size of a water molecule (the mean van der Waals diameter of water is

0.282 nm^[48]), continuum mechanics is not valid as the molecules transport as individual entities. Moreover, the interfacial interactions between the CNT surface and water molecule are weak. The no-slip condition, employed in continuum mechanics, is not valid here. Thus, the high velocities seen here are attributed to the weak interactions between water and the smooth surface of the CNT which enables a very rapid and nearly frictionless transport of water flow through CNT under a pressure-driven force.

The relatively low pressure difference, 5.0 MPa, (compared to previous works as mentioned above) driving the water through the membrane produces a low stream velocity (smaller than 2 m/s in the CNT). Large relative errors in the estimated values are consequently a concern.^[49] For this reason, we performed careful error analyses, accounting for the correlation of successive density and velocity values. Each density and velocity value is averaged by data collected every time step in the NEMD simulation, and the correlation of successive data should be accounted for the error analyses. The integrated autocorrelation time (τ) is calculated from the Equation (2.3) and used to estimate the statistical error of time-correlated data.^[50] The statistical error is calculated by using the number of uncorrelated samples, which is the total number of data points divided by twice the integrated autocorrelation time (2τ).

$$\tau = \frac{1}{2} + \sum_{k=1}^N \frac{\langle a_i \cdot a_{i+k} \rangle - \langle a_i \rangle \langle a_i \rangle}{\langle a_i^2 \rangle - \langle a_i \rangle \langle a_i \rangle} \quad (2.3)$$

where a_i , is the estimated value for density or velocity at i^{th} time step and N is the number of time correlated samples in the simulation.

Instead of repeating simulations several times for directly calculating the error of

independent data, the error of each time-average value in a single simulation is estimated by using the standard deviation of the sampled mean (Equation (2.4)).^[51]

$$\sigma(\bar{a}) = \frac{\sigma}{\sqrt{N/2\tau}} = \frac{\sqrt{\frac{\sum (a_i - \bar{a})^2}{N}}}{\sqrt{N/2\tau}} \quad (2.4)$$

$$E(\bar{a}) = \frac{\sigma(\bar{a})}{\bar{a}}$$

where $\sigma(\bar{a})$ is the standard deviation of \bar{a} (the time-average value of all time correlated data), σ is the standard deviation of all time-correlated data, a_i , is the estimated value for density or velocity at i^{th} time step, N is the number of time-correlated samples in the simulation, τ is integrated autocorrelation time calculated from Eqn. (2.3), and $E(\bar{a})$ is the estimated error of \bar{a} .

Based on the Eqn. (2.4), the statistical error of each density in Figure 2.6 is less than 1%, and the statistical errors of most velocity data in Figure 2.8 are less than 10%. We also investigated errors in the reported density and velocity distributions by using formulas found in Werder,^[51] which are derived from expressions for predicting statistical error in particle simulations reported by Hadjiconstantinou.^[50] Using the formulas found in Werder,^[51] the density error is quite small (<1%), but the velocity error is larger (< 25% for most data). The expression used for calculating velocity error (E_v) is below:

$$E_v = \sqrt{\frac{k_B T}{v_z^2 \rho V (N/2\tau)}} \quad (2.5)$$

where v_z is the average flow-direction velocity, ρ is the density of water at temperature T , V is the volume of a sample section, N is the number of time correlated samples; 2τ is

twice the integrated autocorrelation time.

Equation (2.5) shows that the estimated velocity error depends on the density of water molecules in each section and the section volume. The average velocity in the section of the pore center or the section near the pore surface has a large statistical error ($> 25\%$) caused by the quite low water density and the small section volume. While for the other data points, the average velocities for the sections between the center and the outer sections, mostly show smaller error estimates ($< 25\%$ as mentioned above). Even if the large velocity errors are considered in Figure 2.8, the velocity distributions are still oscillatory and the relative trends are the same. Equation (2.5) is derived from statistical physics, for fluctuations about the mean for a system at equilibrium, and based on the testing body containing a sufficient number of particles.^[52] Therefore, the average velocities in some radial sections, e.g. the section in the pore center and the section near the pore surface, have large statistical errors due to the quite low number of water molecules in the small section volume. Hadjiconstantinou^[50] estimated errors of axial velocities for low temperature liquid argon transport through two parallel solid walls and concluded that Eqn. (2.5) was validated for flow of a dense liquid in a two-dimensional channel. Werder^[52] applied the Eqn. (2.5) for low temperature liquid argon flow passing around a CNT in a slit geometry system. In both cases, significant numbers of particles were present in the testing cells at all times. For our case, particularly in the radial velocity distributions, the cells are small and on the order of size of water molecules so that at any given instant there may be few or no water molecules present and the system is in a nonequilibrium state. We believe these differences between our physical situation

and those used in the assumption of the derivation of the Eqn. (2.5) in Hadjiconstantinou^[50] are the cause for the relatively larger errors calculated by this equation in our work.

We include the error analysis estimated in two ways, the standard deviation of the sampled mean (Eqn. (2.4)) and the error formulae (Eqn. (2.5) and the formula for density error) found in Werder,^[52] for evaluating the density and velocity results, however, we feel the error obtained directly from the standard deviation of the sampled mean is more representative of the actual error in our data as discussed at the end of this section.

C. Flow-direction distributions

The entire system is divided into ten sections of equal space in the flow direction as follows; four, three, and three sections are located at the top water reservoir, CNT membrane, and bottom water reservoir, respectively. The densities and velocities of water molecules as a function of z are averaged over a thin section at z (cylindrical sections in the pore and square cuboids sections in the water reservoirs). The statistical errors of the density and velocity data points were estimated in two ways as mentioned in Section 2.4.1.B. For each membrane according to both estimates, the errors in density distributions are less than 1% and in velocity distributions are larger (less than 15% for most data).

The density distributions along the flow direction of the CNT membrane models with different pore sizes are shown in Figure 2.9. The density in the CNT is slightly lower (about 5–10% lower) than that in the water reservoirs, and the densities in the water

reservoirs are nearly equal among these CNT membrane models. Water molecules, in bulk solution (such as in the water reservoirs) can orient into a relatively dense fluid because of the strong hydrogen bonds. However, in the small pores the water molecules become more ordered but less dense because of lower hydrogen bonding and reduced space for the molecules to orientate into the higher density arrangements possible in bulk solution.

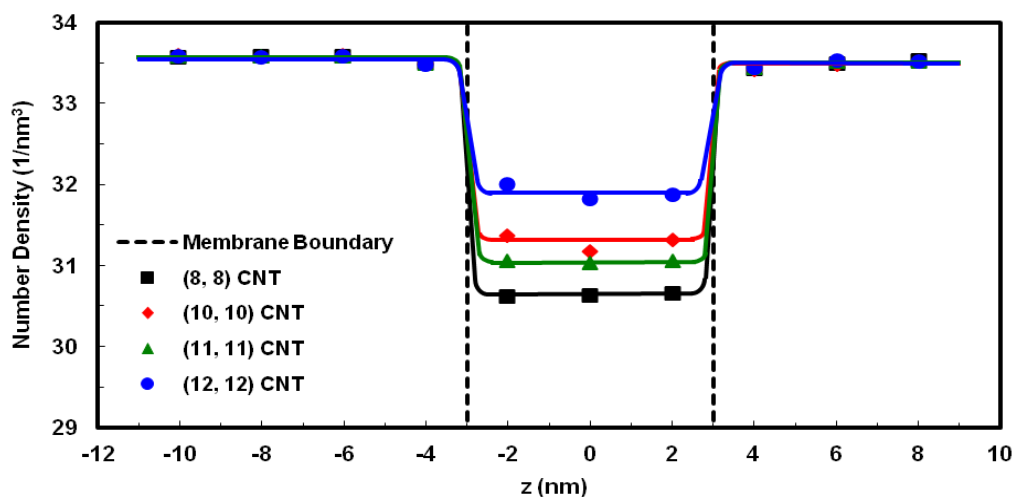


Figure 2.9 Effect of pore size on the density distributions along the flow direction for the four membrane models: density as a function of z ; values are averaged over a thin section at z (cylindrical sections in the pore and cuboid sections in the water reservoirs). The points are based on membrane simulations on CNT #1 to #4 (Table 2.1): #1 (8, 8), #2 (10, 10), #3 (11, 11), and #4 (12, 12) CNT, respectively: $L_z = 6.0$ nm; $\Delta P = 5.0$ MPa; $T = 300$ K. Dashed lines are the membrane boundaries along z direction separating the system in three parts from left to right: the water reservoir at high pressure side, the pore of the CNT membrane, and the water reservoir at low pressure side. Solid lines are the trend curves based on the simulation results. The statistical error for each data point is less than 1%.

It is seen that the pore size only affects the density in the CNT but not that in the bulk fluids, as expected. The density in the CNT generally increases with increasing pore size, again as expected. However, the pore size of the #3 membrane model has a slightly lower density than the smaller size #2 membrane model. The orthographic snapshot in

Figure 2.7(b) shows that the #2 membrane model is more tightly packed than the larger pore size #3 membrane model (radii of 0.677 nm and 0.745 nm, respectively). Apparently, the pore size of the #2 membrane model is more ideally suited to fitting layered water than the #3 membrane model, producing a higher density.

The velocity distributions along the flow direction of different CNT membranes are shown in Figure 2.10. Because of the constant water density in each reservoir, the water velocity in the reservoir is assumed constant with respect to the position along flow direction and is represented by the average velocity of each movable wall. The water flow is driven much faster in the CNT than in the water reservoirs, and the velocity increases with increasing pore size, as expected. The lower density and much higher velocity in the CNT than in the water reservoirs is caused by the nanoscale pore size of the CNT, the smooth and frictionless CNT surface, less hydrogen bonding interactions between water molecules in the CNT, and the weak interactions between water and CNT surface. The movement of water molecules passing through a cylindrical pore driven by a pressure difference is restricted by the pore size. The CNT membrane with larger pore size has a faster water flow, in accord with the variation of flux shown in Figure 2.5.

2.4.2. The effect of membrane thickness

The #4–7 CNT membrane models with different thicknesses in Table 2.1 are used to study the transport properties of water flow passing through the CNT membranes under the pressure difference of 5.0 MPa. The simulation flux and distributions were investigated, and the estimated errors of fluxes, densities, and flow direction velocities are

similar to the results for the #1–4 membranes mentioned above (and given in the Figure captions).

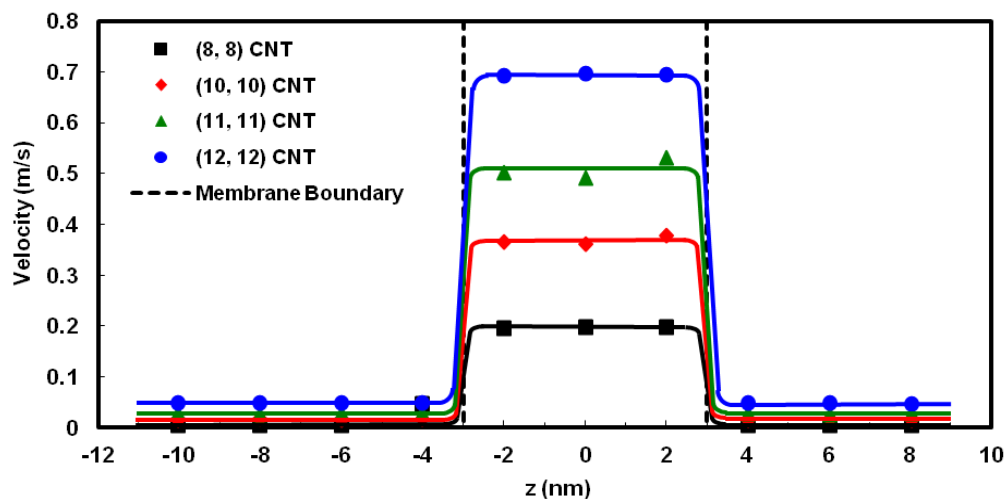


Figure 2.10 Effect of pore size on the velocity (in z direction) distributions along the flow direction for the four membrane models: velocity as a function of z ; values are averaged over a thin section at z (cylindrical sections in the pore and square cuboids sections in the water reservoirs). The points are based on membrane simulations on CNT #1 to #4 (Table 2.1): #1 (8, 8), #2 (10, 10), #3 (11, 11), and #4 (12, 12) CNT, respectively: $L_z = 6.0$ nm; $\Delta P = 5.0$ MPa; $T = 300$ K. Dashed lines are the membrane boundaries along z direction separating the system in three parts from left to right: the water reservoir at high pressure side, the pore of the CNT membrane, and the water reservoir at low pressure side. Solid lines are the trend curves based on the simulation results. The statistical error for each data point is less than 15%.

Figure 2.11 shows the effect of membrane thickness on the water flux (rate per membrane area). According to the Hagen-Poiseuille equation, the simulation flux varies approximately as the reciprocal of the membrane thickness. Otherwise, simulation fluxes are much higher than the theoretical fluxes - due to the smooth surface, the quite narrow pore size, and the weak interactions between water and the CNT membrane as discussed above. Enhancement factors of the #4–7 CNT membranes, shown in Table 2.3,

decrease from 13.5 to 11.4 as membrane thickness increases from 3.0 nm to 15.0 nm. In the limit of infinite length pores the simulation flux approaches the theoretical flux from the H-P Equation. As mentioned above the experimental fluxes for CNT membranes having thicknesses of tens to hundreds of micrometers, the experimentally measured fluxes are still much higher than the theoretical flux and do not approach theoretical flux as implied in Figure 2.11.

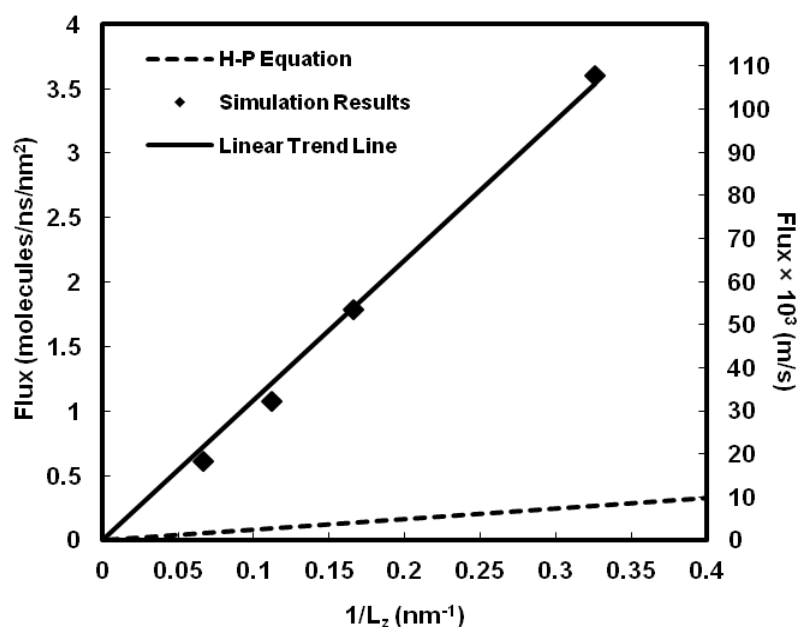


Figure 2.11 Flux (rate per membrane area), shown both as molecular flux and conventional flux (in m/s), as a function of the inverse membrane thickness. The points are based on membrane simulations on CNT #5, #4, #6, and #7 (Table 2.1) corresponding to different lengths of 3.0 nm, 6.0 nm, 9.0 nm, and 15.0 nm, respectively: $r_p = 0.643$ nm; $\Delta P = 5.0$ MPa; $T = 300$ K. H-P Equation refers to the Hagen-Poiseuille Equation (Eqn. (2.1)), and the solid line is the trend based on the simulation results. The statistical error for each data point is less than 0.5% (see Figure 2.4 for the case of #4 membrane).

Suk^[19] investigated water transport through CNT membranes driven by pressure difference of 100 MPa and found that the membranes modeled by using (10, 0) CNTs had

almost constant water fluxes with increasing membrane thickness from 2 nm to 10 nm. The water flux independent of the tube length is also found for (6, 6) CNTs^[46, 53] and (7, 7) CNTs^[22] at pressure differences larger than 200 MPa. The single-file water flow is formed in both the (10, 0) and (6, 6) CNTs, and there is a double-file water flow in (7, 7) CNTs.^[47] These works showed that the single-file or double-file water flow passing through the CNT of a small pore size has an extremely fast flow rate at higher pressure difference (> 100 MPa) which is almost unaffected by the CNT length. Suk^[19] also found that water flux through (20, 20) CNTs slightly decreases but did not change significantly at pressure difference of 100 MPa, similar to the results of (10, 0) CNTs. The reasons for the constant water flow with membrane thickness or tube length are explained by a negligible pressure drop in the CNT and the effectively frictionless region increasing in proportion to the tube length.^[19, 22]

Table 2.3 Enhancement factors^a of the #4–7 CNT membranes at 5.0 MPa pressure difference.

CNT type	Membrane model	Membrane thickness (L_z) nm	Enhancement factor
(12, 12)	5	3	13.5
	4	6	13.2
	6	9	11.8
	7	15	11.4

^aThe enhancement factor is the ratio of the flux to that predicted by the Hagen-Poiseuille theory (Eqn. (1))

Clearly, our results of simulations at 5.0 MPa pressure difference show different behaviour. In our work the four (#4–7 shown in Table 2.1) membranes are modeled by (12, 12) CNT, where two water layers of the pressure-driven water flow are formed in the pore as shown in Figure 2.7(d). Apparently the pore of (12, 12) CNT are not small enough to form a single-file or double-file water flow, and also are not as large as (20, 20) CNTs with a diameter of 2.71 nm in which water in the CNT is no longer in a hydration-layer formation as in a smaller pore (with the diameter smaller than 2.48 nm) so that water located at the center of the larger CNT behaves more like bulk water.^[47] Moreover, the common characteristics of these previous works are the high pressure difference (> 100 MPa); the pressure difference here is too low to see this very large enhancement of water flux and the flux independent of pore length as shown in these works. The enhancement factors seen in Table 2.3 are not as high as the factors larger than 100 found in Nicholls' work.^[22] The low enhancement factors might be due to the much lower pressure difference in our simulations (5.0 MPa) than in Nicholls' simulations (200 MPa). Nicholls^[22] argued that the water flow driven by a large pressure difference becomes effectively frictionless in the center region of the CNT and this frictionless region accelerates the water flow. The effectively frictionless region increases proportionally with increasing the tube length, offsetting the deceleration predicted by the Hagen-Poiseuille equation, and then resulting in a constant simulation flux as a function of the CNT length. For our work, with much shorter tubes and much lower pressures, we do not see the effectively frictionless region so the simulation flux

still decreases with increasing the membrane thickness. Therefore, the two water layers in (12, 12) CNT and/or the low pressure difference might explain why the water flux is dependent on the membrane thickness from 3.0 nm to 15.0 nm in our work.

The density and velocity distributions along the radial direction of the CNT membrane models, with different membranes thickness, are shown in Figure 2.12. The oscillatory density distributions of the four CNT membranes represented overlap perfectly. The density is clearly not affected by the membrane thickness in the 3–15 nm range considered here. Water molecules align entering the pore and move through the pore in a parallel fashion independent of pore length. The velocity profiles of the CNT models in Figure 2.12(b) are oscillatory and unlike the Navier-Stokes parabolic distribution, except for the 15.0 nm length pore. The velocity distribution for the 15.0 nm pore length is smoothed out and has a roughly parabolic profile except near the center of the pore. The observed velocity oscillations with the position along radial direction are consistent with flow in layers of water. Water molecules that fit well within the layered pattern flow fastest through the pores. The fastest flow is for the innermost layer within the 3.0 nm pore length. The observed decrease in velocity values with increasing membrane thickness is in accord with observed fluxes (Figure 2.11) and the Navier-Stokes equation.

Figure 2.13 shows the effect of membrane thickness on the density and velocity distributions along flow direction. Recall that the water in the CNT has a lower density than that in the neighboring water reservoirs, as discussed Section 2.4.1.C and Figure 2.9. As shown in Figure 2.13(a), the density values are nearly constant (separately in the

reservoirs and in the pores) in the flow direction and essentially the same for all four CNT membrane models. This similarity parallels the essentially constant radial distribution among the same four membranes shown in Figure 2.12(a). These results show, again, that the water molecules align and move through the pore in a parallel fashion due to the ordered structure of the water in the restricted pores.

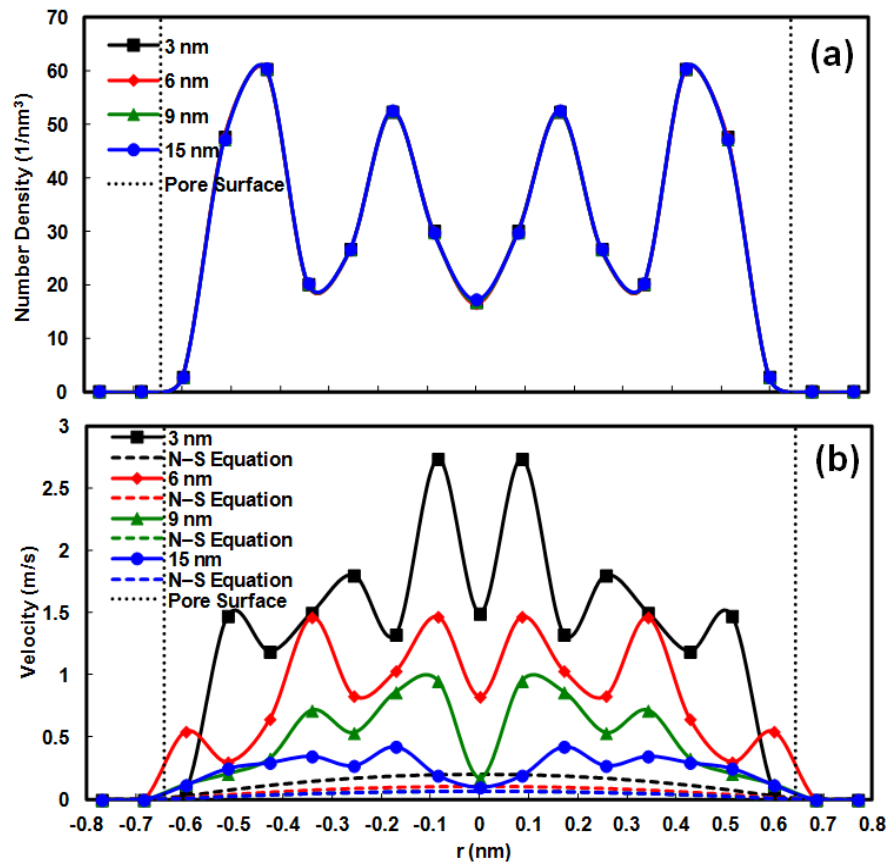


Figure 2.12 Effect of membrane thickness on the distributions along the radial direction for the four membrane models; values are averaged over a thin annular section in the pore at r (excluding the entrance and exit regions): (a) Density as a function of r ; (b) Velocity, in z direction, as a function of r . The points are based on membrane simulations on CNT #5, #4, #6, and #7 (Table 2.1) corresponding to (12, 12) CNT with different lengths of 3.0 nm, 6.0 nm, 9.0 nm, and 15.0 nm, respectively: $r_p = 0.643$ nm; $\Delta P = 5.0$ MPa; $T = 300$ K. N-S equation refers to the Navier-Stokes Equation (Eqn. (2.2)). Dashed lines are the trends based on the Navier-Stokes Equation, solid lines are the trend curves based on the simulation results, and dotted lines are the pore surface represented by the effective pore radius (0.643 nm). The statistical error for each density data point is less than 1% and the statistical errors for most data points are less than 10%.

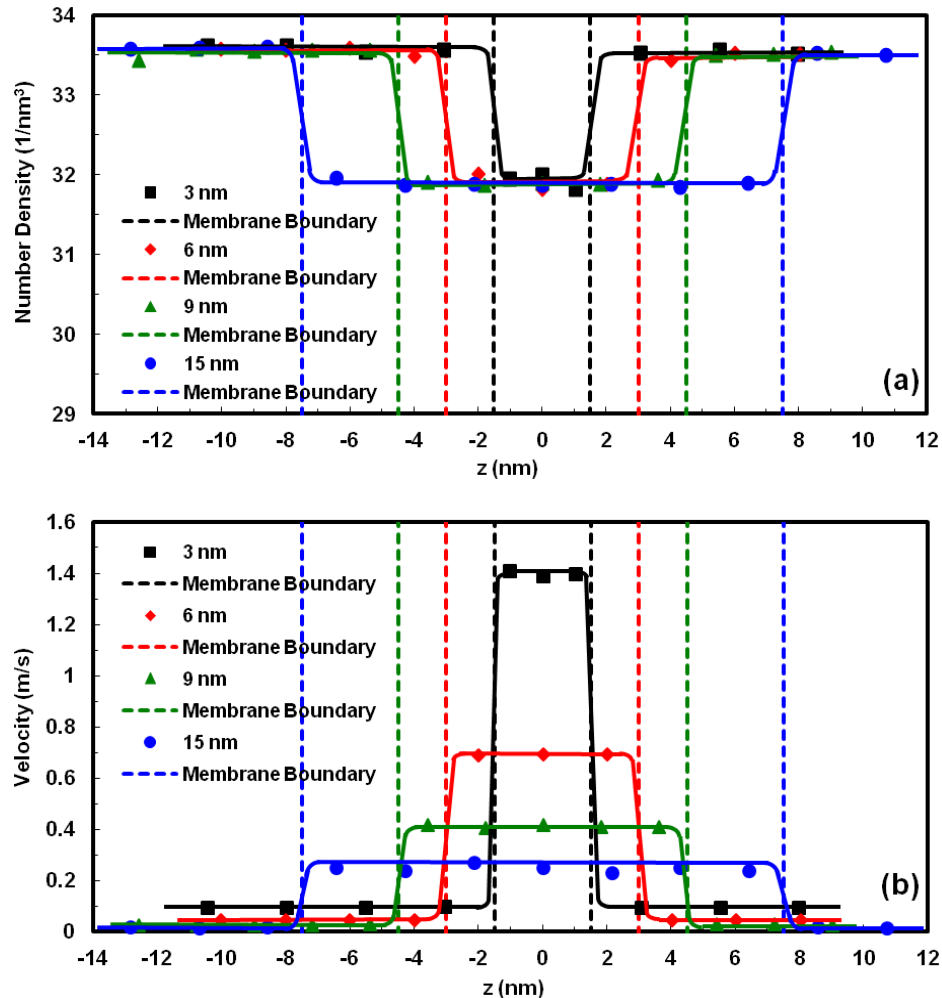


Figure 2.13 Effect of membrane thickness on the distributions along flow direction for the four membrane models; values are averaged over a thin section at z (cylindrical sections in the pore and square cuboids sections in the water reservoirs): (a) Density distributions as a function of z ; (b) Velocity, in z direction, as a function of z . The points are based on membrane simulations on CNT #5, #4, #6, and #7 (Table 2.1) corresponding to (12, 12) CNT with different length of 3.0 nm, 6.0 nm, 9.0 nm, and 15.0 nm, respectively: $r_p = 0.643$ nm; $\Delta P = 5.0$ MPa; $T = 300$ K. Dashed lines are the membrane boundaries along the z direction separating the system in three parts, from left to right: the water reservoir at high pressure side, the pore of the CNT membrane, and the water reservoir at low pressure side. Solid lines are the trend curves based on the simulation results. The statistical error for each density data point and each velocity data point are less than 1%, and less than 15%, respectively.

The velocity distributions along flow direction, in Figure 2.13(b), show the velocity dramatically increases when water molecules enter and decreases when water molecules

exit the CNT membrane. This change is consistent with the changes in cross sectional area between the reservoirs and the pore - the flux of water (rate/area) is constant at steady state at all positions. Similar to Figure 2.11, the velocity distribution along flow direction decreases with increasing membrane thickness. Thicker membranes exhibit greater resistance.

2.5. Conclusions

NEMD simulations of pressure-driven water flow through CNT membranes are analyzed to obtain transport properties, including flux, density and velocity distributions along the r and z directions.

The water flux and the velocity distribution along the radial direction are compared with the theoretical values calculated by the Hagen-Poiseuille equation and the Navier-Stokes equation, respectively. The results suggest that the classical equations are unable to describe the dynamic behavior of a water flow through a CNT membrane under pressure difference. The latter flow has the unique properties of a very fast flow and a non-parabolic velocity distribution along the radial direction in the CNT. The extremely high flux is due to the nanoscale pore size, the smooth surface of the CNT, and the weak interactions between water and CNT membrane. The water molecules align into layers in the restricted pores that facilitate rapid flow, in accord with literature on transport in nanotubes. Similar to the trend of the flux and velocity predicted by the continuum equations, the flux and velocity increase with increasing pore size or decreasing membrane thickness. The oscillation density distributions along radial direction in the

CNT show that the water molecules form well-ordered structures parallel to the CNT surface due to the restricted space and the relatively weak interactions between water and the CNT surface. The density distributions along flow direction show that the water molecules in the CNT are slightly less dense (about 5%-10%) than in the reservoirs. This difference is because of the unique alignment of the water molecules in the narrow pores compared to more compact water formation in free solution (in the neighboring reservoirs). The velocity in the CNT is higher than that in the water reservoirs simply because of the change in cross-sectional flow area. The membrane thickness has little effect on the density distributions along radial or flow direction. However, the density distributions depend on pore size with generally higher average density and more hydration layers in the CNT membranes with larger pore size.

We conclude that the NEMD simulation system and the simulation method presented in this work provides a useful tool for studying pressure-driven water fluid through CNT membranes under NF operating conditions. The expected significance of this work is a better understanding of the fundamentals, namely pressure-driven water transport mechanisms of CNT membranes, and to help in the design CNTs membranes and improvement of NF processes particularly for water treatment and environmental applications. It can be projected that a CNT membrane, having comparable pore size to organic liquid solute molecules could exhibit very high flux and high rejection in NF applications in, for instance, water treatment for environmental purposes.

References

- [1] N. P. Valentin, Mater. Sci. Eng. R. **43**, 61 (2004).
- [2] G. Che, B. B. Lakshmi, C. R. Martin, E. R. Fisher, and R. S. Ruoff, Chem. Mater. **10** 260 (1998).
- [3] J. K. Holt, A. Noy, T. Huser, D. Eaglesham, and O. Bakajin, Nano Lett. **4** 2245 (2004).
- [4] J. K. Holt, H. G. Park, Y. Wang, M. Stadermann, A. B. Artyukhin, C. P. Grigoropoulos, A. Noy, and O. Bakajin, Science **312** 1034 (2006).
- [5] B. J. Hinds, N. Chopra, T. Rantell, R. Andrews, V. Gavalas, and L. G. Bachas, Science **303** 62 (2004).
- [6] K. Gethard, O. Sae-Khow, and S. Mitra, ACS Appl. Mater. Interfaces **3** 110 (2011).
- [7] S. Kim, J. R. Jinschek, H. Chen, D. S. Sholl, and E. Marand, Nano Lett. **7** 2806 (2007).
- [8] N. Hilal, H. Al-Zoubi, N. A. Darwish, A. W. Mohammad, and M. Abu Arabi, Desalination **170** 281 (2004).
- [9] J. Schaep, B. Van der Bruggen, S. Uytterhoeven, R. Croux, C. Vandecasteele, D. Wilms, E. Van Houtte, and F Vanlerberghe, Desalination **119** 295 (1998).
- [10] B. Van der Bruggen and C. Vandecasteele, Environ. Pollut. **122** 435 (2003).
- [11] R. Rautenbach and A. Gröschl, Desalination, **77** 73 (1990).
- [12] S. Ramakrishna, Z. Ma, and T. Matsuura, *Polymer membranes in biotechnology: preparation, functionalization and application*, (Imperial College, London, 2011).
- [13] D. C. Rapaport, *The art of molecular dynamics simulation (Second edition)*,

(Cambridge University Press, Cambridge, 2004).

- [14] H. C. Andersen, *J. Chem. Phys.* **72** 2384 (1980).
- [15] H. J. C. Berendsen, J. P. M. Postma, W. F. Vangunsteren, A. Dinola, and J. R. Haak, *J. Chem. Phys.* **81** 3684 (1984).
- [16] G. J. Martyna, D. J. Tobias and M. L. Klein, *J. Chem. Phys.* **101**, 4177 (1994).
- [17] H. A. Stern, *J. Comput. Chem.* **25**, 749 (2004).
- [18] M. Bhandarkar, A. Bhatele, E. Bohm, R. Brunner, F. Buelens, C. Chipot, A. Dalke, S. Dixit, G. Fiorin, P. Freddolino, P. Grayson, J. Gullingsrud, A. Gursoy, D. Hardy, C. Harrison, J. H énin, W. Humphrey, D. Hurwitz, N. Krawetz, S. Kumar, D. Kunzman, C. Lee, R. McGreevy, C. Mei, M. Nelson, J. Phillips, O. Sarood, A. Shinozaki, D. Tanner, G. Zheng, and F. Zhu, *NAMD user's guide (Version 2.8)*, (The Board of Trustees of the University of Illinois, Urbana, 2011).
- [19] M. E. Suk and N. R. Aluru, *J. Phys. Chem. Lett.* **1** 1590 (2010).
- [20] J. A. Thomas and A. J. H. McGaughey, *Phys. Rev. Lett.* **102** 184502 (2009).
- [21] J. A. Thomas and A. J. H. McGaughey, *Nano Lett.* **8** 2788 (2008).
- [22] W. D. Nicholls, M. K. Borg, D. A. Lockerby, and J. M. Reese, *Microfluid. Nanofluid.* **12** 257 (2012).
- [23] J. M. D. Macelroy, *J. Chem. Phys.* **101** 5274 (1994).
- [24] R. F. Cracknell, D. Nicholson, and N. Quirke, *Phys. Rev. Lett.* **74** 2463 (1995).
- [25] H. Takaba, E. Matsuda, and S. Nakao, *J. Phys. Chem. B* **108** 14142 (2004).
- [26] C. Huang, K. Nandakumar, P. Choi, and L. W. Kostiuk, *J. Chem. Phys.* **124** 234701

(2006).

- [27] C. Huang, P. Choi, K. Nandakumar, and L. W. Kostiuk, *J. Chem. Phys.* **126** 224702 (2007).
- [28] C. Huang, P. Choi, K. Nandakumar, and L. W. Kostiuk, *Phys. Chem. Chem. Phys.* **10** 186 (2008).
- [29] C. Huang, P. Choi, K. Nandakumar, and L. W. Kostiuk, *J. Nanosci. Nanotechnol.* **9** 793 (2009).
- [30] H. Takaba, Y. Onumata, and S. Nakao, *J. Chem. Phys.* **127** 054703 (2007).
- [31] L. Wang, R. S. Dumont, and J. M. Dickson, "Comparison of two nonequilibrium molecular dynamics simulation systems for the pressure-driven water permeation through carbon nanotube membrane", *Microfluid. Nanofluid.* submitted (2012).
- [32] J. Phillips, R. Braun, W. Wang, J. Gumbart, E. Tajkhorshid, E. Villa, C. Chipot, R. D. Skeel, L. Kalé and K. Schulten, *J. Comput. Chem.* **26** 1781 (2005).
- [33] A. D. MacKerell, N. Banavali, and N. Foloppe, *Biopolymers* **56** 257 (2001).
- [34] W. Humphrey, A. Dalke, and K. Schulten, *J. Mol. Graphics* **14** 33 (1996).
- [35] W. L. Jorgensen, J. Chandrasekhar, J. D. Madura, R. W. Impey, and M. L. Klein, *J. Chem. Phys.* **79** 926 (1983).
- [36] M. Sprik, *Effective Pair Potential and Beyond*, in: M. P. Allen and D. J. Tildesley (Eds.), *Computer simulation in chemical physics*, (Kluwer Academic Publishers, The Netherlands, 1993).
- [37] W. C. Swope, H. C. Andersen, P. H. Berens, and K. R. Wilson, *J. Chem. Phys.* **76**

637 (1982).

- [38] T. Darden, D. York, and L. Pedersen, *J. Chem. Phys.* **98** 10089 (1993).
- [39] J. Goldsmith and C. C. Martens, *J. Phys. Chem. Lett.* **1** 528 (2010).
- [40] A. Noy, H. G. Park, F. Fornasiero, J. K. Holt, C. P. Grigoropoulos, and O. Bakajin, *Nano Today* **2** 22 (2007).
- [41] U. Kaatzke, *Radiat. Phys. Chem.* **45** 539 (1995).
- [42] J. H. Irving and J. G. Kirkwood, *J. Chem. Phys.* **18** 817 (1950).
- [43] M. Majumder, N. Chopra, R. Andrew, and B. J. Hinds, *Nature* **438** 44 (2005).
- [44] M. Majumder, N. Chopra, and B. J. Hinds, *ACS Nano* **5** 3867 (2011).
- [45] X. Qin, Q. Yuan, Y. Zhao, S. Xie, and Z. Liu, *Nano Lett.* **11** 2173 (2011).
- [46] B. Corry, *J. Phys. Chem. B* **112** 1427 (2008).
- [47] J. Goldsmith and C. C. Martens, *Phys. Chem. Chem. Phys.* **11** 528 (2009).
- [48] F. Franks, *Water: a matrix of life (Second edition)*, (Royal Society of Chemistry, Cambridge, 2000).
- [49] N. G. Hadjiconstantinou, A. L. Garcia, M. Z. Bazant, and G. He, *J. Comput. Phys.* **187** 274 (2003).
- [50] W. Janke, Statistical analysis of simulations: data correlations and error estimation, in *Quantum Simulations of Complex Many-Body Systems: From Theory to Algorithms*, edited by G. Johannes, D. Marx, A. Muramatsu (John von Neumann Institute for Computing, Jülich, 2002).
- [51] T. Werder, J. H. Walther, and P. Koumoutsakos. *J. Comput. Phys.* **205** 373 (2005).

- [52] L. D. Landau and E. M. Lifshitz, *Statistical Physics (Part 1)*, (Pergamon Press, Oxford, 1980).
- [53] A. Kalra, S. Garde, and G. Hummer. Proc. Natl. Acad. Sci. U.S.A. **100** 10175 (2003).

Chapter 3 Comparison of Two Nonequilibrium Molecular Dynamics Simulation Systems for the Pressure-Driven Water Permeation through Carbon Nanotube Membranes

3.1. Abstract

Two kinds of nonequilibrium molecular dynamics (NEMD) simulation systems are constructed to investigate the pressure-driven water flows passing through carbon nanotube (CNT) membranes under similar operation conditions. The two different periodic boundary condition (PBC) systems simulated are a two-dimensional (2D PBC) system and three-dimensional (3D PBC) system. These two systems use the same CNT membrane model to simulate the effect of the pressure difference (in the range of 1.0 to 8.0 MPa) on the pure water transport properties. The pressure difference associated with the two systems is created using different NEMD simulation methodologies; the former with pressure set independently on each side of the membrane (at the moving walls) and the latter with the pressure difference fixed to create the pressure-driven flow. The simulation results show that the two systems exhibit similar transport phenomenon of water through CNT membranes including unusually fast water permeation and a periodic (non-parabolic) radial velocity distribution unlike the parabolic form characteristic of continuum flow in the CNT membrane. Although the simulation results obtained from the two systems are similar, the 3D PBC system has a higher water flux (and hence

velocity) than the 2D PBC system because of both the different PBC and the different methodologies used to produce the pressure-driven water flows. The effect of pressure difference on water transport is shown and discussed. Conclusions are drawn that the 2D PBC with movable walls better represents the system, even at the expense of more computational time. In general, the NEMD simulation method is shown to be a feasible and valuable tool for studying pressure-driven permeation processes such as nanofiltration through these studies with model CNT membrane. These studies give the detailed behavior of such systems on a molecular scale and can potentially help the design and operation of pressure-driven permeation systems.

3.2. Introduction

Nanofiltration (NF) is a type of pressure-driven membrane process with properties in between reverse osmosis and ultrafiltration processes. The NF process is operated at low pressure with high water flux and good rejection of divalent or trivalent salts and many organic solute molecules. NF membranes are commercially manufactured usually as thin film composite (TFC) polymeric membranes with a three-layer structure. The transport phenomenon of the TFC NF membrane is primarily decided by the top layer, which is a relatively dense and ultra-thin skin having a pore size in the range of 1 – 10 nm coated on a porous membrane substrate.^[1] In the NF process, solutes of the feed mixture are rejected by the membrane, while the solvent passes through producing both a concentrated stream (retentate) and a purified water stream (permeate). The major industrial application of the NF process is the removal of contaminants from an aqueous

liquid mixture, including drinking water purification, water softening, waste water treatment, removal of organic solutes, recovery of specific chemicals, and concentration of industry products.^[2]

It has been shown through molecular dynamics (MD) simulations that the carbon nanotube (CNT) membranes with quite narrow pore sizes exhibit fast water flow (compared to conventional membrane transport theory).^[3-5] MD simulation is a novel technique to simulate microscopic motions of molecules based on the known physics and the interactions between the molecules, with the goal of better understanding the real system. CNT membranes have been produced experimentally, and studied for potential applications in gas or liquid mixture separations. These real membranes show an improvement of flux and rejection over conventional polymeric membranes.^[6-11] Therefore, CNT membranes have great potential as future commercial NF membranes with improved separation performance.

Transport in NF is driven by the pressure difference between the two sides of the membrane with a concentration gradient across the membrane. Therefore, the NF process cannot be studied by equilibrium MD simulation, and also cannot be studied by the dual-control volume grand canonical ensemble molecular dynamics (DCV-GCMD)^[12-14] which is often used for the simulation of gas systems. However, nonequilibrium molecular dynamics (NEMD) simulations are feasible methods to study a liquid transport process induced by an external field. To study a pressure-driven transport, like a NF process, the NEMD simulation must produce a pressure difference and keep it constant in a nonequilibrium condition. There are two kinds of NEMD

simulation systems reported in the literature to study pressure-driven liquid flows passing through nanoporous membranes under a constant pressure difference - each uses different periodic boundary conditions (PBC). In MD simulations, PBC is used for studying a quite large system by only simulating a small part that is far from the edge. The small part is a unit simulation system repeated periodically to form a large system without edge effects.

The first kind of system simulates pressure-driven liquid flow passing through a porous membrane with two-dimensional PBC (not in the flow direction). There are different external forces applied on either side of the system to generate high and low pressures on the two sides of the membrane. Variations of this kind of system differ in the way the external forces are applied to control these pressures. For instance, some systems are “open” and some are “closed”; “open” being the case where as transport takes place water molecules are added to the upstream side of the membrane and simultaneously water molecules are removed from the downstream side, while in “closed” systems molecules pass through the membrane but do not enter or leave the system. Nicholls,^[15] for example, reported an open NEMD simulation system with two-dimensional PBC to study water flows; the external forces are applied on two control zones, which are composed of water molecules located at the far extreme upstream and downstream boundaries of the system. In this system, water molecules are continually inserted to the upstream and removed from the downstream control zones as water molecules pass through the membrane. To avoid the steady dynamics of the water flow being disturbed by inserting and removing molecules during the simulation, Nicholls used the USHER algorithm^[16] to

ensure a steady state.^[15] In addition to this open system, Huang^[17] and Takaba^[18] both reported a similar closed NEMD system with two-dimensional PBC to study liquid argon flows; the external forces are applied on two movable walls located perpendicular to the flow direction, which move as frictionless pistons in the flow direction. Both Huang^[17, 19-21] and Takaba^[18] used liquid argon fluid at a low simulation temperature (133 K and 85 K, respectively) in order to keep argon in a liquid state. While these results are interesting, the studies are far from real NF processes that generally operate at about 300 K or higher.

In the second kind of NEMD simulation method the PBC is applied in three-dimensional directions (including flow direction) and the pressure difference across the membrane is generated by applying an external constant force on all or parts of molecules of the liquid flow. These systems are often used to investigate the pressure-driven transport of aqueous liquids through different types of membranes including: CNT membranes^[3, 4, 22], palmitoylcholine phosphatidylethanolamine membranes,^[23] and other membranes.^[24, 25] Although these published works using this method are simulated under similar temperatures with real NF processes, very high pressure differences are used; up to a hundred times that of a real NF process.

Our former work (of the first kind of system) modeled different CNT membranes with smooth surfaces and uniform straight pores of typical NF pore sizes, and investigated the transport phenomenon of pure water flow through these membranes under NF operation conditions by using NEMD simulations.^[5] The NEMD system we constructed is derived from the simulation method reported by Huang^[17] and Takaba^[18], and contains a

CNT membrane model with a single straight pore, two water reservoirs connected by the membrane model, and two graphene sheets as movable walls to produce the pressure difference. However, our work was done at a more realistic pressure difference of 5.0 MPa and emphasized the effect of membrane thickness on membrane flux, velocity profiles, and density distributions for several CNT membranes of different thickness and pore size. In the current work, two different NEMD simulation systems are derived from the two methods mentioned above. The primary purpose is to compare these two kinds of simulation systems under realistic NF operating conditions. Here we constructed simulations to study pure liquid water passing through CNT membranes with fixed pore size and membrane thickness under different pressure differences. The first kind and second kind of system are referred to as the “2D PBC system” and the “3D PBC system”, respectively. The effect of the pressure difference on the transport phenomenon is investigated and the simulation results from the two systems are compared to evaluate the two “kinds” of simulation system.

3.3. Simulation Methods

NAMD (NAnoscale Molecular Dynamics) package^[26] and VMD (Visual Molecular Dynamics) package^[27] are used to run and analyze NEMD simulations. Water molecules are treated using the flexible TIP3P (transferable intermolecular potential three-point) water model^[28] in CHARMM (Chemistry at HARvard Molecular Mechanics) force field;^[29] all intramolecular and intermolecular interactions in the system are those of the CHARMM force field. The detailed simulation methodology (force field parameters,

integration algorithm, calculations of long-range interactions, and temperature/pressure control) is the same as in our previous work.^[5]

The two systems model the same (12, 12) type, single-walled CNT membrane (shown in Figure 3.1), which is perpendicularly embedded in two graphene sheets (the membrane surfaces) with the CNT in the center. The length of the CNT, the membrane thickness, is 6.0 nm. The pore size of the CNT membrane depends on the effective radius of the CNT; 0.643 nm for the (12, 12) type CNT.^[3,4] Two water reservoirs are connected by the CNT membrane model to simulate a pressure-driven water flow through the CNT membrane from the top reservoir to the bottom reservoir. The CNT is oriented along z direction, while the surface of the membrane extends in the x and y directions – a 4 nm by 4 nm square. In all simulations, the CNT membrane model is fixed in position; forces associated with water-membrane interactions are only applied to the water molecules.

The 2D PBC system (only applied to x , y directions) shown in Figure 3.2(a) consists of two graphene sheets (acting as the moveable walls for controlling the pressure difference), the CNT membrane model, and two water reservoirs. A higher external force (f_t , in Figure 3.2(a)) along $z+$ direction is applied to each carbon atom of the top wall, and a lower external force (f_b , in Figure 3.2(a)) along $z-$ direction is applied to each carbon atom of the bottom wall. This creates the pressure difference between the high pressure (top) and low pressure (bottom) sides of the membrane to drive the water flow. The Particle Mesh Ewald (PME) method for calculating the electrostatic interactions is used for both systems. For the 2D PBC method, the PBC size in the z direction is set to be at least ten times the system size in z direction. This 2D PBC system uses a three-dimensional PBC

so that electrostatic interactions can be computed using the PME method. The PBC size along the z direction is large enough to make potential contributions from repeat units in this direction negligible.

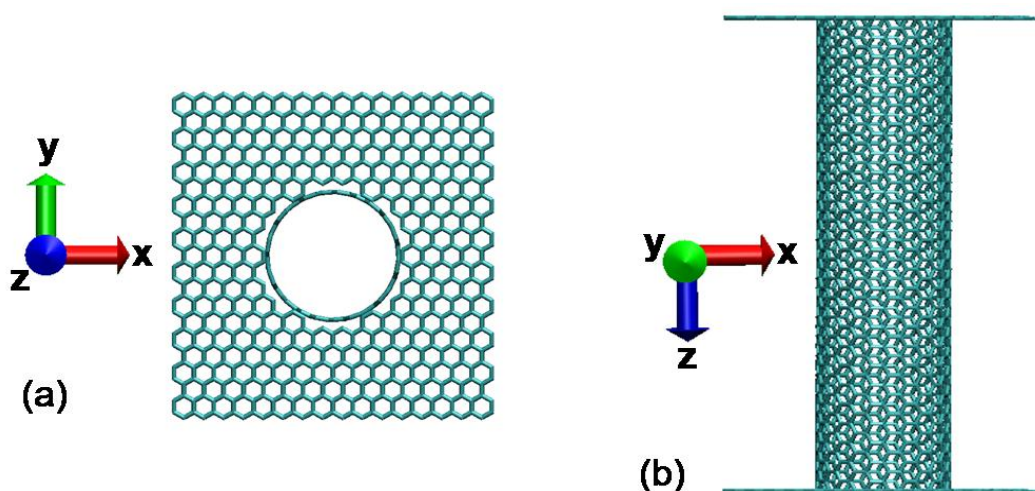


Figure 3.1 Orthographic snapshots of the CNT membrane model produced by the VMD package for the MD simulation. (a) Top view down through the CNT membrane model: the graphene sheet, with an approximated hole in the center, to match the pore size of the CNT. (b) Side view of the CNT membrane model: two graphene sheets are located at the ends of the CNT. Used, with permission from reference [5].

Unlike the 2D PBC system, the 3D PBC system has a real three-dimensional periodic system (PBC applied in all directions) as implied by the name. The 3D PBC system consists only of the CNT membrane model and two water reservoirs, as shown in Figure 3.2(b). The pressure difference across the membrane is generated by applying an external constant force (f , in Figure 3.2(b)), along the z direction, to each oxygen atom of the two water control layers (each of thickness 0.25 nm) located near to the top boundary and the bottom boundary.

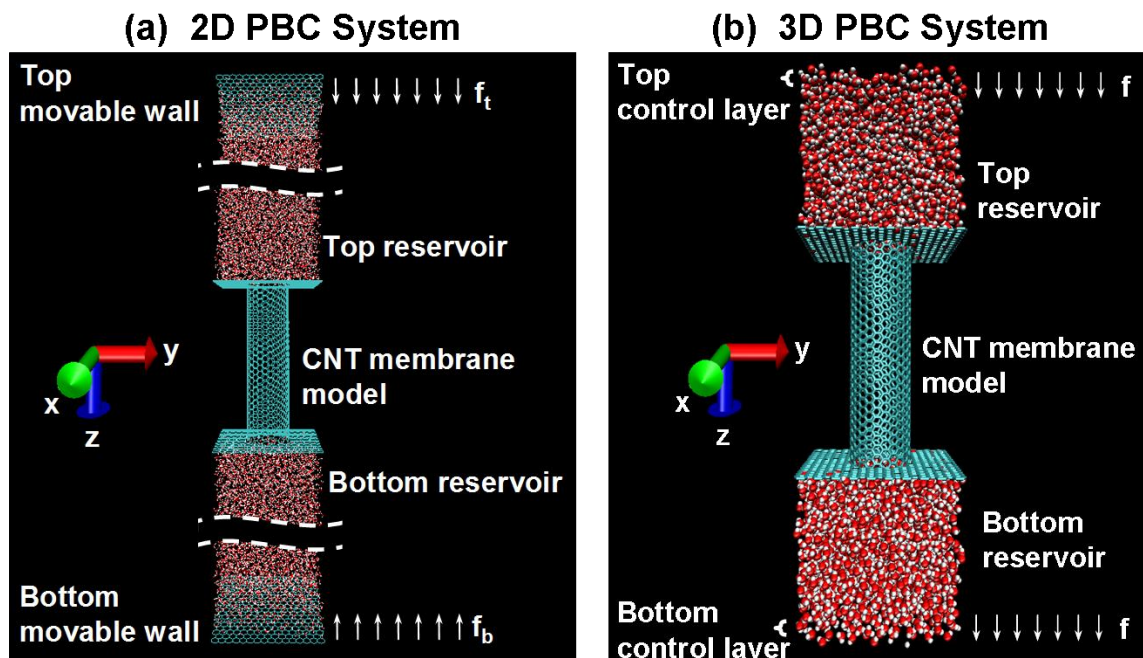


Figure 3.2 Perspective snapshots of the simulation systems produced by the VMD package at the beginning state of the MD simulations. Carbon atoms are green, hydrogen atoms white, and oxygen atoms red. (a) 2D PBC System (adapted from the figure in reference [5]): two water reservoirs connected by the CNT membrane model shown in Figure 3.1; and the two graphene sheets acted as the movable walls where the force f_t or f_b is applied on each carbon atom of the top or bottom wall. (b) 3D PBC System: two water reservoirs connected by the CNT membrane model shown in Figure 3.1; forces f is applied on each oxygen atom of the water control layers located near the top and bottom boundaries within 0.25 nm.

The CNT membrane is initially empty without any water molecules filling the CNT, for both simulation systems, as shown in Figure 3.2; an equilibrium MD simulation is run to allow the water molecules in the two reservoirs to fill but not to pass through the CNT membrane. The equilibrium MD simulation for each system is kept at 2.0 ns with 0.5 fs time step at constant temperature and pressure (300 K and 0.1 MPa); after that the system should reach an equilibrium state at the desired temperature and pressure. The resulting system state provides the initial conditions for a NEMD simulation with external forces

applied on the system, using 1.0 fs time steps at 300 K. The trajectory data are collected for every time step, and the first 1.0 ns (or longer) trajectory data are abandoned as the system is not yet at steady state.

To investigate the effect of pressure difference on the pure water transport properties for the two systems defined above a series of NEMD simulations are run under different pressure differences: 1.0, 3.0, 5.0 and 8.0 MPa. Note that for the 2D PBC system, the lower pressure applied on the bottom side is kept at 0.1 MPa in each simulation, while for the 3D PBC only the pressure difference can be set. The results of NEMD simulations are analyzed to calculate the time average values of the flux, the density and velocity (in z direction) distributions both along the radial direction and along the flow direction.

3.4. Results and Discussion

The forward flux is the number flow rate per unit area along the $z+$ direction, and the backward flux is the number flow rate per unit area along the $z-$ direction. Each forward or backward number flow rate of the 2D or 3D PBC system is determined by counting the water molecules passing through the CNT membrane from one water reservoir to the other reservoirs (entering the CNT from one reservoir and then leaving the CNT to the other reservoir) in the simulation time. The detailed method to track the movement of water molecules and count the number flow rate is derived from the method to obtain water permeation through a CNT reported by Cohen.^[30] The net water flux is defined as the net number flow rate per membrane area: for the 2D PBC system, the net number flow rate is determined by counting the increasing number of water molecules in the

bottom reservoir, which is the same as in our former work;^[51] for the 3D PBC system, the net number flow rate is the difference between the forward flow rate and the backward flow rate. Each flux value is calculated in the units of both ‘molecules/(ns nm²)’ and ‘m³/(m² s)’ or equivalently ‘m/s’.

The number of water molecules passing through the membrane model is counted every 50-200 ps within the total NEMD simulation time and plotted as a function of the simulation time. The slope of the plotted linear profile (through the origin) is the number flow rate to calculate the simulation flux (forward, backward, or net flux). For each flux value, the estimated error of the flux is represented by the standard error on the slope with the assumption of uncorrelated data. The error analysis for the simulation flux is as shown in our former work.^[51]

To investigate the radial distributions, the pore of the CNT membrane is divided into ten annular sections of equal space in the radial direction: for all densities and velocities in the pore as a function of r , the values are averaged over a thin annular section in the pore at r (excluding the entrance and exit regions). The entire system is divided into several sections of equal space in the flow direction from the top water reservoir to the bottom water reservoir; there are ten sections in the top reservoir for the 2D PBC system and five sections for the 3D PBC system followed by three sections within the CNT for both systems. For all densities and velocities of water molecules as a function of z , values are averaged over a thin section at z (cylindrical sections in the pore and square cuboid sections in the water reservoirs). The overall value of each radial or flow direction section in the simulation time is averaged by the data collected in the unit

simulation time. The NEMD trajectory is saved every time step and the collected successive data are time correlated. The error analyses are performed including the integrated autocorrelation time^[31] for both density and velocity values as shown and discussed in our previous work.^[5] The integrated autocorrelation time is determined for time correlated data, and the statistical error of each density or velocity data point is calculated directly from the standard deviation of the sampled mean by using the number of uncorrelated samples.^[5]

The theoretical flux (Eqn. (3.1), also called Hagen-Poiseuille equation) and the theoretical radial velocity in z direction (Eqn. (3.2) referred to as the Navier-Stokes equation) can both be derived from the Navier-Stokes equations used for describing the liquid fluid through a cylindrical channel.

$$J_w = L_p \Delta P = \frac{r_p^2}{8\eta(L_z/A_K)} \Delta P \quad (3.1)$$

$$A_K = \frac{\pi \cdot r_p^2}{A_{mem}} = \frac{\pi \cdot r_p^2}{L_x \cdot L_y}$$

$$v_z = \frac{\Delta P}{4\eta L_z} (r_p^2 - r^2) \quad (3.2)$$

where L_p is the permeability coefficient of the water fluid, r_p is the pore radius, η is the viscosity of water at the operating temperature, and L_z/A_K is the ratio of the membrane effective thickness to the membrane porosity, ΔP is the pressure difference, and r is the radial position. The water density of 1000 kg/m^3 and the viscosity of $8.54 \times 10^{-4} \text{ Pa s}$ ^[32] at 300 K are used to calculate the theoretical values of flux and velocity (from Eqns. (3.1) and (3.2)), which are compared with the simulation results.

3.4.1. Comparisons of the two systems

The 2D PBC system and the 3D PBC system are used to study pure water flow passing through the same CNT membrane model under the same pressure differences; there are some differences between the two systems as listed in Table 3.1. Firstly, the two systems use different PBC for running NEMD simulations as the description of their names implies: two-dimensional PBC (x , y directions) in the 2D PBC system and three-dimensional PBC in the 3D PBC system. The 3D PBC system is replicated not only in x , y direction (same as the 2D PBC system) but also in z direction. For the 3D PBC system the water molecules repeatedly pass the CNT membrane from the top reservoir to the bottom reservoir and then leave the bottom reservoir to enter the top reservoir. In the 2D PBC system the water molecules of the top reservoir passing the CNT membrane are stored in the bottom reservoir or go back to the top reservoir by passing the CNT membrane again but along z - direction back through the membrane. With water flow passing through the CNT membrane, the number of water molecules in each water reservoir is constant for the 3D PBC system due to the PBC along the z direction, while the number of water molecules in top water reservoir gradually decreases and the number of water molecules in the bottom reservoir gradually increases for the 2D PBC system.

Different methodologies are used for the two NEMD system simulations to produce the pressure difference. In the 2D PBC system, the movement of each movable wall is controlled by the total force exerted on it, including the externally applied force and the

forces produced by water molecules because of the intermolecular interactions. The 2D PBC system using two movable walls to control pressures is derived from the NEMD studies presented by Huang^[17, 19-21] and by Takaba,^[18] and their previous work has shown that this kind of simulation system can achieve a constant pressure difference inducing a steady flow through a membrane. They both used the Irving–Kirkwood method^[33] to estimate the local pressures in the liquid argon reservoirs, and the results showed that the pressures in the reservoirs corresponded to the targeted values at the walls.^[18, 20] Therefore, the 2D PBC system can produce both the higher and lower pressures (thus generating the target pressure difference) on the two sides of the membrane.

In the 3D PBC system, water molecules passing out of the bottom control layer appear in the top control layer due to the z direction PBC, and the external force (f along the z + direction, shown in Figure 3.2(b)) is applied on each oxygen atom of the water molecules in the two water control layers. The PBC requires symmetry between the top and bottom control layers (as one is just a “continuation” of the other – as molecules pass out of the bottom control layer they appear in the top control layer) so that only the pressure difference across the membrane can be set. The pressure difference between the top and bottom water reservoirs is the total force (f times the total number of O atoms in the combined top and bottom control layers) over the cross sectional area (in x, y directions) of the system. This method has been used in many previous works to study pressure-driven flows through membranes.^[3, 4, 22-25] Suk^[22] studied water flows passing through graphene and CNT membranes driven by the pressure difference of 100 MPa, and also used the Irving–Kirkwood method^[33] to estimate the local pressures in the water

reservoirs. The two pressures in the water reservoirs at the two sides of the membrane are about 80 MPa and -20 MPa, respectively, resulting in a 100 MPa pressure difference.^[22] In the case of the 3D PBC system, the pressure difference across the membrane can be produced at a target value, and positive and negative pressures may exist in the reservoirs.

Table 3.1 Comparison of the two systems

	2D PBC System	3D PBC System
PBC directions	<i>x, y</i>	<i>x, y, and z</i>
Number of water molecules in each reservoir	Variable	Constant
External forces applied on	Two moveable walls	Two water control layers
Pressure difference	High pressure and low pressure at target values	A target pressure difference
Water molecules	> 13 000	About 4000
CPU Time (days/ns)^a	14	5

^aCPU Time is the time used for one CPU to process 1.0 ns of the NEMD simulation while the real CPU time depends on the number of parallel processors running simultaneously (on SHARCNET). For instance, the 2D PBC system (14 CPU days/ns) takes about 14.5 days for a 50 ns NEMD simulation using 48 parallel processors.

As shown in Table 1, the number of water molecules in the 2D PBC system is more than 3 time of that in the 3D PBC. The larger simulation size of the 2D PBC system is required to avoid the effect of the wall-membrane interactions on water transport, the system is size independent above a certain size. The larger the system size, the greater

the number of calculations in the NEMD simulation because there are more intramolecular and intermolecular forces and potential energies to be calculated. The Table 1 also lists example CPU time for 1.0 ns of NEMD simulation: the 2D PBC system takes nearly 3 times the CPU time than the 3D PBC system.

The sections below compare the transport properties between the 2D PBC and 3D PBC systems. To determine whether the observed differences are due to difference in size of the system, another 3D PBC system was considered. This additional 3D system had two thicker water reservoirs and the same simulation size (the total number of water molecules in the system) as the size of the 2D PBC system. Two simulations were carried out to simulate pressure-driven water transport at 8.0 MPa using the same simulation method but using two different 3D PBC systems – specifically, the larger 3D PBC system and the standard 3D PBC system (Figure 3.2(b)). The difference between the two simulations is within 5% (not shown here) in terms of the investigated transport properties. The similarity of these two 3D PBC systems supports the use of the smaller system for comparison to the 2D PBC system in terms of the transport properties discussed below.

3.4.2. The effect of pressure on flux

To compare results between the two simulation systems, the fluxes as a function of pressure difference are shown in Figures 3.3 and 3.4. The standard error of each flux data, estimated as described above, is less than 0.5%.

As shown in Figure 3.3, the net fluxes obtained from the two systems both increase

with increasing pressure difference, and the simulation fluxes are much higher than the theoretical fluxes calculated from the Hagen-Poiseuille equation (Eqn. 3.1). A continuum flow in a cylinder channel is described by the Hagen-Poiseuille equation. However, the water flow in the CNT forms a nanoscale flow and is no longer dominated by the bulk properties. The water molecules in the CNT are quite near to the CNT pore surface within a few angstroms. Therefore, the transport of the nanofluid (the water flow in the CNT) is dependent on the water-pore interactions: strong interactions reduce flow, while weak interactions speed up flow. A combination of the smooth and frictionless CNT surface, the quite narrow pore size, and the weak interactions between water molecules and the CNT surface causes fast pressure-driven water flow. The high simulation flux is not governed by the Hagen-Poiseuille equation, similar results to those seen in our former work^[5] and others^[15, 34, 35].

As shown in Figure 3.3, the net flux of the 3D PBC system increases faster than the flux of the 2D PBC system with increasing pressure difference. Upon increasing the pressure difference from 1.0 MPa to 8.0 MPa, the 2D PBC system shows a more linear trend of increasing flux (the solid line) than the 3D PBC system. The two systems both have a trend line curving upward with increasing flux, while the 3D PBC system (the dotted line) has a stronger curved trend than the 2D PBC system (the solid line).

The forward and backward fluxes of the two systems, as a function of pressure difference, are shown in Figure 3.4; forward flux increases, while backward flux decreases, with increasing pressure difference. Forward and backward fluxes show the same differences as the net fluxes. Figure 3.4(a) shows the forward flux of the 3D PBC

system is lower than that of the 2D PBC system at the lower pressure difference of about 1.0 to 4.8 MPa and then gradually increases to higher than that of the 2D PBC system at higher pressure differences. Moreover, Figure 3.4(b) shows the backward flux of the 3D PBC system becomes zero at the higher pressure difference about 4.3 MPa while the backward flux of the 2D PBC system is non-negligible for the whole pressure difference (1.0 – 8.0 MPa) range. The forward flow is primarily driven by the pressure difference, while the backward flow is caused by molecular diffusion. Of course, there are always some water molecules moving in both $z+$ and $z-$ directions (and even passing through the membrane) due to diffusion. What we are seeing is that the relative importance of backward ($z-$ direction) diffusion decreases with increasing pressure driving force. Note that z increases from top to bottom – i.e. it increases downward. These results, in Figures 3.3 and 3.4 can be interpreted as stated below.

In the 2D PBC system, the external forces applied on the movable walls produce two fixed constant pressures, one on each side of the membrane; the water in these reservoirs is similar to bulk water at the same conditions (pressure and temperature). So water molecules throughout the system move both upward and downward with a net preference for the $z+$ direction, consequently a lower backward flux and a higher forward flux are obtained at each pressure difference.

For the 3D PBC system the three-dimensional PBC means that some of the water molecules in the bottom water control layer moving in the $z+$ direction leave the lower control layer and enter the top water control layer. Thus water molecules can move from the lower reservoir to the upper reservoir by a path other than passing through the

membrane. It is important to realize that this is an anomaly of the 3D PBC system; this flow is not real but instead is the result of the computational method. The number of water molecules in each zone (each water control layer, each water reservoir, or the CNT) is constant: when water molecules leave/enter a zone, some other molecules must enter/leave this zone by material balance (at steady state). Due a combination of the 3D PBC and this material balance there is an enhanced flow in the $z+$ direction. Again this flow is an artifact of the 3D PBC system and is not a real contribution to membrane water transport. For the 2D PBC system there is no movement (except by diffusion) of water molecules from the bottom reservoir directly to the top reservoir as there is in the 3D PBC case. As shown in Figure 3.3 as the pressure driving force increases more molecules are transported in the $z+$ direction and this is likely the cause of the increased flux compared to the 2D PBC simulation. As well, this artifact of the computational method for the 3D PBC system effectively causes a reduced backward flux ($z-$ direction) compared to the 2D PBC (as shown in Figure 3.4(b)).

Stated in another way, the above characteristic of the PBC (for the 3D PBC case) causes a positive feedback in the forward flux that could be responsible for the observed curved trends in flux versus pressure difference. As such, the observed enhanced flow in the $z+$ direction that is likely an artifact of the 3D PBC system and is not a true representation of water transport across membranes. Note, in particular, the elimination of backward flux ($z-$ direction) in 3D PBC system at higher pressure differences (shown in Figure 3.4(b)). Molecules passing from the lower control volume and appearing in the upper control volume impede the backward flow at the top and suppress backward

flux. This feedback is not consistent with flow across a real membrane. We conclude that results obtained with the 3D PBC method are not a reliable representation of flux through a real membrane. These explanations are consistent with those of Suk who explained their results in terms of positive and negative pressures existing in the upper and lower water reservoirs, respectively, while using a simulation system similar to the 3D PBC system.^[22] The negative pressure in the bottom reservoir contributes to the transport of the water molecules through the membrane into the bottom reservoir, consistent with the above statements about the enhanced forward flow for the 3D PBC system.

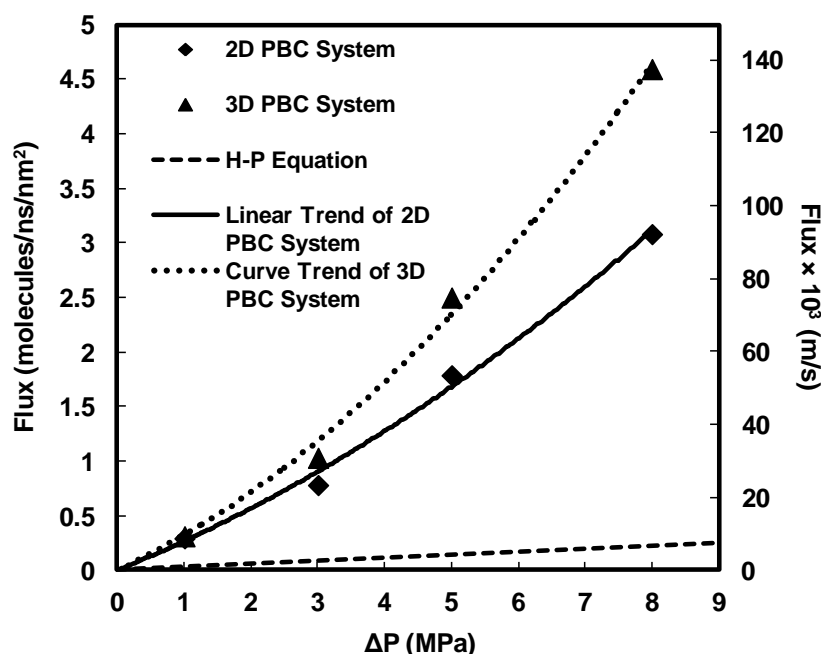


Figure 3.3 Flux (rate per membrane area), shown both as molecular flux and conventional flux (in m/s), as a function of the pressure difference (ΔP) for the two kinds of simulation systems. The statistical error for each data point is less than 0.5%. The points are based on membrane simulations modeled by (12, 12) CNT: $r_p = 0.643$ nm, $L_z = 6.0$ nm, $T = 300$ K. H-P Equation refers to the Hagen-Poiseuille equation (Eqn. (3.1)) represented by the dashed line. The solid line is the linear trend through origin based on the simulation fluxes estimated by 2D PBC system, while the dotted line is the curve trend through origin based on the simulation fluxes estimated by 3D PBC system.

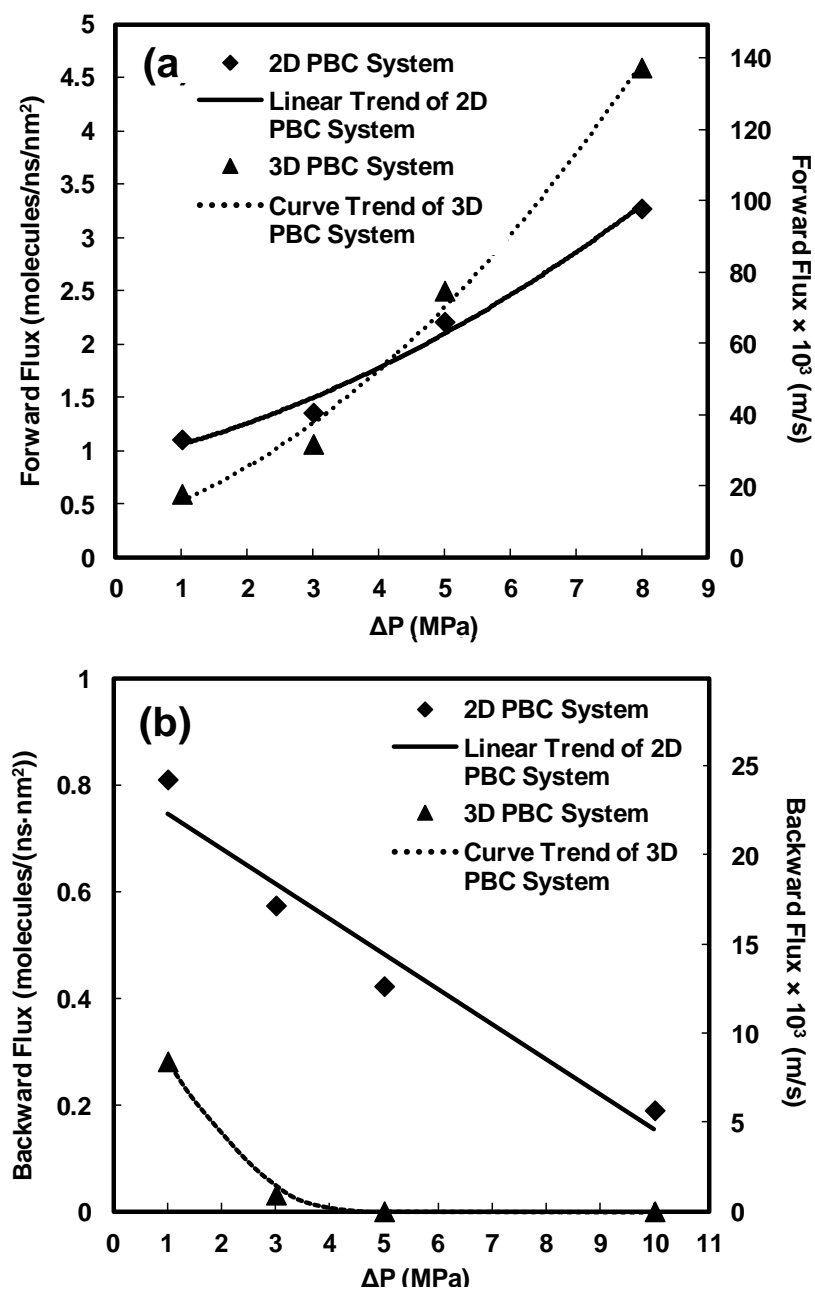


Figure 3.4 Forward and backward fluxes (rate per membrane area), shown both as molecular flux and conventional flux (in m/s), as a function of the pressure difference (ΔP) for the 2D PBC and 3D PBC systems: (a) Forward flux vs. ΔP ; (b) Backward flux vs. ΔP . The statistical error for each data point is less than 0.5%. The points are based on membrane simulations modeled by (12, 12) CNT: $r_p = 0.643$ nm, $L_z = 6.0$ nm, $T = 300$ K. The solid line and dotted line are trend lines based on the simulation results.

With increasing pressure difference (driving force), the net preference for the $z+$ direction enhances. For the 2D PBC system, the high pressure increases but the low pressure is fixed at 0.1 MPa; consequently, the forward flow increases while the backward flow decreases but cannot disappear due to the constant pressure of 0.1 MPa in the bottom reservoir. For the 3D PBC system, the external force applied on the water control layers increases. Furthermore, for the 3D PBC system (as described above), the more water molecules moving along the $z+$ (with increasing pressure difference) means that fewer water molecules pass through the membrane from the bottom reservoir to the top reservoir. From the Figure 3.4 (b) shows that essentially no backward flux is observed in the 4.8 to 8.0 MPa range. Any backward flux from molecular water diffusion is insignificant at pressure differences higher than about 4.8 MPa because of this positive feedback in the forward flux. The curved trends for water flux as a function of pressure difference (lower than 150 MPa) have been observed with CNT and SiC nanotube membranes by using a similar 3D PBC system.^[36]

Therefore, the differences of the forward and the backward flux between the two systems (shown in Figure 3.4 and discussed above) are caused by the effect of diffusion on the water transport, and this effect is dependent on the simulation methodology. In summary, the 3D PBC method artificially increases water transport through the membrane as an artifact of the application of the 3D period boundary condition. For this reason, we believe the 2D PBC system is better than the 3D PBC system as the latter is not a true representation of pressure-driven water transport across membranes – it is not like a real NF process. In general, the 2D PBC system can better simulate a water flow

driven by high and low positive pressures across a membrane and include diffusion as in the real membrane system.

3.4.3. Radial-direction distributions

The CNT is divided into ten annular cylinders – i.e. the radial coordinate is divided into ten intervals - to investigate the associated density and velocity distributions. Each data error in the reported density and velocity distributions is investigated by the standard deviation of the sampled mean (accounting for time correlations, as mentioned above). The density errors are all less than 1%, and the velocity errors are higher than density errors but less than 20% for most data (comparable to the errors reported in our previous paper.^[5]

Figure 3.5 shows two sets of the density distributions along the radial direction at different pressure differences: Figure 3.5(a) for the 2D PBC system and Figure 3.5(b) for the 3D PBC system. For each distribution profile, the density with respect to radial position is oscillatory. The oscillations are center symmetric with two pairs of symmetrical peaks corresponding to two cylindrical rings of water molecules within the CNT. For each system, the density distributions at four different pressure differences are almost perfectly overlapped. The water density distribution is insensitive to the pressure difference in the 1.0 to 8.0 MPa range.

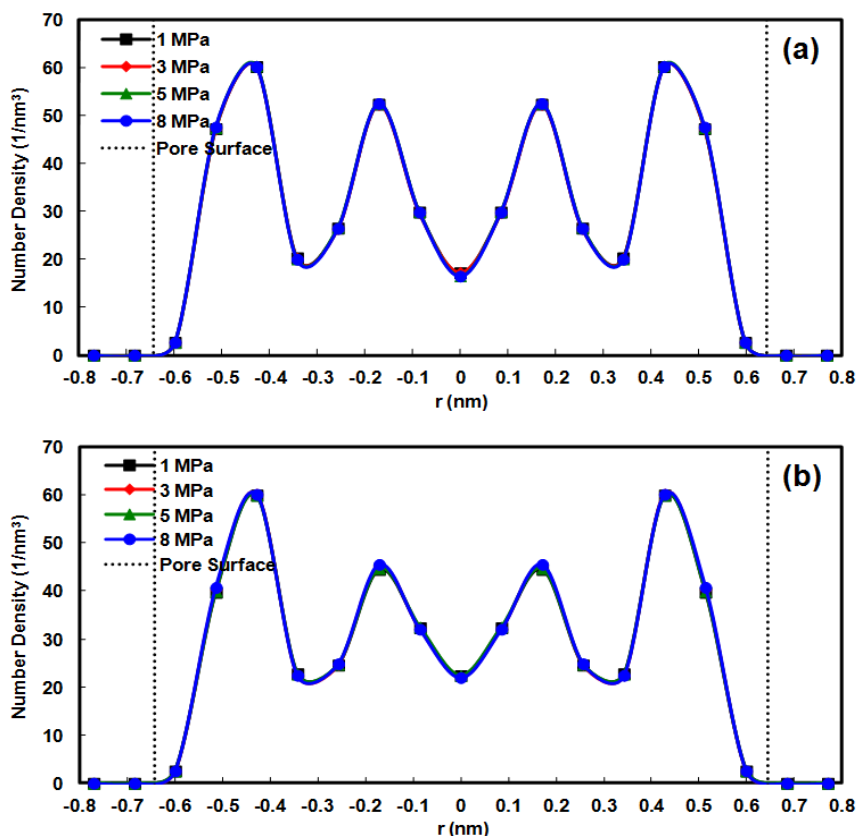


Figure 3.5 Effect of pressure difference on the density distributions along the radial direction for the 2D PBC and 3D PBC systems; values are averaged over a thin annular section in the pore at r (excluding the entrance and exit regions): (a) 2D PBC system; (b) 3D PBC system. The statistical error for each data point is less than 1%. The points are based on membrane simulations on (12, 12) CNT: $r_p = 0.643$ nm, $L_z = 6.0$ nm, $T = 300$ K. The solid lines are the trend curves based on the simulation results, and the dotted lines are the pore surface represented by the effective pore radius (0.643 nm).

The two radial density distributions at 1.0 MPa obtained from the two kinds of systems are plotted in Figure 3.6 for direct comparison. The two oscillatory distributions are similar, but the distribution of the 2D PBC system shows sharper peak pairs in the pore center and wider peak pairs near the pore surface than in the 3D PBC system distribution. Mostly, however, the simulation methodology has little effect on the arrangement of water molecules in the CNT.

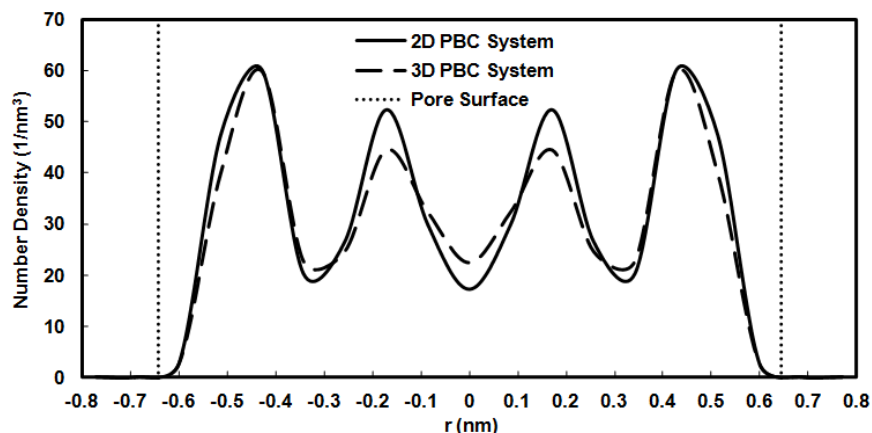


Figure 3.6 Comparison of the radial density distributions of the 2D PBC and 3D PBC systems at 1.0 MPa pressure difference: the solid line for the 2D PBC system, from Figure 3.5(a); the dashed lines for the 3D PBC system, from Figure 3.5(b). The statistical error for each data point is less than 1%. The dotted lines are the pore surface represented by the effective pore radius (0.643 nm).

Figure 3.7 shows two sets of the velocity (along the z direction) distributions along the radial direction at different pressure differences: Figure 3.7(a) for the 2D PBC system and Figure 3.7(b) for the 3D PBC system. For each distribution profile, the axial velocity with respect to radial position is an oscillatory distribution – it is not parabolic in accord with the Navier-Stokes equations. The simulation velocities are much higher than the theoretical values predicted by the Navier-Stokes equations at the same radial positions. The non-parabolic profile of the velocity as a function of the radial position has been described in our former work.^[5] Briefly, the comparable size between the CNT pore and the water molecule results in water molecules being quite close to the CNT surface and a non-uniform distribution of water molecules formed in the CNT.

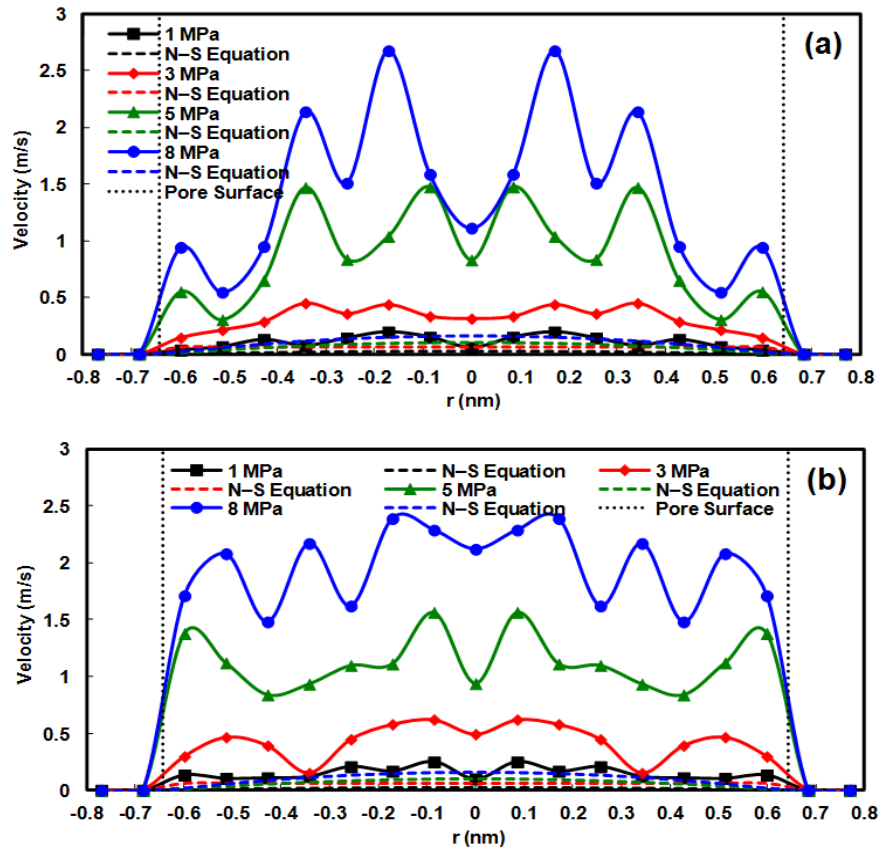


Figure 3.7 Effect of pressure difference on the velocity (in z direction) distributions along the radial direction for the 2D PBC and 3D PBC systems; values are averaged over a thin annular section in the pore at r (excluding the entrance and exit regions): (a) 2D PBC system; (b) 3D PBC system. The statistical errors for most data points are less than 20%. The points are based on membrane simulations on (12, 12) CNT: $r_p = 0.643$ nm, $L_z = 6.0$ nm, $T = 300$ K. N-S equation refers to the Navier-Stokes Equation (Eqn. (3.2)). The dashed lines are the trends based on the Navier-Stokes Equation, the solid lines are the trend curves based on the simulation results, and the dotted lines are the pore surface represented by the effective pore radius (0.643 nm).

The Navier-Stokes equation fails to predict the velocities in the z direction of the rapid pressure-driven water flow passing through the CNT membrane. The high deviation of the simulation velocity from the theoretical velocity arises for reasons already discussed

when we considered flux through the membrane: the weak interactions between water molecules and the CNT membrane, and the nearly frictionless CNT surface. Figure 3.7 shows that the velocity of the water flow in the CNT is sensitive to the pressure difference - water flow velocity increases with higher pressure difference. The velocity distributions of the two kinds of systems are compared directly at each pressure difference in Figure 3.8.

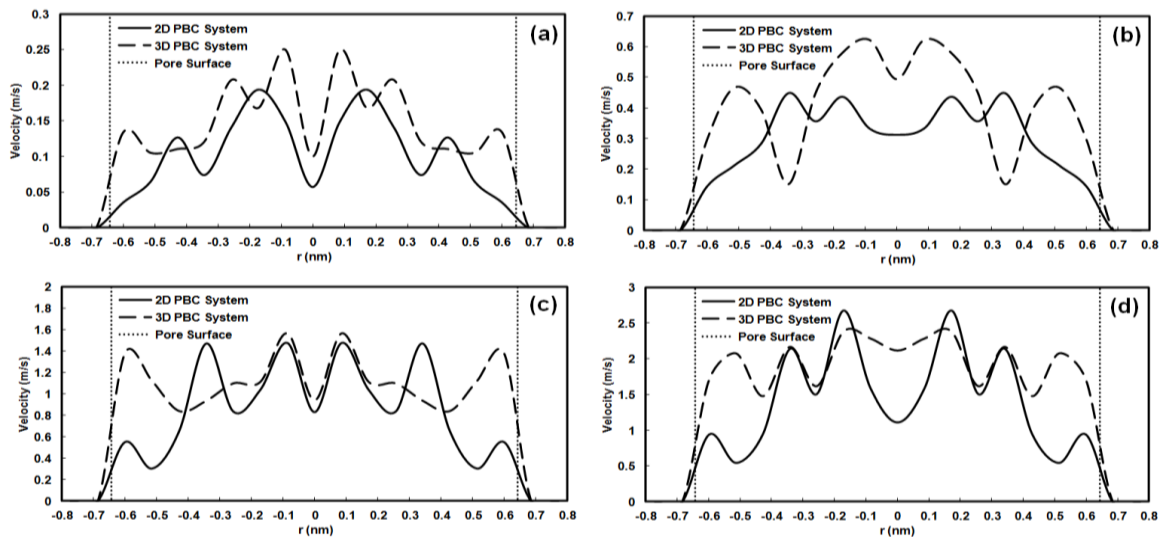


Figure 3.8 Comparison of the 2D PBC and 3D PBC systems of the velocity (in z direction) distributions along the radial direction at different pressure difference: (a) 1.0 MPa, (b) 3.0 MPa, (c) 5.0 MPa, and (d) 8.0 MPa. The statistical errors for most data points are less than 20%. Each solid/dashed line is the trend curve of the radial distribution of the velocity values: the solid lines for the 2D PBC system, from Figure 3.7(a); the dashed lines for the 3D PBC system, from Figure 3.7(b). The dotted lines are the pore surface represented by the effective pore radius (0.643 nm).

Most notably, the distributions are generally quite different, while the 3D PBC system generally exhibiting higher velocities, especially near the pore surface. Figure 3.6 (see

Figure 3.5 for the data points) shows higher density near the pore surface for the 2D PBC system, indicating more water molecules near the pore surface in the 2D PBC system. The lower velocity of the outer water ring of water in the 2D PBC system (seen in Figure 3.7) may correlate with the stronger interactions with the CNT due to closer proximity to the pore surface.

3.4.4. Flow-direction distributions

The density and velocity distributions along the flow direction of the two systems are shown in Figure 3.9 and Figure 3.10, where the CNT is divided into three sections of equal space in the flow direction.

The stream velocity of water flow in the reservoirs is too low because of the low pressure difference and the relatively large area of the reservoirs, so the average velocity is difficult to be obtained with reasonable accuracy through the NEMD simulation. For the 2D PBC system, the water velocity in each reservoir is represented by the velocity of each movable wall, which can be calculated through the linear relationship between the moved distance of the wall and the simulation time. For the 3D PBC, the water velocity in each reservoir is represented by the conventional net flux (Figure 3.3). The estimated errors in density distributions are lower than 1%. The estimated errors in velocity distributions are less than 15% at 3.0 – 8.0 MPa pressure difference, and are higher to about 25% for 1.0 MPa pressure difference.

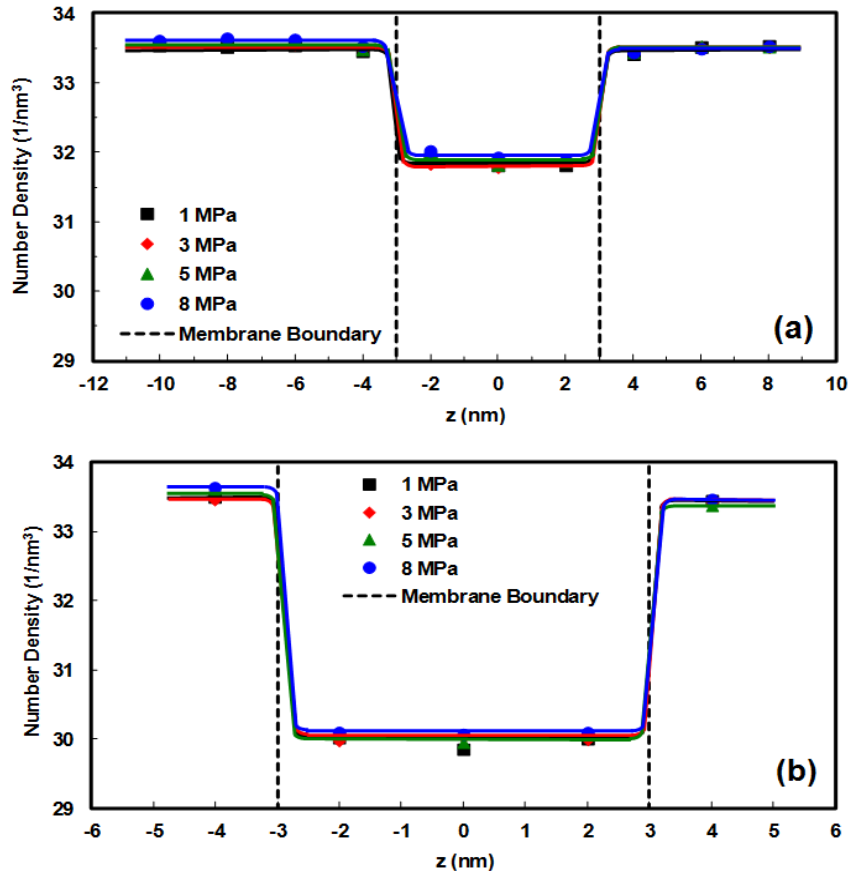


Figure 3.9 Effect of pressure difference on the density distributions along flow direction for the 2D PBC and 3D PBC systems; values are averaged over a thin section at z (cylindrical sections in the pore and square cuboids sections in the water reservoirs): (a) 2D PBC system; (b) 3D PBC system. The statistical error for each data point is less than 1%. The points are based on membrane simulations on (12, 12) CNT: $r_p = 0.643$ nm, $L_z = 6.0$ nm, $T = 300$ K. The dashed lines are the membrane boundaries along z direction separating the system in three parts from left to right: the water reservoir at high pressure side, the pore of the CNT membrane, and the water reservoir at low pressure side. The solid lines are the trend curves based on the simulation results.

Figure 3.9 compares density distributions along the flow direction for different pressure differences, for both simulation systems. The distributions are insensitive to pressure difference, for each system. This is expected, considering the insensitivity of the radial distributions to pressure difference (seen in Figure 3.5). While water density in the CNT does not depend on pressure difference, it is sensitive to pore size.^[5]

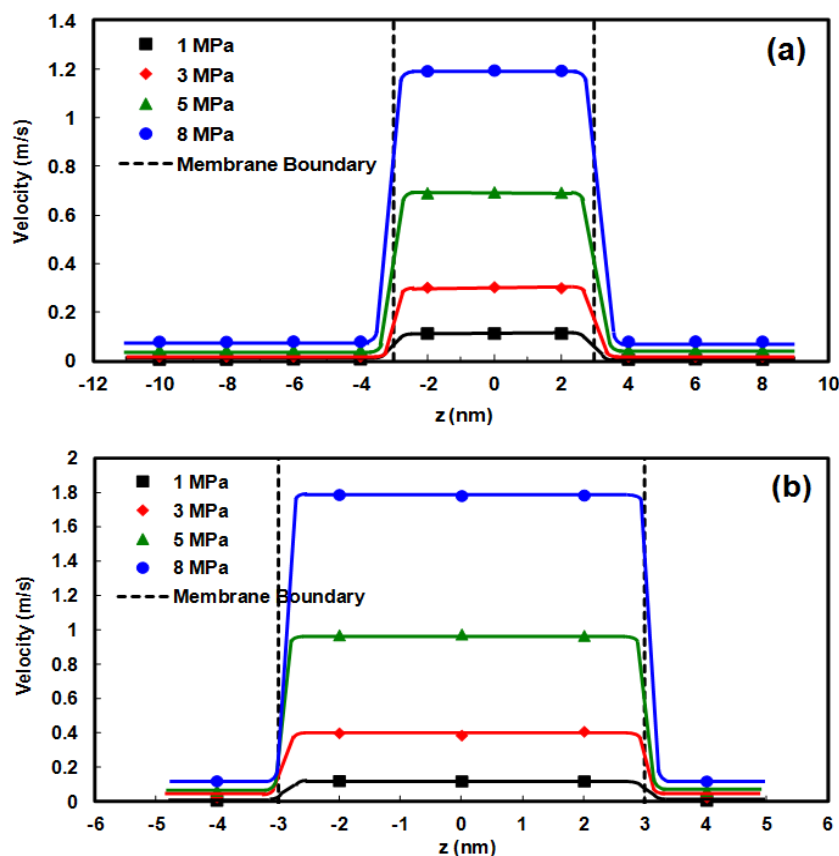


Figure 3.10 Effect of pressure difference on the velocity (in z direction) distributions along flow direction for the 2D PBC and 3D PBC systems; values are averaged over a thin section at z (cylindrical sections in the pore and square cuboids sections in the water reservoirs): (a) 2D PBC system; (b) 3D PBC system. The statistical error are less than 15% for data points at 3.0 – 8.0 MPa and are about 25% for data points at 1.0 MPa. The points are based on membrane simulations on (12, 12) CNT: $r_p = 0.643$ nm, $L_z = 6.0$ nm, $T = 300$ K. The dashed lines are the membrane boundaries along z direction separating the system in three parts from left to right: the water reservoir at high pressure side, the pore of the CNT membrane, and the water reservoir at low pressure side. The solid lines are the trend curves based on the simulation results.

Density in the CNT is slightly lower (about 4-10%) than in the water reservoirs, due to the ordered configuration of water molecules in the nanopore versus the strong hydrogen bonds of water molecules in bulk solution (the water reservoir). This effect is most pronounced for the 3D PBC system with water density in the CNT about 2 molecules/nm³ less than that for the 2D PBC system. The higher CNT density in the 2D PBC case is

less obvious when spread out as a radial distribution of density.

The velocity distributions along the flow direction in Figure 3.10 all show that the water flow is much faster in the CNT than in the water reservoirs, consistent with the much smaller cross-sectional area of the nanopore. Also, velocity increases with pressure difference – the latter being the driving force for a nonzero velocity. Comparing results for the two simulation methods, we see that the 3D PBC system produces the greatest velocities – especially when the pressure difference is large. This is expected, given the larger fluxes of the 3D PBC system, discussed above. The higher velocities of the 3D PBC system compensate for the lower densities to generally produce larger fluxes more than the 2D PBC system.

Overall, we see that the two simulation methodologies produce different transport properties along the flow direction – most evident in the velocity distributions, but also evident in the density.

3.5. Conclusions

We compare simulation results, using two different NEMD simulation systems, the 2D PBC system and the 3D PBC system to investigate pressure-driven water flows through a CNT membrane. The two systems contain the same CNT membrane model, but use different methodologies to produce the pressure difference across the membrane, and employ different PBC to mimic macroscopic-scale systems.

The two systems both show some common water transport properties: 1. pressure-driven water flow through the CNT membrane exhibits an extraordinary fast

flow; 2. the water molecules in the CNT show a non-parabolic velocity distribution along the radial direction; 3. simulation flux and axial velocity both increase with increasing pressure difference; 4. water density distributions along the radial or flow direction are independent of pressure difference. The unique properties of the CNT, the nanoscale pore size, the smooth surface of the CNT, and the weak water–CNT interactions, cause the high flux and the fast velocity of the pressure-driven water flow passing through the CNT membrane, which cannot be described by the continuum equations .

The transport properties modeled by the two systems have some significant differences. Density in the CNT for the 3D PBC system is about 2 molecules/nm³ (about 7%) smaller than the 2D PBC system. More significantly, the flow direction water velocity is higher for the 3D PBC system, especially when the pressure difference is high. It is notable that, for the higher pressure difference (> 3.0 MPa), the backward flux is almost completely suppressed in the 3D PBC – the 2D PBC system shows a more modest suppression of backward flux that seems more realistic. The different transport properties obtained from the two systems may be caused by the positive feedback in the forward flux, due to the different NEMD simulation methodology. The positive feedback in the forward flux for the 3D PBC is an anomaly of the z direction period boundary condition. Molecules from the bottom of the low pressure reservoir are cycled back to the top of the high pressure reservoir which causes a water flux that increases with pressure faster than expected based on the conventional theory (which predicts a linear relationship) and based on the results obtained using the 2D PBC method.

Overall, we prefer the 2D PBC system for use in future CNT membrane simulation studies. The NEMD simulation method can be a feasible tool for studying pressure-driven permeation and the simulation studies can provide the detailed dynamic behavior on a molecular scale, which can potentially improve pressure-driven permeation systems.

References

- [1] S. Ramakrishna, Z. Ma, and T. Matsuura, *Polymer membranes in biotechnology: preparation, functionalization and application*, (Imperial College, London, 2011).
- [2] A. I. Schäfer, A. G. Fane, and T. D. Waite, *Nanofiltration – Principles and applications*, (Elsevier, Oxford, 2005).
- [3] J. Goldsmith and C. C. Martens, *J. Phys. Chem. Lett.* **1** 528 (2010).
- [4] A. Noy, H. G. Park, F. Fornasiero, J. K. Holt, C. P. Grigoropoulos, and O. Bakajin, *Nano Today* **2** 22 (2007).
- [5] L. Wang, R. S. Dumont, and J. M. Dickson, *J. Chem. Phys.* **134** 044102 (2012).
- [6] G. Che, B. B. Lakshmi, C. R. Martin, E. R. Fisher, and R. S. Ruoff, *Chem. Mater.* **10** 260 (1998).
- [7] J. K. Holt, A. Noy, T. Huser, D. Eaglesham, and O. Bakajin, *Nano Lett.* **4** 2245 (2004).
- [8] J. K. Holt, H. G. Park, Y. Wang, M. Stadermann, A. B. Artyukhin, C. P. Grigoropoulos, A. Noy, and O. Bakajin, *Science* **312** 1034 (2006).
- [9] B. J. Hinds, N. Chopra, T. Rantell, R. Andrews, V. Gavalas, and L. G. Bachas,

Science **303** 62 (2004).

- [10] K. Gethard, O. Sae-Khow, and S. Mitra, ACS Appl. Mater. Interfaces **3** 110 (2011).
- [11] S. Kim, J. R. Jinschek, H. Chen, D. S. Sholl, and E. Marand, Nano Lett. **7** 2806 (2007).
- [12] J. M. D. Macelroy, J. Chem. Phys. **101** 5274 (1994).
- [13] R. F. Cracknell, D. Nicholson, and N. Quirke, Phys. Rev. Lett. **74** 2463 (1995).
- [14] H. Takaba, E. Matsuda, and S. Nakao, J. Phys. Chem. B **108** 14142 (2004).
- [15] W. D. Nicholls, M. K. Borg, D. A. Lockerby, and J. M. Reese, Microfluid. Nanofluid. **12** 257 (2012).
- [16] R. Delgado-Buscalioni, P. V. Coveney, J. Chem. Phys. **119** 978 (2003).
- [17] C. Huang, K. Nandakumar, P. Choi, and L. W. Kostiuk, J. Chem. Phys. **124** 234701 (2006).
- [18] H. Takaba, Y. Onumata, and S. Nakao, J. Chem. Phys. **127** 054703 (2007).
- [19] C. Huang, P. Choi, K. Nandakumar, and L. W. Kostiuk, J. Chem. Phys. **126** 224702 (2007).
- [20] C. Huang, P. Choi, K. Nandakumar, and L. W. Kostiuk, Phys. Chem. Chem. Phys. **10** 186 (2008).
- [21] C. Huang, P. Choi, K. Nandakumar, and L. W. Kostiuk, J. Nanosci. Nanotechnol. **9** 793 (2009).
- [22] M. E. Suk and N. R. Aluru, J. Phys. Chem. Lett. **1** 1590 (2010).
- [23] F. Zhu, E. Tajkhorshid, and K. Schulten, Biophys. J. **83** 154 (2002).

- [24] K. Leung and S. B. Rempe, *J. Comput. Theor. Nanosci.* **6** 1948 (2009).
- [25] J. Goldsmith and C. C. Martens, *Phys. Chem. Chem. Phys.* **11** 528 (2009).
- [26] J. Phillips, R. Braun, W. Wang, J. Gumbart, E. Tajkhorshid, E. Villa, C. Chipot, R. D. Skeel, L. Kalé and K. Schulten, *J. Comput. Chem.* **26** 1781 (2005).
- [27] W. Humphrey, A. Dalke, and K. Schulten, *J. Mol. Graphics* **14** 33 (1996).
- [28] W. L. Jorgensen, J. Chandrasekhar, J. D. Madura, R. W. Impey, and M. L. Klein, *J. Chem. Phys.* **79** 926 (1983).
- [29] A. D. MacKerell, N. Banavali, and N. Foloppe, *Biopolymers* **56** 257 (2001).
- [30] J. Cohen, F. Zhu F, and E. Tajkhorshid, Simulation of water permeation through nanotubes, (NAMD/VMD tutorial, 2010
<http://www.ks.uiuc.edu/Training/Tutorials/science/nanotubes/nanotubes-html/index.html>).
- [31] W. Janke, *Statistical Analysis of Simulations: Data Correlations and Error Estimation*, in: G. Johannes, D. Marx, A. Muramatsu (Eds.), *Quantum Simulations of Complex Many-Body Systems: From Theory to Algorithms*, (John von Neumann Institute for Computing, Jülich, 2002).
- [32] U. Kaatze, *Radiat. Phys. Chem.* **45** 539 (1995).
- [33] J. H. Irving and J. G. Kirkwood, *J. Chem. Phys.* **18** 817 (1950).
- [34] J. A. Thomas and A. J. H. McGaughey, *Nano Lett.* **8** 2788 (2008).
- [35] B. Corry, *J. Phys. Chem. B* **112** 1427 (2008).
- [36] F. Moradi Garakani and R. Kalantarinejad, *Int. J. Nano Dimens.* **2** 151 (2012).

Chapter 4 Nonequilibrium Molecular Dynamics Simulation of Pressure-Driven Water Transport through Modified CNT Membranes

4.1. Abstract

Nonequilibrium molecular dynamics (NEMD) simulations are presented to investigate the effect of water–membrane interactions on the transport properties of pressure-driven water flow passing through carbon nanotube (CNT) membranes. The CNT membrane is modified with different physical properties to alter the van der Waals interactions or the electrostatic interactions between water molecules and CNT membranes. The unmodified and modified CNT membranes are models of simplified nanofiltration (NF) membranes with the same pore size and membrane thickness. All NEMD simulations are run with the same pressure difference, consistent with NF operating conditions. The water flow rate, density, and velocity (in flow direction) distributions are obtained by analyzing the NEMD simulation results to compare transport through the modified and unmodified CNT membranes. The pressure-driven water flow through CNT membranes is from 11 to 21 times faster than as predicted by the Navier-Stokes equations. When water passing through the modified membrane with stronger van der Waals or electrostatic interactions, the fast flow is reduced giving lower flow rates and velocities. These investigations show the effect of water–CNT membrane interactions on water

transport under NF operating conditions. This work about the water/CNT cases can provide and improve the understanding how the membrane characteristics affect membrane performance through different solution–membrane interactions in real NF processes.

4.2. Introduction

Molecular dynamics (MD) simulation provides a dynamic view of microscopic systems. Water flow through nanoscale channels, driven by external fields, is critical to many phenomena – for example, biological channels, drug delivery, membrane separations, fuel cells, and novel nanofluidic applications (nanopumps, nanosyringes, nanosensors, etc.). In recent years, MD simulations have been used to study water flow driven by external fields such as pressure difference^[1-3], osmotic pressure difference^[4, 5], and electric field^[6].

Nanofiltration (NF) is a common membrane separation process driven by a pressure difference between the two sides of the NF membrane, where a concentrated stream on the high pressure side passes through the NF membrane and becomes a purified stream on the low pressure side. Applications of NF worldwide have increased primarily in the water treatment industry,^[7] such as water softening, organics removal, radium and heavy metal removal from waste water; and sulfate removal from seawater. Also, NF has been applied in other industries: pulp and paper effluent treatment in the paper-making industry, removal of dyes and other coloring agents in the textile industry, concentration of intermediates and antibiotics in the pharmaceutical industry.^[8] With the growing industry applications of NF, the transport mechanism of NF is examined using MD

simulation with the goal of improve the NF separation performance.

To understand the microscopic dynamics properties of the NF process with MD simulation, nonequilibrium molecular dynamic (NEMD) simulations must be used because pressure-driven fluid flow corresponds to a nonequilibrium conditions. NEMD is a valuable tool to study fluid flow through nanoscale channels, induced by a pressure difference.^[1, 2, 9-11] The key to a NEMD simulation of a NF process is a mean of imposing different constant pressures on the two sides of the NF membrane. In our previous study, we reported a NEMD simulation system derived by Huang^[9] and Takaba^[10] to study the transport phenomena of pressure-driven water flow through CNT membranes under NF operating conditions.^[12, 13]

The real NF membranes are generally made from synthetic polymers. The membrane structure (pore size and membrane thickness) and the polymer characteristics (functional groups, electric charge, hydrophilicity/hydrophobicity, etc.) both can affect membrane performance. The interactions between solution and the polymeric NF membrane is one of the most important factors to design the membrane separation and transport performance. In our previous work, the effect of membrane structure on water transport through CNT membranes has been investigated.^[12] This work investigates the effect of water–CNT membrane interactions through modified CNT membranes of different membrane characteristics. Although the solution–membrane interactions in a real NF process are stronger and more complicated than the water–CNT interactions, this work can provide fundamental understanding how the membrane characteristics affect membrane performance.

The modified CNT membranes have the same membrane structure (pore size and membrane thickness) as the unmodified CNT membrane, while the van der Waals interactions and electrostatic interactions between water molecules and CNT membranes are altered. The transport phenomenon of the unmodified CNT membrane and modified CNT membranes are compared to establish the role of the water–CNT interactions in determining observed transport properties. This work highlights a unique advantage of MD simulation – the water–membrane interaction can be adjusted to reveal the effect on the NF transport.

4.3. Simulation Methods

The system model in Cartesian coordinates is shown in Figure 4.1. The system consists of two graphene sheets acted as moveable walls, two water reservoirs, and a CNT membrane model. The moveable walls and the membrane model are all in $4 \times 4 \text{ nm}^2$ in the x, y plane. The thickness and the pore size of the CNT membrane is decided by the (12, 12) type CNT, which has a 6.0 nm length and 0.643 nm internal radius.^[1, 14] The top and bottom water reservoirs connected by the CNT membrane model provide the source and sink of the water flow passing through the membrane, along the z direction. External force is applied on each carbon atom of moveable walls to produce 8.1 MPa pressure on the top water reservoir and 0.1 MPa on the bottom water reservoir. We use a simulated pressure difference across the CNT membrane that is a little bit higher than typical NF systems, but this pressure difference still need the simulations run for a high time scale.

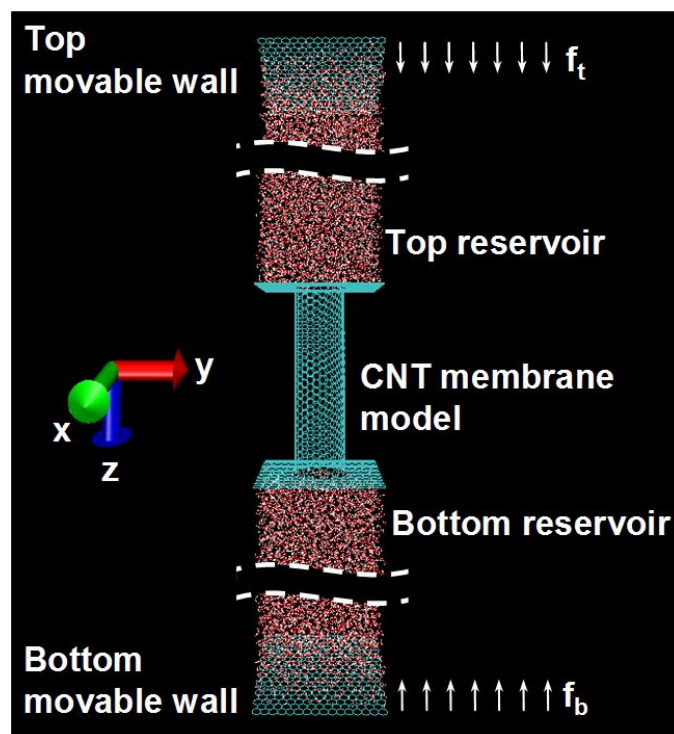


Figure 4.1 Perspective snapshots of the simulation systems produced by VMD package at the beginning status of MD simulations (adapted from the figure in reference [12]). Shown is the beginning empty CNT membrane model connecting two liquid filled reservoirs, and the two graphene sheets acted as the movable walls where the force f_t or f_b is applied on each carbon atom of the top or bottom wall. Carbon atoms in green, hydrogen atoms in white, and oxygen atoms in red.

An equilibrium MD simulation in an isothermal–isobaric (NPT) ensemble is carried out first to energy-minimize and equilibrate the system; and then a NEMD simulation is carried out to simulate a pressure-driven water flow through the CNT membrane. Each simulation is at 300 K, and takes about 14 CPU days for 1.0 ns of simulation. The detailed simulation methodology (force field parameters, integration algorithm, periodic boundary conditions, etc.) and simulation procedures are the same as in our previous work.^[12]

All MD simulations are performed using NAMD (NAnoscale Molecular Dynamics) package^[15] and VMD (Visual Molecular Dynamics) package^[16] in the CHARMM (Chemistry at HARvard Molecular Mechanics)^[17] force field. The water molecule is represented by the modified flexible TIP3P (transferable intermolecular potential three-point) water model^[18]. The CHARMM force field includes several terms representing intermolecular and intramolecular interactions. The intermolecular potential energy (also called long-range potential energy) includes the Lennard-Jones 6-12 potential and the Coulomb potential to describe van der Waals and electrostatic interactions, respectively. The mathematical expressions of the Lennard-Jones 6-12 type potential (E_{VW}) and Coulomb potential (E_{elect}) are shown in Eqns. (4.1) and (4.2):

$$E_{VW} = \sum_{nonbonded\ atom\ pairs} \varepsilon_{(ij)} \left[\left(\frac{R_{min(ij)}}{r_{ij}} \right)^{12} - 2 \left(\frac{R_{min(ij)}}{r_{ij}} \right)^6 \right] \quad (4.1)$$

$$E_{elect} = \sum_{nonbonded\ atom\ pairs} \frac{q_i q_j}{4\pi\epsilon_0 r_{ij}^2} \quad (4.2)$$

where $\varepsilon_{(ij)}$ is the Lennard-Jones well-depth between atoms i and j and $R_{min(ij)}$ is the distance at the Lennard-Jones minimum interaction energy between atoms i and j ; q_i and q_j are the partial atomic charges of atoms i and j ; ϵ_0 is the electric constant with a value of $8.854 \times 10^{-12} \text{ C}^2/(\text{N} \cdot \text{m}^2)$; and r_{ij} is the distance between atoms i and j , respectively. The Lorentz-Berthelot combining rules^[19] are used to calculate the interaction terms for the Lennard-Jones parameters between two different species of atoms i and j , definition functions of $R_{min(ij)}$ and $\varepsilon_{(ij)}$ shown in Eqns. (4.3) and (4.4):

$$R_{min(ij)} = \frac{R_{min(ii)} + R_{min(jj)}}{2} \quad (4.3)$$

$$\varepsilon_{(ij)} = \sqrt{\varepsilon_{(ii)} \cdot \varepsilon_{(jj)}} \quad (4.4)$$

where the $R_{min(ij)}$ is an arithmetic mean and the $\varepsilon_{(ij)}$ is a geometric mean.

Two series of modified CNT membranes are produced by varying the carbon atom Lennard-Jones well-depth value ($\varepsilon_{(CC)}$), and setting the atomic charges on CNT carbon atoms (patterns of balanced positive and negative charges are placed on the CNT), respectively. This modification affects the interactions between water molecules and the CNT membrane. NEMD simulations are carried out for unmodified and modified CNT membranes to analyze the NF transport phenomenon of pressure-driven water flow in terms of water flow rate, density, and velocity (in z direction) distributions along both radial and flow directions.

4.4. Results and Discussion

The theoretical flux and velocity in the z direction are calculated by using the Navier-Stokes equations for a cylindrical channel (Eqns. (4.5) and (4.6)). Equation (4.5) is also called the Hagen-Poiseuille equation, and we will simply refer to Eqn. (4.6) as the Navier-Stokes Equation:

$$J_w = L_p \Delta P = \frac{r_p^2}{8\eta(L_z / A_K)} \Delta P \quad (4.5)$$

$$A_K = \frac{\pi \cdot r_p^2}{A_{mem}} = \frac{\pi \cdot r_p^2}{L_x \cdot L_y}$$

$$v_z = \frac{\Delta P}{4\eta L_z} (r_p^2 - r^2) \quad (4.6)$$

where L_P is the permeability coefficient of the water fluid, r_p is the pore radius, η is the viscosity of water at the operating temperature, L_e/A_K is the ratio of the membrane effective thickness to the membrane porosity, ΔP is the pressure difference, and r is the radial position. The density and viscosity of water at 300 K are 1000 kg/m^3 and $8.54 \times 10^{-4} \text{ Pa} \cdot \text{s}$, respectively,^[20] and theoretical flux is converted to theoretical flow rate in ‘molecules/ns’ to compare with the simulation flow rate.

The simulation water flow rate is defined as the number flow rate (molecules/ns), which is calculated by the slope of the linear trend of the number of water molecules in the bottom reservoir as a function of the simulation time. To obtain the density and velocity distributions along the radial direction, the pore is divided into ten annular sections evenly spaced in the radial direction. The distributions along the flow direction are studied by dividing the entire system evenly into ten sections with equal distance along the flow direction: four sections in the top water reservoir, three in the CNT, and three in the bottom water reservoir. Average density and velocity values for each section are obtained from effective collected trajectory data of the NEMD simulation. The stream velocity of water flow in the water reservoirs is too low because of the low pressure difference, so the average velocity is hard to be obtained with a reasonable accuracy through the NEMD simulation. The water velocity in each reservoir is represented by the velocity of each movable wall, which can be calculated through the linear relationship between the moved distance of the wall and the simulation time.

The number of water molecules passing through the membrane model are counted every 50 ps and plotted as a function of the simulation time. The slope of the linear

profile (through origin) is the number flow rate. For each flow rate value, the estimated error of the flow rate is represented by the standard error on the slope with the assumption of uncorrelated data (a correlation time shorter than 50 ps). An example of the error analysis for the simulation flow rate is shown in our previous work.^[12] The error analyses for density or velocity values are performed by considering the integrated autocorrelation time, which is used to calculate the effective sample number of time correlated data (the number of uncorrelated samples).^[21] The statistical error of each density or velocity data point is calculated directly from the standard deviation of the sampled mean using the number of uncorrelated samples.

4.4.1. The modified Lennard-Jones parameters of the CNT membranes

To study the effect of van der Waals interactions between water and the membrane with respect to the transport phenomenon, the Lennard-Jones parameters of carbon atoms in the CNT model are modified. As listed in Table 4.1, the well-depth parameter of the carbon atom is set as the well-depth parameter value of a hydrogen (the case I) or oxygen (the case II) atom in the modified CNT models (corresponding to smaller and larger well depth, respectively). The distance of the Lennard-Jones minimum interaction energy is kept at the same value – i.e. that of a carbon atom. The value of the well-depth parameter reflects the strength of the van der Waals interaction between two atoms: a larger value means a stronger interaction.

Table 4.1 The Lennard-Jones parameters of the unmodified and modified CNT membranes

Lennard-Jones Parameters ^a	Unmodified	Modified Case I	Modified Case II
ϵ_{mem} (kcal/mol)	0.07 = $\epsilon_{(CC)}$	0.046 = $\epsilon_{(HH)}$ ^b	0.1521 = $\epsilon_{(OO)}$ ^c
$R_{min}/2$ (nm)	0.19924	0.19924	0.19924

^aThe values of the parameters are based on CHARMM force field.^[17]

^bSet to the well depth parameter for hydrogen, $\epsilon_{(HH)}$; a smaller interaction

^cSet to the well depth parameter for oxygen, $\epsilon_{(OO)}$; a larger interaction

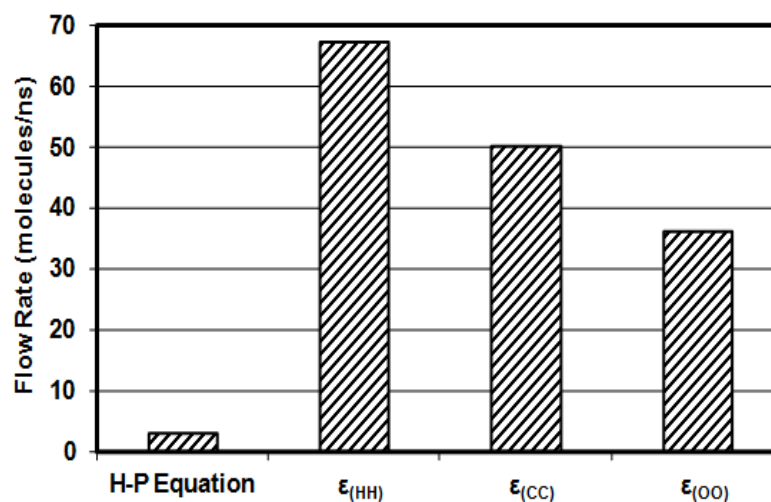


Figure 4.2 Bar chart of simulation and theoretical flow rates (molecules/ns) of unmodified and modified CNT membranes. The results are based on membrane simulations using the (12, 12) CNT, $L_z = 6.0$ nm; $\Delta P = 8.0$ MPa; $T = 300$ K. The statistical error for each flow rate data is less than 0.5%. H-P equation refers to the Hagen-Poiseuille equation (Eqn. (4.5)), and the values of the well-depth parameters ($\epsilon_{(CC)}$, $\epsilon_{(HH)}$, and $\epsilon_{(OO)}$) are shown in Table 4.1.

According to the Eqns. (4.1) and (4.3), the Lennard-Jones potential energy between the water molecules and the membrane surfaces depends on the square root of the well-depth parameter of the CNT membrane. Figure 4.3 illustrates the relationship between the

simulation flow rate and the water–membrane interaction which is represented by the square root of the well-depth parameter of the unmodified and modified CNT membranes. Here, we see the inverse relationship between flow rate and well depth. With only three points, the details of this relationship are not clear – only that flow rate decreases with increasing well depth. Clearly, stronger attraction of water to the pore surface reduces the flow.

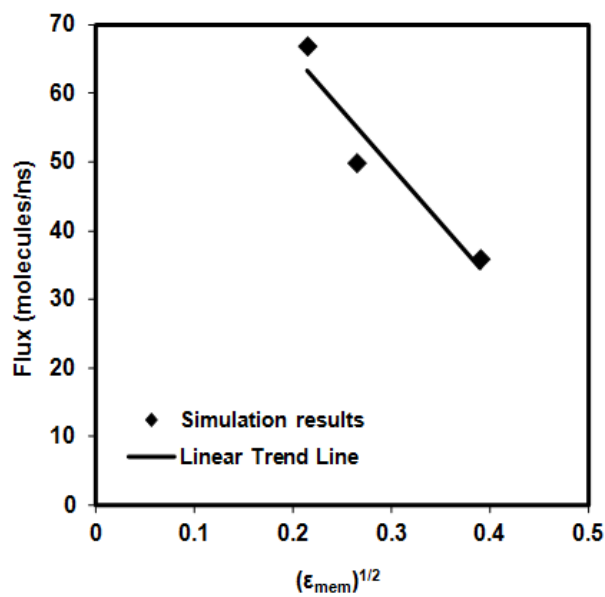


Figure 4.3 Simulation flow rate (molecules/ns) as a function of the square root of the well-depth parameter. The data points are based on membrane simulations using the (12, 12) CNT, $L_z = 6.0$ nm; $\Delta P = 8.0$ MPa; $T = 300$ K. The statistical error for each data point is less than 0.5%. The solid line is the linear trends based on the simulation results.

Figures 4.4 and 4.5 show the density distributions along the radial and axial directions for the three CNT membrane models. The radial distributions of density all exhibit similar oscillatory waves, with low density in the pore center and two pairs of symmetrical peaks – there are two cylindrical rings of water molecules within the pore. The effect of increasing the CNT well-depth parameter is to shift the outer ring toward the

pore surface and increase the strength of the density oscillations. Increasing the van der Waals attraction between water and the CNT draws water closer to the pore surface and increases the density of water molecules near the pore surface, shown as outer peaks better separated from the inner peaks in Figure 4.4. With stronger interactions the inner density peaks become sharper illustrating that the inner water ring is also affected by the van der Waals interaction between water and the pore surface. As the outer ring moves closer to the wall then the inner ring can become more well defined separate from the outer water ring.

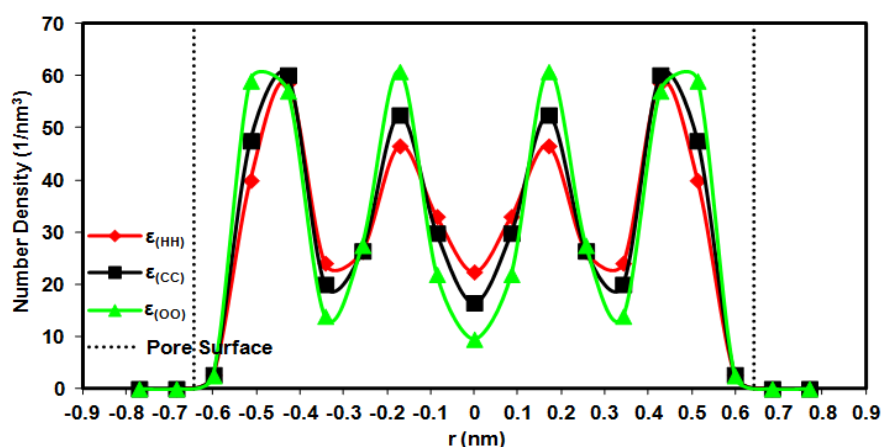


Figure 4.4 Effect of van der Waals interactions between water and membrane, represented by the well-depth parameter of the Lennard-Jones potential, on the density distributions along the radial direction: density values are averaged over thin annular sections in the pore at the indicated r values over the entire NEMD simulation. The data points are based on membrane simulations using the (12, 12) CNT, $L_z = 6.0$ nm; $\Delta P = 8.0$ MPa; $T = 300$ K. The statistical error for each data point is less than 1%. The values of the well-depth parameters ($\epsilon_{(CC)}$, $\epsilon_{(HH)}$, and $\epsilon_{(OO)}$) are shown in Table 4.1. The solid lines are the trend curves based on the simulation results, and the dotted lines are the pore surface represented by the effective pore radius (0.643 nm).

For the axial direction, as shown in Figure 4.5 the density remains constant throughout the length of the pore for all three well depths. However, the constant value is sensitive to the well depth. If the carbon well depth is increased from that of hydrogen (the case

I), carbon and oxygen (the case II), the density in the pore increases and the bulk values in the reservoirs are constant. Overall the increase in density from hydrogen to carbon and hydrogen to oxygen wall-depth parameters is about 2 molecules/nm³ (6%) and 4 molecules/nm³ (13%), respectively. The increasing density in the CNT pore is attributable to the increasing hydrophobicity of a carbon nanotube as modeled by the 6-12 Lennard-Jones interaction with an increasing well-depth parameter.

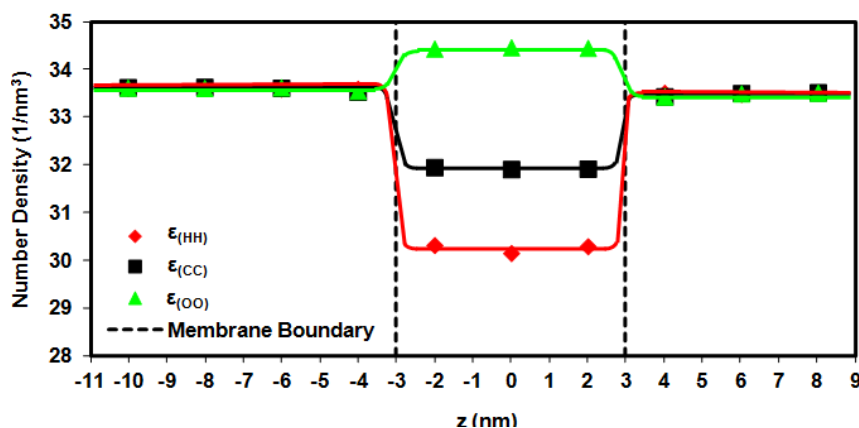


Figure 4.5 Effect of van der Waals interactions between water and membrane, represented by the well-depth parameter of the Lennard-Jones potential, on the density distributions along the flow direction: density values are averaged over thin sections about the indicated z values (cylindrical sections in the pore and cuboid sections in the water reservoirs) over the entire NEMD simulation. The data points are based on membrane simulations using the (12, 12) CNT, $L_z = 6.0$ nm; $\Delta P = 8.0$ MPa; $T = 300$ K. The statistical error for each data point is less than 1%. The values of the well-depth parameters ($\epsilon_{(CC)}$, $\epsilon_{(HH)}$, and $\epsilon_{(OO)}$) are shown in Table 4.1. The solid lines are the trend curves based on the simulation results. The dashed lines are the membrane boundaries along z direction separating the system in three parts from left to right: the water reservoir at high pressure side, the pore of the CNT membrane, and the water reservoir at low pressure side.

The radial velocity distribution for continuum flow through a cylindrical pore has a parabolic profile determined by the Navier-Stokes equations. Figure 4.6, shows the oscillatory velocity distributions along the radial direction observed for pressure-driven water flow through these CNT membranes. The velocity profiles obtained from the

NEMD simulations are higher than the theoretical values predicted by the Navier-Stokes equations. The non-parabolic distribution of water velocity in the CNT membrane is explained in our previous work.^[12, 13]

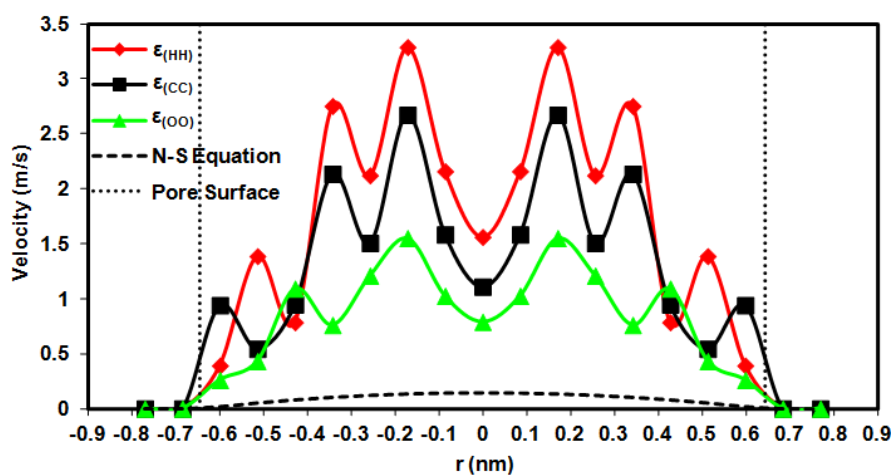


Figure 4.6 Effect of van der Waals interactions between water and membrane, represented by the well-depth parameter of the Lennard-Jones potential, on the velocity distributions (in z direction) as a function of radial position: velocity (in z direction) values are averaged over thin annular sections in the pore at the indicated r values over the entire NEMD simulation. The data points are based on membrane simulations using the (12, 12) CNT, $L_z = 6.0$ nm; $\Delta P = 8.0$ MPa; $T = 300$ K. The statistical errors for most data points are less than 10%. N-S equation refers to the Navier-Stokes Equation (Eqn. (4.6)), and the values of the well-depth parameters ($\epsilon_{(CC)}$, $\epsilon_{(HH)}$, and $\epsilon_{(OO)}$) are shown in Table 4.1. The solid lines are the trend curves based on the simulation results, the dashed lines are the trends based on the Navier-Stokes Equation, and the dotted lines are the pore surface represented by the effective pore radius (0.643 nm).

The velocity profiles along the axial (flow) direction are shown in Figure 4.7, where that velocity dramatically increases / decreases when water molecules enter / exit any of the CNT membranes. Like the density function the velocities are constant along the pore length and are larger than the velocities in the reservoirs due to the much smaller cross-sectional area in the pore compared to in the reservoirs. It can be seen from Figures 4.6 and 4.7 that increasing the strength of the interaction decreases the velocity of

the water flow in the CNT. The weaker interactions between water and the CNT membrane result in the CNT having a more frictionless pore and this increases the flow rate, while the strong interactions increase the attraction to the pore wall and decrease the flow rate.

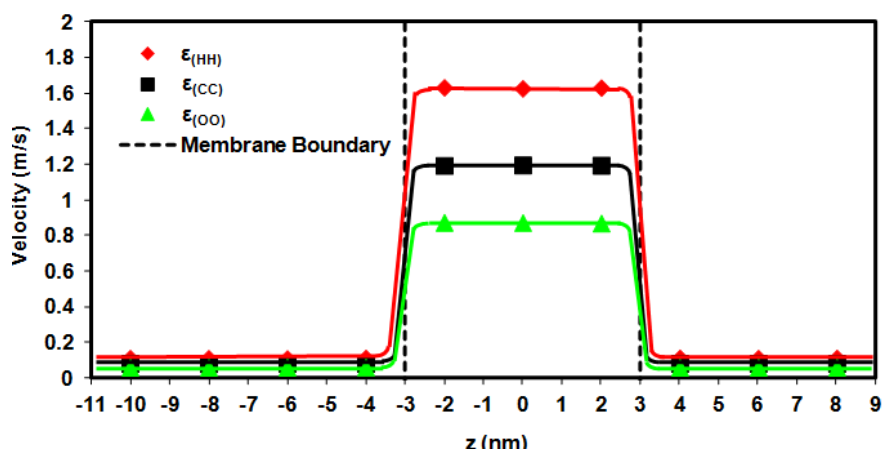


Figure 4.7 Effect of van der Waals interactions between water and membrane, represented by the well-depth parameter of the Lennard-Jones potential, on the velocity distributions (in z direction) along the flow direction: velocity (in z direction) values are averaged over thin sections about the indicated z values (cylindrical sections in the pore and cuboid sections in the water reservoirs) over the entire NEMD simulation. The data points are based on membrane simulations using the (12, 12) CNT, $L_z = 6.0$ nm; $\Delta P = 8.0$ MPa; $T = 300$ K. The statistical error for each data point is less than 10%. The values of the well-depth parameters ($\epsilon_{(CC)}$, $\epsilon_{(HH)}$, and $\epsilon_{(OO)}$) are shown in Table 4.1. The solid lines are the trend curves based on the simulation results. The dashed lines are the membrane boundaries along the z direction separating the system in three parts from left to right: the water reservoir at high pressure side, the pore of the CNT membrane, and the water reservoir at low pressure side.

4.4.2. The polarized CNT membranes

It has been shown that the delocalized π -electrons of the CNT carbon atoms can result in polarized CNTs,^[22-25] and positive and negative partial charges of the polarized CNT are formed in a sequential order.^[26] Simplified charge distributions (as shown in Figure 4.8) are proposed here: positive and negative partial charges arranged in distinct

patterns are set on the unmodified CNT to model a factitiously polarized CNT. Unlike the unmodified CNT membrane, the polarized CNT membrane can interact with water through electrostatic interactions. The water transport properties of the unmodified and polarized CNT membranes are investigated to show the effect of electrostatic interactions on the transport properties.

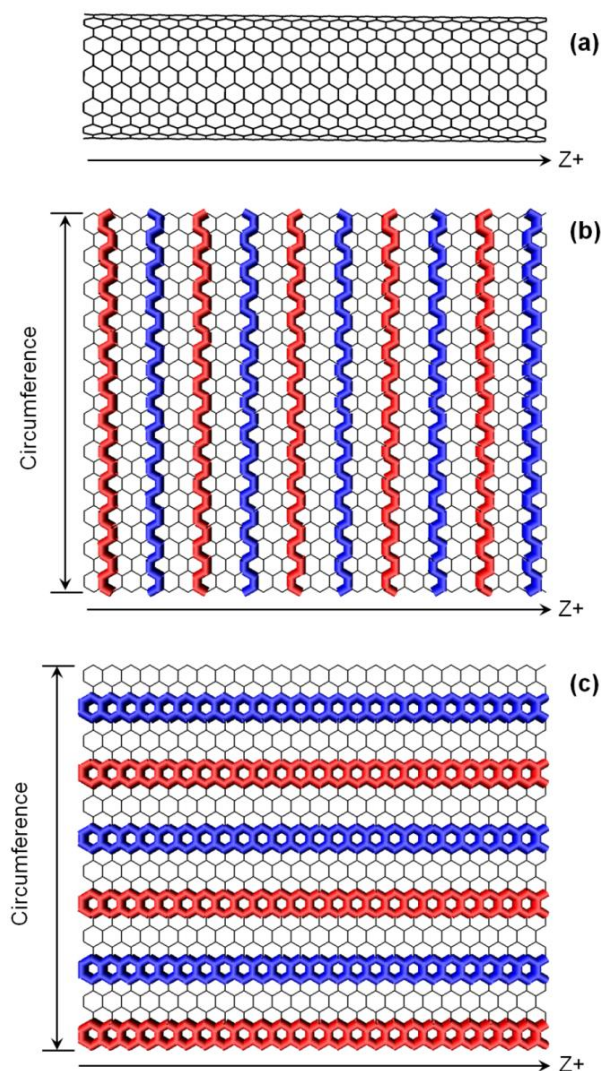


Figure 4.8 Charge patterns of the unmodified and modified CNTs: (a) unmodified CNT, (b) unwrapped CNT of the ring polarized model, and (c) unwrapped CNT of the band polarized model. This figure illustrates the bonds between neutral atoms in black, between positive atoms in red, and between negative atoms in blue.

Two modified CNTs with different charge patterns (Figure 4.8) are used to model the polarized CNT membranes. Each CNT has a total charge of zero, with positive and negative atomic charges on selected carbon atoms along the length or circumference of the CNT. Figure 4.8(b) shows the ring polarized CNT with ten alternating charged rings with equal magnitude along the length. Figure 4.8(c) shows the band polarized CNT with six alternating charged bands with equal magnitude along the circumference. The atomic charges of each charged ring or band have the same magnitude, and the adjacent positive and negative rings or bands are placed evenly to form orderly charge patterns. Each charged ring or band and neighbouring uncharged atoms form a charged pore surface having a surface charge density of 1.0 C/m^2 or -1.0 C/m^2 , which corresponds to set $\pm 0.040765 e$ on charged carbon atoms of the ring polarized CNT or $\pm 0.031958 e$ on charged carbon atoms of the band polarized CNT.

The water flow rates of different CNT membranes are compared with the theoretical flow rate in Figure 4.9. The flow rates of the two polarized CNT membranes are both smaller than the unmodified CNT membrane and larger than the theoretical flow rate calculated by the Hagen-Poiseuille equation. In addition, as the two polarized CNT membranes exhibit similar flow rates, which are about 88% and 84% of the flow rate for the unmodified CNT membrane, respectively, the charge pattern apparently has little influence on the transport properties.

The positive and negative charges of the polarized membranes give rise to electrostatic interactions between water and the pore surface, which attracts water molecules near the pore surface. Since water has an electrical dipole consisting of a partial negative

charge on the O atom and partial positive charges on the H atoms (net neutral, of course) then the water molecules can interact electrostatically with polarized groups on the membrane this attraction results in a reduced water flow through the CNT membrane. Although the electrostatic interaction makes the total interactions between water and the CNT membrane stronger, the water–CNT interactions are apparently still sufficiently weak to reduce the flow to the Hagen-Poiseuille equation level.

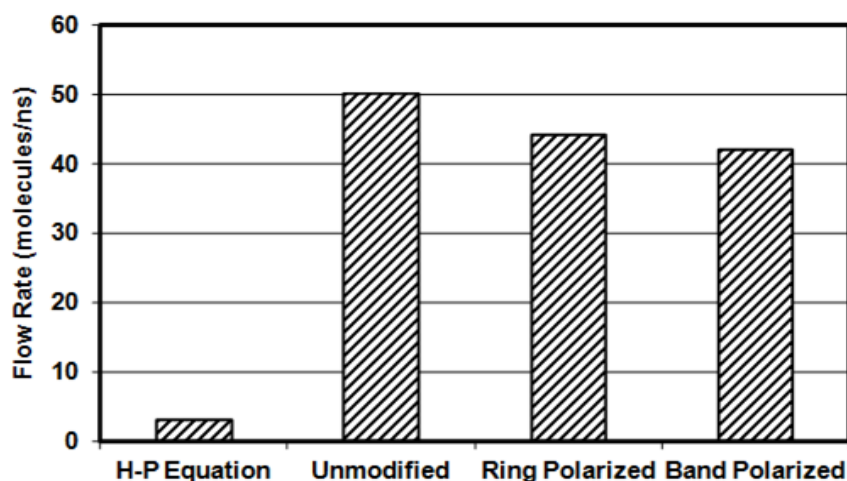


Figure 4.9 Bar chart of simulation and theoretical flow rates (molecules/ns) of unmodified and modified polarized CNT membranes. The results are based on membrane simulations using the (12, 12) CNT, $L_z = 6.0$ nm; $\Delta P = 8.0$ MPa; $T = 300$ K. The statistical error for each flow rate data is less than 0.5%. H-P equation refers to the Hagen-Poiseuille equation (Eqn. (4.5)), and the charge patterns of the modified polarized CNTs are shown in Figures 4.8(b) and 4.8(c).

The density distributions resulting from polarized CNT membranes are shown in Figures 4.10 and 4.11. The radial distributions of density in all three CNTs are similar. The only effect of the CNT polarization is to shift the outer peaks lower and nearer to the pore surface. The higher density values of water in the polarized CNTs are seen from the density profile along the axial (flow) direction, shown in Figure 4.11. Polarization of

the CNT increases the hydrophilicity of the pore, contributing to higher density of water molecules in the CNT. Through analyzing the average number of water molecules in the CNT for each membrane, the results show that the water molecules in the polarized CNT are about four more molecules than in the unmodified CNT. Figure 4.11 also shows water density in the CNT is uniformly lower than in the bulk reservoirs for all the CNT membranes. The effect of polarizing the CNT membrane is similar to that of increasing the van der Waals attraction, except not as pronounced. The similar density distributions for the two polarized CNT membranes tell us that the pattern of polarization is largely immaterial.

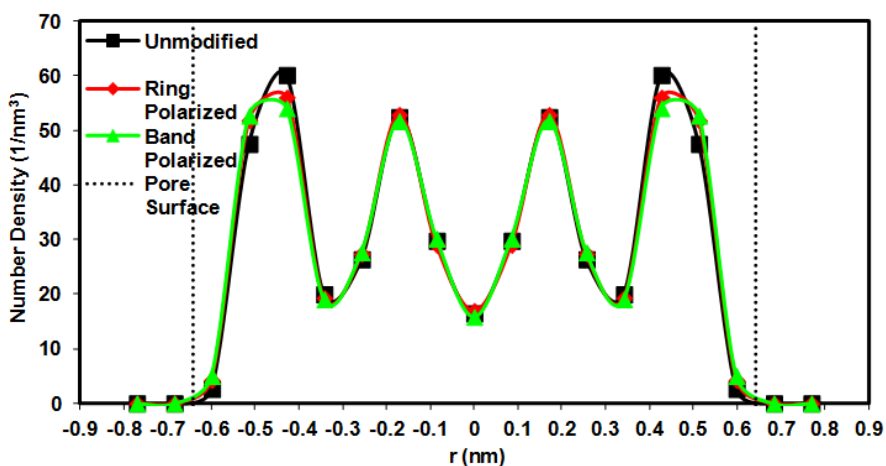


Figure 4.10 Effect of electrostatic interactions between water and membrane, caused by the charge patterns within the CNT, on the density distributions along the radial direction: density values are averaged over thin annular sections in the pore at the indicated r values over the entire NEMD simulation. The data points are based on membrane simulations using the (12, 12) CNT, $L_z = 6.0$ nm; $\Delta P = 8.0$ MPa; $T = 300$ K. The statistical error for each data point is less than 1%. The charge patterns of the modified polarized CNTs are shown in Figures 4.8(b) and 4.8(c). The solid lines are the trend curves based on the simulation results, and the dotted lines are the pore surface represented by the effective pore radius (0.643 nm).

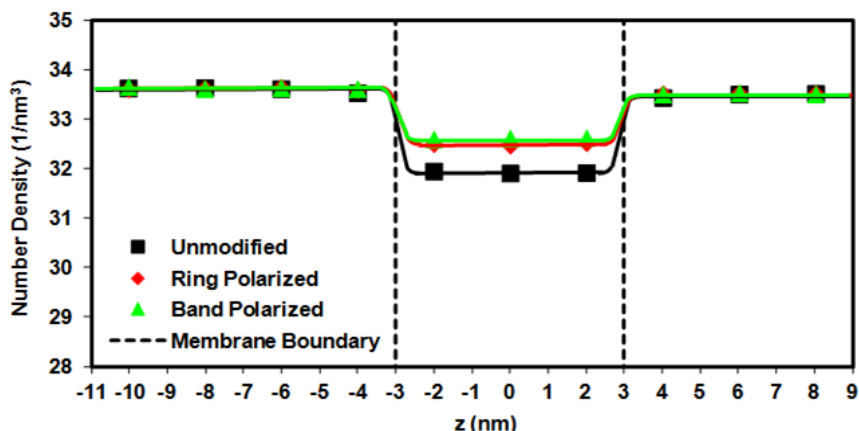


Figure 4.11 Effect of electrostatic interactions between water and membrane, caused by the charge patterns within the CNT, on the density distributions along the flow direction: density values are averaged over thin sections about the indicated z values (cylindrical sections in the pore and cuboid sections in the water reservoirs) over the entire NEMD simulation. The data points are based on membrane simulations using the (12, 12) CNT, $L_z = 6.0$ nm; $\Delta P = 8.0$ MPa; $T = 300$ K. The statistical error for each data point is less than 1%. The charge patterns of the modified polarized CNTs are shown in Figures 4.8(b) and 4.8(c). The solid lines are the trend curves based on the simulation results. The dashed lines are the membrane boundaries along the z direction separating the system in three parts from left to right: the water reservoir at high pressure side, the pore of the CNT membrane, and the water reservoir at low pressure side.

Radial distributions of velocity for unmodified and polarized CNT membranes are shown in Figure 4.12 along with the parabolic profile predicted by the Navier-Stokes equation. Again, observed velocity profiles are non-parabolic and much higher than predicted by the Navier-Stokes equation. The electrostatic interactions between the water molecules and the polarized CNTs lead to lower velocities near the pore surface. Otherwise, the radial distributions of velocity are all very similar. The polarization increases the hydrophilicity of the pore, and as seen in Figure 4.10 that density increases near the pore surface.

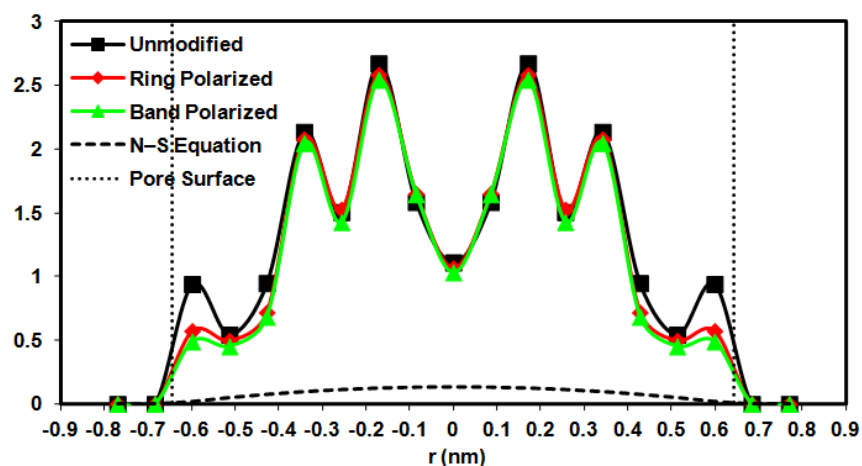


Figure 4.12 Effect of electrostatic interactions between water and membrane, caused by the charge patterns of the CNT, on the velocity (in z direction) distributions along the radial direction: velocity (in z direction) values are averaged over thin annular sections in the pore at the indicated r values, over the entire NEMD simulation. The data points are based on membrane simulations using the (12, 12) CNT, $L_z = 6.0$ nm; $\Delta P = 8.0$ MPa; $T = 300$ K. The statistical errors for most data points are less than 10%. N-S equation refers to the Navier-Stokes Equation (Eqn. (4.6)), and the charge patterns of the modified polarized CNTs are shown in Figures 4.8(b) and 4.8(c). The solid lines are the trend curves based on the simulation results, the dashed lines are the trends based on the Navier-Stokes Equation, and the dotted lines are the pore surface represented by the effective pore radius (0.643 nm).

The net effect of polarization is lower average velocity, and associated lower flow rate. The lower velocities of the polarized membranes can be observed from the velocity profile along the direction of flow, shown in Figure 4.13. In this figure, we see that polarization of the CNT reduces velocity uniformly within the pore, though the velocity values in the CNT are still higher than bulk values. The pattern of polarization is seen to have little impact, though band polarization does appear to reduce flow a little more than ring polarization. The difference is too small to prove a charge pattern effect, however.

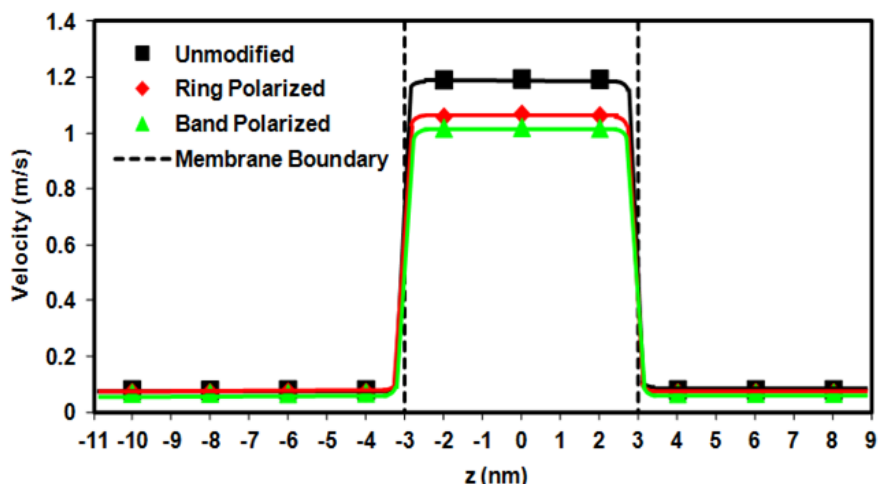


Figure 4.13 Effect of electrostatic interactions between water and membrane, caused by the charge patterns of the CNT, on the velocity (in z direction) distributions along the flow direction: velocity (in z direction) values are averaged over thin sections about the indicated z values (cylindrical sections in the pore and cuboid sections in the water reservoirs) over the entire NEMD simulation. The data points are based on membrane simulations using the (12, 12) CNT, $L_z = 6.0$ nm; $\Delta P = 8.0$ MPa; $T = 300$ K. The statistical error for each data point is less than 10%. The charge patterns of the modified polarized CNTs are shown in Figures 4.8(b) and 4.8(c). The solid lines are the trend curves based on the simulation results. The dashed lines are the membrane boundaries along the z direction separating the system in three parts from left to right: the water reservoir at high pressure side, the pore of the CNT membrane, and the water reservoir at low pressure side.

4.5. Conclusions

The effect of interactions between water and CNT on water transport has been investigated by simulating pressure-driven water flow through modified CNT membranes. In one set of membranes, the interaction is modified by varying the water–CNT van der Waals interactions. In another set of membranes, electrostatic interactions are introduced by putting charges on the CNT. The transport properties investigated – simulation flow rate, radial and axial distributions of density and velocity – show that

increasing the water–CNT interactions increases density within the pore while reduces velocity and overall flow rate through the pore.

As discussed above, the increasing interactions between water and the CNT draws water molecules to the pore surface and reduces the pressure-driven water flow – the pore interacts more strongly with the water molecules. Here introducing electrostatic interactions have similar effects as the increasing van der Waals interactions. The transport of water through the modified membranes is reduced but is still much faster than that predicted by the Navier-Stokes equation. The modified membranes still produce non-uniform nanofluid flow with lower friction than that consistent with the Navier-Stokes equation. Overall, the increases in water–CNT considered here are not sufficient to eliminate the flow enhancement characteristic of a CNT membrane system. The nanoscale interior of the CNT and the smooth surface, features retained by the modified CNT membranes, are apparently the key to the observed flow enhancement. Polarized CNT membranes with zero net charge are constructed with two different patterns of polarization, while the pattern of polarization on the polarized CNTs also makes little difference.

This work reveals that the weak water–CNT interactions are important in determining the degree of flow enhancement seen in CNT membrane systems and the modified CNT membrane systems with increased water–CNT interactions still show enhanced flow, though less so. The membrane performance (water transport) can be controlled through manufacturing/modifying CNT membranes having weak or strong solution–membrane interactions, which could have a more significant effect on organic solutes/liquids than

pure water considered here. Real polymeric NF membranes are more complex than a CNT membrane model and water flow through the NF membrane would not be as fast as through CNT membranes due to the much stronger water–NF membrane interactions. The expected significance of this work in the future is to help to understand the transport mechanisms of CNT membranes and polymeric membranes, and then to improve applications of NF process.

References

- [1] J. Goldsmith and C. C. Martens, *J. Phys. Chem. Lett.* **1** 528 (2010).
- [2] K. Leung and S. B. Rempe, *J. Comput. Theor. Nanosci.* **6** 1948 (2009).
- [3] F. Zhu, E. Tajkhorshid, and K. Schulten, *Biophys. J.* **83** 154 (2002).
- [4] A. Kalra, S. Garde, and G. Hummer, *Proc. Natl. Acad. Sci. U.S.A.* **100** 10175 (2003).
- [5] A. N. Raghunathan and N. R. Aluru, *Phys. Rev. Lett.* **97** 024501 (2006).
- [6] J. Su and H. Guo, *ACS Nano* **5** 351 (2011).
- [7] X. Lu, X. Bian, and L. Shi, *J. Membr. Sci.* **210** 3 (2002).
- [8] A. I. Schäfer, A. G. Fane, T. D. Waite, *Nanofiltration: Principles and Applications*, (Elsevier Advanced Technology, Oxford, 2005).
- [9] C. Huang, K. Nandakumar, P. Choi, and L. W. Kostiuk, *J. Chem. Phys.* **124** 234701 (2006).

- [10] H. Takaba, Y. Onumata, and S. Nakao, *J. Chem. Phys.* **127** 054703 (2007).
- [11] I. Hanasaki and A. Nakatani, *Model. Simul. Mater. Sci. Eng.* **14** 9 (2006).
- [12] L. Wang, R. S. Dumont, and J. M. Dickson, *J. Chem. Phys.* **134** 044102 (2012).
- [13] L. Wang, R. S. Dumont, and J. M. Dickson, “Comparison of two nonequilibrium molecular dynamics simulation systems for the pressure-driven water permeation through carbon nanotube membrane”, *Microfluid. Nanofluid.* submitted (2012).
- [14] A. Noy, H. G. Park, F. Fornasiero, J. K. Holt, C. P. Grigoropoulos, and O. Bakajin, *Nano Today* **2** 22 (2007).
- [15] J. Phillips, R. Braun, W. Wang, J. Gumbart, E. Tajkhorshid, E. Villa, C. Chipot, R. D. Skeel, L. Kalé and K. Schulten, *J. Comput. Chem.* **26** 1781 (2005).
- [16] W. Humphrey, A. Dalke, and K. Schulten, *J. Mol. Graphics* **14** 33 (1996).
- [17] A. D. MacKerell, N. Banavali, and N. Foloppe, *Biopolymers* **56** 257 (2001).
- [18] W. L. Jorgensen, J. Chandrasekhar, J. D. Madura, R. W. Impey, and M. L. Klein, *J. Chem. Phys.* **79** 926 (1983).
- [19] M. Sprik, *Effective Pair Potential and Beyond*, in: M. P. Allen and D. J. Tildesley (Eds.), *Computer simulation in chemical physics*, (Kluwer Academic Publishers, The Netherlands, 1993).
- [20] U. Kaatz, *Radiat. Phys. Chem.* **45** 539 (1995).
- [21] W. Janke, *Statistical Analysis of Simulations: Data Correlations and Error Estimation*, in: G. Johannes, D. Marx, A. Muramatsu (Eds.), *Quantum Simulations of Complex Many-Body Systems: From Theory to Algorithms*, (John von Neumann

Institute for Computing, Jülich, 2002).

- [22] L. X. Benedict, S. G. Louie, and M. L. Cohen, *Phys. Rev. B* **52** 8541 (1995).
- [23] T. Dumitrica, C. M. Landis, and B. I. Yakobson, *Chem. Phys. Lett.* **360** 182 (2002).
- [24] G. Y. Guo, K. C. Chu, D. S. Wang, and C. G. Duan, *Comput. Mater. Sci.* **30** 269 (2004).
- [25] S. M. Hou, Z. Y. Shen, X. Y. Zhao, and Z. Q. Xue, *Chem. Phys. Lett.* **373** 308 (2003).
- [26] D. Lu, Y. Li, U. Ravaioli, and K. Schulten, *J. Phys. Chem. B* **109** 11461 (2005).

Chapter 5 Nonequilibrium Molecular Dynamics Simulation of Pressure-Driven Water Transport through Charged CNT Membranes

5.1. Abstract

The selective layer of the nanofiltration (NF) membrane is modeled by a carbon nanotube (CNT) membrane, which provides an ideal and simplified NF membrane having a single straight pore channel with a nanoscale pore size and a smooth pore surface. The effects of membrane charge are investigated in the cases of a charged pore surface, both membrane surfaces charged, and all surfaces charged (i.e. pore and membranes). Surface charge is expected to affect the transport of water due to electrostatic interactions between water molecules and the charged surfaces. These effects are studied using nonequilibrium molecular dynamics (NEMD) simulations carried out under NF operating conditions. The NEMD simulations provide transport properties, including water flow rate, density and flow direction velocity within the pore. Water is driven through CNT membrane by an imposed pressure difference consistent with commercial NF systems. The simulated flow is at least 7 times as fast as expected from the Navier-Stokes equations. Water flow in the charged membrane systems is reduced in comparison with a similar uncharged membrane system. This reduced flow rate is due to the attraction between water and the charged membrane. The effect occurs only when the pore is

charged; charging the membrane surfaces does not inhibit the flow. Similar transport properties are observed whether the charge is positive or negative.

5.2. Introduction

Nanofiltration (NF) is a widely accepted separation technology, with separation achieved by forcing a concentrated stream through the NF membrane *via* a pressure gradient. A purified permeate stream is obtained on the low pressure side along with a concentrated retentate stream on the high pressure side. The NF process is used in a wide range of applications and has many advantages, compared to traditional separation or other membrane separation processes, such as low operation pressure, high flow rate, high rejection, relatively low investment and low operation and maintenance costs. The most important application of NF membranes is water softening, which exploits the relative selectivity for divalent salts, associated with water hardness, versus monovalent salts. Other applications include removal of organics, dyes or other coloring agents, heavy metals, intermediates, antibiotics, and so forth.^[1-5]

Most commercial NF membranes are polymeric membranes fabricated in a thin-film composite structure which is a three-layer structure including an ultra-thin, denser polymer coating as the active skin layer, a porous layer used as a supporting base, and a non-woven polyester fabric as substrate. The top layer of the TFC membrane, with a pore diameter about 1 nm and a thickness of 15-220 nm provides the selectivity, consists of cellulose acetate, polyamide, sulfonated polyethersulfone, sulfonated polysulfone, polyvinyl alcohol, polyphenylene oxide, polyethylenimine, or other possibilities.^[6-8]

Most NF membranes are charged, usually with a negative charge, due to dissociation of a functional group in the membrane polymer and/or the adsorption of ions on the membrane.^[9, 10] The charge of the NF membrane affects the electrical potential developed across the membrane, and has a significant effect on the membrane separation performance.

There is much interest in the transport mechanism of water flow through nanochannels. Water transport is fundamental to many important phenomena; for example: biological channels, drug delivery, fuel cells, membrane separations including NF and reverse osmosis, and some novel nanofluidic devices such as nanopumps, nanosyringes, nanosensors, etc. Molecular dynamics (MD) simulation provides a unique window into the details of water flow through nanochannels on the scale of individual molecules. Direct investigation of the affects of intermolecular interactions on the dynamical properties of flowing water molecules is made possible by MD simulation. Water flow driven by a pressure difference, as in the NF process, is a challenge for MD simulation because of the nonequilibrium conditions. Nonequilibrium molecular dynamics (NEMD) simulations provide means of addressing this challenge, and have been used to investigate pressure-driven flows.^[11-16]

In our previous work^[16-18], NEMD simulation systems are used to study transport phenomena of pure water flow through carbon nanotube (CNT) membranes at 300 K with a 1.0 – 8.0 MPa pressure difference – i.e. conditions typical of NF systems. Results show that CNT membranes have great potential as NF membranes because of the high observed water flow rates. The enhance water flow passing through CNTs or CNT

membranes has been reported in other studies both through using MD simulations.^[11, 19, 20] The great transport performance of CNTs or CNT membranes (experimentally produced) has also been proved through experimental measurements.^[21-24] Therefore CNT membranes could be great candidates for future commercial NF membranes with improved membrane separation performance.

The CNT membranes in our previous works are neutral and hydrophobic membranes with extremely smooth pore surfaces, whereas most real NF membranes are polymeric membranes with negative or positive charges and complex intermolecular interactions between water and membrane surfaces. Here, we model several charged CNT membranes to investigate the effects of electrostatic interactions on pressure-driven water flow through the membranes. NEMD simulations are carried out by using uncharged and charged CNT membranes to analyze the NF transport phenomenon of pressure-driven water flow, including water flow rate, density and velocity (in z direction) distributions along both radial and flow directions.

5.3. Simulation Methods

All MD simulations are performed using the NAMD (NANoscale Molecular Dynamics)^[25] and VMD (Visual Molecular Dynamics)^[26] packages in the CHARMM (Chemistry at HARvard Molecular Mechanics)^[27] force field. Water molecules are represented by the modified flexible TIP3P (transferable intermolecular potential three-point) water model.^[28] In the CHARMM force field, electrostatic interactions are described by the Coulomb potential (E_{elect}),

$$E_{elect} = \sum_{nonbonded\ atom\ pairs} \frac{q_i q_j}{4\pi\epsilon_0 r_{ij}^2} \quad (6.1)$$

where q_i and q_j are the partial atomic charges of atoms i and j ; ϵ_0 is the electric constant with a value of $8.854 \times 10^{-12} \text{ C}^2/(\text{N} \cdot \text{m}^2)$; and r_{ij} is the distance between atoms i and j , respectively.

The simulation system is shown in Figure 5.1, containing two water reservoirs connected by the uncharged CNT membrane model and two graphene sheets (at the top of the top reservoir and bottom of the bottom reservoir) act as moveable walls. The uncharged CNT membrane is constructed from two graphene sheets with approximate holes in the center of each sheet perpendicularly to the ends of a (12, 12) type single-walled CNT. The CNT, 6.0 nm in length with internal radius of 0.643 nm,^[11, 19] provides the nanopore, while the graphene sheets provide the membrane surfaces. The charged CNT membranes have the same structure as the uncharged CNT membrane with carbon atoms assigned positive or negative atomic charges. Cartesian coordinates are chosen such that the movable walls and the membrane surfaces are parallel to the x, y plane – in squares with area 16 nm^2 . The water flow passes through the CNT along the z direction. The pressure difference is modeled by applying a constant force to each atom of the moveable membranes (the outer two), corresponding to a pressure of 8.1 MPa on the top side and 0.1 MPa on the bottom side.

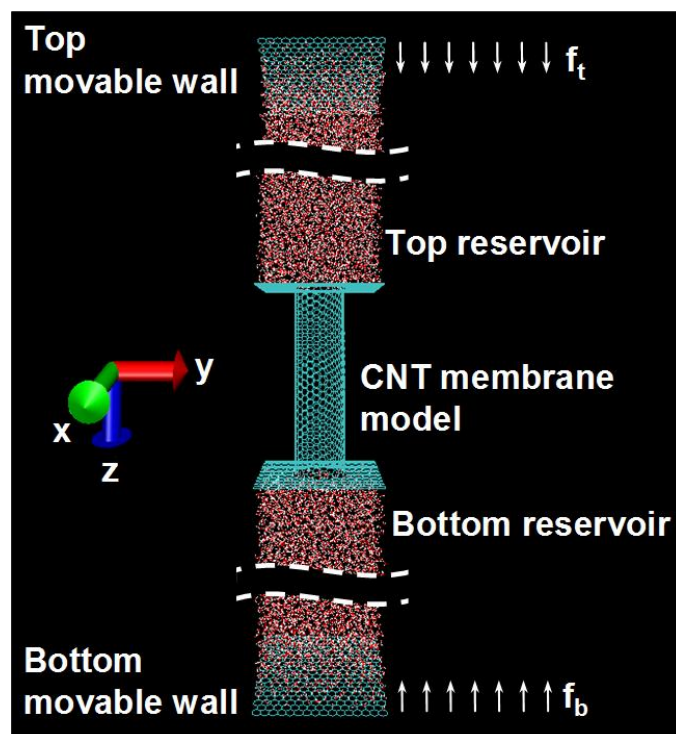


Figure 5.1 Perspective snapshots of the simulation systems produced by VMD package at the beginning status of MD simulations (adapted from the figure in reference [16]). Shown is the beginning empty CNT membrane model connecting two liquid filled reservoirs, and the two graphene sheets acted as the movable walls where the force f_t or f_b is applied on each carbon atom of the top or bottom wall. Carbon atoms in green, hydrogen atoms in white, and oxygen atoms in red.

An equilibrium MD simulation in an isothermal–isobaric (NPT) ensemble is carried out first to energy-minimize and equilibrate the system; and then a NEMD simulation in a canonical (NVT) ensemble is carried out to simulate a pressure-driven water flow through the CNT membrane. Each simulation is at 300 K, and takes about 5 CPU days for 1.0 ns of simulation. The detailed simulation methodology (force field parameters, integration algorithm, periodic boundary conditions, etc.) and simulation procedures are the same as in our previous work,^[16] except for computing electrostatic interactions. The cut-off radius is 1.2 nm with a switching function starting at 1.0 nm for computing long-range

interactions (van der Waals interactions and electrostatic interactions). Truncating the electrostatic interactions at the cutoff radius is not as accurate as the using Particle Mesh Ewald (PME) method.^[29] However, PME cannot be used as a neutral system is required which is not applicable in this investigation.

5.4. Results and Discussion

The theoretical flux, J_w , and velocity, v_z , in the z direction are calculated using the Navier-Stokes equations for a cylindrical channel as:

$$J_w = L_p \Delta P = \frac{r_p^2}{8\eta(L_z / A_K)} \Delta P \quad (6.2)$$

$$A_K = \frac{\pi \cdot r_p^2}{A_{mem}} = \frac{\pi \cdot r_p^2}{L_x \cdot L_y}$$

$$v_z = \frac{\Delta P}{4\eta L_z} (r_p^2 - r^2) \quad (6.3)$$

where L_p is the permeability coefficient of the water fluid, r_p is the pore radius, η is the viscosity of water at the operating temperature, L_z / A_K is the ratio of the membrane effective thickness to the membrane porosity, ΔP is the pressure difference, and r is the radial position. Equation (6.2) is also called the Hagen-Poiseuille equation, and Equation (6.3) refers to as the Navier-Stokes equation.

The simulation water flow rate is defined as the number flow rate (molecules/ns), which is obtained by counting the number of water molecules passing through the membrane model in a unit simulation time. The density and viscosity of water at 300 K are 1000 kg/m^3 and $8.54 \times 10^{-4} \text{ Pa} \cdot \text{s}$,^[30] which are used to determine the theoretical flux

via the Hagen-Poiseuille equation (Eqn. (6.2)). The theoretical flux is converted into flow rate (using total membrane area) as ‘molecules/ns’ for comparison with the simulation flow rate.

The interior of the CNT is divided into ten annular sections of equal space in the radial direction to investigate the radial density and velocity distributions. The distributions along the flow direction are studied by dividing the system evenly into ten sections; four in the top reservoir, three in the CNT, and three sections in the bottom reservoir. The density and velocity distributions are obtained through the time average values of density and velocity in each section calculated by averaging all data collected in a unit simulation time. The stream velocity of water flow in the water reservoirs is too low because of the low pressure difference, so the average velocity is hard to be obtained with a reasonable accuracy through the NEMD simulation. The water velocity in each reservoir is represented by the velocity of each movable wall, which can be calculated through the linear relationship between the moved distance of the wall and the simulation time.

The number of water molecules passing through the membrane model is counted every 50 ps and plotted as a function of the simulation time. The slope of the plotted linear profile (through origin) is the number flow rate. For each water flow rate, the estimated error of the flow rate is represented by the standard error on the slope with the assumption of uncorrelated data (a correlation time shorter than 50 ps). An example of the error analysis for the simulation flux (the flow rate per membrane area) is shown in our former work.^[16] The error analyses for density and velocity values include the integrated autocorrelation time, which is used to determine the effective number of uncorrelated

data.^[31] The statistical error of each density or velocity data point is calculated directly from the standard deviation of the sampled mean by using the number of uncorrelated samples. NEMD simulations are run until error estimates are within acceptable limits.

Two simulations are carried out for the uncharged CNT membrane using different methods to calculate the electrostatics interactions – specifically, the PME method and cutoff radius method. The two simulations show similar transport properties (not shown here): the difference between the two simulations is within 2% in terms of the investigated transport results (the simulation flow rate, and the distributions). This similarity supports us to use the cutoff radius to calculate the electrostatics interactions in the simulations of the charged membranes.

Four charged CNT membranes (#1 – 4 membranes in Table 5.1) are modeled with negative or positive atomic charges set on different parts of the CNT membrane, including the CNT internal pore surface and the two graphene sheet as the membrane surfaces. For each charged part, a constant negative charge is assigned to each carbon atom of this part to achieve a charge density of -1.0 C/m^2 for the negatively charged membranes (#1 – 3 membranes) or a charge density of 1.0 C/m^2 for the positively charged membrane (#4 membrane). The charges assigned to the CNT and to the graphene sheets are different because of the different number of the carbon atoms per unit area in the CNT and the sheets. In the first charged CNT membrane, the #1 membrane, a constant negative charge (-0.015979 e) is assigned to each carbon atom of the CNT – only the pore surface is charged in this case. The #2 membrane has a constant negative charge (-0.015238 e) assigned to each carbon atom of the two graphene sheets. The #3 or #4

membrane combines the charged parts of the pore charged model and surface charged model, so that the whole CNT membrane is charged.

Table 5.1 Specifications (charged parts and charge densities) of the #1–4 membranes.

Charged Membrane Model	Charged Parts	Charge Density (C/m²)
#1	Negative charges on the pore surface	-1
#2	Negative charges on the two membrane surface	-1
#3	Negative charges on the whole membrane	-1
#4	Positive charges on the whole membrane	1

5.4.1. The effect of charge distribution

Figure 5.2 shows the theoretical flow rate and the simulation flow rates of uncharged and three negatively charged CNT membranes (#1 – 3 membranes in Table 5.1): the uncharged membrane has the highest simulation flow rate, while the #3 membrane (charges on the whole membrane) has the lowest flow rate. Water has dipole nature,^[32] partial positive charges on the hydrogen atoms and a partial negative charge on the oxygen atom, so the water transport is dependent on the electrostatic interactions between water and the charged membrane. The simulation flow rates in Figure 5.2 shows the negatively charged CNT membranes all have a lower flow rate than the uncharged membrane, due to the stronger attractive interactions between water and the charged membrane. This stronger water–membrane interaction results that the charged

membranes become more hydrophilic than the uncharged membrane.

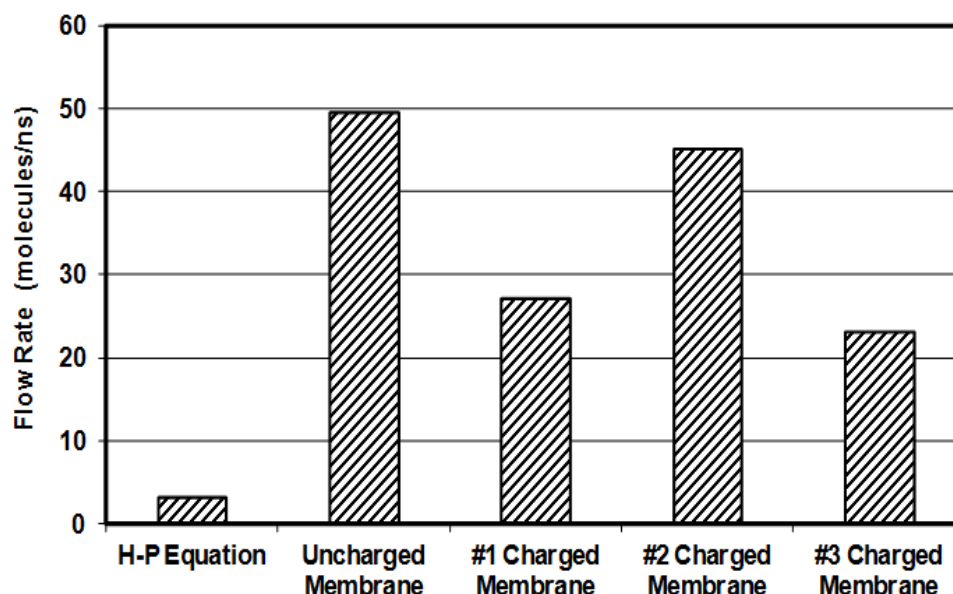


Figure 5.2 Bar chart of simulation and theoretical flow rates (molecules/ns) of uncharged and negatively charged (#1 – 3) CNT membranes. The results are based on membrane simulations using the (12, 12) CNT, $L_z = 6.0$ nm; $\Delta P = 8.0$ MPa; $T = 300$ K. The statistical error for each flow rate data is less than 0.5%. H-P equation refers to the Hagen-Poiseuille equation (Eqn. (6.2)). The charges are on the pore surface, the two membrane surfaces, and the whole membrane for the #1, #2, and #3 membranes, respectively (Table 5.1).

As shown in Figure 5.2, the simulation flow rate of the #2 membrane (charges on the membrane surfaces) is about 9% lower than that of the uncharged membrane, while the difference of the simulation flow rates between the #1 membrane (charges on the pore surface) and the #3 membrane (charges on the whole surface) is about 4 molecules/ns. The similar flow rates of the uncharged membrane and the #2 membrane implies the charges on the membrane surfaces (the two graphene sheets) have little influence on the flow of water passing through the CNT membrane. Negative charges placed on the graphene sheets interact strongly with the water molecules near the membrane surfaces in the reservoirs, but do not affect water flow in the CNT. The #1 and #3 membranes both

have negative charges on the pore surface (the CNT) which attract water molecules and reduce flow in the CNT. The simulation flow rates of the #1 and #3 membranes are both about half of the flow rate of uncharged membrane. The effect of a charged CNT on water has been seen in other literature,^[33] where it is reported that water can speed filling of a charged CNT but slow passage through the charged CNT filled with water. Similar to the #2 membrane has a slightly slower flow than the uncharged membrane due to the charges on the membrane surfaces, the additional electrostatic interactions between water and the membrane surface of the #3 membrane also produce a lower flow rate of the #3 membrane than the #1 membrane.

Nevertheless, all of the four CNT membranes considered (uncharged and charged) exhibit flow rates much higher (from 7-15 times higher) than the theoretical flow rate predicted by the Hagen-Poiseuille equation. The flow rate of the #2 or #3 membranes is half of the flow rate of uncharged membrane but is still 7 times higher than the theoretical flow rate. As explained in our former works^[16], the reasons of the high simulation flow rates of CNT membranes are the narrow pore size, the smooth CNT surface and the weak interactions between water molecules and CNT membrane. The fast water flow through the CNT membrane under pressure difference is much more sensitive to charges on the pore than charges on the membrane surfaces.

The density distributions of water in the four CNT membranes along the radial direction are shown in Figure 5.3. All of the density profiles are oscillatory with respect to the radial position, with two symmetrical pairs of wave peaks (two water rings in the CNT). The density profiles of the four membranes are all similar, except for the lower

and slight wider density peaks near the pore surface in the cases of the #1 and #3 membranes. As shown in Figure 5.3, the #1 and #3 membranes both have lower outer density peaks but higher water densities at the radial positions from 0.5 nm to 0.6 nm than the uncharged and #2 membranes. The higher density values near the pore surfaces of the #1 or #3 membrane correspond to the outer water ring in the CNT of the membrane closer to the pore surface, due to the electrostatic attractions between water and the charges on the pore surface.

Figure 5.4 shows the density distribution along the flow direction, where water density in the reservoirs is insensitive to the charges on the membrane and water density within the CNT is sensitive only to the charges on the pore surface. For the #1 and #3 membranes, water density is higher near the entrance and exit to the pore - comparable to the bulk value. The higher density of water near the top and bottom membrane boundaries of the CNT is similarly due to the electrostatic attraction of water to the charged pore of the #1 or #3 membrane. This higher density of water near the openings of the pore coincides with the cases of slower water flow seen in Figure 5.2 in case of the #1 or #3 membrane. Note that the density distributions of the #1 or #3 charged membrane shown here are different with the density distributions of polarized neutral membranes as studied in our previous work.^[18]

The flow rate and the density distributions of Figures 5.2-5.4 divide the four different CNT membranes into two groups: the uncharged membrane and the #2 membrane, and the #1 and #3 membranes.

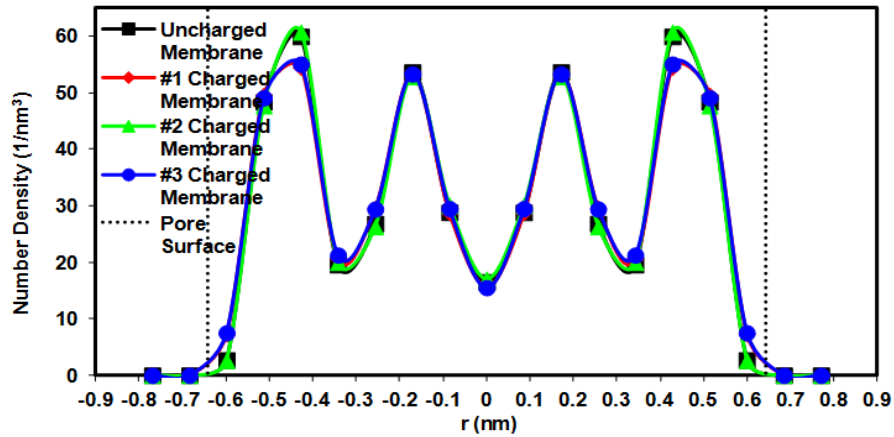


Figure 5.3 Effect of electrostatic interactions between water and membrane, caused by the negative charges on the CNT membrane, on the density distributions along the radial direction: density as a function of r ; values are averaged over a thin annular section in the pore at r (excluding the entrance and exit regions). The data points are based on membrane simulations using the (12, 12) CNT, $L_z = 6.0$ nm; $\Delta P = 8.0$ MPa; $T = 300$ K. The statistical error for each data point is less than 1%. The charged types are shown in Table 5.1. The solid lines are the trend curves based on the simulation results, and the dotted lines are the pore surface represented by the effective pore radius (0.643 nm).

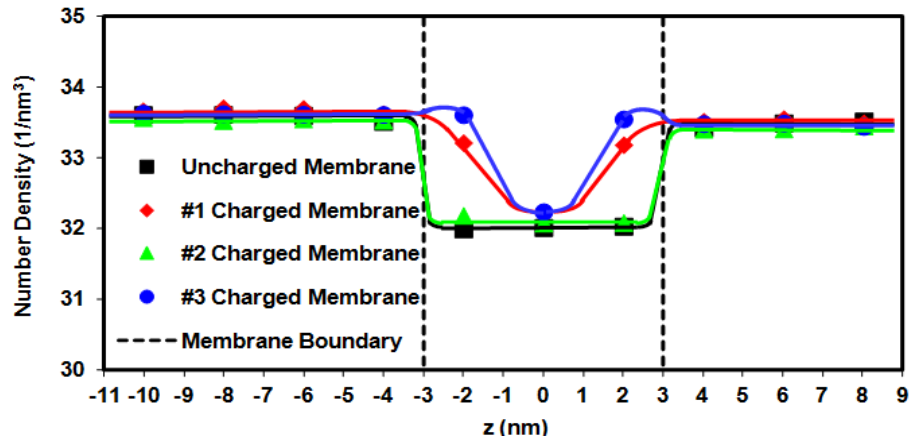


Figure 5.4 Effect of electrostatic interactions between water and membrane, caused by the negative charges of the CNT membrane, on the density distributions along the flow direction: density as a function of z ; values are averaged over a thin section at z (cylindrical sections in the pore and cuboid sections in the water reservoirs). The data points are based on membrane simulations using the (12, 12) CNT, $L_z = 6.0$ nm; $\Delta P = 8.0$ MPa; $T = 300$ K. The statistical error for each data point is less than 1%. The charged types are shown in Table 5.1. The solid lines are the trend curves based on the simulation results. The dashed lines are the membrane boundaries along z direction separating the system in three parts from left to right: the water reservoir at high pressure side, the pore of the CNT membrane, and the water reservoir at low pressure side.

Figure 5.5 shows the radial distributions of z component velocity for the different CNT membranes. These velocity distributions are all non-parabolic and much higher than that predicted using the Navier-Stokes equation. As discussed in previous works,[16] the fast z component velocities are a consequence of the non-uniform nanofluid formed when the pore size of a CNT is not much larger than a water molecule, the weak interactions between water and the CNT, and the very smooth pore surface. In the cases of the #1 or #3 membranes, the water–membrane electrostatic interactions do not break the nonuniformity of water flow in the CNT: the radial distribution of velocity is still non-parabolic and much higher than the theoretical velocity calculated by the Navier-Stokes equation.

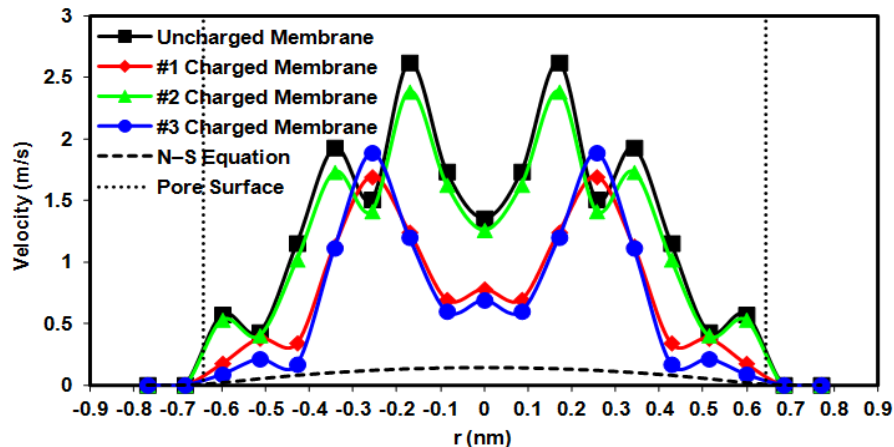


Figure 5.5 Effect of electrostatic interactions between water and membrane, caused by the negative charges of the CNT membrane, on the velocity (in z direction) distributions along the radial direction: velocity (in z direction) values are averaged over a thin annular section in the pore at r (excluding the entrance and exit regions). The data points are based on membrane simulations using the (12, 12) CNT, $L_z = 6.0$ nm; $\Delta P = 8.0$ MPa; $T = 300$ K. The statistical errors for most data points are less than 15%. N-S equation refers to the Navier-Stokes Equation (Eq. (2)), and the charged types are shown in Table 5.1. The solid lines are the trend curves based on the simulation results, the dashed lines are the trends based on the Navier-Stokes Equation, and the dotted lines are the pore surface represented by the effective pore radius (0.643 nm).

Figure 5.6 compares the velocities of the four CNT membranes at various positions along the flow direction: for each membrane, the velocities in the CNT increase/decrease when water molecules enter/leave the CNT membrane, and the velocity is independent of position along the flow direction, for all of the membranes, as seen in previous studies.[16]

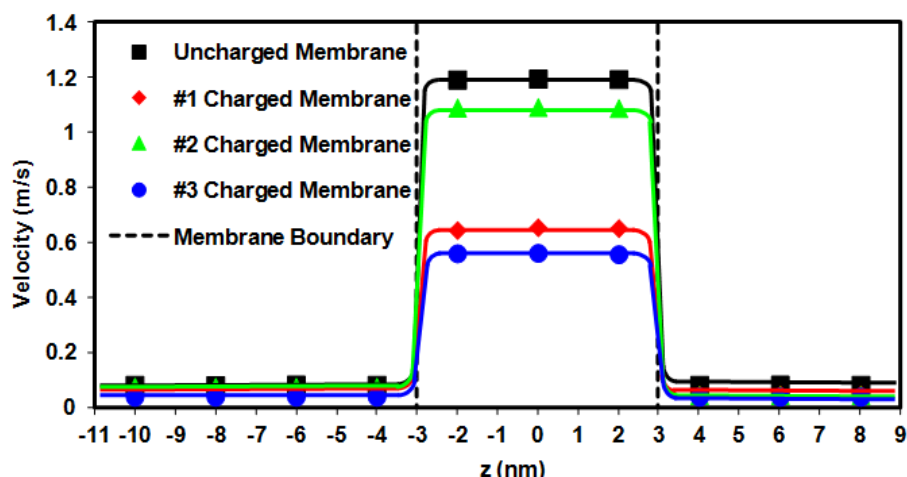


Figure 5.6 Effect of electrostatic interactions between water and membrane, caused by the negative charges of the CNT membrane, on the velocity (in z direction) distributions along the flow direction: velocity (in z direction) values are averaged over thin sections about the indicated z values (cylindrical sections in the pore and cuboid sections in the water reservoirs) over the entire NEMD simulation. The data points are based on membrane simulations using the (12, 12) CNT, $L_z = 6.0$ nm; $\Delta P = 8.0$ MPa; $T = 300$ K. The statistical error for each data point is less than 10%. The charged types are shown in Table 5.1. The solid lines are the trend curves based on the simulation results. The dashed lines are the membrane boundaries along z direction separating the system in three parts from left to right: the water reservoir at high pressure side, the pore of the CNT membrane, and the water reservoir at low pressure side.

As already noted, the electrostatic interactions between water and charges on the membrane surfaces have little influence on the pressure-driven water flow, and charges on the pore surface strongly affect the water flow because of the water–pore electrostatic interaction. The velocity distributions in Figures 5.5 and 5.6 show the reduced velocity profiles of the #1 and #3 membranes compared with the uncharged and #2 membranes.

Like the density distributions of Figures 5.3 and 5.4, the velocity distributions in Figures 5.5 and 5.6 divide the four CNT membranes into two groups and the two CNT membranes in each group mentioned above have almost overlapping velocity profiles. The effect of charges on the pore surface is to reduce velocity; charges on the membrane surfaces have a similar, but much smaller, effect. Therefore, the membrane with charges on the membrane surfaces has slightly lower velocity profiles along the radial and flow directions than the other membrane in each group.

In the charged CNT, water molecules are attracted to move towards (stick on) the pore surface due to the charges on the pore surface, and there are more water molecules near the pore openings than in the pore center as shown in Figure 5.4. The water molecules sticking on the pore surface and staying near the pore openings tend to reduce the effective pore size of the charged CNT. In Figure 5.5, there is a shift in peaks and troughs of the oscillatory velocity distribution along the radial direction, in case of the membrane with charges on the pore surface, which is probably caused by the reducing effective pore size of the charged CNT. Whereas the water-pore electrostatic attraction enhances water densities near the pore openings of the #2 or #3 membrane shown in Figure 5.4, Figure 5.6 shows a uniform water flow throughout the charged CNT. The section near the top / bottom pore opening has about 3 molecules more than the center section. Thus, the variation in the density along the pore has no counterpart in the velocity profile.

In summary, charges on the membrane surface charge have a small effect on water transport, while the greatest impact comes from charges on the pore surface. The effect

of charges on the CNT membrane is to reduce the pressure-driven water flow passing through the membrane.

5.4.2. The effect of charge type

The #3 and #4 membranes, both having charges on the whole membrane (Table 5.1), are negatively and positively charged membranes, respectively. These two charged membranes are compared with the uncharged CNT membrane to study the effect of charge type on the transport properties. Figures 5.7-5.11 show the simulation flow rates, the density distributions along the radial and flow directions, and the velocity distributions along the radial and flow directions.

In Figure 5.7, the simulation flow rates of the two charged membranes are both less than half of the flow rate of the uncharged CNT membrane and are both about 7 times as the theoretical flow rate calculated by using the Hagen-Poiseuille equation. Recall the negative charges on the pore reduce the water flow as discussed above, the positive charges on the pore have the similar effect on the water flow due to the water-pore electrostatic interaction. Due to dipole nature of water, the effects of positive charge and negative charge on the neutral water flow are almost the same for the flow rate. This similarity between the two charged membranes also can be observed from the velocity distributions along the radial and flow directions (Figures 5.10 and 5.11): the two charged membranes have lower velocities and the #4 membrane exhibits a slightly slower water flow than the #3 membrane. The density distributions along the radial and flow direction are a little more distinct (Figures 5.8 and 5.9), due to the orientation of water

molecules dependent on the charge type.

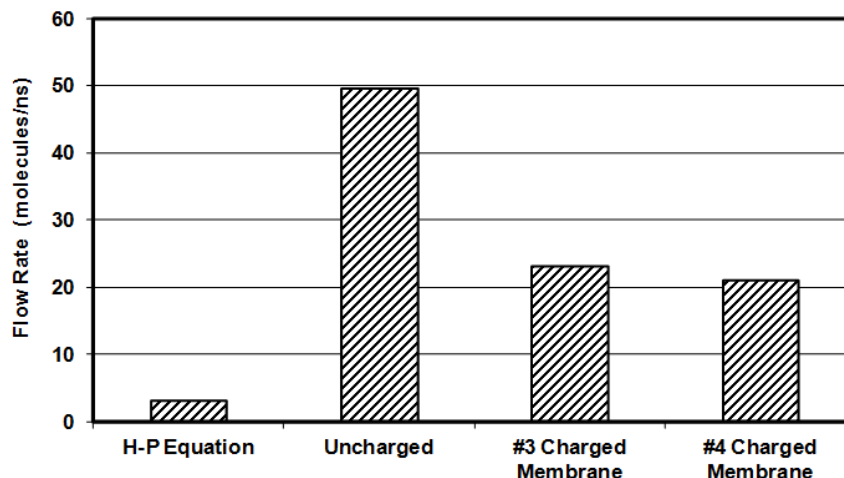


Figure 5.7 Bar chart of simulation and theoretical flow rates (molecules/ns) of uncharged and charged (#3 and #4) CNT membranes. The results are based on membrane simulations using the (12, 12) CNT, $L_z = 6.0$ nm; $\Delta P = 8.0$ MPa; $T = 300$ K. The statistical error for each data point is less than 0.5%. H-P equation refers to the Hagen-Poiseuille equation (Eqn. (6.2)). The charges are on the whole membrane for the #3 or #4 membranes (Table 5.1): the #3 membrane is negatively charged and the #4 membrane is positively charged.

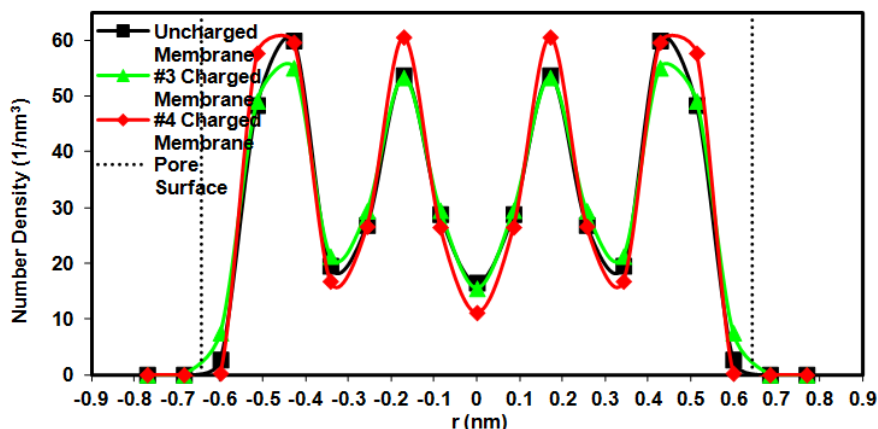


Figure 5.8 Effect of electrostatic interactions between water and membrane, caused by the positive or negative charges of the CNT membrane, on the density distributions along the radial direction: density as a function of r ; values are averaged over a thin annular section in the pore at r (excluding the entrance and exit regions). The data points are based on membrane simulations using the (12, 12) CNT, $L_z = 6.0$ nm; $\Delta P = 8.0$ MPa; $T = 300$ K. The statistical error for each data point is less than 1%. The charged types are shown in Table 5.1. The solid lines are the trend curves based on the simulation results, and the dotted lines are the pore surface represented by the effective pore radius (0.643 nm).

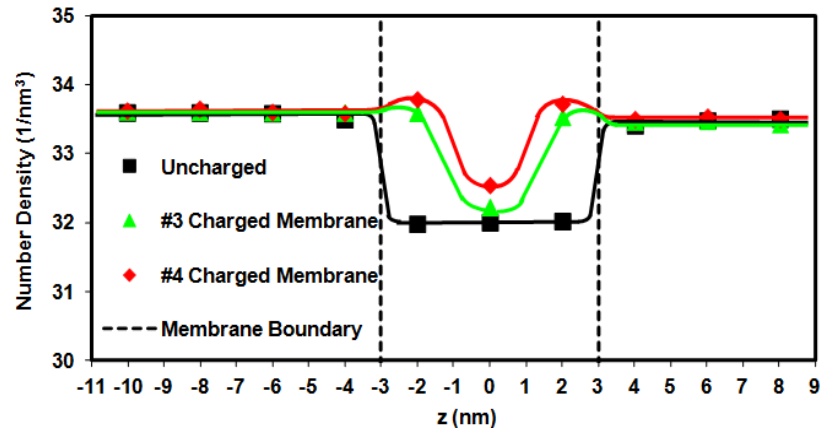


Figure 5.9 Effect of electrostatic interactions between water and membrane, caused by the positive or negative charges of the CNT membrane, on the density distributions along the flow direction: density as a function of z ; values are averaged over a thin section at z (cylindrical sections in the pore and cuboid sections in the water reservoirs). The data points are based on membrane simulations using the (12, 12) CNT, $L_z = 6.0$ nm; $\Delta P = 8.0$ MPa; $T = 300$ K. The statistical error for each data point is less than 1%. The charged types are shown in Table 5.1. Solid lines are the trend curves based on the simulation results. The dashed lines are the membrane boundaries along z direction separating the system in three parts from left to right: the water reservoir at high pressure side, the pore of the CNT membrane, and the water reservoir at low pressure side.

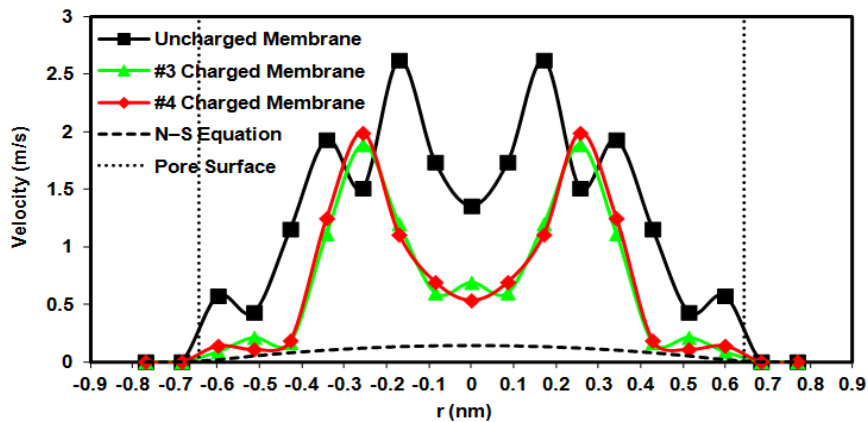


Figure 5.10 Effect of electrostatic interactions between water and membrane, caused by the positive or negative charges of the CNT membrane, on the velocity (in z direction) distributions along the radial direction: velocity (in z direction) values are averaged over a thin annular section in the pore at r (excluding the entrance and exit regions). The data points are based on membrane simulations using the (12, 12) CNT, $L_z = 6.0$ nm; $\Delta P = 8.0$ MPa; $T = 300$ K. The statistical errors for most data points are less than 15%. N-S equation refers to the Navier-Stokes Equation (Eq. (2)), and the charged types are shown in Table 5.1. The solid lines are the trend curves based on the simulation results, the dashed lines are the trends based on the Navier-Stokes Equation, and the dotted lines are the pore surface represented by the effective pore radius (0.643 nm).

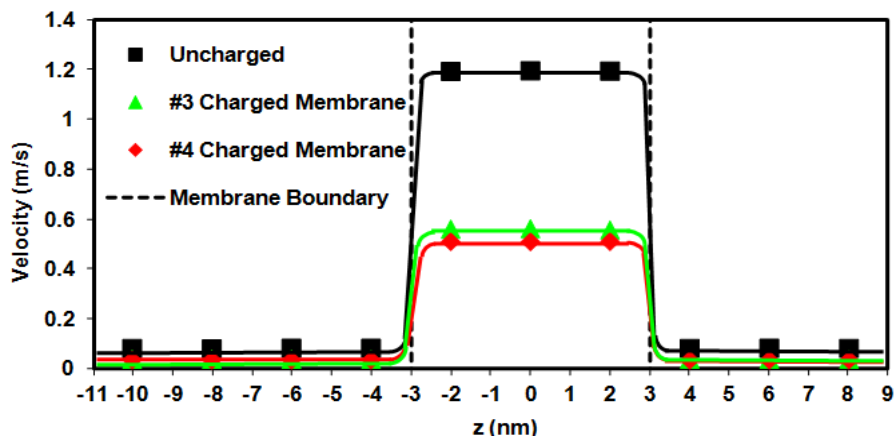
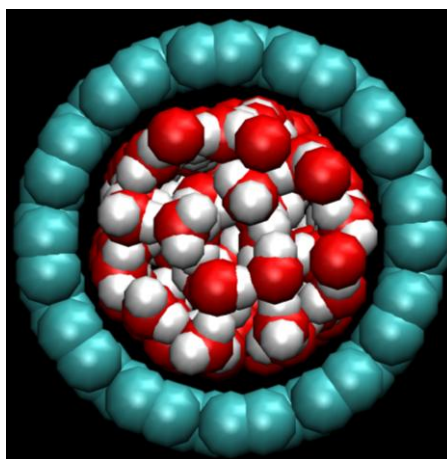


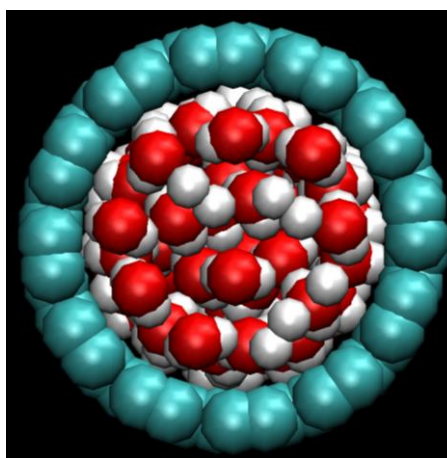
Figure 5.11 Effect of electrostatic interactions between water and membrane, caused by the positive or negative charges of the CNT membrane, on the velocity (in z direction) distributions along the flow direction: velocity (in z direction) values are averaged over thin sections about the indicated z values (cylindrical sections in the pore and cuboid sections in the water reservoirs) over the entire NEMD simulation. The data points are based on membrane simulations using the (12, 12) CNT, $L_z = 6.0$ nm; $\Delta P = 8.0$ MPa; $T = 300$ K. The statistical error for each data point is less than 10%. The charged types are shown in Table 5.1. The solid lines are the trend curves based on the simulation results. The dashed lines are the membrane boundaries along z direction separating the system in three parts from left to right: the water reservoir at high pressure side, the pore of the CNT membrane, and the water reservoir at low pressure side.

Figure 5.12 shows snapshots of the cross section view of the water flow in the CNT of each membrane model (negatively and positively charged membranes). The electrostatic attraction between hydrogen atoms in the outer water ring and negatively charged wall result in hydrogen atoms facing towards the wall for the #3 membrane. Contrarily oxygen atoms in the outer water ring face towards the wall for the #4 membrane. Due to the orientation of water molecules in the CNT affected by the charges on the membrane, the two charged membranes have different density distributions along the radial direction in Figure 5.8. The centers of hydrogen atoms in the water ring molecules near the pore surface of the #3 membrane can be closer to the pore surface than the oxygen atoms near the pore surface of the #4 membrane, because of

a smaller van der Waals radius of hydrogen. Consequently, the higher densities near the pore surface of the #3 membrane are observed as shown in Figure 5.8, although the outer water ring looks closer to the pore surface of the #4 membrane than the #3 membrane as shown in Figure 5.12. The higher density peaks of the #4 membrane in Figure 5.8 is caused by more oxygen atoms existing in the annular sections and oxygen having a higher atomic mass.



(a) Water in the #3 (negatively charged) CNT membrane



(b) Water in the #4 (positively charged) CNT membrane

Figure 5. 12 Orthographic snapshots of water molecules in the #3 (a) and #4 (b) CNT membranes. The illustrations are based on membrane simulations using the (12, 12) CNT, $L_z = 6.0$ nm; $\Delta P = 8.0$ MPa; $T = 300$ K. Atoms are shown by balls with the van der Waals volumes: carbon atoms in green, hydrogen atoms in white, and oxygen atoms in red.

Figure 5.9 shows the #4 membrane has higher density values in the CNT along the flow direction than the #3 membrane. There are about 2 more water molecules in the CNT of the #4 membrane than that of the #3 membrane, caused by the electrostatic interaction between water and positive charges on the #4 membrane resulting in more water molecules attracted into the CNT. As the orientation of water molecules in the CNT or near the membrane changes, the van der Waals interaction between water and the membrane will be different. Generally, oxygen atoms have a strong van der Waals interaction with nanotube carbon atoms than hydrogen atoms. The other possible reason for the slightly higher density in the CNT of the #4 membrane (in Figure 5.9) could be the larger attractive van der Waals interaction between water and the membrane resulting from the oxygen atoms towards the positive charges on the membrane.

In summary, the different charge type on the membrane has a small effect on water transport through the charged membrane, while some differences between the positively charged membrane and the negatively charged membrane are seen in the configuration of water molecules in the CNT.

5.5. Conclusions

The effects of charged CNT membranes on pressure-driven water transport have been investigated using NEMD, under NF operating conditions.

All CNT membranes studied have the same pore size and membrane thickness. Both uncharged and charged CNT membranes exhibit the same general characteristics of pressure-driven water transport – specifically, the fast flow with a non-parabolic velocity

distribution along the radial direction. The Navier-Stokes equations fail to predict the flow rate and the radial velocity profile due to the non-uniform nanofluid structure within the nanoscale pore-size CNT, the smooth pore surface, and the weak water–membrane interactions.

The charged CNT membrane is more hydrophilic than the uncharged CNT membrane because of the electrostatic attraction between water and the charged CNT membrane, and has a slower pressure-driven water flow. The charges on the membrane surface have little effect on the water flow, while the charges on the pore surface (the CNT) play the greatest role in reducing the water flow. Among the three negatively charged CNT membranes, the #3 membrane (with charges on the whole membrane) has the slowest water flow which is just a little bit lower than the flow rate of the #2 membrane (with charges on the pore surface); the #1 membrane with charges on the two membrane surfaces has water flow rate quite close to the flow rate of the uncharged membrane. Moreover, the charges on the pore surface also play an important role on the water density distributions along the radial and flow direction. There are a fewer more water molecules in the charged CNT than the uncharged CNT. Charging the membrane positively or negatively has only a small effect on the water transport properties, such as mostly similar flow rates, velocity and density distributions. The orientation of water molecules is dependent on the charge type of the charged membrane, resulting in the differences between the density distributions of the positively charged and negatively charged membranes.

The results of NEMD simulations reveal the dynamic transport mechanism of

pressure-driven water flow through the charged CNT membranes, which is quite unlike a continuum-based description of the flow process. We have seen that although charges on the membrane reduce water flow, the water flow through the CNT membrane is still significantly larger than that predicted by the Navier-Stokes equation. Real NF membranes are, of course, much more complex. However, it can be projected that these studies provide a useful guide to understand pressure-driven transport, and an aid to the design of new membrane applications.

References

- [1] N. Hilal, H. Al-Zoubi, N. A. Darwish, A. W. Mohammad, and M. Abu Arabi, *Desalination* **170** 281 (2004).
- [2] J. Schaep, B. Van der Bruggen, S. Uytterhoeven, R. Croux, C. Vandecasteele, D. Wilms, E. Van Houtte, and F Vanlerberghe, *Desalination* **119** 295 (1998).
- [3] B. Van der Bruggen and C. Vandecasteele, *Environ. Pollut.* **122** 435 (2003).
- [4] X. Lu, X. Bian, and L. Shi, *J. Membr. Sci.* **210** 3 (2002).
- [5] A. I. Schäfer, A. G. Fane, T. D. Waite, *Nanofiltration: Principles and Applications*, (Elsevier Advanced Technology, Oxford, 2005).
- [6] W. Ho and K. Sirkar, *Membrane Handbook*, (Van Nostrand Reinhold, New York, 1992).
- [7] M. Mulder, *Basic Principles of Membrane Technology*, (Kluwer, London, 1996).

- [8] R. Petersen, *J. Membr. Sci.* **83** 81 (1993).
- [9] L. E. Applegate, *Chem. Eng. (New York)* **91** 64 (1984).
- [10] L. D. Nghiem, Removal of emerging trace organic contaminants by nanofiltration and reverse osmosis, (PhD thesis, School of Civil, Mining and Environmental Engineering, University of Wollongong, Wollongong, Australia, 2005).
- [11] J. Goldsmith and C. C. Martens, *J. Phys. Chem. Lett.* **1** 528 (2010).
- [12] K. Leung and S. B. Rempe, *J. Comput. Theor. Nanosci.* **6** 1948 (2009).
- [13] C. Huang, K. Nandakumar, P. Choi, and L. W. Kostiuk, *J. Chem. Phys.* **124** 234701 (2006).
- [14] H. Takaba, Y. Onumata, and S. Nakao, *J. Chem. Phys.* **127** 054703 (2007).
- [15] I. Hanasaki and A. Nakatani, *Model. Simul. Mater. Sci. Eng.* **14** 9 (2006).
- [16] L. Wang, R. S. Dumont, and J. M. Dickson, *J. Chem. Phys.* **134** 044102 (2012).
- [17] L. Wang, R. S. Dumont, and J. M. Dickson, "Comparison of two nonequilibrium molecular dynamics simulation systems for the pressure-driven water permeation through carbon nanotube membrane", *Microfluid. Nanofluid.* submitted (2012).
- [18] L. Wang, R. S. Dumont, and J. M. Dickson, "Nonequilibrium molecular dynamics simulation of pressure-driven water transport through modified carbon nanotube membranes", to be submitted (2012).
- [19] A. Noy, H. G. Park, F. Fornasiero, J. K. Holt, C. P. Grigoropoulos, and O. Bakajin, *Nano Today* **2** 22 (2007).
- [20] W. D. Nicholls, M. K. Borg, D. A. Lockerby, and J. M. Reese, *Microfluid.*

Nanofluid. **12** 257 (2012).

- [21] J. K. Holt, H. G. Park, Y. Wang, M. Stadermann, A. B. Artyukhin, C. P. Grigoropoulos, A. Noy, and O. Bakajin, *Science* **312** 1034 (2006).
- [22] M. Majumder, N. Chopra, R. Andrew, and B. J. Hinds, *Nature* **438** 44 (2005).
- [23] M. Majumder, N. Chopra, and B. J. Hinds, *ACS Nano*, **5** 3867 (2011).
- [24] X. Qin, Q. Yuan, Y. Zhao, S. Xie, and Z. Liu, *Nano Lett.* **11** 2173 (2011).
- [25] J. Phillips, R. Braun, W. Wang, J. Gumbart, E. Tajkhorshid, E. Villa, C. Chipot, R. D. Skeel, L. Kalé, and K. Schulten, *J. Comput. Chem.* **26** 1781 (2005).
- [26] W. Humphrey, A. Dalke, and K. Schulten, *J. Mol. Graphics* **14** 33 (1996).
- [27] A. D. MacKerell, N. Banavali, and N. Foloppe, *Biopolymers* **56** 257 (2001).
- [28] W. L. Jorgensen, J. Chandrasekhar, J. D. Madura, R. W. Impey, and M. L. Klein, *J. Chem. Phys.* **79** 926 (1983).
- [29] T. Darden, D. York, and L. Pedersen, *J. Chem. Phys.* **98** 10089 (1993).
- [30] U. Kaatz, *Radiat. Phys. Chem.* **45** 539 (1995).
- [31] W. Janke, *Statistical Analysis of Simulations: Data Correlations and Error Estimation*, in: G. Johannes, D. Marx, A. Muramatsu (Eds.), *Quantum Simulations of Complex Many-Body Systems: From Theory to Algorithms*, (John von Neumann Institute for Computing, Jülich, 2002).
- [32] P. L. Silvestrelli and M. Parrinello, *J. Chem. Phys.* **111** 3572 (1999).
- [33] B. Huang, Y. Xia, M. Zhao, F. Li, X. Liu, Y. Ji, and C. Song, *J. Chem. Phys.* **122** 084708 (2005).

Chapter 6 Study of Pressure-Driven Organic Flows through CNT Membranes by Nonequilibrium Molecular Dynamics Simulations

6.1. Abstract

Nonequilibrium molecular dynamics (NEMD) simulations are presented to investigate the transport properties of organic flows and water flow under nanofiltration (NF) operation conditions. The liquid flows of different molecular masses, viscosities, and molecular structures are simulated to pass through carbon nanotube (CNT) membranes of different pore sizes at constant pressure driving force (8.0 MPa). Liquids investigated are water, ethanol, 1-pentanol, pentane, 1,5-pentanediol, and benzene; these liquids are compared to show the effects of the molecular mass, viscosity, and molecular structure on the liquid transport properties (flux and density distributions). In general, the simulation flux increases with increasing molecular mass and/or decreasing liquid viscosity. The aromatic benzene liquid is slower than the linear liquids of similar molecular masses and liquid viscosities to benzene, due to the large molecular size and π -bond structure of benzene. The liquids (except for the benzene flow) all show a higher simulation flux than the theoretical flux calculated by the Navier-Stokes equation. The Navier-Stokes equation fails to predict the fast liquid for any of the liquids (except for the benzene flow) however the effect of viscosity on the simulation flux is consistent with the

Navier-Stokes equations. The effect of membrane pore size on the transport properties revealed: for linear molecular structures the simulation flux increases as the pore size increases while the benzene flux exhibits an irregular changing trend with increasing pore size due to the large molecular size and unique π -bond structure of benzene. The density distributions of liquid molecules along the radial and flow directions are strongly dependent on the molecular size and molecular structure of liquid and the membrane pore size of the CNT membrane. This work studies the dynamic behaviors of the pressure-driven organic liquids passing through the CNT membranes on a molecular scale and helps to get a fundamental understanding of NF transport.

6.2. Introduction

Nanofiltration (NF) is a typical membrane separation process driven by the pressure difference across the membranes and has already been applied in a broad spectrum of fields. Due to the advantages of NF, including low operation pressure, high flux, high rejection, and relatively low costs, the applications of NF worldwide have increased. The NF applications are primarily in water treatments and to separate organic solutes from organic solvents or water.

For the last few decades, using NF technology to remove organic micropollutants from drinking water has increased significantly.^[1, 2] The organic micropollutants can be found in a wide range of man-made chemicals used in industry and our daily life, such as pesticides, hormones, endocrine disrupting compounds, pharmaceutically active compounds, personal care products, and so forth. The occurrence of the organic

micropollutants in the water system has become an environmental problem and raises human-health concerns, due to the toxicity and potential health effects. Some traditional models have been applied to describe the NF transport of removing organic solutes from water,^[3-5] but the existing models have only been partially successful in predicting the membrane performances. A deep understanding of the transport of small organic compounds through NF membranes is still a challenging issue.

Molecular dynamics (MD) simulation, as a novel experiment and a complement to study a liquid transport, can directly give an analysis and visualization of the flow on a molecular scale, which cannot be shown through traditional mathematical models. A pressure-driven transport is a nonequilibrium transport and can be studied through a nonequilibrium molecular dynamics (NEMD) simulation. To study pressure-driven liquid flows passing through nanoporous membranes, two NEMD methods are frequently used in published works.^[6-15] The key difference between the two methods is the methodology to produce a constant pressure difference across the membrane and the periodic boundary conditions (PBC) along the flow direction. Huang^[6-9] and Takaba^[10] both studied pressure – driven liquid argon flows by using similar NEMD methods (the first kind), in which external forces are applied on the two movable walls located at the two stream boundaries to control pressures and the PBC is not set in the flow direction. The second NEMD method is commonly used to simulate an aqueous flow.^[11-15] In the second method, external forces are applied on all or part of water molecules and/or ions of the flow, and the PBC is set in the flow direction. The second NEMD simulation method is not suitable for investigating a pressure-driven organic flow of a large

molecular size (larger than water or ion), since it is hard to apply external forces evenly on the large organic molecules and the movement of the organic molecules is strongly affected by the external forces. While the first method generates two different pressures in the two streams by applying external forces on the solid walls and the movement of liquid molecules in each stream is only affected by the generated pressure.

In our previous works,^[16-19] a NEMD simulation system is derived from the studies by Huang^[6-9] and Takaba^[10] (the first method as mentioned above) to simulate pressure-driven water flows through carbon nanotube (CNT) membranes at low pressure differences. The results show the CNT membrane exhibits a fast water flow due to a combination of the nanoscale pore size, the smooth CNT surface, and the weak interactions between water and the CNT. Moreover, the effects of membrane structure (pore size and membrane thickness),^[16] pressure difference,^[17] and the water–membrane interactions^[18, 19] on pressure-driven water transport have been investigated. Few works have been reported on the transport properties of pressure-driven organic liquid flows.

The NEMD simulation study presented here is to simulate pure organic flows and water flow passing through CNT membranes at the same pressure difference, using the NEMD simulation method as in our previous works. The transport properties of each system are investigated, including simulation flux and the density distributions along both the radial and flow directions.

6.3. Simulation Methods

Six liquid molecules (in Table 6.1) are modeled: water is described by the flexible

TIP3P (transferable intermolecular potential three-point) water model^[20] in CHARMM (Chemistry at HARvard Molecular Mechanics)^[21] force field, and the organic molecules are modeled by using the CHARMM General Force Field^[22]. NAMD (NANoscale Molecular Dynamics) package^[23] and VMD (Visual Molecular Dynamics) package^[24] are both used in the CHARMM force field for all MD simulations.

The force field parameters for the organic molecules are from the topology and parameter files for the CHARMM General Force Field.^[40] Each organic molecule is used to build a liquid box, and the built box is equilibrated for 5.0 ns at 300 K and 0.1 MPa with three-dimensional PBC to obtain an equilibrated liquid box as the reservoir in the NEMD simulation system. Figure 6.1 shows the simulation system in Cartesian coordinates for setting a pressure-driven liquid flow along the $z+$ direction. The system includes two graphene sheets in the x, y plane as moveable walls, two liquid reservoirs (showing ethanol reservoirs as an example), and a CNT membrane model containing a (12, 12) CNT of 6.0 nm length and 0.643 nm internal radius^[11, 12]. The lengths in the x and y directions of the system are both 4.0 nm, and the two-dimensional PBC is set in the x, y directions. Large force along the $z+$ direction is applied to each carbon atom of the top moveable wall to produce 8.1 MPa pressure on the top liquid reservoir, and small force along the $z-$ direction applied on the bottom wall exerts 0.1 MPa on the bottom liquid reservoir. The generated 8.0 MPa pressure difference across the CNT membrane is to drive the liquid flow passing through the membrane.

An equilibrium MD simulation in an isothermal–isobaric (NPT) ensemble is carried out first to energy-minimize and equilibrate the system; and then a NEMD simulation in a

canonical (NVT) ensemble is carried out to simulate a pressure-driven liquid flow through the CNT membrane. Each simulation is at 300 K, and takes about 15 CPU days for 1.0 ns of simulation. The detailed simulation methodology (force field parameters, integration algorithm, periodic boundary conditions, etc.) and simulation procedures are the same as in our previous work,^[16] while the trajectory of the NEMD simulation is saved for every 1000 time steps.

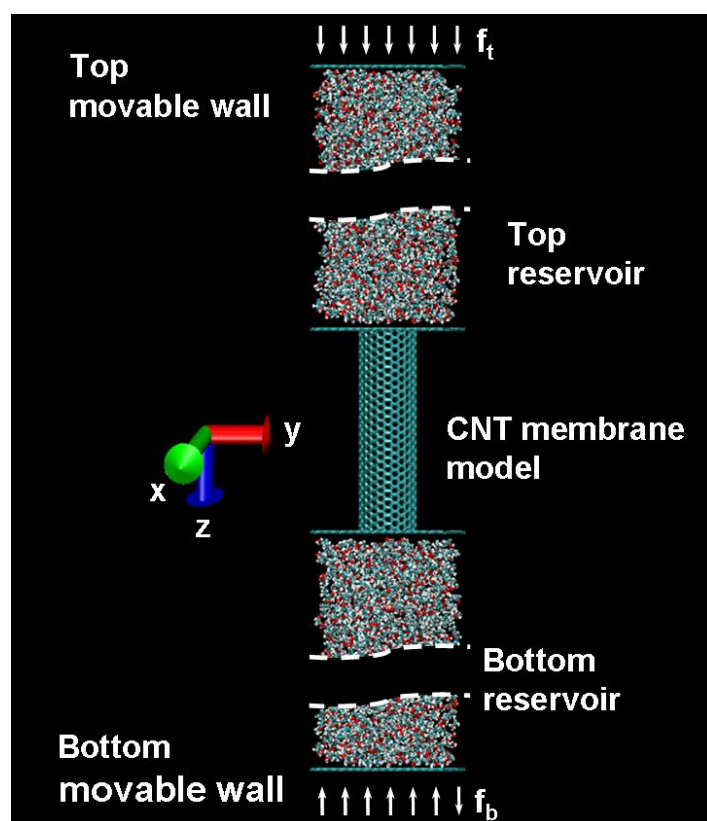
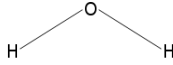
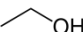
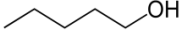
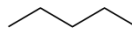
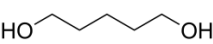
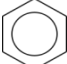


Figure 6.1 Perspective snapshots of the simulation at the beginning state for simulating ethanol transport. Shown is the beginning empty CNT membrane model connecting two liquid filled reservoirs (ethanol molecules for example) with the two graphene sheets acting as movable walls where the force, f_t or f_b , is applied on each carbon atom of the top or bottom wall. Carbon atoms in green, hydrogen atoms in white, and oxygen atoms in red.

6.4. Results and Discussion

Water and five organic (ethanol, 1-pentanol, pentane, 1,5-pentanediol, and benzene) flows are used to investigate the effects of liquid properties and membrane pore size on pressure-driven liquid transport. The physical properties of the six liquid molecules are listed in Table 6.1. As shown in Table 6.1, the six molecules have different molecular masses, viscosities, and molecular structures.

Table 6.1 Physical properties of liquid molecules.

Molecule	Molecular formula	Chemical structure	Molecular mass (kg/kmol)	Viscosity ^a [25-27] $\times 10^3$ (Pa · s)	Density ^b (kg/m ³)
Water	H ₂ O		18	0.854	997
Ethanol	C ₂ H ₆ O		46	1.016	785
1-Pentanol	C ₅ H ₁₂ O		88	3.504	814
Pentane	C ₅ H ₁₂		72	0.212	626
1,5-Pentanediol	C ₅ H ₁₂ O ₂		104	87.5	994
Benzene	C ₆ H ₆		78	0.579	874

^aViscosity data are given for pure liquids at 300 K and 1 atm.

^bDensity data are given for pure liquids in the standard state (25 °C and 100 kPa).

The liquids were selected as follows. The first three molecules have the structure ROH where R = H for water and then ethanol, and 1-pentanol which form a series of alcohol molecules (assuming water as a trivial case of an alcohol) with different chain lengths (molecular mass/size). The pentane, 1-pentanol, and 1,5-pentanediol molecules all have a five-carbon length but have quite different liquid viscosities. The benzene as

an aromatic compound has a ring structure and a molecular mass of 78 kg/kmol which is similar to pentane with a linear structure (72 kg/kmol), so the comparison between benzene and pentane can tell the different transport properties caused by the molecular configuration. Therefore, the effects of molecular mass/size, viscosity and configuration can be investigated these six liquids (Table 6.1). The results of water flows are from our former work,^[17] and the analyses of the simulation results for each organic flow are as presented below.

Every single molecule is viewed as containing several parts according to the total atom number, and each atom of the molecule has a fractional number based on the atom size over the molecule size. The simulation flow rate ‘molecule/ns’ is defined by the total fractional number of atoms passing through the membrane in a unit simulation time. The fractional number of atoms passing through the membrane are counted every 0.1-10 ns (the interval time depends on the liquid flow rate) and plotted as a function of the simulation time. The slope of the linear profile (through the origin) gives the average flow rate for the simulation time. For each flow rate, the estimated error is represented by the standard error of the slope with the assumption of uncorrelated data (a correlation time less than the interval time); an example of the error analysis is shown in our former work.^[16] The simulation flux is the flow rate per membrane area (molecule/ns/nm²) which is converted to the conventional flux (‘m³/(m²·s)’ or equivalently ‘m/s’) for each flow.

The theoretical flux is calculated by the Navier-Stokes equations for describing a liquid passing through a straight cylindrical channel, also called the Hagen-Poiseuille equation:

$$J_w = L_p \Delta P = \frac{r_p^2}{8\eta(L_z/A_K)} \Delta P \quad (6.1)$$

$$A_K = \frac{\pi \cdot r_p^2}{A_{mem}} = \frac{\pi \cdot r_p^2}{L_x \cdot L_y}$$

where L_p is the pure liquid permeability coefficient, r_p is the pore radius of the membrane, η is the viscosity of the liquid, L_z/A_K is the ratio of the membrane effective thickness to the membrane porosity, ΔP is the pressure difference, and A_{mem} is the membrane square area and equals the x direction length (L_x) times the y direction length (L_y).

The CNT is divided equally into several sections along the radial and the flow directions to get the density distributions: the radial section is a thin annular section except for the pore center section; the flow direction sections include four square cuboids sections in the top liquid reservoirs, three cylindrical sections in the pore, and three square cuboids sections in the bottom liquid reservoirs. The number density value of each section from the trajectory data is calculated by averaging the total fraction numbers of atoms in the section; the time average value of density in each section is calculated by averaging all data collected in the simulation time. The statistical error of each density data point is calculated directly from the standard deviation of the sampled mean by using the number of trajectory data, under an assumption that the trajectory data saved every 1000 steps would be uncorrelated.. The details of the error analysis was shown in our former work.^[16]

6.4.1. The effect of liquid properties

Six liquids with different liquid properties (molecular masses, viscosities, and

linear/ring structures) are used to investigate the relationship between the liquid transport properties and the liquid properties. The (12, 12) CNT is used to construct the membrane model in the NEMD simulation system (as shown in Table 6.1), and these six liquids are simulated to passing through the same CNT membrane at the same pressure difference (8.0 MPa).

A. Flux

Figure 6.2 shows the simulation flux and theoretical flux for each liquid, where the simulation flux is higher than the theoretical flux except for benzene. Our previous work has explained the reasons for the exceptionally high water flux, which are the narrow pore size, the very smooth CNT surface, and the weak interactions between water molecules and the CNT surface.^[16] This reason is also to explain the fast organic liquids through the CNT. The reason for the unique properties of benzene liquid will be discussed later.

For the small molecules, the molecular mass is related to the molecular size, which affects liquid transport due to the nanoscale pore size of the CNT membrane. The pore size is comparable to the molecular size, particularly for the liquids with higher molecular masses. The relationship between the simulation flux and the molecular mass is presented in Figure 6.3. In general, the liquid of a higher molecular mass results in a lower flux, due to the larger molecular size; while the pentane liquid shows the highest flux even the water liquid have the lowest molecular mass. For the water and simple alcohols (ethanol and 1-pentanol) liquids, represented by the molecular structure with one

–OH group, the length of the molecule chain increases but the simulation flux decreases from water to 1-pentanol, as shown in Figures 6.2 and 6.3. This decreasing flux from water to 1-pentanol is in a linear trend from the simulation flux as a function of the molecular mass, as shown by the solid trend line in Figure 6.3.

As shown in the Hagen-Poiseuille equation, the liquid flux is an inverse proportion of the liquid viscosity; and Table 6.1 shows the liquid viscosities are in a wide range from $0.21 \times 10^{-3} \text{ Pa} \cdot \text{s}$ to $88 \times 10^{-3} \text{ Pa} \cdot \text{s}$. Figures 6.4 and 6.5 shows the relationships between the simulation flux and the viscosity where it is observed again that the Hagen-Poiseuille equation fails to predict the fast flow (except for the benzene flow) passing through the CNT membrane. The ratio of the simulation flux to the theoretical flux as a function of the reciprocal of the viscosity is shown in Figure 6.5, where the water flow has the highest enhancement and the benzene flow does not show an enhanced flux.

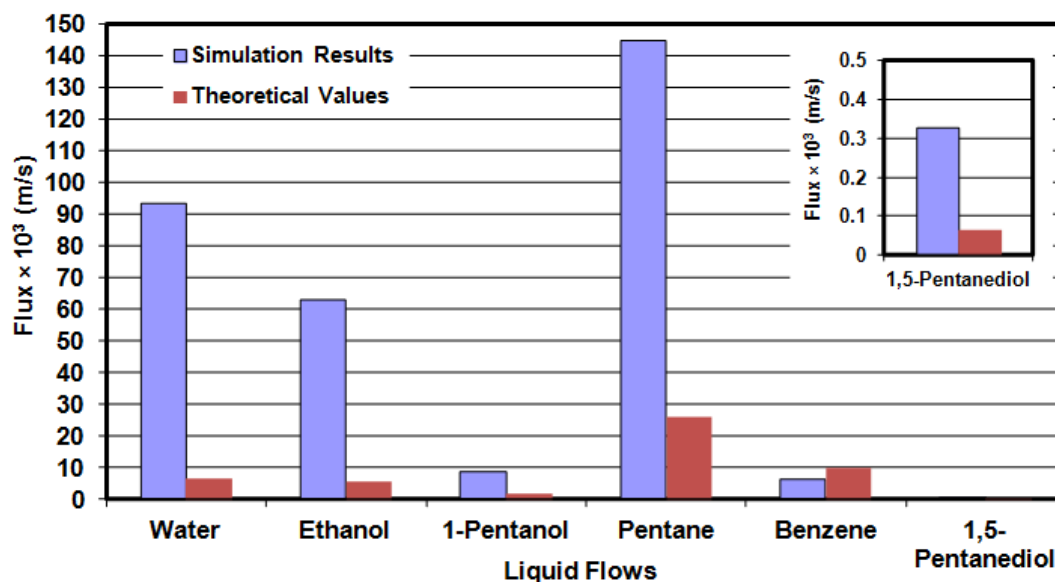


Figure 6.2 Bar chart of simulation and theoretical volume fluxes (m/s) for the six liquids through the (12, 12) CNT membrane; $L_z = 6.0 \text{ nm}$; $\Delta P = 8.0 \text{ MPa}$; $T = 300 \text{ K}$. The statistical error for each flux data is less than 10%. The theoretical flux is calculated from the Hagen-Poiseuille equation (Eqn. (6.1)).

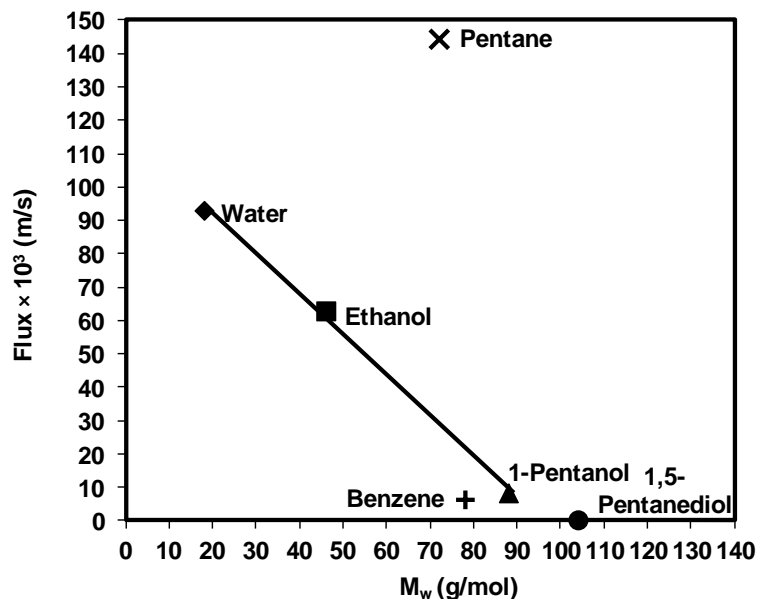


Figure 6.3 Simulation volume flux (m/s) as a function of the molecular mass for the six liquids through the (12, 12) CNT membrane; $L_z = 6.0$ nm; $\Delta P = 8.0$ MPa; $T = 300$ K. The statistical error for each data point is less than 10%. The solid line is the linear trend based on the simulation results.

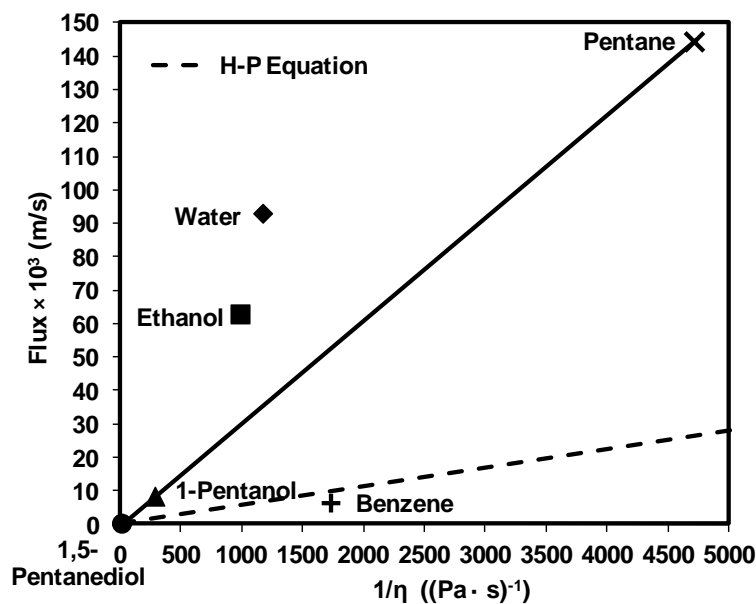


Figure 6.4 Simulation and theoretical volume fluxes (m/s) as a function of the inverse liquid viscosity, for the six liquids through the (12, 12) CNT membrane; $L_z = 6.0$ nm; $\Delta P = 8.0$ MPa; $T = 300$ K. The statistical error for each flux data is less than 10%. H-P Equation refers to the Hagen-Poiseuille Equation (Eqn. (6.1)) represented by the dashed line, and the solid line is the trend, for 5 carbon molecules, based on the simulation results.

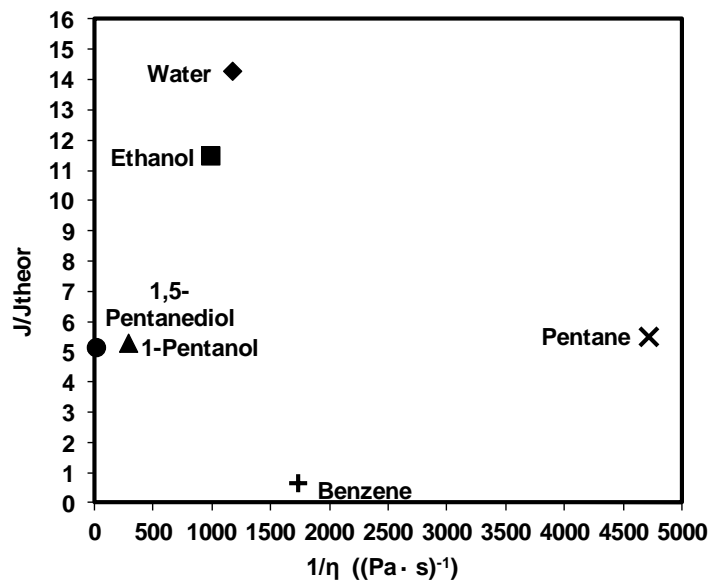


Figure 6.5 The ratio of the simulation flux to the theoretical flux as a function of the inverse liquid viscosity, for the six liquids through the (12, 12) CNT membrane; $L_z = 6.0$ nm; $\Delta P = 8.0$ MPa; $T = 300$ K. The statistical error for each flux data is less than 10%. The theoretical flux is calculated from the Hagen-Poiseuille equation (Eqn. (6.1)), and the dashed line represents the simulation flux equal to the theoretical flux.

Corresponding to the Hagen-Poiseuille equation, the simulation flux decreases with increasing the liquid viscosity from pentane to 1-pentanol. The higher the liquid viscosity, then the higher the resistance force is applied on the liquid and hence the harder it is for the liquid to pass the CNT membrane. So the simulation flux decreases with increasing liquid viscosity and approaches the theoretical value. Due to the high viscosity of 1,5-pentenediol (87.5×10^{-3} Pa·s), the lowest flux is observed and is only a fraction of the simulation flux for any of the liquids. However, the lowest 1,5-pentenediol is consistently higher than the theoretical flux (shown in Figures 6.2 and 6.5) and the reason is as explained above.

For the water, ethanol, and 1-pentanol liquids, the liquid viscosity also increases with increasing molecular mass as listed in Table 6.1. The decreasing simulation flux from

water to 1-pentanol (shown in Figure 6.4) may be caused by a combination of the increasing molecular size and liquid viscosity, as the molecular mass increases. Moreover, the ratio of the simulation flux to the theoretical flux decreases with increasing molecular mass from water to 1-pentanol, as shown in Figure 6.5. For these three liquids with simple linear structures, increasing the molecular mass gives rise to increasing the molecular size. As mentioned above, the nanoscale pore size of the CNT membrane is one of the reasons for the enhanced liquid and the pore size is comparable to the molecular size of liquid. Therefore, a liquid of a smaller molecular size to pass through the CNT membrane is easier to be enhanced and shows a higher enhancement of the simulation flux, like the water or ethanol flow in this work. It can be expected an organic flow of a high molecular mass (a large molecular size) could exhibit a simulation flux close to the theoretical flux when passing through the nanoscale pore of a CNT membrane.

For the pentane, 1-pentanol, and 1,5-pentanediol liquids, the three molecules has different end groups but similar chain lengths, resulting in similar molecular sizes. The molecular masses of these three organic compounds are in a narrow range from 72 g/mol to 104 g/mol, while the liquid viscosities are quite different. Therefore, the flux is significantly dependent on the liquid viscosity, as shown by the solid trend line in Figure 6.4. These three liquids shows a decreasing simulation flux with increasing liquid viscosity; while the enhancements of these three liquids are all about 5.5, as shown in Figures 6.5. Remind the decreasing enhancement with increasing molecular mass for the water, ethanol, and 1-pentanol liquids, the similar enhancements of the pentane,

1-pentanol, and 1,5-pentanediol liquids suggests that the enhanced flow through the CNT membrane is more dependent on the molecular mass (the molecular size) than the liquid viscosity.

Among these six liquids, only the benzene liquid has a lower simulation flux than the theoretical flux. As discussed above, the molecular mass and the liquid viscosity both can affect liquid transport through the CNT membrane. The molecular mass and the liquid viscosity of benzene are both similar to pentane, while the benzene flux is much lower than the pentane flow. The key difference between benzene and pentane is the molecular structure: pentane of a linear structure, and benzene of an aromatic ring structure. The aromatic ring of benzene is formed by twelve atoms linked in the same plane, and the diameter of the benzene molecule is close to the nanoscale pore size of the CNT. Consequently, the benzene flow is harder to enter and pass the CNT membrane than the liquid of a linear structure, like the pentane liquid.

Recently, pressure-driven water and organic flows through membranes has been measured experimentally, and these CNT membranes are experimentally produced from aligned arrays of multi-walled or double-walled CNTs.^[28-30] Majumder^[28, 29] fabricated CNT membranes using multi-walled CNTs with a pore diameter of 7 nm and a length of 126 μm to experimentally investigate liquid (water, ethanol, *iso*-propanol, hexane, and decane) transport through the CNT membranes at 1bar. The experimental flow velocity obtained were three to four orders of magnitude faster than the theoretical velocity calculated by using Eqn. (6.1). Similarly, Du^[30] found that CNT membranes, fabricated from double-walled CNTs with a pore diameter of 10 nm and a length of about 4000 μm ,

exhibited experimental liquid (water, ethanol, hexane, and dodecane, and N,N-dimethylformamide) flux at least two orders of magnitude faster than the theoretical value. The experimental enhancement of the water and organic liquids are more than ten times higher than the simulation results shown in Figure 6.5. In this study, the CNT membranes are modeled by using a single CNT with a nanoscale pore radius (0.643 nm) and length (6.0 nm), so possible reasons for the difference between simulation results and the experimental results relate to the different pore sizes, membrane thicknesses, and membrane configurations (a single CNT or aligned arrays of CNTs). Other experimental studies about water transport through CNTs or CNT membranes have been introduced and discussed in our previous work.^[16]

Although the simulation and experimental studies show quite different liquid enhancements, Majumder^[28, 29] and Du^[30] both found that the ethanol flux is about 61% and 0.02% of the water flux, respectively, which is similar to the lower ethanol flux (68% of the water flux, shown in Figure 6.2) in this study. Moreover, Majumder's work showed that the liquid flow became slower from water, ethanol to *iso*-propanol.^[28, 29] This decreasing trend corresponds to the decreasing liquid flux from water, ethanol, to 1-pentanol. For the hexane and decane liquids investigated by Majumder, the hexane flux is about half of the water flux while the decane flux is lower than 10% of the water flux.^[28, 29] As the viscosity and flux of hexane are both lower than water, Majumder concluded that liquid flow is faster for more hydrophilic liquids (like water and ethanol) than alkane liquid (like hexane).^[28] On the contrary, Du^[30] found that the hexane and dodecane fluxes are 167% and 41% higher than the water flux, respectively, through

experimental studies. Du^[30] also did MD simulations to investigate water and hexane flows passing through a single-walled carbon nanotube of 5.0 nm in length and 4.0 nm in diameter, and the simulation results showed that the hexane flow is faster than the water flow. The faster hexane fluxes from the experimental and simulation studies by Du^[30] are similar to the higher pentane flux in this study, where the pentane flux is the highest value among the six liquids and about 1.5 times of the water flux. As mentioned above, the different results between the simulation studies and the experimental studies may be caused by the different pore sizes, membrane thicknesses, and membrane configurations.

So far, it is not practical to do MD simulation studies for liquid flows passing a CNT membrane having such a membrane thickness as the experimentally produce membrane, due to computational limitations. However, our simulation studies show some similarities to the experimental studies as discussed above, and these similarities indicate that MD simulations can provide some significant results for organic liquids through CNT membranes.

B. Radial-direction distributions

Figure 6.6 shows the density distributions along the radial direction of each liquid in the CNT, where the density distributions are all in an oscillatory profile. As discussed in our previous work of water transport through CNT membranes,^[16] the oscillatory density distribution is caused by the well-ordered arrangement of water molecules in the CNT and each symmetrical density pair corresponds to a cylindrical water ring paralleled with the CNT pore surface. As shown in Figure 6.6, the water flow shows the density distribution with two pairs of density peaks, suggesting two water rings formed in the

CNT. Except for the benzene flow, other four organic flows all show a three-peak density distribution with the highest peak in the pore center, which indicates that the organic molecules in the CNT cannot be well-ordered in two liquid rings like water.

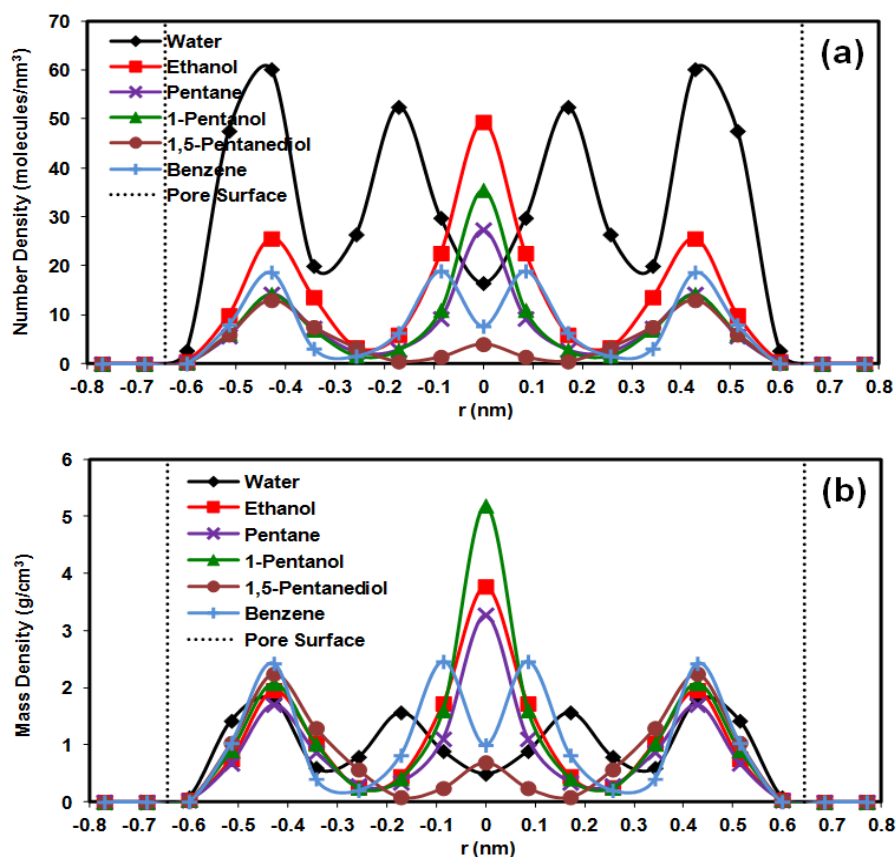
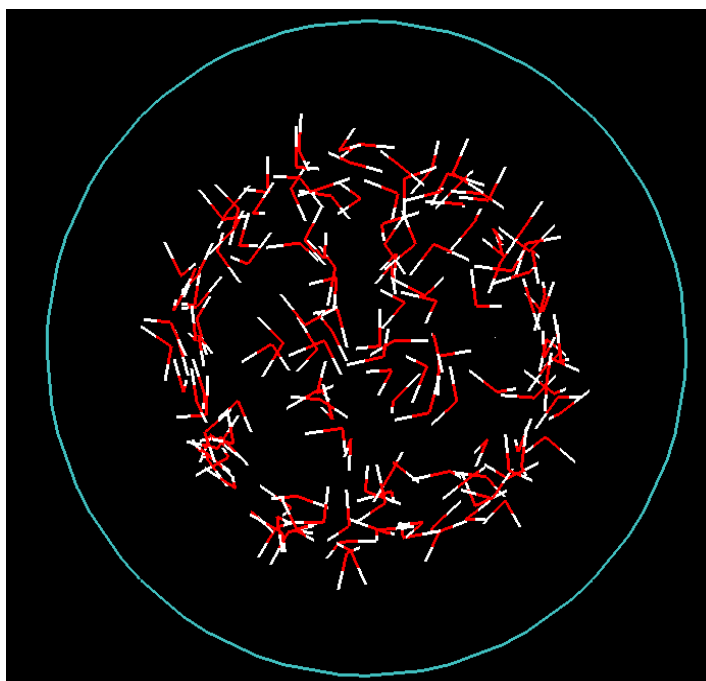


Figure 6.6 Density distributions, (a) molecule number density and (b) mass density, along the radial direction for the six liquids: density as a function of r ; values are averaged over a thin annular section in the pore at r (excluding the entrance and exit regions). The CNT membrane is modeled by the (12, 12) CNT, $L_z = 6.0$ nm; $\Delta P = 8.0$ MPa; $T = 300$ K. The statistical error for each data point is less than 1%. The solid lines are the trend curves based on the simulation results, and the dotted lines are the pore surface represented by the effective pore radius (0.643 nm).

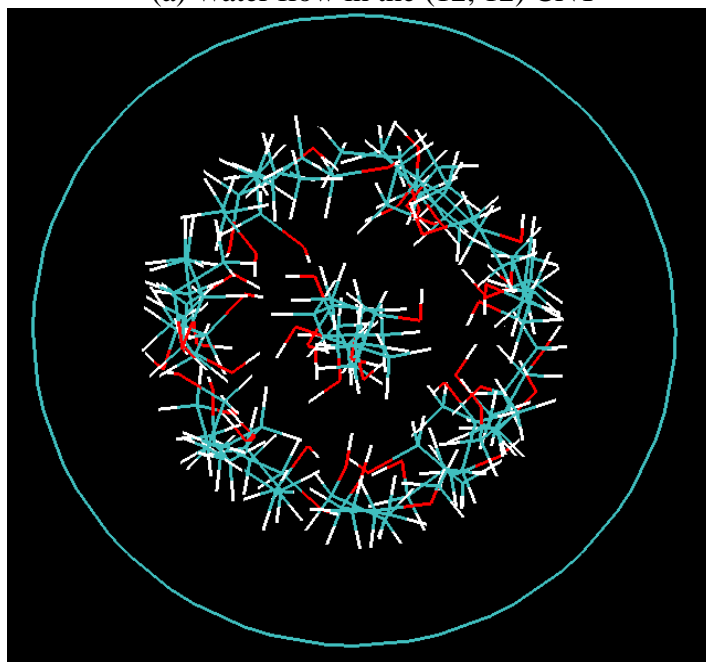
Figure 6.7 shows the snapshot of the cross section view of each flow in the (12, 12) CNT: a liquid ring near the CNT surface exists for each flow, quadruple water molecules are formed as a smaller inner ring in the center of the CNT, and organic molecules are aligned along the flow direction in a single-file configuration in the center

of the CNT. For the liquid of a longer linear molecular structure (like the 1-pentanol, pentane, or 1,5-pentanediol flow), the linear liquid molecules near the pore surface tend to be parallel to the pore surface (not to align along the axial direction) and be arrayed together in a ring. The snapshots of the cross section view correspond to the density distributions: for each flow, the outer peak pair is caused by the liquid ring near the pore surface; the inner peak pair of the water density distribution is caused by the inner water ring, and the center peaks of the density distributions for the 1-pentanol, pentane, or 1,5-pentanediol flow are caused by the single-file flows in the pore center.

The cross section view of the benzene flow in the CNT in Figure 6.7(f) shows a benzene ring near the pore surface and a single-file arrangement of the benzene molecules in the pore center. This configuration, one ring and one chain of the benzene flow in the CNT, is the same as the other organic flows shown in Figure 6.7(b)-(d). The aromatic ring planes of the benzene molecules in the pore center tend to be perpendicular to the flow direction, resulting in the two density peaks in the pore center (Figure 6.6). Therefore, the four-peak density distribution of the benzene flow does not suggest two liquid rings formed in the CNT (like the water flow in the CNT). Moreover, Figure 6.7(f) shows the aromatic ring planes of the benzene molecules near the pore surface are almost paralleled to the hexagon rings of the CNT. The benzene flow through the CNT membrane is dependent on the aromatic diameter for the molecules near the pore surface and the aromatic ring area for the molecules in the pore center. The large molecular size of benzene is one possible reason for the slow flow rate, and the unique π -bond structure of benzene is the other reason as discussed below.

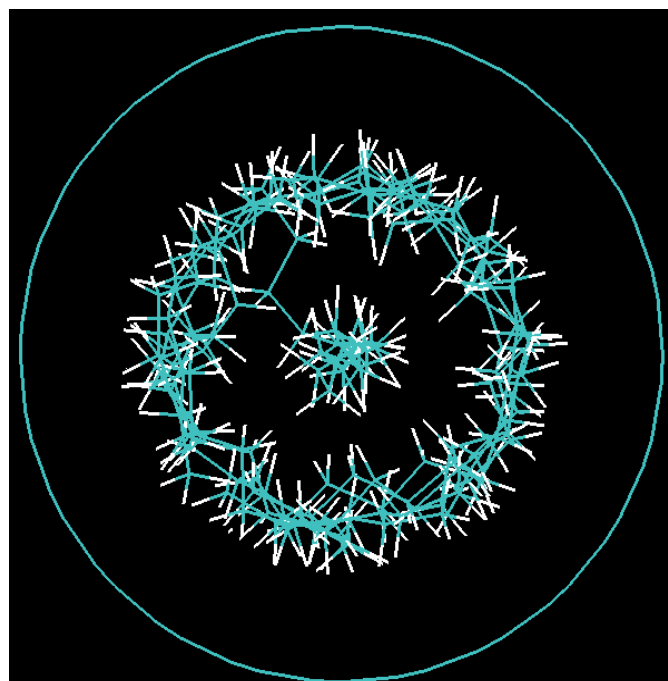


(a) Water flow in the (12, 12) CNT

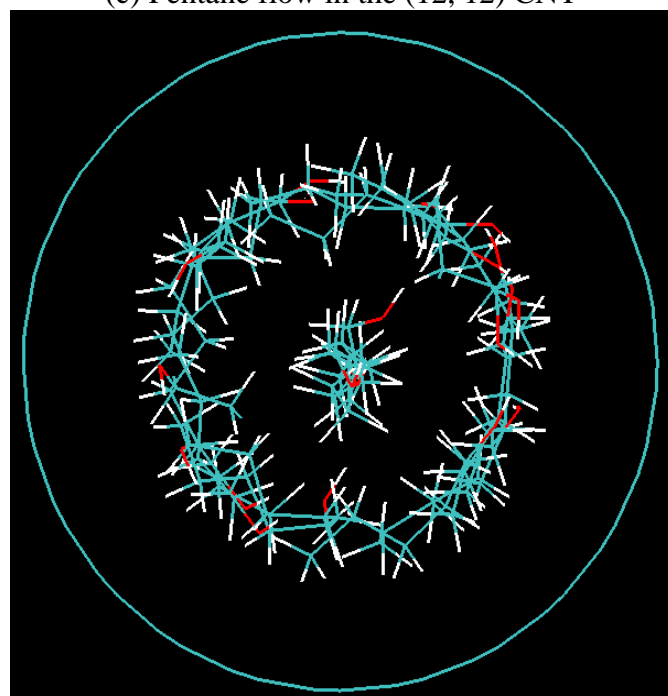


(b) Ethanol flow in the (12, 12) CNT

Figure 6.7 Orthographic snapshots (stick figures) of liquid molecules in the CNT membrane modeled by (12, 12) CNT: (a) water, (b) ethanol, (c) pentane, (d) 1-pentanol, (e) 1,5-pentanediol, and (f) benzene flows, as shown in Table 6.1. Molecules are represented by bonds and in different color: carbon atoms in green, hydrogen atoms in white, and oxygen atoms in red.

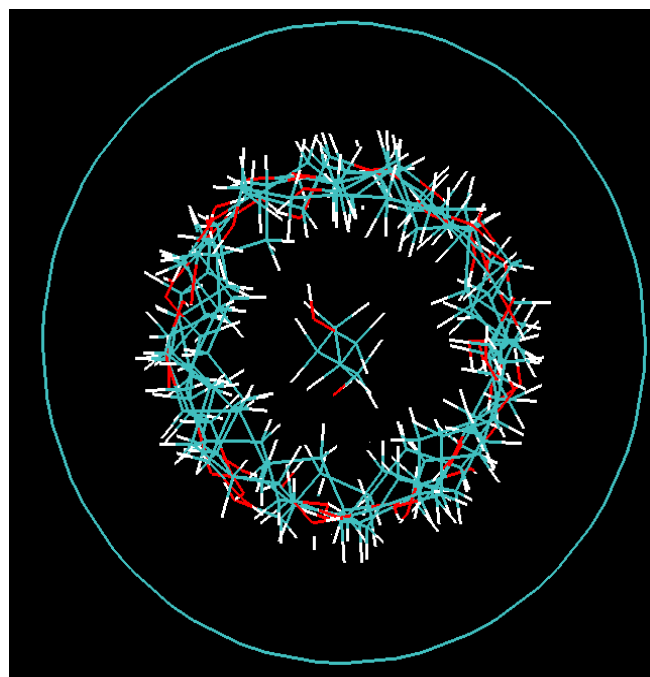


(c) Pentane flow in the (12, 12) CNT

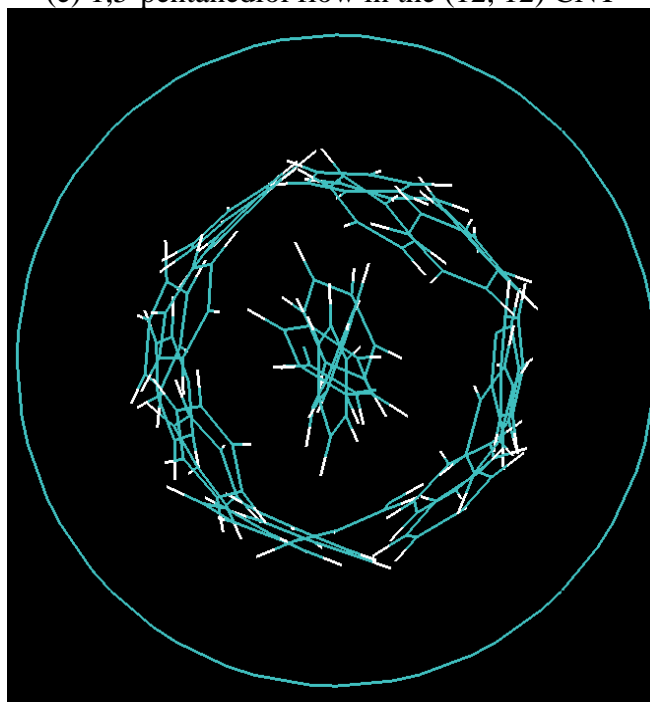


(d) 1-pentanol flow in the (12, 12) CNT

Figure 6.7 Orthographic snapshots (stick figures) of liquid molecules in the CNT membrane modeled by (12, 12) CNT: (a) water, (b) ethanol, (c) pentane, (d) 1-pentanol, (e) 1,5-pentanediol, and (f) benzene flows, as shown in Table 6.1. Molecules are represented by bonds and in different color: carbon atoms in green, hydrogen atoms in white, and oxygen atoms in red.



(e) 1,5-pentanediol flow in the (12, 12) CNT



(f) Benzene flow in the (12, 12) CNT

Figure 6.7 Orthographic snapshots (stick figures) of liquid molecules in the CNT membrane modeled by (12, 12) CNT: (a) water, (b) ethanol, (c) pentane, (d) 1-pentanol, (e) 1,5-pentanediol, and (f) benzene flows, as shown in Table 6.1. Molecules are represented by bonds and in different color: carbon atoms in green, hydrogen atoms in white, and oxygen atoms in red.

The hexagon rings of benzene and the CNT are almost the same: each ring is composed of six carbon atoms bonded entirely by sp^2 bonds, and the C–C bond lengths of the benzene molecule and the CNT are the same. As shown in Figure 6.7(f), the aromatic rings of the benzene molecules near the pore surface parallel to the hexagon carbon rings of the CNT. The paralleled two layers of hexagon carbon rings can form a structure like a double-walled CNT, which is quite stable due to the intermolecular interactions at an approximate interlayer distance. This stable two-layer structure of the benzene flow in the CNT can be viewed as the benzene molecules sticking on the pore surface and decreasing the pore size, since only the molecules in the pore center can easily pass through the CNT membrane without the stable intermolecular interactions. Therefore, the slow benzene flow, even lower than the theoretical flux as shown in Figures 6.2 and 6.4, is caused by the large molecular size and π -bond structure of benzene.

The snapshots in Figure 6.7 shows that the radial density distribution of liquid molecules in the CNT is dependent on the difference between the liquid molecular size and the pore size of the CNT membrane. The molecular size of any of the organic liquids is larger than water, and the number of liquid molecules in the CNT decreases with increasing the molecular size. Therefore, the water flow shows the highest density profile and the ethanol flow shows the second highest density profile, in terms of the molecule number density as shown in Figure 6.6(a). With considering the different molecular masses of these liquids, the mass density distributions in Figure 6.6(b) show that the density peaks near the pore surface become similar for these different liquids.

The liquid molecules near the pore surface are arrayed tightly due to the larger space than in the pore center and the tight arrangement exists for each liquid in the CNT, as shown in Figure 6.7. Therefore, the mass density values of the outer density peaks are similar for different liquids at the same radial position near the pore surface.

The liquid viscosity can strongly affect the liquid flux as discussed above, but has little influence on the liquid density distribution along the radial direction (as shown by the similar density profiles in Figure 6.6). For the pentane, 1-pentanol, and 1,5-pentanediol liquids, the key difference among the radial density distributions of these three flows is the density values in the center of the CNT: the density values of the 1-pentanol and 1,5-pentanediol flows are the highest and lowest values, respectively. The one -OH end group of the 1-pentanol molecule can form hydrogen bonds between molecules in the CNT, giving rise to a denser configuration than the pentane flow without the hydrogen bond effect. The lowest density values of the 1,5-pentanediol flow in the pore center are probably because the viscosity is so high that it is difficult for the 1,5-pentanediol molecules to fully fill the narrow space within the outer liquid ring in the pore center. The snapshot of the 1,5-pentanediol flow in Figure 6.2(e) shows only one molecule in the pore center, matching the lowest density values. The liquid molecules in the CNT is determined by the molecular size and pore size but not the liquid viscosity, consequently the little effect of liquid viscosity on the density distribution is observed.

C. Flow-direction distributions

To compare the nanoflow formed in the CNT with the bulk flows in the liquid

reservoirs, the density distributions along the flow direction for the six liquids are shown in Figure 6.8. For the water, 1,5-pentanediol, or benzene liquid, the density profile in the CNT is lower than that in the top or bottom water reservoir; and for any of the other three liquids (ethanol, pentane, and 1-pentanol), the density profile in the CNT is higher.

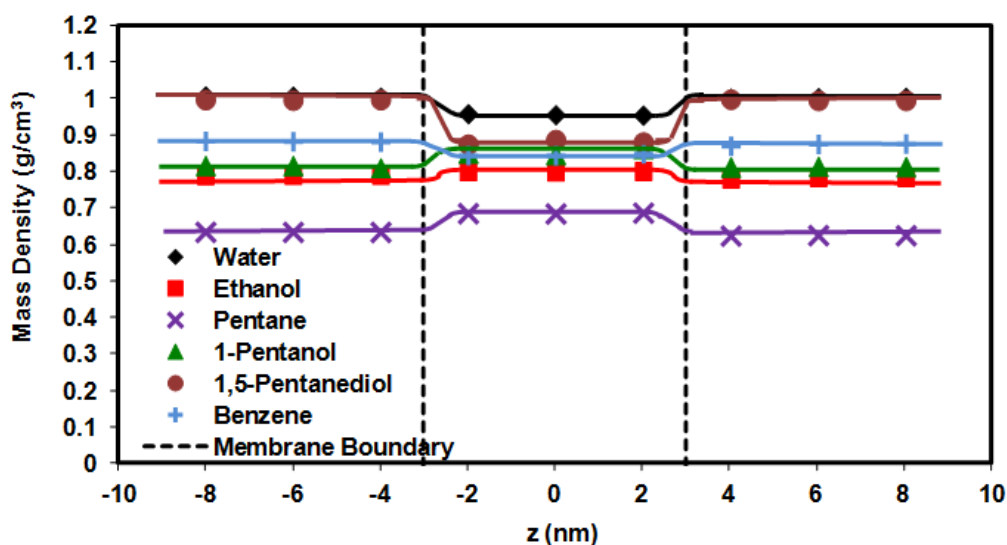


Figure 6.8 Density distributions, (a) molecule number density and (b) mass density, along the flow direction for the water, ethanol, and 1-pentanol flows: density as a function of z ; values are averaged over a thin section at z (cylindrical sections in the pore and cuboid sections in the water reservoirs). The CNT membrane is modeled by the (12, 12) CNT, $L_z = 6.0$ nm; $\Delta P = 8.0$ MPa; $T = 300$ K. The statistical error for each data point is less than 1%. The solid lines are the trend curves based on the simulation results. The dashed lines are the membrane boundaries along z direction separating the system in three parts from left to right: the top reservoir, the pore of the CNT membrane, and the bottom reservoir.

The lower densities of water in the CNT is caused by the fewer hydrogen bonds between water molecules in the CNT than in the water bulk flow; and the lack of hydrogen bonds may be the reason for the low density of 1,5-pentanediol in the CNT. The two hydroxyl groups of 1,5-pentanediol can form more hydrogen bonds between

1,5-pentanediol molecules in the bulk flow than in the CNT, since the 1,5-pentanediol molecules cannot fully fill the CNT due to the high viscosity. Therefore, the 1,5-pentanediol flow exhibits higher densities in the reservoirs than in the CNT. For the benzene liquid in the CNT, the large molecular size and the configuration of benzene in the CNT (shown in Figure 6.7(f)) restrict the benzene molecules in the CNT to be as close as in the bulk flow, which contributes the lower density profile of benzene in the CNT. Among these three liquids, the density of 1,5-pentanediol in the CNT shows the largest decreasing trend, which may be caused by the highest viscosity of 1,5-pentanediol.

As discussed above, the liquid (ethanol, pentane, or 1-pentanol) of a linear molecular structure has a well-ordered arrangement of the liquid molecules in the CNT: a liquid ring near the pore surface and a single-file liquid chain in the pore center. This configuration of the liquid molecules in the CNT may be more ordered than in the bulk flow, resulting a denser nanoflow in the CNT. Except for the 1,5-pentanediol liquid, the liquid of a linear molecular structure show a denser flow in the CNT than in the bulk flow; and the denser flow in the CNT is not seen for the benzene liquid due to the aromatic ring structure of benzene. For the five organic liquids, the density difference between in the CNT and in the reservoirs is more dependent on the liquid viscosity or molecular structure than the molecular mass.

6.4.2. The effect of membrane pore Size

The effect of membrane pore size on the transport properties of pure water flows passing through the CNT membranes is investigated in our previous work.^[16] The

results show the water flux increases with increasing pore size and the configurations of the water flows in the CNT are strongly influenced by the pore size.

Above discussion are based on the results of the (12, 12) CNT. Other two CNT membranes are modeled by using (8, 8) and (10, 10) CNTs with the same length of 6.0 nm, respectively. The three CNT membranes have the same membrane thickness but differ in the pore size, as listed in Table 6.2. Ethanol, 1-pentanol, and benzene flows passing through the three CNT membranes are simulated at the same pressure difference of 8.0 MPa and the same temperature of 300 K, in order to study the effects of membrane pore size on the transport properties of the organic flows.

Table 6.2 Effective radii of the three CNTs.

CNT Type	Effective Radius, ^c r_p (nm)
(8, 8)	0.372
(10, 10)	0.507
(12, 12)	0.643

^cThe effective radius is the tube radius minus the van der Waals radius of carbon atom, where the tube radius is defined as the distance measured between the centers of carbon atoms and the pore center.^[11, 12]

The dependence of flux on the pore size is shown in Figure 6.9 for each organic flow. The simulation fluxes of the ethanol and 1-pentanol flows both increase with increasing pore size and are higher than the theoretical values calculated from the Hagen-Poiseuille equation, but the simulation flux of benzene flow fluctuates. Ethanol or 1-pentanol is in a linear molecular structure, and the transport is decided by the size difference between

the end group of the linear molecule and the pore of the CNT membrane as discussed above. Therefore, the pore size plays an important role in the transport of the organic flow of a linear molecular structure, and there is a slower pressure-driven flow through the CNT membrane with a smaller pore. Moreover, the ethanol flux is higher than the 1-pentanol flux for each CNT membrane, due to the smaller molecular size or molecular mass of ethanol, as explained above (the section 3.1). Due to the aromatic ring structure of benzene and the comparable size between benzene and the pore, increasing the pore size from 0.372 nm to 0.643 nm cannot strongly affect the benzene flux, which shows an irregular changing profile with respect to the three pore sizes. As shown in Figure 6.9, the benzene liquid passing through the (8, 8) CNT membrane is enhanced about 8 times of the theoretical flux. Increasing the pore size decreases the enhancement of benzene liquids: the benzene flux is similar to the theoretical flux for the (10, 10) CNT membrane, and is lower than the theoretical flux for the (12, 12) CNT membrane (as shown and discussed above).

Figures 6.10 and 6.11 show the radial density distributions and the snapshots of the cross section view of each organic flow in the three CNT membranes. For each flow, the density distributions show only one pair of symmetric density peaks for the smaller (8, 8) or (10, 10) CNT and one or two additional density peaks appearing in the pore center for the larger (12, 12) CNT. As the pore size increases from the (8, 8) CNT to the (12, 12) CNT, the outer density peaks of each organic flow move toward the pore surface, which indicates that the liquid molecules in the CNT prefer to locate near the pore surface and a liquid ring near the pore surface is formed in each CNT due to the liquid-CNT

interactions.

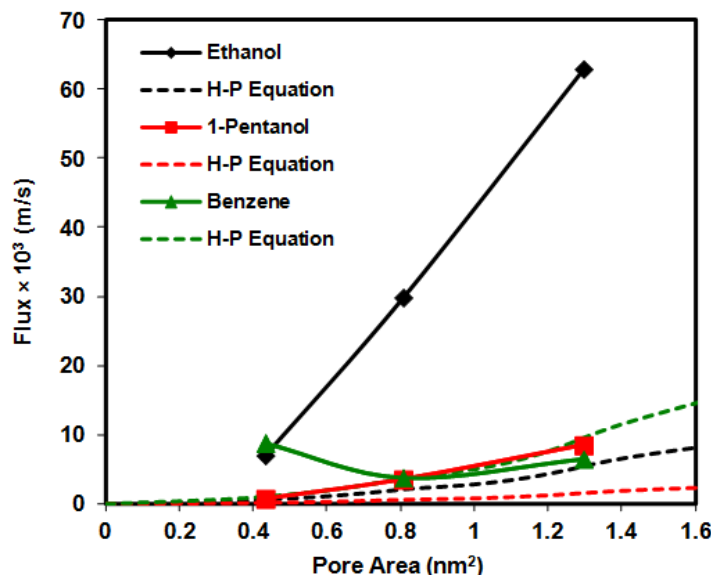


Figure 6.9 Simulation flux (m/s) as a function of the membrane pore size as represented by the pore area for the ethanol, 1-Pentanol, and benzene flows. The points are based on three CNT membranes modeled by (8, 8) CNT, (10, 10) CNT, and (12, 12) CNT, shown in Table 6.2; $L_z = 6.0$ nm; $\Delta P = 8.0$ MPa; $T = 300$ K. The statistical error for each data point is less than 10%. The solid line is the trend based on the simulation results. H-P Equation refers to the Hagen-Poiseuille Equation (Eqn. (6.1)), and the dashed line is the trend based on the Hagen-Poiseuille Equation.

For the ethanol or 1-pentanol flow, the liquid ring near the pore surface enlarges with increasing pore size and there are some liquid molecules in a single-file arrangement along the flow direction in the pore center of the (12, 12) CNT, as shown in Figures 6.11(a) and 6.11(b). It can be imagined that the number of the liquid rings formed in the CNT could increase from one to two with continually increasing pore size: a larger liquid ring near the pore surface and a smaller liquid ring in the pore center, like the two water rings formed in the (12, 12) CNT shown in Figure 6.7(a).

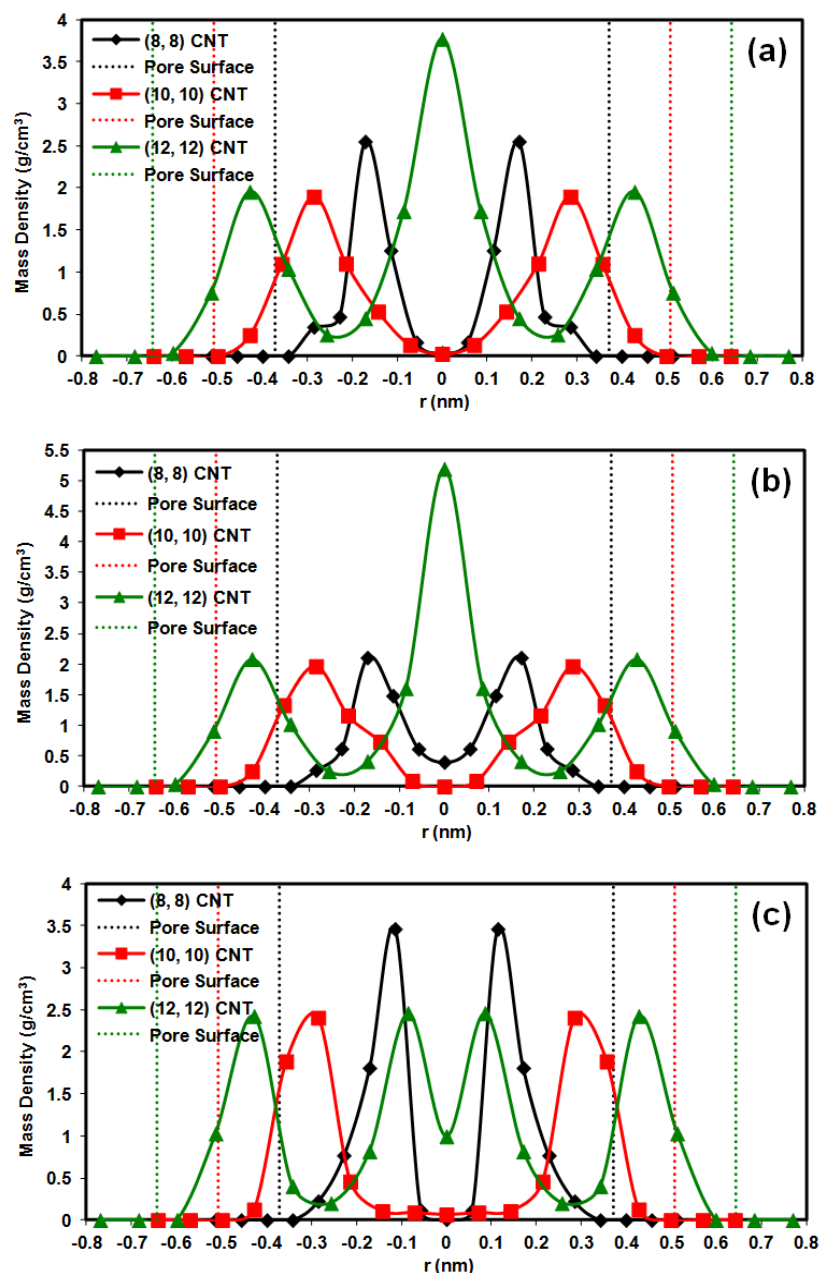


Figure 6.10 Effect of pore size on mass density distributions along the radial direction for the (a) ethanol, (b) 1-Pentanol, and (c) benzene flows, respectively: density as a function of r ; values are averaged over a thin annular section in the pore at r (excluding the entrance and exit regions). The points are based on three CNT membranes modeled by (8, 8) CNT, (10, 10) CNT, and (12, 12) CNT, shown in Table 6.2; $L_z = 6.0$ nm; $\Delta P = 8.0$ MPa; $T = 300$ K. The statistical errors for most data points are less than 1%, and the larger errors ($< 10\%$) are found for some data points in the pore center sections. The solid lines are the trend curves based on the simulation results, and the dotted lines are the pore surfaces represented by the effective pore radii (Table 6.2).

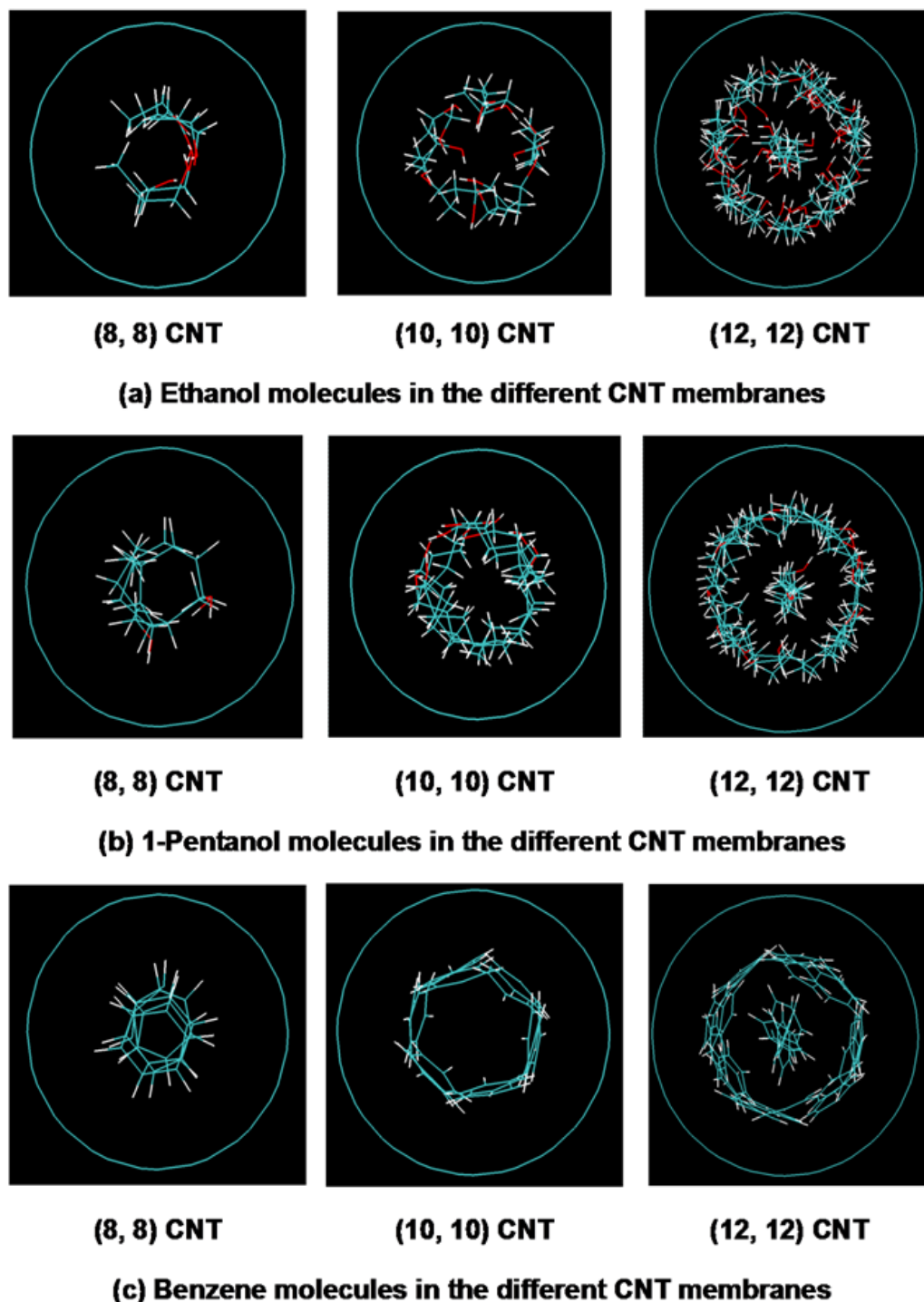


Figure 6.11 Orthographic snapshots (stick figures) of (a) ethanol, (b) 1-Pentanol, and (c) benzene molecules in the different CNT membranes: three CNT membranes are modeled by (8, 8) CNT, (10, 10) CNT, and (12, 12) CNT, shown in Table 6.2. Molecules are shown by bonds and in different color: carbon atoms in green, hydrogen atoms in white, and oxygen atoms in red.

As shown in Figure 6.11(c), there is a single-file benzene flow in the (8, 8) CNT and the ring planes of the benzene molecules are almost perpendicular to the flow direction. The benzene rings perpendicular to the flow direction contribute to the two symmetric density peaks of the benzene flow in the (8, 8) CNT in Figure 6.10(c). Due to the benzene flow in (8, 8) CNT forming a single-file flow but not a benzene ring parallel to the pore surface, the (8, 8) CNT membrane with the smallest pore shows the fastest benzene flow and the highest enhancement among the three membranes. The benzene planes almost fully fill the pore of the (8, 8) CNT shown in Figure 6.11(c), which indicates a benzene liquid may be highly rejected by a CNT membrane with a pore size smaller than the plane area of the benzene molecule.

With increasing the pore size to the (10, 10) CNT, a benzene ring near the pore surface formed by the benzene rings parallel to the pore surface is observed in Figure 6.11(c), corresponding to the two symmetric density peaks in Figure 6.10(c). The configuration of the benzene flow in the (12, 12) CNT is a combination of the benzene configurations in the (8, 8) CNT and the (10, 10) CNT: a single-file benzene flow in the pore center and a benzene ring near the pore surface in Figure 6.11(c); and four density peaks in Figure 6.10(c). As explained above, the stable intermolecular interactions between the benzene ring near the pore surface and the (12, 12) CNT result in the slow benzene flow passing through the (12, 12) CNT membrane. Similar stable intermolecular interactions exist between the benzene flow and the (10, 10) CNT, which is probably the reason for the slowest benzene flow observed for the (10, 10) CNT membrane. Therefore, an

enhanced liquid through the (10, 10) or (12, 12) CNT membrane cannot be observed for benzene. While the (12, 12) CNT shows a faster benzene flow than the (10, 10) CNT membrane, due to the additional single-file benzene flow formed in the pore center of the (12, 12) CNT. In summary, the ring molecular structure of benzene contributes the large steric hindrance effect and the special benzene–CNT interactions, which give rise to the low simulation flux and the irregular changing trend of the flux as a function of the three pore sizes, shown in Figure 6.9.

Figure 6.12 shows the density distributions along the flow direction for each organic flow, where the liquid density in the CNT increases with increasing pore size. As discussed above, the configuration of the liquid molecules in the CNT is strongly depended on the pore size. The larger space of a large pore allows more liquid molecules to fill the pore, resulting in the higher liquid density of the liquid molecules in the CNT of a larger pore. For each flow through the (8, 8) CNT membrane or the (10, 10) CNT membrane, the density profile in the CNT is lower than that in the liquid reservoirs. The liquid molecules in bulk solution can gather closely to form a dense solution, while fewer liquid molecules filling the (8, 8) CNT or the (10, 10) CNT are well-ordered but cannot form a nanoflow as dense as the bulk flow. As the pore size increases to the (12, 12) CNT, there are more liquid molecules in a well-ordered arrangement to tightly fill the larger pore, resulting in a denser flow in the (12, 12) CNT than the smaller CNTs. In particular, the ethanol or 1-pentanol flow in the (12, 12) CNT exhibits higher density values than in the reservoirs.

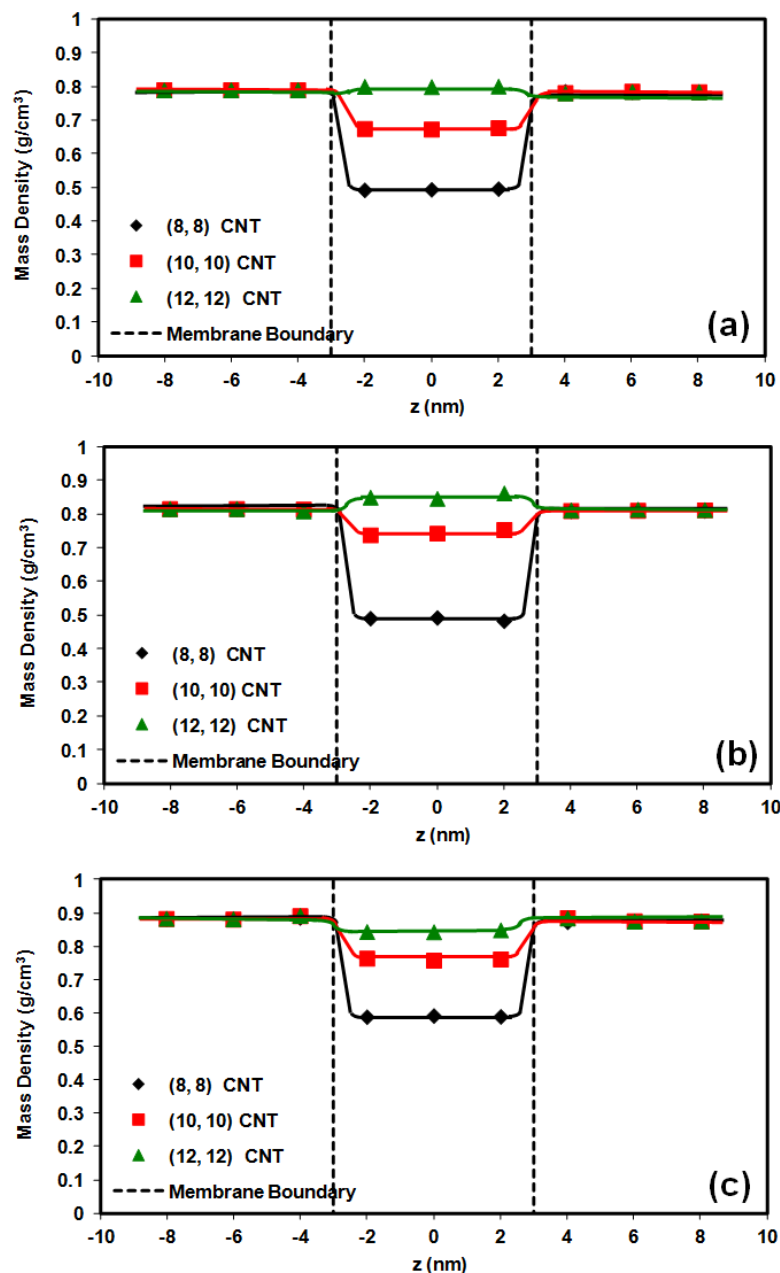


Figure 6.12 Effect of pore size on mass density distributions along the radial direction for the (a) ethanol, (b) 1-Pentanol, and (c) benzene flows, respectively: density as a function of r ; values are averaged over a thin annular section in the pore at r (excluding the entrance and exit regions). The points are based on three CNT membranes modeled by (8, 8) CNT, (10, 10) CNT, and (12, 12) CNT, shown in Table 6.2; $L_z = 6.0$ nm; $\Delta P = 8.0$ MPa; $T = 300$ K. The statistical error for each data point is less than 1%. The solid lines are the trend curves based on the simulation results. The dashed lines are the membrane boundaries along z direction separating the system in three parts from left to right: the top reservoir, the pore of the CNT membrane, and the bottom reservoir.

6.5. Conclusions

This work is to study pressure-driven organic flows through CNT membranes by NEMD simulations. Water flow and five organic flows (ethanol, 1-pentanol, pentane, 1,5-pentanediol, and benzene flows) are used to investigate the effects of liquid properties and membrane pore size on the transport phenomenon, including flux and density distributions along both the radial and flow directions.

Each liquid, except for the benzene flow, shows a much higher simulation flux than the theoretical flux calculated by the Navier-Stokes equation, due to the nanoscale pore size, the smooth surface of the CNT, and the weak liquid–CNT interactions. For the liquids of similar linear molecular structures, the liquid transport is dependent on the molecular mass: a higher molecular mass contributed to a lower simulation flux due to the large molecular size. For the liquids of similar molecular masses, the simulation flux decreases with increasing liquid viscosity due to the large resistance force on the viscous flow, corresponding to the Navier-Stokes equation. For the ethanol and 1-pentanol flows passing through different CNT membranes, the simulation flux of each flow increases with increasing pore size. The benzene flow exhibits a low simulation flux, which is close to the theoretical flux; and the benzene flux shows an irregular changing trend as a function of pore size, caused by the large molecular size and π -bond structure of benzene.

Each liquid in the CNT has an oscillatory density distribution along the radial direction, corresponding to the configuration of liquid rings formed in the CNT. The liquid in the CNT is affected by the liquid molecular structure and the pore size of the CNT membrane.

There are more liquid rings formed for the liquid of a smaller molecular size in the CNT membrane with a larger pore size. For the different organic liquids passing through the same CNT membrane, the density difference between the nanoflow in the CNT and the bulk flow in the reservoirs is dependent on the liquid properties (liquid viscosity, and molecular structure); for the same organic liquid passing through different CNT membranes, the liquid density values in the CNT increase with increasing pore size.

To sum up, the NEMD simulations are feasible to study the transport phenomenon of pure organic flows passing through CNT membranes under NF operating conditions. The dynamic behavior of the liquid transport can be directly obtained on a molecular scale, which can help to get a better understanding of the fundamentals of NF transport. This work can be expected to help in the improvement of NF processes for separating organic solutes – water mixtures.

References

- [1] S. A. Snyder, S. Adham, A. M. Redding, F. S. Cannon, J. DeCarolis, J. Oppenheimer, E. C. Wert, and Y. Yoon, *Desalination* **202** 156 (2006).
- [2] C. H. Huang and D. L. Sedlak, *Environ. Toxicol. Chem.* **20** 133 (2001).
- [3] L. D. Nghiem, A. I. Schafer, and M. Elimelech, *Environ. Sci. Technol.* **38** 1888 (2004).
- [4] Y. Yoon and R. M. J. *Membr. Sci.* **261** 76 (2005).

- [5] A. R. D. Verliefde, E. R. Cornelissen, S. G. J. Heijman, J. Q. J. C. Verberk, G. L. Amy, B. Van der Bruggen, and J. C. van Dijk, *J. Membr. Sci.* **32** 252 (2008).
- [6] C. Huang, K. Nandakumar, P. Choi, and L. W. Kostiuk, *J. Chem. Phys.* **124** 234701 (2006).
- [7] C. Huang, P. Choi, K. Nandakumar, and L. W. Kostiuk, *J. Chem. Phys.* **126** 224702 (2007).
- [8] C. Huang, P. Choi, K. Nandakumar, and L. W. Kostiuk, *Phys. Chem. Chem. Phys.* **10** 186 (2008).
- [9] C. Huang, P. Choi, K. Nandakumar, and L. W. Kostiuk, *J. Nanosci. Nanotechnol.* **9** 793 (2009).
- [10] H. Takaba, Y. Onumata, and S. Nakao, *J. Chem. Phys.* **127** 054703 (2007).
- [11] J. Goldsmith and C. C. Martens, *J. Phys. Chem. Lett.* **1** 528 (2010).
- [12] A. Noy, H. G. Park, F. Fornasiero, J. K. Holt, C. P. Grigoropoulos, and O. Bakajin, *Nano Today* **2** 22 (2007).
- [13] F. Zhu, E. Tajkhorshid, and K. Schulten, *Biophys. J.* **83** 154 (2002).
- [14] K. Leung and S. B. Rempe, *J. Comput. Theor. Nanosci.* **6** 1948 (2009).
- [15] J. Goldsmith and C. C. Martens, *Phys. Chem. Chem. Phys.* **11** 528 (2009).
- [16] L. Wang, R. S. Dumont, and J. M. Dickson, *J. Chem. Phys.* **134** 044102 (2012).
- [17] L. Wang, R. S. Dumont, and J. M. Dickson, "Comparison of two nonequilibrium molecular dynamics simulation systems for the pressure-driven water permeation through carbon nanotube membrane", *Microfluid. Nanofluid.* submitted (2012).

- [18] L. Wang, R. S. Dumont, and J. M. Dickson, “Nonequilibrium molecular dynamics simulation of pressure-driven water transport through modified carbon nanotube membranes”, to be submitted (2012).
- [19] L. Wang, R. S. Dumont, and J. M. Dickson, “Nonequilibrium molecular dynamics simulation of pressure-driven water transport through charged carbon nanotube membranes”, to be submitted (2012).
- [20] W. L. Jorgensen, J. Chandrasekhar, J. D. Madura, R. W. Impey, and M. L. Klein, J. Chem. Phys. **79** 926 (1983).
- [21] A. D. MacKerell, N. Banavali, and N. Foloppe, Biopolymers **56** 257 (2001).
- [22] K. Vanommeslaeghe, E. Hatcher, C. Acharya, S. Kundu, S. Zhong, J. Shim, E. Darian, O. Guvench, P. Lopes, I. Vorobyov, and A. D. Jr. MacKerell, J. Comput. Chem. **31** 671 (2010).
- [23] J. Phillips, R. Braun, W. Wang, J. Gumbart, E. Tajkhorshid, E. Villa, C. Chipot, R. D. Skeel, L. Kalé and K. Schulten, J. Comput. Chem. **26** 1781 (2005).
- [24] W. Humphrey, A. Dalke, and K. Schulten, J. Mol. Graphics **14** 33 (1996).
- [25] U. Kaatze, Radiat. Phys. Chem. **45** 539 (1995).
- [26] D. S. Viswanath, T. K. Ghosh, D. H. L. Prasad, N. V. K. Dutt, and K. Y. Rani, *Viscosity of Liquids: Theory, Estimation, Experiment, and Data (First Edition)*, (Springer, Netherlands, 2006).
- [27] G. Czechowski and J. Jadżyn, Z. Naturforsch. A **58a** 317 (2003).
- [28] M. Majumder, N. Chopra, R. Andrew, and B. J. Hinds, Nature **438** 44 (2005).

- [29] M. Majumder, N. Chopra, and B. J. Hinds, *ACS Nano* **5** 3867 (2011).
- [30] F. Du, L. Qu, Z. Xia, L. Feng, and L. Dai, *Langmuir* **27** 8437 (2011).

Chapter 7 Molecular Dynamics Simulations of Pressure-Driven Water Transport through Polyamide Membranes

7.1. Abstract

Molecular dynamics (MD) simulations are carried out to model amorphous aromatic polyamide (PA) membranes as nanofiltration (NF) membranes, and nonequilibrium molecular dynamics (NEMD) simulations are presented to study pressure-driven water flows passing through the PA membranes. The PA membrane is modeled as a cubic membrane composed of several linear PA polymer molecules, and the number of linear PA polymers in the membrane is selected to give different densities to the final membrane. The membrane structure is represented by the membrane density, fractional free volume (FFV), and free volume pore size. With increasing number of PA polymers in the membrane, the membrane density increases while the FFV and the pore size both decrease. The effects of membrane structure and pressure difference on water transport are investigated from 1.0 to 100 MPa pressure difference. The simulation results show that the water flux and the water permeability coefficient both decrease with decreasing pore size. When the pore radius of the membrane is smaller than 0.2 nm, the water flow is blocked by the membrane even at 100 MPa pressure difference. The membrane structures and the transport properties of the modeled PA membranes are compared with

the PA top layer of a commercial NF membrane, the FilmTec[®] NF 90 membrane. The comparisons shows that the simulation results of the modeled PA membrane are close to the experimental results of the real NF 90 membrane, and the deviations between the simulation and experimental results are acceptable. The MD/NEMD simulations are feasible to be used for studying pressure-driven water transport through an amorphous polymeric membrane on a molecular scale, and provide a direct way to reveal the free volume pore properties of the polymeric membrane.

7.2. Introduction

Membrane technology has been more and more important in many industry fields, especially in separation process and water treatment. One of the most popular membrane techniques for water treatment is nanofiltration (NF), which becomes increasingly competitive and superior to the traditional water treatment technology.^[1] NF membranes can be categorized by the materials into organic polymeric membranes, inorganic ceramic membranes, and organic/inorganic hybrid membranes. The polymeric NF membranes are usually fabricated in thin-film composite (TFC) membranes, and a TFC membrane consists of three layers, including an ultra-thin polymer coating, a porous interlayer usually made from polymers, and a non-woven polyester fabric. The top coating is an active layer to provide and decide the selectivity of the TFC membrane, and can be made from cellulose acetate, polyamide (PA), sulfonated polyethersulfone, sulfonated polysulfone, polyvinyl alcohol, polyphenylene oxide, polyethylenimine, and other polymers.^[2-4]

NF as a pressure-driven membrane separation process can effectively remove salts or organic solutes from water. Some traditional mathematical models have been applied to describe the separation and transport phenomenon of NF membranes.^[5-15] However, the transport mechanisms of NF processes have not been well understood so far; and these existing models have only been partially successful, as the models require the determination of adjustable parameters. Molecular dynamics (MD) simulations provide a new way to study a NF transport phenomenon without adjustable parameters and visualize the transport on a molecular scale.

A polymeric membrane should be modeled appropriately in order to simulate and study NF transport of the modeled polymeric membrane. For modeling polymers by MD simulations, two different simulation methods are generally used: one is a coarse-graining simulation in which a molecule model is represented by several groups of atoms and these groups as coarse-graining sites connected by bonds, the other is a full atomistic simulation in which a molecule model contains atomistic information for every atom. The coarse-graining MD simulation allows a longer time scale or time step and requires less high computational resource than the full atomistic MD simulation. It is hard to determine the empirical parameters for a coarse-grained polymer model, which should match appropriate experimental data or full atomistic simulations of the corresponding polymer. The full atomistic simulation requires many more calculations than the coarse-graining MD simulation, due to the larger number of intramolecular or intermolecular potential energies in the system. Thus, the full atomistic simulation can result in a good accuracy and reliability but need high computational cost.

Many successful works have been reported for modeling permeable polymers through MD simulations and studying gas transport in these modeled polymers, such as polycarbonate,^[16 - 18] poly(2,6-dimethyl-1,4-phenylene oxide),^[19] polyimide,^[20 - 22] polydimethylsiloxane,^[23-25] and so forth. Some simulation studies have concerned on studying liquid transport of polymeric membranes, such as water-ethanol mixtures through a polydimethylsiloxane membrane by pervaporation,^[26] ionic conduction of nanoscale porous polyethylene terephthalate (PET),^[27] solubilities of drugs in block copolymers,^[28,29] and water through cross-linked PA membranes by reverse osmosis.^[30-34] The gas or liquid transport properties of polymers in most previous MD works are studied upon equilibrium MD simulations to obtain diffusivity or solubility of small molecules in a polymer. Fewer works have been focused on pressure-driven liquid transport through polymeric membranes, like NF transport.

Derived from a collapsing-annealing MD procedure for modeling a porous PET membrane proposed by Cruz-Chu,^[27] a series of amorphous uncross-linked PA membranes are modeled as the PA layer of a TFC NF membrane through full atomistic MD simulations. In our previous work,^[35] the effect of membrane structure on pressure-driven water flows through carbon nanotube membranes was investigated through nonequilibrium molecular dynamics (NEMD) simulations. In this work, the transport properties of pressure-driven water flows through the PA membranes are studied through NEMD simulations, and the polymeric membrane structures and water transport properties of the PA membranes are analyzed to show the effect of membrane structure on water transport.

7.3. Simulation Methods

All MD/NEMD simulations are performed in NAMD package^[36] with the Velocity Verlet algorithm^[37] to integrate the equation of motion, and the simulation results are visualized and analyzed by using VMD package^[38]. PA polymers used in the simulations are modeled in CHARMM General Force Field, and water molecules are described by using flexible TIP3P (transferable intermolecular potential three-point) water model^[39] in CHARMM General force field.^[40]

The van der Waals interactions and the electrostatic interactions are described by the Lennard-Jones 6-12 type potential and the Coulomb potential, respectively. For calculating the van der Waals and electrostatic interactions without periodic boundary conditions (PBC), the cut-off radius is set as 1.2 nm with a switching function starting at 1.0 nm; while the electrostatic interactions in PBC are calculated using the PME (Particle Mesh Ewald) method.^[41] The Langevin dynamics method and Langevin Nosé-Hoover piston method are used to control a constant temperature and pressure, respectively. The simulations in this chapter consist of two separate simulations in series: one for modeling the PA membranes and the other for simulating the pressure-driven water flow through the membranes.

7.3.1. Modeling of PA membranes

The FilmTec[®] NF 90 serial membrane from Dow Chemical Company is one of several commercially successful NF membranes with TFC structures. The chemical structure of the active layer of the NF 90 membrane is a fully aromatic and partially cross-linked

PA,^[42, 43] as shown in Figure 7.1. In this work, a PA membrane is composed of several linear PA polymers to model a PA membrane without cross-linked bonds between PA polymers. The modeled uncross-linked PA membrane is a simplified version of the real cross-linked PA in NF 90 membrane.

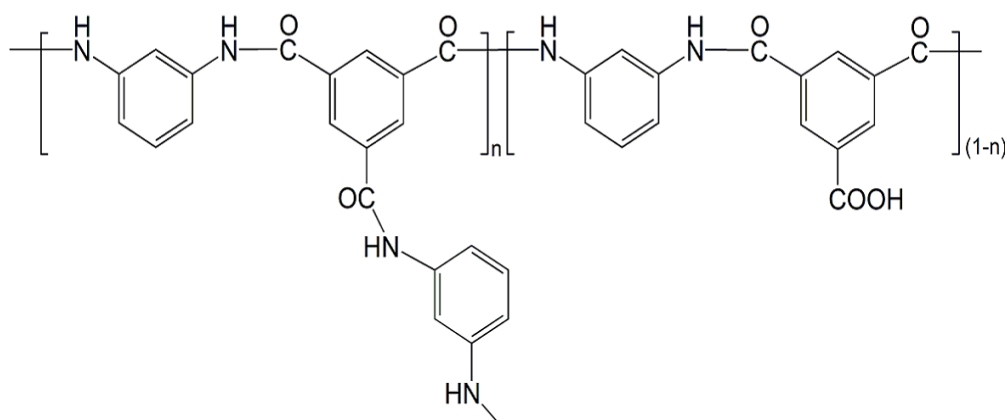


Figure 7.1 Chemical structure of the PA active layer of the NF 90 membrane (adapted from reference [42]): the symbol n denotes the degree of cross-linking with value in between 0–1 ($n=1$ for a fully cross-linking structure, and $n=0$ for a fully linear structure).

The MD simulation method used in this work for modeling PA membranes are derived from a collapsing-annealing MD procedure as described in Cruz-Chu's work.^[27] An overview of the simulation process is as follows. Each linear PA polymer is first assembled (as in Figure 7.2) with random arrangement of the pendant carboxylic acid groups. A number of these chains are loosely collected, shrunk to the desired size, and hydrated with water all using MD simulations. Then water is pushed through the hydrated polymer to simulate the performance of a real membrane, using a NEMD simulation. The details of this procedure are given below.

The linear PA polymer (as in Figure 7.2) has two carboxyl acid groups as end groups, and there are, in total, 40 repeat units of the linear PA polymer: 30 repeat units with carboxyl acid groups and 10 repeat units without carboxyl acid groups. The percentage of repeat units with carboxyl acid groups in the linear PA polymer (75%) is close to that of the uncross-linked repeat units in the NF 90 membrane (about 74.4%^[44]). A collection of 30 different linear PA polymers are constructed with linear chain structures and the repeat units with or without the carboxyl acid groups are arranged randomly in each linear PA polymer. This random arrangement is achieved by generating 10 random numbers from 1 to 40, using a scripting language, with the numbers from 1 to 40 corresponding sequentially to the 40 repeat units of each PA polymer. The force field parameters for the repeat units and end groups of the linear PA polymer are derived in analogy to known parameterized molecules and from the topology and parameter files for the CHARMM General Force Field.^[40] Each PA polymer is built in a perfect linear structure, and then is equilibrated for 2.0 ns at 1000 K and vacuum to form an equilibrated configuration of the polymer chain. The high temperature is used to prevent polymer chain folding.

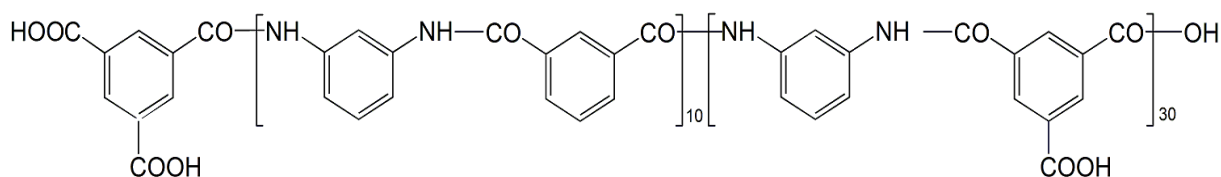


Figure 7.2 Chemical structure of the linear PA polymer used to begin the modeling of the PA membranes. The 10 non-carboxylated units and 30 carboxylated units are arranged randomly with carboxyl acid groups as end groups.

After the equilibrium MD simulations for all the linear PA polymers, several PA polymers are randomly selected from the 30 PA polymers and are symmetrically placed in a 50 nm \times 50 nm \times 50 nm cubic box. In the cubic simulation box, the polymers cannot overlap and the distance between any two PA polymers is kept at least 5.0 nm. A MD simulation is performed to collapse the PA box to 7.0 nm \times 7.0 nm \times 7.0 nm at 1000 K and vacuum. During the collapsing simulation, an external force keeps being applied on any carbon atom located outside of the desired size to push the carbon atom toward the center of the box. After the desired size is reached through the collapsing simulation, the resulting dense PA box is used in a 5.0 ns MD simulation to equilibrate the PA membrane in a three-dimensional PBC at 1000 K and 0.1 MPa. Then the PA box is cooled to 300 K at 0.1 MPa through a cooling MD simulation in PBC and the cooling rate is 500 K per nanosecond. The cooling rate is selected based on Cruz-Chu's work,^[27] while the effect of cooling rate on the membrane structure is unknown. After the temperature reaches 300 K, a MD simulation is carried out for 4.0 ns in an isothermal–isobaric (NPT) ensemble to obtain a dry amorphous PA membrane model with a complex and random pore structure.

Four PA membranes are modeled using the same MD simulation method described above and in the same cubic size, except for the number of linear PA polymers in the membrane. Then 18, 21, 24, and 27 linear PA polymers several PA polymers are randomly selected from the original 30 PA polymers. Figure 7.3 shows the resulted PA membrane model composed of 21 PA polymers.

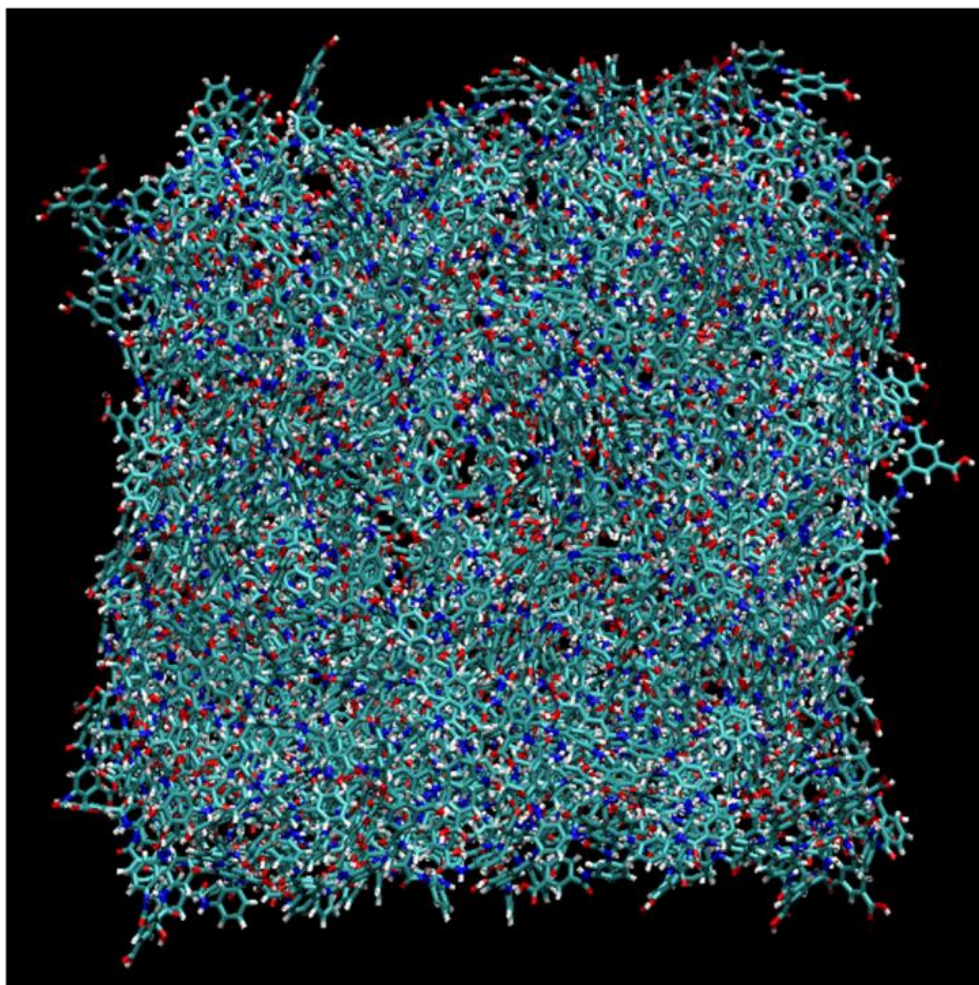


Figure 7.3 A snapshot of the dry (prehydrated) #2 membrane (a cubic PA membrane model composed of 21 PA polymers). Molecules are shown by bonds: carbon atoms in green, hydrogen atoms in white, oxygen atoms in red, and nitrogen atoms in blue.

To obtain a hydrated PA membrane, a dry PA membrane model is dissolved in a large water box ($25 \text{ nm} \times 25 \text{ nm} \times 25 \text{ nm}$) and is placed in the center of this water box. After the system is energy-minimized, an equilibrium simulation is carried out at 300 K and 0.1 MPa with three-dimensional PBC to obtain the configuration of a water-hydrated PA membrane by allowing the water molecules to fill the PA membrane in the simulation. During this equilibrium simulation, the PA polymers are flexible and the external force is still applied on any carbon atom of PA located outside of the desire size (as mentioned

above) to keep the membrane size. The hydrated PA membrane is obtained and is used as a membrane part of a NEMD simulation system for simulating a pressure-driven water flow passing through the PA membrane. All simulations for modeling dry and hydrated membranes use 1.0 fs time step.

7.3.2. Molecular dynamics simulations of water transport

The NEMD simulation system in Cartesian coordinates can be generated from the equilibrated water box containing the hydrated PA membrane through the formerly described series of simulations. Figure 7.4 shows a NEMD simulation system for a pressure-driven water flow along the $z+$ axis. The water molecules and PA polymers in the equilibrated water box are selected to form a cuboid system, which contains two water reservoirs with the same size ($7.0 \text{ nm} \times 7.0 \text{ nm} \times 3.0 \text{ nm}$) and the hydrated PA membrane connecting the two reservoirs.

A 2.0 ns equilibrium MD simulation is performed with 1.0 fs time step with PBC at constant temperature and pressure (300 K and 0.1 MPa), and the water density of each reservoir should be 1000 kg/m^3 after the equilibrium MD simulation. The equilibrated system is used in a NEMD simulation for simulating a pressure-driven water flow passing through the PA membrane from the top reservoir to the bottom reservoir. In the NEMD simulation, an external constant force along the $z+$ direction is applied on each oxygen atom of two water control layers located near to the top and bottom boundaries. The thickness of each water layer is 0.25 nm and the total external forces form a net force along the $z+$ direction to generate a net pressure drop (the total forces on the two control

layers divided by the membrane area in x, y plane) across the membrane. A temperature of 300 K is used for running the NEMD simulation with 2.0 fs time step, and the trajectory is gained through saving data every 1000 steps. The first 1.0 ns (or longer) trajectory information is used to steady the constant pressure drop and is not used for analyzing the transport properties. In all simulations, the PA membrane (the PA polymers) is fixed at the position and is rigid, only the water molecules can move.

Similar to the system shown in the Figure 7.4, other two NEMD simulation systems are constructed for simulating water flows through the same PA membrane along the $x+$ and $y+$ directions, respectively. The equilibrium and NEMD simulations for each of these two systems are similar as introduced above for the water flow along the $z+$ direction. The results of the three NEMD simulations for the same membrane are averaged to represent the transport properties of the PA membrane in order to avoid the effect of spatial differences of the cubic membrane on the transport phenomenon.

The NEMD simulation system used in this work, which is a 3D PBC system, is a simple and common system to study pressure-driven transport at a constant pressure difference, while this system eliminates diffusion even at a low pressure difference (5 MPa)^[45] and produces a negative pressure in the bottom reservoir.^[46] This kind of NEMD system is not a representation of pressure-driven water transport across membranes (like a real NF process), and this work shows an approximation of transport properties based on this NEMD simulation system. Other NEMD systems (specifically a 2D PBC) have been proposed to study pressure-driven water flows driven by two different pressures (both positive) at the two sides of a membrane.^[45, 47] In the case of

CNT membranes, our previous study shows this 3D PBC kind of system requires fewer computational demands than (about 35% of) the other system we proposed.^[45] In this PA membrane case, this kind of NEMD system is chosen to reduce computational demands, as the large system size used here (including water and PA) takes about 10 CPU days per nanosecond of simulation (instead of about 3 times that amount).

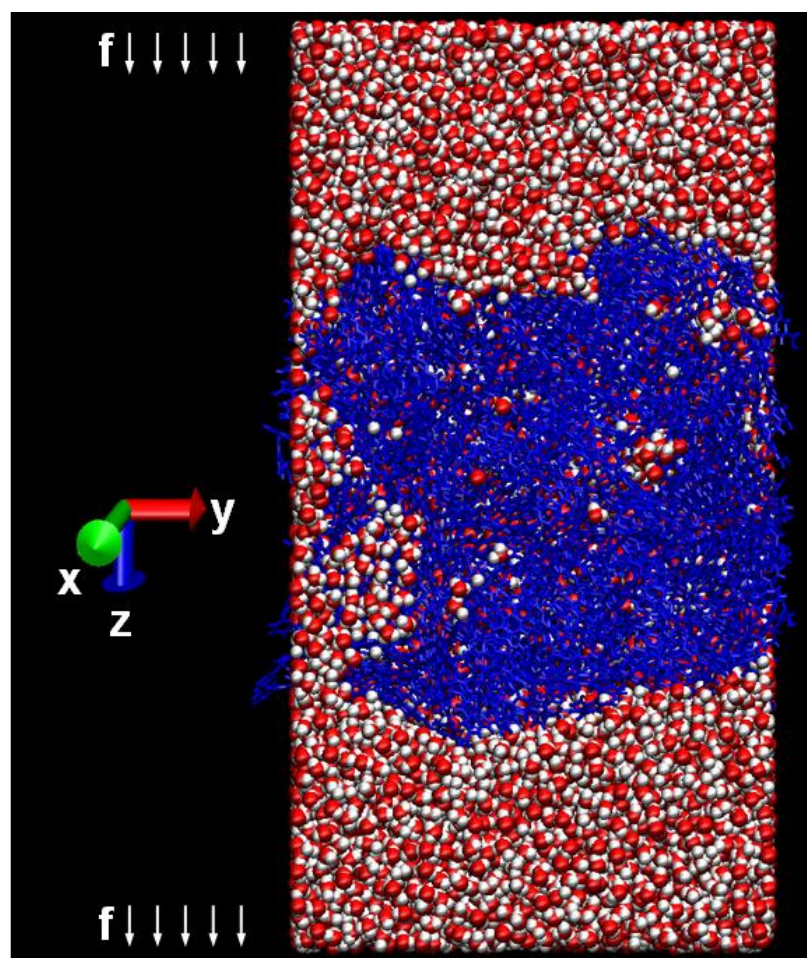


Figure 7.4 The snapshot of the NEMD simulation system including the PA membrane model and two water reservoirs to simulate pressure-driven water flow along the $z+$ direction. The PA membrane shown by bonds in blue; the hydrogen atoms and oxygen atoms of water molecule showed by van der waals atoms in white and red, respectively. The external force (f) is applied on each water molecule of the two water layers near the top and bottom boundaries along the $z+$ direction.

7.4. Results and Discussion

As described above, the four PA membranes with different membrane densities are composed of 18, 21, 24, or 27 linear PA polymers in the same membrane size, to simulate pressure-driven water flows through the PA membranes. Each PA membrane is an amorphous membrane with free volume pores through which the water is transported. The simulation results are analyzed to obtain the membrane properties (the FFV and the free volume radius) and the transport properties (the water flux and the permeability coefficient), and then to investigate the effect of membrane structure on water transport.

7.4.1. PA membrane properties

The four PA membrane models have different membrane densities, and the number of PA polymers in each membrane decides the membrane density. The hydrated PA membrane is formed by water molecules dissolved in the free volume of the dry PA membrane. Therefore, the free volume properties of the PA membrane are related to the water content in the membrane.

The equilibrated NEMD simulation system is used to show the water density distribution from the top reservoir to the bottom reservoir (the flow direction), and the results of the three systems for the same PA membrane are averaged to represent the membrane properties. Figure 7.5 shows the water density as a function of the position along the flow direction for each membrane, where each density profile is the average for density profiles in each of the $x+$, $y+$, and $z+$ directions. The water density (kg of water in the membrane/(m³ of wet membrane)) in the membrane is based on the volume of the

thin cuboid section ($7.0 \text{ nm} \times 7.0 \text{ nm} \times 0.4 \text{ nm}$). The variation in between each of the Cartesian directions (represented by the standard error of the three data sets) is small ($< 10\%$ for most results) indicating that the membranes are close to axisymmetric. Even though each membrane is close to axisymmetric, we still do NEMD simulations for three directions separately and use the average results to represent better the transport properties of each membrane.

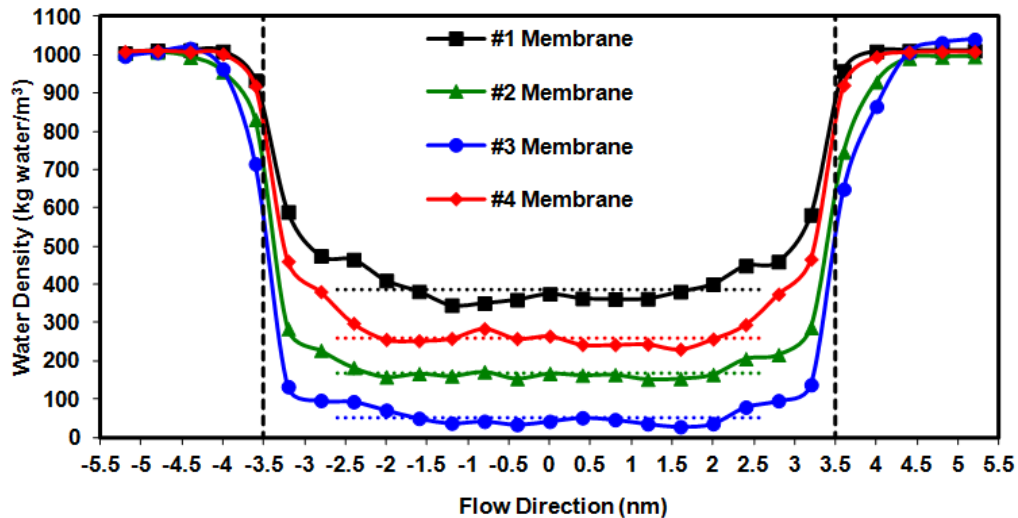


Figure 7.5 Average water density distributions along the $x+$, $y+$, and $z+$ directions for the #1–4 PA membranes (see Table 7.1). The points of each membrane are based on the equilibrated status of the NEMD system at 300 K and 0.1 MPa. Each data point is the average of three density values from the cuboid sections at the same position along the $x+$, $y+$, and $z+$ directions; and the standard error of the three densities is less than 10% for most average density values. The solid lines are the trend curves based on the simulation results, and the dotted lines represent the average density values from -2.6 nm to $+2.6 \text{ nm}$. The dashed lines are the membrane boundaries along the flow direction separating the system in to three parts from left to right: the water reservoir at the high pressure side, the PA membrane, and the water reservoir at the low pressure side.

It can be observed from Figure 7.5 that the water densities near the top and bottom membrane boundaries are at least twice of the nearly constant densities at the middle sections of the membranes (the dotted lines in Figure 7.5). The higher water densities

near the membrane surfaces are caused by the uneven membrane surfaces; more water molecules can be adsorbed on/in the membrane surfaces resulting in higher water densities near the membrane boundaries. For each membrane, the density values from -2.6 nm to +2.6 nm show only a small variation. The standard error of densities in this range is about 10% for the #1–3 membranes to about 40% for the #4 membrane due to the low densities in the central section of the #4 membrane. The membrane composed of fewer PA polymers exhibits a higher water density as expected, due to the larger free volume of the membrane allowing more water molecules to fill the membrane. The highest density profile of the average water density from -2.6 nm to +2.6 nm for the #1 membrane is about 14 times that of the lowest density profile for the #4 membrane, as shown in Figure 7.5.

Table 7.1 lists, for each wapore membrane, the densities of the dry and hydrated membranes and the water content in the hydrated membranes. With increasing number of PA polymers in the membrane, the density of the dry membrane increases as expected. Correspondingly, the water content decreases due to the decreasing free volume of the PA membrane. The decreasing water content corresponds to the water density profiles in Figure 7.5. The density of each hydrated PA membrane is decided by the total mass of the PA polymers and water molecules in the membrane, thus the densities of the four hydrated PA membranes are similar and all about 1400 kg/m^3 .

The free volume of each PA membrane is evaluated by the “accessible free volume” method reported by Kruse.^[48] In Kruse’s method, small standard spherical tracers (each tracer of a 0.15 nm radius) are used to fill unoccupied spaces of a polymeric cell to detect

free volume pores in the cell, and the accessible space of each free volume hole is calculated by the total volume of standard tracers in each hole.^[48] This evaluation method depends on the size of the standard tracer and the free volume of the polymeric cell cannot be fully occupied by spherical tracers, so the resultant free volume is actually smaller than the real free volume of the polymeric cell.

Table 7.1 Membrane properties of the #1–4 membranes.^{a, b}

PA membranes	#1	#2	#3	#4
Number of PA Polymers	18	21	24	27
Dry membrane density (kg/m³)	950.3	1088	1226	1368
Hydrated membrane density (kg/m³)	1386	1403	1426	1433
Water content (wt%)	31	22	14	4.5

^aThe conditions are: T = 300 K, P = 0.1 MPa.

^bThe results are based on the whole 7.0 nm × 7.0 nm × 7.0 nm membrane.

In this work, water molecules in the hydrated PA membrane are viewed as tracers to evaluate the free volume and the free volume pores. Water molecule are assumed to have a spherical shape with the radius of 0.14 nm (the mean van der Waals radius of water^[49]). The fractional free volume, FFV, is a common parameter to represent the free volume properties of a polymer and is usually defined by the ratio of the free volume to the total polymer volume as a percentage or a fraction. Each FFV value is calculated by the total free volume in a thin cuboid section per section volume (7.0 nm × 7.0 nm × 0.4 nm). The FFV distributions for the PA membranes are shown in Figure 7.6, where each

FFV profile is based on the equilibrated NEMD simulation systems for each membrane and averaged by three distribution results along the $x+$, $y+$, and $z+$ directions. Similar to the water density distributions shown in Figure 7.5, the FFV profile decreases with increasing the number of PA polymers in the membrane (from the #1 membrane to the #4 membrane) and the higher FFV values are observed near the top and bottom membrane surfaces due to more water molecules near the water–membrane interfaces. The standard error of FFV values from -2.6 nm to $+2.6$ nm is the same as the error of water densities (see above) for each membrane, as the FFV property is calculated from the number of water molecules in the membrane.

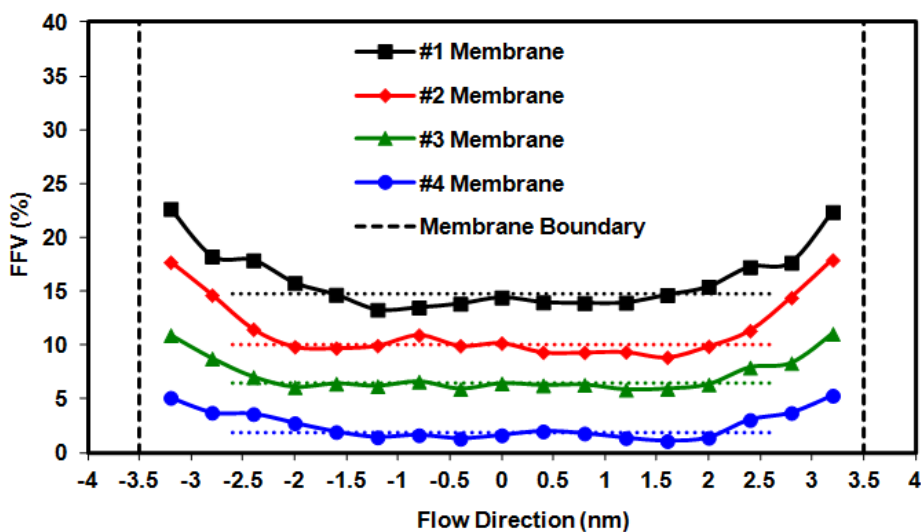


Figure 7.6 Average FFV distributions along the $x+$, $y+$, and $z+$ directions for the #1–4 PA membranes (see Table 7.1). The points of each membrane are based on the equilibrated status of the NEMD system at 300 K and 0.1 MPa. Each data point is the average of three FFV values from the cuboid sections at the same position along the $x+$, $y+$, and $z+$ directions; and the standard error of the three densities is less than 10% for most FFV values. The solid lines are the trend curves based on the simulation results, and the dotted lines represent the average FFV values from -2.6 nm to $+2.6$ nm. The dashed lines are the membrane boundaries along the flow direction separating the system in to three parts from left to right: the water reservoir at the high pressure side, the PA membrane, and the water reservoir at the low pressure side.

To avoid the influence of the irregular membrane surfaces, each PA membrane is analyzed by the water molecules existing in the central part of the membrane ($6.0 \text{ nm} \times 6.0 \text{ nm} \times 6.0 \text{ nm}$). When a water molecule or a group of directly neighboring water molecules is isolated from other water molecules in the membrane (within $6.0 \text{ nm} \times 6.0 \text{ nm} \times 6.0 \text{ nm}$), the occupied space of this molecule or this group of molecules is detected as a free volume hole. Therefore, each free volume hole in the PA membrane is occupied by at least one water molecule and the total accessible volume of the water molecules represents the hole volume. Each free volume hole is idealized as a spherical shape, and the spherical radius of each of these sphere volumes is used as the hole radius. Thus the hole radius is only related to the free volume but not the hole shape; the holes with the same volumes are represented by the same hole radius even if the holes are different shapes. Note the holes detected by the water molecules in the membrane include closed holes and open holes (passing through the membrane), and the open holes are membrane pores which significantly affect the membrane transport properties. One view of evaluating the free volume properties is as follows.

Figure 7.7 shows the free volume hole distribution of each PA membrane, which is represented by the number of holes as a function of the corresponding hole radius. Generally, the smaller the hole, the more the holes of the same corresponding size exist in the PA membrane. To give an idea of the distribution of the data a log-normal distribution has been fit to the data and shown in Figure 7.7. As a first-attempt fit the data are approximately fit by this distribution. For the membrane #4 the log-normal fit is poor. These results indicate that a polymeric membrane with lower membrane density

(larger FFV) might have free volume holes with different volumes in a log-normal distribution. With increasing number of PA polymers in the membrane, the larger free volume holes gradually disappear: the largest hole of the #1 membrane is about 0.66 nm in radius, which is almost 5 times of the smallest hole radius (0.14 nm); while, the #4 membrane only exhibits hole sizes in a small range (from 0.14 nm to 0.32 nm in radius).

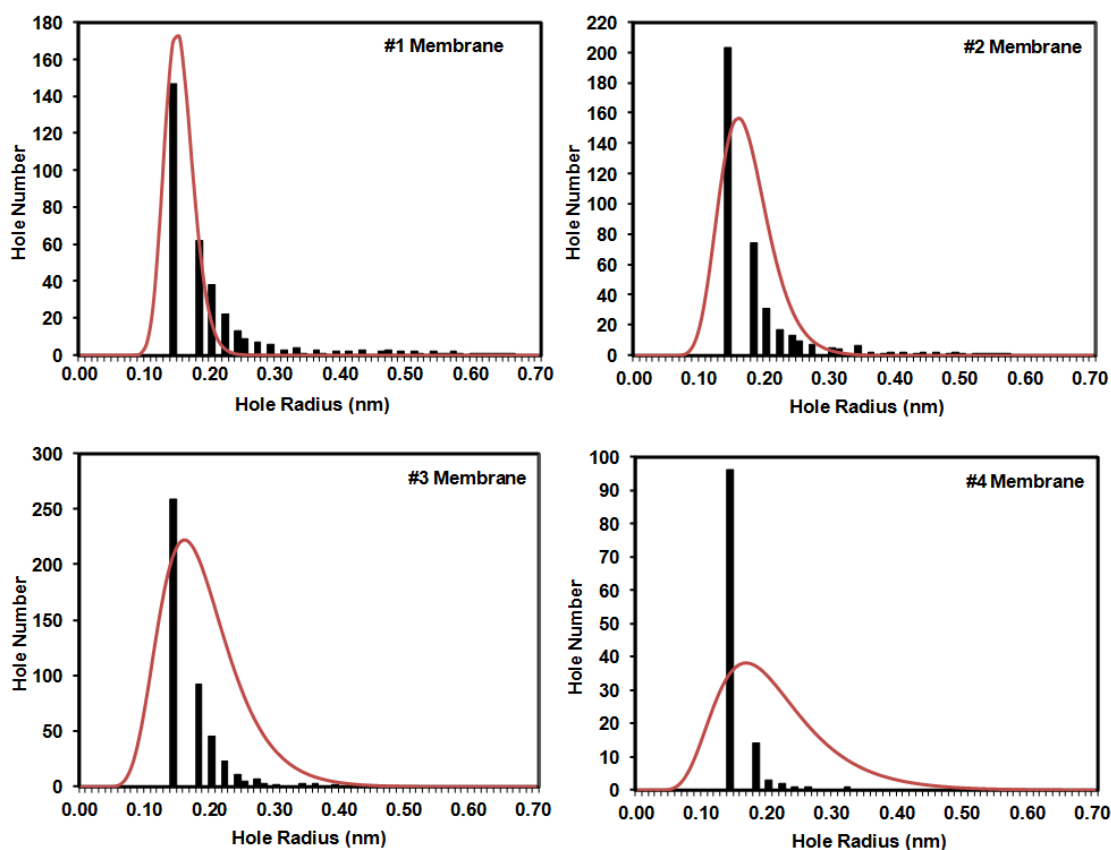


Figure 7.7 Free volume hole distributions of the #1–4 PA membranes: the hole number as a function of the hole radius. The results are based on the equilibrated state of the system at 300 K and 0.1 MPa, and the properties of the #1–4 PA membranes are shown in Table 7.1. The solid curved is the log-normal distribution trend based on the free volume hole distribution for each PA membrane.

Figure 7.8 shows the total FFV value of the holes with the same size as a function of the corresponding hole radius. Each total FFV value in Figure 7.8 is dependent on both

the number of holes and the same free volume of these holes, so Figure 7.8 exhibits different distributions than Figure 7.7. The FFV value of the larger but fewer holes is comparable with that of the smaller but more holes: in Figure 7.7, the number of holes with a larger hole radius (i.e. > 0.4 nm) is much smaller than (several percent of) the number of holes with a smaller hole radius (i.e. < 0.2 nm); while, in Figure 7.8, the FFV of the larger hole size is a significant fraction of or even larger than the FFV of the smaller hole size. The number of the smaller holes is more than that of the larger holes, but the smaller holes cannot be pores (larger and open holes) contributing to water transport through the membrane.

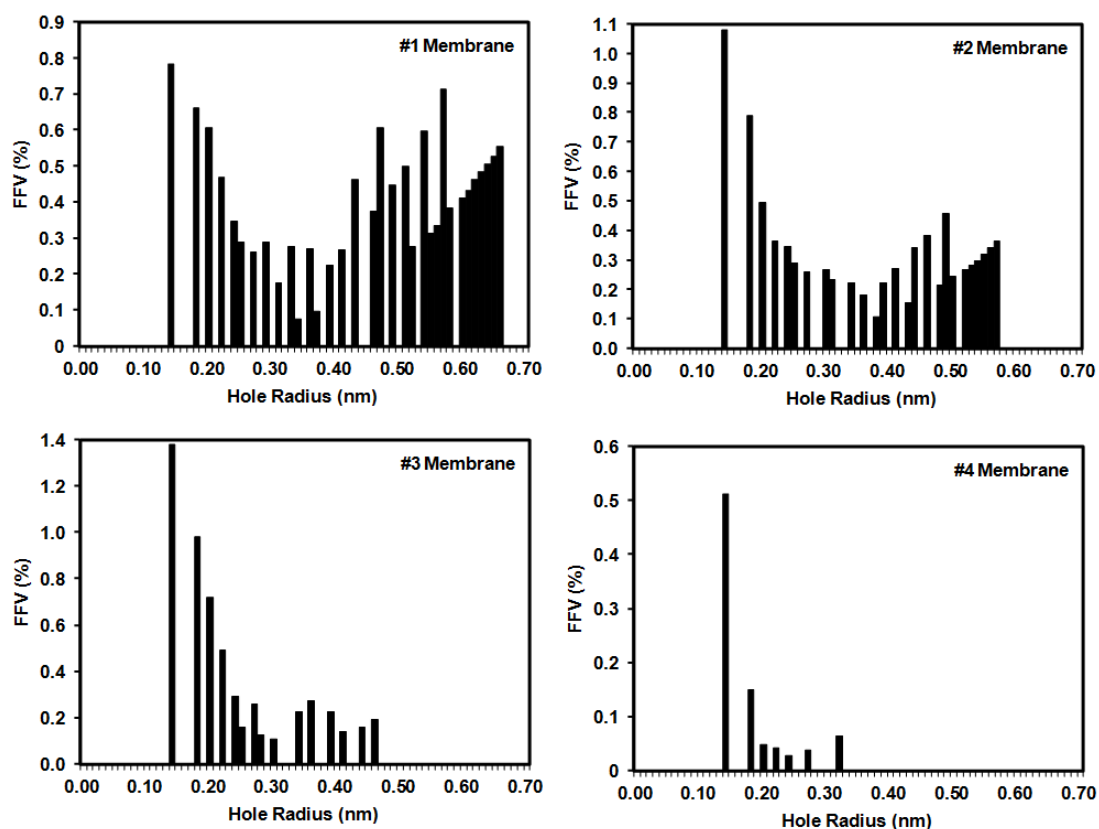


Figure 7.8 FFV distributions of the #1–4 PA membranes: the FFV value as a function of the hole radius. The results are based on the equilibrated state of the system at 300 K and 0.1 MPa, and the properties of the #1–4 PA membranes are shown in Table 7.1.

To relate the free volume properties with the membrane transport properties, an average/mean volume is used to represent the free volume holes of the membrane. The average volume of all free volume holes in each PA membrane is a number average value defined as the total free volume divided by the total hole number. The spherical radius of the average volume is calculated (as above for calculating each hole radius) and called the “average free volume radius” in this work. Kruse^[48] also a mean free volume value (V50) for a polymer, which is equal to the half of the sum of all free volumes. It means the sum of the free volumes smaller than the volume V50 is half of the total free volume of the polymer. Then a spherical radius can be calculated based on the V50 value and is called the “mean free volume radius” in this work. The mean free volume radius accounts for more contributions of larger holes than the average radius but still includes the close smaller holes, and the smaller holes cannot be “pores” (continuous pathways through the membrane) contributing to water transport through the membrane. Therefore, the mean free volume radius can be a more reasonable representation for the free volume but not the free volume pores.

Table 7.2 lists the FFV values of the #1–4 membranes and two radii (the average radius and the mean radius) for each PA membrane. As expected, the average and mean radii both decrease with decreasing FFV of the membrane. The FFV result of each membrane is lower than FFV distribution in Figure 7.6, since the FFV in Table 7.2 is calculated based on the central part of the membrane (6.0 nm × 6.0 nm × 6.0 nm). The range of the mean radii of the four membranes is wider than the range of the average radii. The difference in average and mean radii is due to the asymmetric (non Gaussian)

distribution of the free volume size distribution. According to the calculation methods, the mean radius is calculated through FFV values considering the relative contribution of hole sizes and hole numbers, while the average radius is simply calculated through the number average volume. Therefore, the mean radius accounts for more contributions of larger holes (pores) than the average radius, and consequently is a more reasonable representation for the free volume pores. Here the pore size of each PA membrane is represented by the mean radius, which is called as “free volume radius” below.

Table 7.2 FFV values and free volume radii of the #1–4 PA membranes.^a

PA membranes	#1	#2	#3	#4	NF 90
Number of PA Polymers	18	21	24	27	Cross-linked PA
FFV (%)	13.5	8.79	5.72	0.88	
Average free volume radius (nm)	0.27	0.23	0.19	0.16	0.34 ^[50]
Mean free volume radius (nm)	0.48	0.35	0.20	0.13	

^aThe FFV and radius results are analyzed through water molecules located within the 6.0 nm × 6.0 nm × 6.0 nm part of each hydrated PA membrane.

In Table 7.2, the free volume (mean) radii of the PA membranes are compared with the pore radius of the real commercial NF 90 membrane, which was evaluated by Nghiem^[50]

through a series of liquid transport experiments using the NF 90 membrane. Among the #1–4 membranes, the free volume radius of the #2 membrane composed of 21 PA polymers is closest to (about 3% larger than) the radius of the NF 90 membrane. The free volume radius of the PA membrane we measured is related to the membrane free volume including closed and open free volume holes, while the pore radius evaluated experimentally is from a series of retention experiments. However, the similarity between the simulation and experimental radii implies that the pore size and transport properties are related to the free volume properties. The simulation transport properties of the membranes are compared with the experimental transport property of the NF 90 membrane below.

7.4.2. Transport properties

The NEMD simulations are carried out to obtain the transport properties of water passing through each PA membrane at different pressure differences of 1.0 MPa, 10 MPa, 50 MPa, and 100 MPa. The pressure difference of 50 MPa or 100 MPa is much higher than the usual range of pressure in a real NF process (0.5–2 MPa) but are included here because of the less computational time/cost required and to see if any water transport could be obtained for membrane #4. At a high pressure difference, the water transport is obtained with relatively low statistical error and with relatively short simulation time due to the faster water permeation. At lower pressure differences, these PA membrane have a much lower water flux and therefore require a longer simulation time to achieve statistically accurate results.

The water flux is defined as the number flow rate per membrane area which is calculated in the units of both ‘molecules/(ns nm²)’ and ‘m³/(m²·s)’ or equivalently ‘m/s’. The number of water molecules passing through the membrane along the flow direction is counted every 0.01 to 1.0 ns (the interval time depends on the water flow rate) and plotted as a function of the simulation time, and then the slope of the linear profile (through the origin) is the number flow rate. The estimated error of the number flow rate is represented by the standard error on the slope with the assumption of uncorrelated data (a correlation time less than the interval time). An example of the error analysis for the simulation flux is shown in our previous work.^[35] The water flux for a particular PA membrane for each pressure difference is the average of the water fluxes along the $x+$, $y+$, and $z+$ directions, and the estimated error of the average flux is the average of the three errors of the three fluxes as mentioned earlier.

A. The effect of membrane density

The #1–4 PA membranes composed of the difference numbers of PA polymers exhibit different membrane densities and free volume radii as discussed above: the free volume radius decreases with increasing membrane density (shown in Tables 7.1 and 7.2). The dependence of water flux on the free volume radius under each pressure difference is represented in Figure 7.9, where the simulation water flux increases with increasing free volume radius. The #4 membrane with the highest density has the smallest radius of 0.13 nm, and shows the lowest water flux of zero even at the pressure difference of 100 MPa. The #4 PA membrane is too dense to allow water molecules passing through the

membrane, which suggests the corresponding membrane density (1368 kg/m^3) and free volume radius (0.13 nm) listed in Tables 7.1 and 7.2 may be used to estimate if the PA membrane is feasible to be used as a NF membrane allowing water transport.

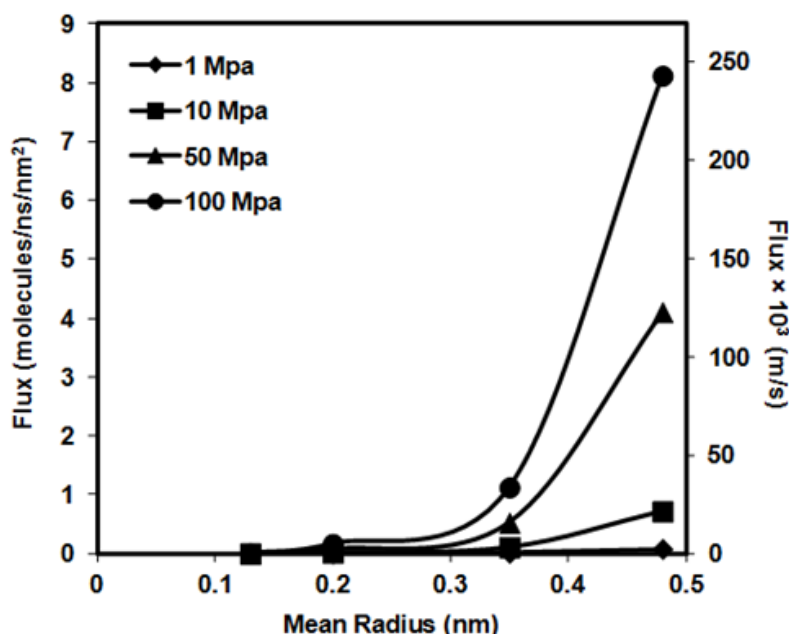


Figure 7.9 Flux (rate per membrane area) at each pressure difference, shown both as molecular flux and conventional flux (in m/s), as a function of the mean free volume radius. The points are based on the NEMD simulations on the #1–4 membranes (Table 7.2): $L = 7.0 \text{ nm}$; and $T = 300 \text{ K}$. The solid curves are the trends through the origin based on the simulation results. The statistical error for each data point is evaluated and less than 10%.

In discussing the flux through a NF membrane, frequently the Hagen-Poiseuille equation (or an equivalent phenomenological equation) is used to represent flux through the membrane. As presented previously,^[51] the Hagen-Poiseuille equation derived from the Navier-Stokes equation is given as,

$$J_w = L_p \Delta P = \frac{r_p^2}{8\eta\tau(L/A_k)} \Delta P \quad (7.1)$$

where L_p is the pure water permeability coefficient, r_p is the pore radius of the membrane,

η is the viscosity of the liquid fluid at the operating temperature, τ is the pore tortuosity, L/A_K is the ratio of the membrane effective thickness to the surface porosity, and ΔP is the pressure difference.

Figure 7.9 shows that the density and hence free volume size of the PA membrane can affect water transport significantly: the flux values of the membranes at 100 MPa clearly show that the water flux increases with free volume (mean) radius as expected; the #1 membrane is about six times the water flux of the #2 membrane. As shown in Table 7.2, the free volume radii of the #1 and #2 membranes decrease from 0.48 nm to 0.35 nm. Due to the small molecular size of water (the van der Waals molecular radius of 0.14 nm^[49]), increasing/decreasing 0.1 nm in the pore radius of the membrane can result in a quite different water flux. The flux is expected to vary with free volume radius squared from Eqn. (7.1), while the results in Figure 7.9 are not linear with free volume radius squared (not shown here). This inconsistency is most likely caused by the origins of Eqn. (7.1) which are based on continuum mechanics and with the molecular size pores simulated here it is not reasonable to consider water as a continuum. Similarly, Eqn. (7.1) failed to predict water flux through carbon nanotubes in our previous work.^[35] As well the disagreement may be caused by the evaluation of the free volume radius; for example, only the free volume holes/pores located within 6.0 nm \times 6.0 nm \times 6.0 nm are used to evaluate the mean radius, while there would/should be larger holes/pores near the membrane surface. Another possible reason is the flux proportional to the pore radius squared is valid for the same porosity and pore tortuosity. However, the porosity and tortuosity of the PA membranes are not constant.

Figure 7.10 shows that the water flux increases linearly with increasing pressure difference for #1–3 membranes (the #4 membrane being nonporous is not included) as expected from Eqn. (7.1). From these data the permeability coefficient of the #1–3 membranes are calculated and listed in Table 7.3.

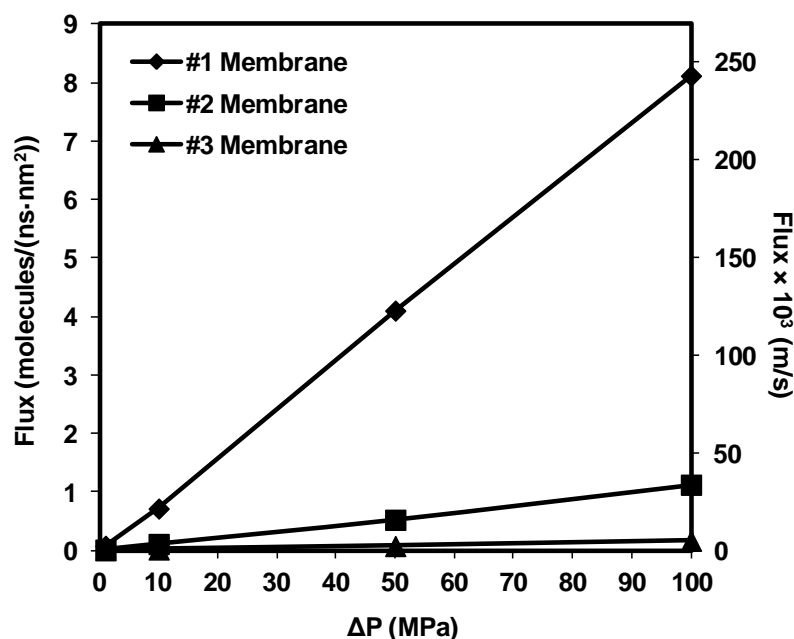


Figure 7.10 Flux (rate per membrane area) of each PA membrane, shown both as molecular flux and conventional flux (in m/s), as a function of the pressure difference. The points are based on the NEMD simulations on the #1–3 membranes (Table 7.2): $L = 7.0$ nm; and $T = 300$ K. The solid lines are the linear trends through the origin based on the simulation results. The statistical error for each data point is evaluated and less than 10%.

The water permeability coefficient decreases quickly with decreasing average pore radius, which indicates that the effect of membrane pore size on the water permeability is significant. While, we cannot simply conclude that the polymers are porous just because a free volume pore size can be measured and related to membrane transport. As mentioned above, the Hagen-Poiseuille equation, based on continuum mechanics, is not

valid for the nanopores here. However, for each PA membrane, the water flux at a desired pressure difference can be predicted by the product of the water permeability coefficient and the pressure difference, which is the same as the effect of pressure difference on the water flux shown by the Hagen-Poiseuille equation.

Table 7.3 Comparisons of the PA membranes and the NF 90 membrane.

PA membranes	Thickness, L (nm)	Water permeability coefficients ^a , $L_p \times 10^5$ (m/s/MPa)	$L \times L_p \times 10^{14}$ (m ² /s/MPa)
#1	7	243	1701
#2	7	33.1	231.7
#3	7	4.78	33.46
NF 90	174 ^b	1.78 ^[50]	309.72

^aThe standard error of each water permeability coefficient for the #1–4 PA membranes is evaluated from the linear regression of the linear trend (through the origin) in Figure 7.10, and is less than 10%.

^bThe thickness of the NF 90 membrane is an average value of 134-214nm^[50].

The simulation water permeability coefficients of the #1–3 membranes are compared with the experimental value of the NF 90 membrane in Table 7.3; to do this the effect of membrane thickness on water transport must be taken into account. In the Hagen-Poiseuille equation (Eqn. (7.1)), the water permeability is inversely proportional to the membrane thickness. An evaluation parameter, the product of the membrane thicknesses and the water permeability coefficient ($L \times L_p$), is shown in Table 7.3 to compare the modeled PA membranes with the NF 90 membrane. Among the three

(#1–3) membranes, the #2 membrane has the evaluation parameter ($L \times L_p$) in the same order of magnitude as the parameter of the NF 90 membrane. The acceptable difference between the parameters ($L \times L_p$) of the #2 membrane and the NF 90 membrane (Table 7.3) indicates that the simulation results correspond to the experimental results, which may be caused by the similar free volume radius and pore radius shown in Table 7.2.

B. The effect of membrane thickness

To study the effect of membrane thickness on water transport, the #2 PA membrane is used to model two series of PA membranes with different membrane thicknesses, 14 nm and 21.0 nm, respectively. Two or three #2 membranes are connected together to form an initial status of a thicker PA membrane in a cuboid shape. For each thickness, three membranes with the same thickness are modeled by stacking the #2 membranes. This stacking is repeated for each of the x , y , and z directions and simulated separately. A MD simulation in a NPT ensemble is carried out for each thicker membrane model to obtain the resulted PA membrane with a 14.0 nm or 21.0 nm thickness but with the same membrane area ($7.0 \text{ nm} \times 7.0 \text{ nm}$) as the #2 membrane. The NEMD simulations are carried out to simulate pressure-driven water flows passing through these thicker membranes. The detail modeling/simulation methods are not described here, and the analysis of the simulation results are the same as explained above. The simulation results of the three membranes with the same thickness are averaged to represent the membrane properties and transport properties of the PA membrane with the corresponding thickness. The variations of membrane and transport properties in between each of the

three directions (represented by the standard error of the three data) are less than 10% (not shown here).

The membrane properties (membrane densities, FFV values, free volume pore radius) of the modeled thicker membranes are analyzed and are similar to the #2 membrane. The detailed membrane properties are not shown here; for example, the average pore radii of the three membranes are almost the same (within 8%), as shown in Table 7.4. These three PA membranes are used to investigate the effect of membrane thickness on water transport.

Table 7.4 Water permeability coefficients of the modeled PA membranes with different membrane thicknesses.

	Thickness, L (nm)	Mean Radius (nm)	Water permeability coefficients, L_p $\times 10^5$ (m/s/MPa)
Modeled PA Membranes	7.0 (#2 membrane)	0.35	33.1
	14.0	0.34	16.7
	21.0	0.35	9.19

Figure 7.11 shows the water flux as a function of the pressure difference from 1 MPa to 100 MPa for each membrane: as expected, the flux is proportional to pressure difference and decreases with increasing membrane thickness. The water permeability coefficients of the three membranes are calculated through the slopes of the linear trend lines in Figure 7.11 and listed in Table 7.4. The water permeability coefficient increases with

decreasing membrane thickness, due to the resistance of membrane thickness on the water flow. The lower water flux of the thicker membrane is similar to the description in the Hagen-Poiseuille equation (Eqn. (7.1)), in which the flux/permeability varies as the reciprocal of the membrane thickness.

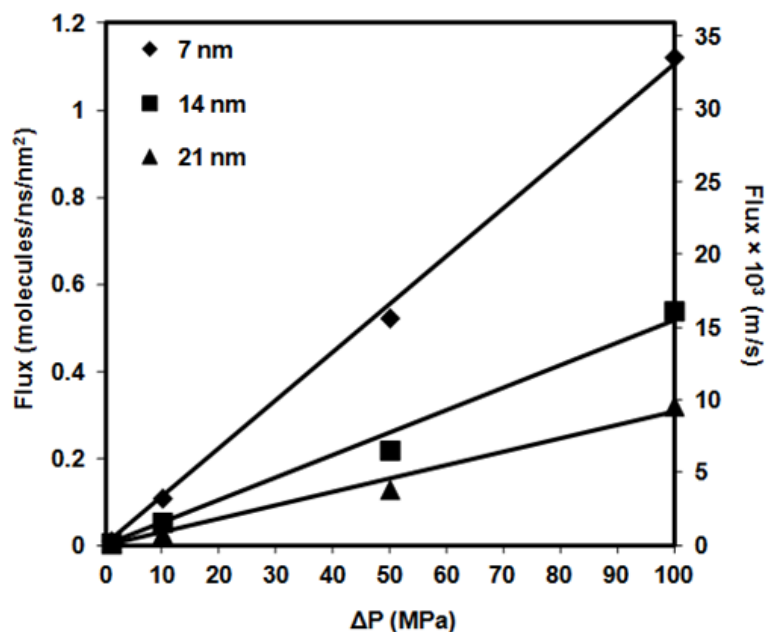


Figure 7.11 Flux (rate per membrane area) of each PA membrane, shown both as molecular flux and conventional flux (in m/s), as a function of the pressure difference (as expected from Eqn. (7.1)). The points are based on the NEMD simulations on the three membranes (Table 7.4) at 300 K. The solid lines are the linear trends through the origin based on the simulation results. The statistical error for each data point is evaluated and is less than 10%.

Considering the membrane thickness, the transport property of the #2 membrane is close to that of the NF 90 membrane as discussed above. In addition the transport properties of the thicker membranes with the thicknesses of 14.0 nm and 21.0 nm are compared with the NF 90 membrane with an average thickness of 174 nm. The water permeability coefficient with respect to the reciprocal of the membrane thickness is

plotted in Figure 7.12, in which a nearly linear line can be observed as expected from Eqn. (7.1). The linear relationship implies the simulation permeability coefficients of the modeled PA membranes correspond to the experimental permeability of the NF 90 membrane. The simulation results consistent with the experimental results imply that the MD/NEMD simulation methods presented in this work could be a simple and feasible way to study the membrane structure and transport phenomenon of a real polymeric NF membrane.

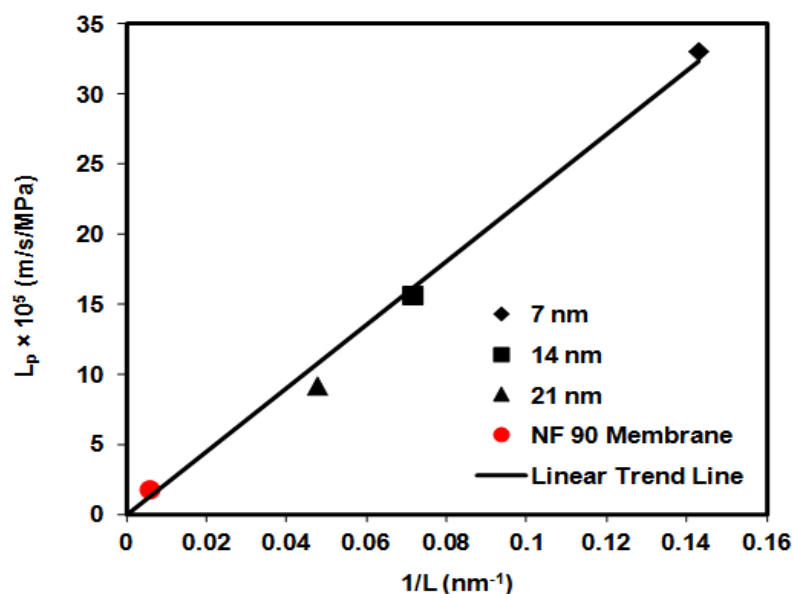


Figure 7.12 Water permeability coefficient as a function of the reciprocal of the membrane thickness. The water permeability coefficients and membrane thicknesses of the membranes are shown in Table 7.2 and Table 7.3. The standard error of each water permeability coefficient for the membrane model is evaluated from the linear regression of the linear trend (through the origin) in Figure 7.11, and is less than 10%.

7.5. Conclusions

The pressure-driven water flows passing through uncross-linked PA membranes are studied by MD/NEMD simulations in this work: the PA membranes are modeled as NF

membranes by using fully atomistic MD simulations, and the pressure-driven water flows are simulated by using NEMD simulations. The MD/NEMD simulation results are analyzed to investigate the membrane structure (membrane density, FFV, and free volume radius) of each PA membrane and then to investigate the effect of membrane structure on the transport properties (water flux and permeability coefficient).

The PA membrane composed of more PA polymers exhibits a higher density for the dry membrane but a lower water content of the hydrated membrane, due to the smaller free volume of the membrane. As the FFV of the PA membrane decreases, the average/mean radius of free volume holes decreases; while the water flux and the water permeability coefficient both decrease with decreasing free volume radius. For each PA membrane, the water flux is proportional to pressure difference, corresponding to the Hagen-Poiseuille equation. For the membranes with similar free volume radii but different thicknesses, the water flux and the water permeability coefficient both decrease with increasing membrane thickness. The membrane structures and the transport properties of the PA membranes are compared with the experimental results of a commercial NF membrane, the NF 90 membrane. The comparisons show that the water transport property of the modeled PA membrane is consistent with that of the NF 90 membrane with considering the effect of membrane thickness.

This work provides a way to study pressure-driven water transport through amorphous polymeric membranes by using MD/NEMD simulations. The expected significance of this work is to get a better understand on the relationship between NF membranes and NF transport, which is helpful to improve the potential of NF processes. It can be

prospected the results of this work would be meaningful for studying other polymeric membranes and membrane transport and helping in the improvement of membrane processes, particularly for water treatment and environmental applications.

References

- [1] X. Lu, X. Bian, and Shi, L. J. Membr. Sci. **210** 3 (2002).
- [2] W. Ho and K. Sirkar, *Membrane Handbook*, (Van Nostrand Reinhold, New York, 1992).
- [3] M. Mulder, *Basic Principles of Membrane Technology*, (Kluwer, London, 1996).
- [4] R. Petersen, J. Membr. Sci. **83** 81 (1993).
- [5] O. Kedem and A. Katchalsky, Biochim. Biophys. Acta. **27** 229 (1958).
- [6] K. Spiegler and O. Kedem, Desalination **1** 311 (1966).
- [7] S. Nakao and S. Kimura, J. Chem. Eng. Jpn. **15** 200 (1982).
- [8] T. Tsuru, S. Nakao, and S. Kimura, J. Chem. Eng. Jpn. **24** 511 (1991).
- [9] X. Wang, T. Tsuru, M. Togoh, S. Nakao, and S. Kimura, J. Chem. Eng. Jpn. **28** 186 (1995).
- [10] X. Wang, T. Tsuru, M. Togoh, S. Nakao, and S. Kimura, J. Chem. Eng. Jpn., **28** 372 (1995).
- [11] X. Wang, , T. Tsuru, S. Nakao, and S. Kimura, J. Membr. Sci. **135** 19 (1997).
- [12] X. Wang, T. Tsuru, S. Nakao, and S. Kimura, J. Membr. Sci. **103** 117 (1995).
- [13] W. R. Bowen, A. Mohammad, and N. Hilal, J. Membr. Sci. **126** 91 (1997).

- [14] W. R. Bowen and J. S. Welfoot, *Chem. Eng. Sci.* **57** 1121 (2002).
- [15] A. R. D. Verliefde, E. R. Cornelissenb, S. G. J. Heijmana, J. Q. J. C. Verberka, G. L. Amyc, B. Van der Bruggend, and J. C. van Dijk, *J. Membr. Sci.* **322** 52 (2008).
- [16] A. A. Gusev and U. W. Suter, *J. Chem. Phys.* **99** 2228 (1993).
- [17] M. Lopez-Gonzalez, E. Saiz, J. Guzman, and E. Riande, *J. Chem. Phys.* **115** 6728 (2001).
- [18] A. A. Gusev, U. W. Suter, and D. J. Moll, *Macromolecules* **28** 2582 (1995).
- [19] J. R. Fried, M. Sadat-Akhavi, and J. E. Mark, *J. Membr. Sci.* **149** 115 (1998).
- [20] M. Heuchel and D. Hofmann, *Desalination* **144** 67 (2002).
- [21] M. Heuchel, D. Hofmann, and P. Pullumibi, *Macromolecules* **37** 201 (2004).
- [22] S. Neyertz and D. Brown, *Macromolecules* **37** 10109 (2004).
- [23] D. Hofmann, L. Fritz, J. Ulbrich, and D. Paul, *Polymer* **38** 6148 (1997).
- [24] D. Hofmann, L. Fritz, J. Ulbrich, and D. Paul, *Comput. Theor. Polym. Sci.* **10** 419 (2000).
- [25] J. S. Yang, K. Choi, and W. H. Jo, *MacroMol. Theor. Simul.* **9** 287 (2000).
- [26] L. Fritz and D. Hofmann, *Polymer* **38** 1035 (1997).
- [27] E. R. Cruz-Chu, T. Ritz, Z. S. Siwy, and K. Schulten, *Faraday Discuss.* **143** 47 (2009).
- [28] S. K. Patel, A. Lavasanifar, P. Choi, *Biomaterials* **31** 345 (2010).
- [29] S. K. Patel, A. Lavasanifar, P. Choi, *Biomacromolecules* **9** 3014 (2008).
- [30] M. J. Kotelyanskii, N. J. Wagner, and M. E. Paulaitis, *J. Membr. Sci.* **139** 1 (1998).

- [31] M. J. Kotelyanskii, N. J. Wagner, and M. E. Paulaitis, *Comput. Theor. Polym. Sci.* **9** 301 (1999).
- [32] E. Harder, D. E. Walters, Y. D. Bodnar, R. S. Faibish, and B. Roux, *J. Phys. Chem. B* **113** 10177 (2009).
- [33] Z. E. Hughes and J. D. Gale, *J. Mater. Chem.* **20** 7788 (2010).
- [34] R. Oizerovich-Honig, V. Raim, and S. Srebnik, *Langmuir* **26** 299 (2010).
- [35] L. Wang, R. S. Dumont, and J. M. Dickson, *J. Chem. Phys.* **134** 044102 (2012).
- [36] J. Phillips, R. Braun, W. Wang, J. Gumbart, E. Tajkhorshid, E. Villa, C. Chipot, R. D. Skeel, L. Kal é and K. Schulten, *J. Comput. Chem.* **26** 1781 (2005).
- [37] W. C. Swope, H. C. Andersen, P. H. Berens, and K. R. Wilson, *J. Chem. Phys.* **76** 637 (1982).
- [38] W. Humphrey, A. Dalke, and K. Schulten, *J. Mol. Graphics* **14** 33 (1996).
- [39] W. L. Jorgensen, J. Chandrasekhar, J. D. Madura, R. W. Impey, and M. L. Klein, *J. Chem. Phys.* **79** 926 (1983).
- [40] K. Vanommeslaeghe, E. Hatcher, C. Acharya, S. Kundu, S. Zhong, J. Shim, E. Darian, O. Guvench, P. Lopes, I. Vorobyov, and A. D. Jr. MacKerell, *J. Comput. Chem.* **31** 671 (2010).
- [41] T. Darden, D. York, and L. Pedersen, *J. Chem. Phys.* **98** 10089 (1993).
- [42] FILMTEC™ Reverse Osmosis Membranes Technical Manual, Dow Water & Process Solutions.
- [43] C. Y. Tang, Y. Kwon, and J. O. Leckie, *Desalination* **242** 149 (2009).

- [44] Y. Kwon, C. Y. Tang, and J. O. Leckie, *J. Appl. Polym. Sci.* **108** 2061 (2008).
- [45] L. Wang, R. S. Dumont, and J. M. Dickson, "Comparison of two nonequilibrium molecular dynamics simulation systems for the pressure-driven water permeation through carbon nanotube membrane", *Microfluid. Nanofluid.* submitted (2012).
- [46] M. E. Suk and N. R. Aluru, *J. Phys. Chem. Lett.* **1** 1590 (2010).
- [47] W. D. Nicholls, M. K. Borg, D. A. Lockerby, and J. M. Reese, *Microfluid. Nanofluid.* **12** 257 (2012).
- [48] J. Kruse, J. Kanzow, K. Rätzke, F. Faupel, M. Heuchel, J. Frahn, and D. Hofmann, *Macromolecules* **38** 9638 (2005).
- [49] F. Franks, *Water: A Matrix of Life, (Second Edition)* (Royal Society of Chemistry, Cambridge, 2000).
- [50] L. D. Nghiem, Removal of emerging trace organic contaminants by nanofiltration and reverse osmosis, (PhD thesis, School of Civil, Mining and Environmental Engineering, University of Wollongong, Wollongong, Australia, 2005).
- [51] A. I. Schäfer, A. G. Fane, T. D. Waite, *Nanofiltration: Principles and Applications*, Elsevier Advanced Technology, Oxford, 2005.

Chapter 8 Molecular Dynamics Simulations of Water Transport through Cross-linked Polyamide Nanofiltration Membranes at Low Pressure

8.1. Abstract

The simulation work is to study water transport through polyamide (PA) membranes at approximate nanofiltration (NF) operation conditions. The neutral and negatively charged PA membranes are modeled by using molecular dynamic (MD) simulations and have similar chemical structures to the aromatic PA active layer of a commercial NF membrane, the FilmTec[®] NF 90 membrane. Nonequilibrium molecular dynamics (NEMD) simulations are carried out to simulate pressure-driven pure water flows passing through the PA membranes. The membrane structures of the modeled PA membranes and the water transport properties are analyzed to investigate the effects of degree of cross-linking and electrical charges on the membrane structure and water transport. For the neutral PA membrane, the fractional free volume (FFV) and the free volume radius both decrease with increasing degree of cross-linking. The smaller the free volume radius of the PA membrane (with a higher degree of cross-linking) the lower the water flow, as expected for a real membrane. The negatively charged PA membrane exhibits a larger free volume radius but a lower water flux than the neutral PA membrane, due to the electrostatic interactions in the charged PA membrane and the electrostatic interactions

between water solution and the charged membrane. The PA membrane having a similar degree of cross-linking with the NF 90 membrane shows transport behavior similar to the experimental behaviour of a real NF 90 membrane.

8.2. Introduction

Membrane filtration has become a developed separation technology to separate or purify liquid/gas mixtures efficiently and economically. Applications of membrane separation technologies have become popular in biomedical devices, water treatment, metal ion recovery, and organic solute fractionation. Nanofiltration (NF) is one of the pressure-driven membrane processes and usually operated at a low pressure (0.5–2 MPa) yielding a high permeate flux and selectivity. The NF applications have increased worldwide, especially in water treatment field, such as water softening, organics removal, radium and heavy metal removal from wastewater, and sulfate removal from seawater.

The FilmTec[®] NF 90 membrane manufactured by DOW Company is one of several commercially successful NF membranes. The top layer of the NF 90 membrane is a cross-linked aromatic polyamide (PA) layer, which is fabricated through interfacial polymerization between trimesoyl chloride (TMC) and m-phenylene diamine (MPD) as shown in Figure 8.1. Some TMC monomer reacts incompletely with MPD monomers resulting in a cross-linked structure with unreacted acid chloride groups, which become carboxylic acid groups in aqueous solution. The degree of cross-linking, n (as in Figure 8.1), is defined by the percentage of cross-linked repeat units of the aromatic PA and the value is 25.6% evaluated by Kwon^[1]. The NF 90 membrane can be operated in a wide

pH range from 2 to 11 is a negatively charged membrane at $\text{pH} > \sim 5$, because the unreacted carboxylic acid groups are deprotonated to form negatively charged carboxylate anions.^[2]

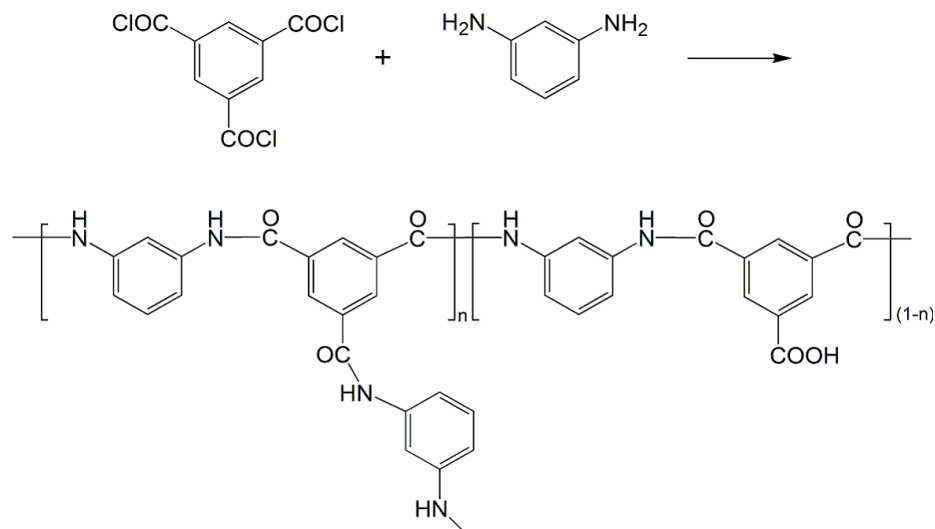


Figure 8.1 The reaction formula of the PA active layer of the NF 90 membrane (adapted from reference [3]): the degree of cross-linking, n , is with value in between 0–1 ($n=1$ for a fully cross-linking structure, and $n=0$ for a fully linear cross-linking structure).

There remains debate as to whether or not the polymeric top layer of a TFC NF membrane is porous or dense. Molecular dynamic (MD) simulations based on high-performance computing provide a new tool to study a polymeric membrane on a molecular scale. Today, MD simulations have been applied to model polymeric materials and to investigate liquid or gas transport properties of polymeric membranes.^[4-9] In some previous works,^[10-15] the cross-linked PA membranes are modeled through MD simulations as a commercial reverse osmosis (RO) membrane, the FilmTec[®] FT 30 membrane. The PA top layer of the FT 30 membrane is similar to that of the NF 90 membrane, so the MD simulation methods for modeling the FT 30 membranes can be

used for modeling the NF 90 membrane. The modeled FT 30 membranes are used to study diffusive behavior through MD simulations or liquid transport at high pressure differences (usually higher than 100 MPa) through nonequilibrium molecular dynamics (NEMD) simulations. Few works have been reported to model polymeric NF membranes and to study pressure-driven liquid transport at NF conditions through MD/NEMD simulations.

Generally, there are three ways to model the cross-linked structure of the PA membrane: firstly, two monomer cells contacting together to simulate interfacial polymerization,^[10, 11] secondly, TMC and MPD monomers randomly mixed in a simulation box to simulate traditional polymerization,^[12, 13] thirdly, modeling linear PA polymers first and then adding MPD cross-linkers between the PA polymers to simulating cross-linking.^[14, 15] The simulation of polymerization (the first or second method) is close to the real membrane fabrication, but needs a reasonable force field to define the molecules/polymers continually formed in the polymerization simulation. The third simulation method only needs to parameterize the polymer and the cross-linker, which is usually easier and faster than the polymerization simulation. Moreover, the degree of cross-linking is hard to be controlled in the polymerization simulation, while the degree of cross-linking is easily controlled in the cross-linking simulation because of the degree of cross-linking depending on the number of the cross-linkers inserted in the polymers.

In our previous work, a MD simulation method derived from a collapsing-annealing MD procedure^[6] is introduced to model uncross-linked PA membranes, and the pressure-driven water transport properties of the modeled PA membranes are investigated

through NEMD simulations.^[16] In this work, neutral PA membranes with different degrees of cross-linking and negatively charged PA membranes are modeled by using a MD simulation method derived from the cross-linking simulation method for the FT 30 membrane (inserting cross-linkers in an uncross-linked membrane,^[14, 15] as introduced above). NEMD simulations are carried out to study pure water transport of the cross-linked PA membranes at low pressure differences (from 1.0 MPa to 10 MPa). The effects of degree of cross-linking and electrical charges on the membrane structure and water transport properties are investigated. This work to study water transport through a PA membrane model at a low pressure difference can reveal fundamentals of a real ND process, can be useful in designing and modifying real membrane processes, and show a molecular scale result about the debate of porous/dense given above.

8.3. Simulation Methods

All simulation works are performed by VMD package^[17] and NAMD package^[18] in CHARMM General Force Field^[19]. The flexible TIP3P (transferable intermolecular potential three-point) water model^[20] are used to describe water molecules. The detailed simulation methodology (MD integration algorithm, calculations of long-range interactions, temperature/pressure control, etc.) is the same as in our previous work.^[16]

8.3.1. Modeling of cross-linked PA membranes

The cross-linked structure of a PA membrane is modeled by inserting MPD cross-linkers between the carboxylic acid groups of linear PA polymers, as shown in Figure 8.2, which is derived from the method for modeling FT 30 RO membrane.^[14, 15]

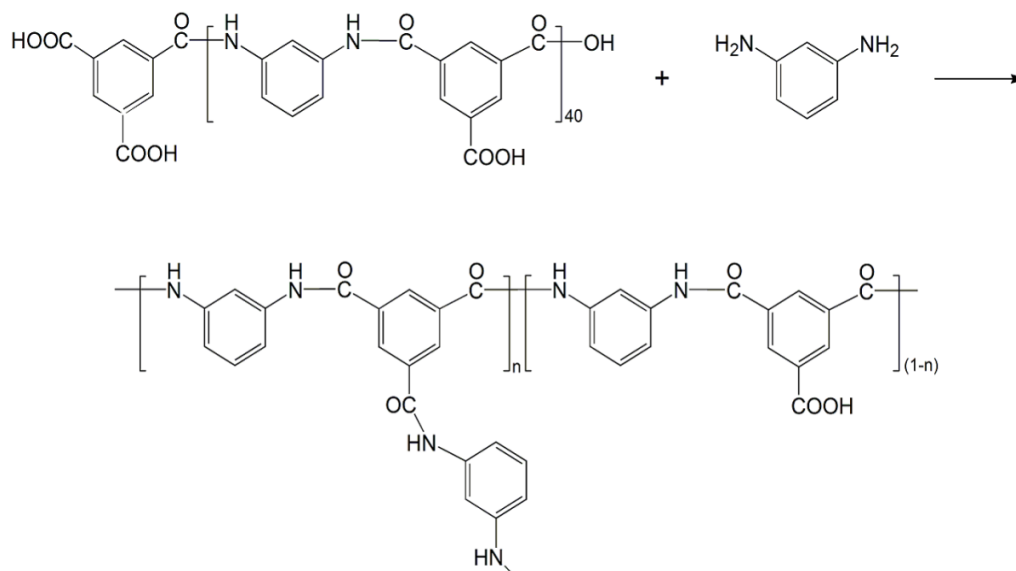


Figure 8.2 Inserting MPD cross-linkers between carboxylic acid groups of different PA reactants to form a cross-linked structure. The degree of cross-linking, n , is decided by the number of MPD cross-linkers inserted in the uncross-linked membrane model.

An initial uncross-linked PA membrane composed of several linear PA polymers is modeled through MD simulations as reported in our previous work.^[16] The linear PA polymer has a total of 40 repeat units; the two end groups of the PA polymer are both carboxyl acid groups, as shown in Figure 8.3. The force field parameters for PA and MPD are derived in analogy to known parameterized molecules and from the topology and parameter files for the CHARMM General Force Field.^[19] 20 unit PA polymers are used to construct the initial PA membrane having a cubic shape of the size in $7.0 \text{ nm} \times 7.0 \text{ nm} \times 7.0 \text{ nm}$. The MD simulation procedures are similar as in our previous work^[16] and not depicted here. The uncross-linked PA membrane does not need to be cooled to 300 K through a cooling MD simulation, and all MD simulations are carried out at 1000 K and vacuum.

In the initial PA membrane, any two carboxylic acid groups of two different PA polymers can be selected to form a cross-linked structure with a MPD cross-linker, and the selectivity is decided by the distance between the two oxygen atoms of the hydroxyl groups. The O–O distance should be within 0.5 ± 0.2 nm, and a MPD molecule is placed between the selected pair of the carboxylic acid groups. The cross-linking structure between two carboxylic acid groups with a MPD molecule is achieved by creating two C-N bonds and by deleting two hydroxyl groups of the carboxylic acid groups and two hydrogen atoms of the amino groups. The number of MPD cross-linkers is dependent on the desired degree of cross-linking, and the pairs of carboxylic acid groups are picked randomly among all optional pairs to form a cross-linked PA membrane.

The cross-linked PA membrane is energy-minimized and equilibrated for 5.0 ns in an isothermal–isobaric (NPT) ensemble (1000 K and 0.1 MPa) with three-dimensional PBC. Then the equilibrated PA membrane is cooled to 300 K through a cooling MD simulation in a cooling rate of 50 K/ns at 0.1 MPa with PBC. After the temperature reaches 300 K, a MD simulation is carried out for 4.0 ns at 300 K and 0.1 MPa with three-dimensional PBC to generate a dry amorphous cross-linked PA membrane. All simulations for modeling dry and hydrated membranes use 1.0 fs time step. Four PA membranes are modeled with the same membrane size ($7.0 \text{ nm} \times 7.0 \text{ nm} \times 7.0 \text{ nm}$) but with different degrees of cross-linking (listed in Table 8.1). Figure 8.3 shows a snapshot of the #3 PA membrane with a degree of cross-linking of 25%. A hydrated PA membrane is modeled

through a MD simulation of the dry PA membrane dissolved in a large water box, as introduced in our previous work.^[16]

Table 8.1 Parameters in the membrane modeling and NEMD simulations.

PA membranes	Number of Cross-linkers	Degree of cross-linking (%)	Neutral or Charged	ΔP (MPa)
#1	0	0	Neutral	1.0, 3.0, 6.0, and 10
#2	21	10	Neutral	1.0, 3.0, 6.0, and 10
#3	102	25	Neutral	1.0, 3.0, 6.0, and 10
#4	164	40	Neutral	1.0, 3.0, 6.0, and 10
#5	102	25	Negatively Charged (deprotonated half of the -COOH groups)	10
#6	102	25	Negatively Charged (deprotonated all the -COOH groups)	10
NF 90		25.6% ^[1]	Negatively Charged at pH = 7	

Each negative charge of the charged PA membranes is formed by deprotonating a carboxylic acid groups of the neutral membrane to generate a carboxylate ion ($-\text{COO}^-$). Two negatively charged membranes (#5 and #6 membranes in Table 8.1) are derived by deprotonating half of and all the remaining carboxylic acid groups of the #3 membrane, respectively. A hydrated negatively charged membrane is generated through a similar MD simulation as the neutral membrane,^[16] but counter ions (Na^+) need to be randomly

added in the water box to neutralize the simulation system, due to the PME method requiring a neutral system.

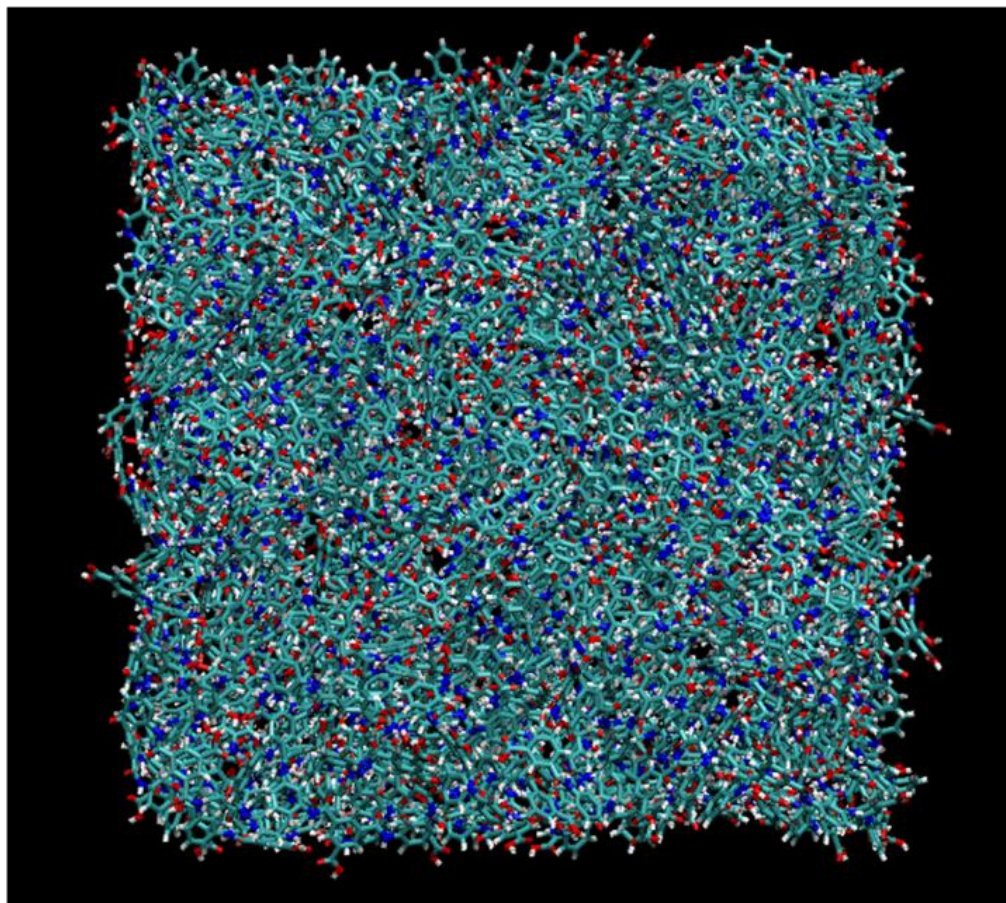


Figure 8.3 A snapshot of the dry (prehydrated) #3 PA membrane with the degree of cross-linking of 25% (Table 8.1). Molecules are shown by bonds: carbon atoms in green, hydrogen atoms in white, oxygen atoms in red, and nitrogen atoms in blue.

The resulted water box containing the hydrated neutral or negatively charged PA membrane is used to construct a NEMD simulation system for simulating pressure-driven water transport through the PA membrane.

8.3.2. Molecular dynamics simulations of water transport

The NEMD simulation methodology in this work, such as constructing the NEMD simulation system and the detailed simulation procedures, is almost the same as introduced and discussed in our previous work,^[16] except for using the modeled cross-linked PA membranes and adding counter ions in the NEMD simulation system containing a charged membrane. The NEMD system used here is chosen to reduce computational demands compared with the other system we proposed,^[21] and here each NEMD simulation using 2.0 fs time step takes about 10 CPU days per nanosecond.

Figure 8.4 shows an example NEMD simulation system in Cartesian coordinates used for simulating a pressure-driven water flow passing through the membrane along the $z+$ direction. The system includes a hydrated #3 membrane (fixed at the position during simulations) and two water reservoirs connected by the membrane along the flow direction, and the top and bottom water reservoirs both have the same size of $7.0 \text{ nm} \times 7.0 \text{ nm} \times 3.0 \text{ nm}$. For the negatively charged PA membrane, additional counter ions (Na^+) should be randomly added in the water reservoirs to neutralize the NEMD simulation system.

The water transport properties of each PA membrane are studied through three NEMD simulation systems to simulate pressure-driven water flows passing the same membrane along three ($x+$, $y+$, and $z+$) directions. To avoid the spatial differences of the cubic membrane, the transport properties are averaged by the simulation results of the three systems. The pressure difference in each NEMD simulation is achieved by applying a constant external force along the flow direction ($x+$, $y+$, or $z+$ direction) on each oxygen

atom and/or Na^+ ion of two water control layers near the top and bottom boundaries of the system. The pressure difference equals to the total forces divided by the membrane area, and four pressure differences (1.0 MPa, 3.0 MPa, 6.0 MPa, and 10 MPa) are kept to investigate the effect of pressure difference on the water transport phenomenon.

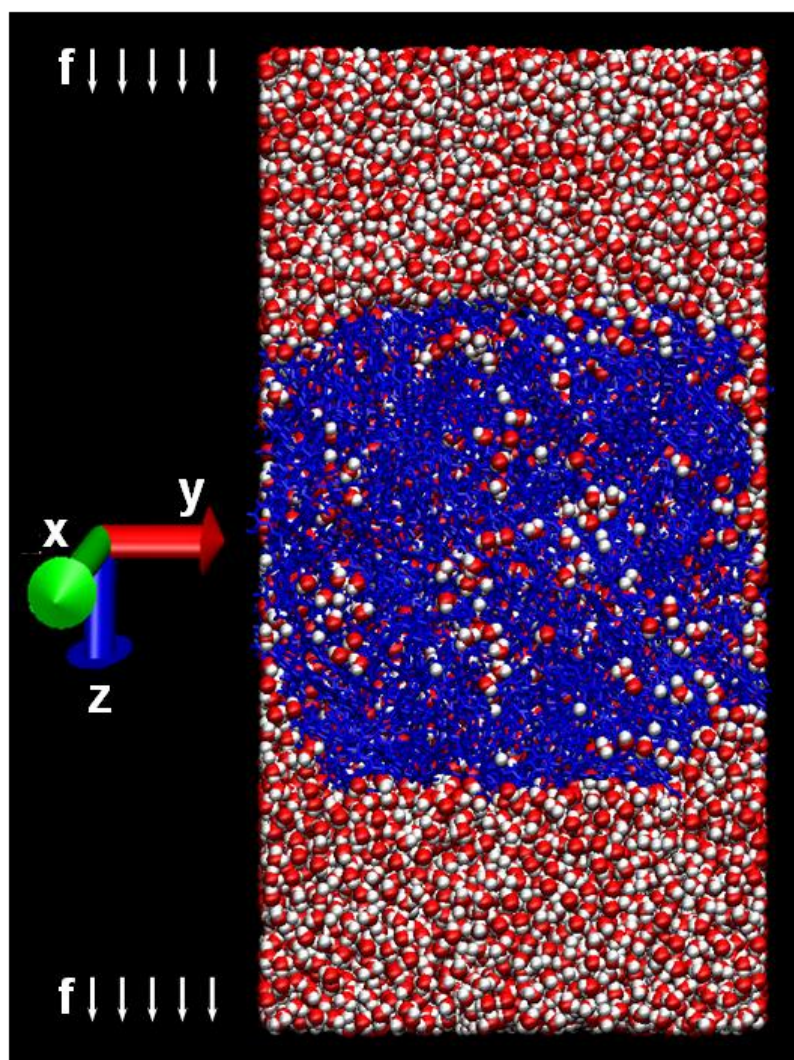


Figure 8.4 The snapshot of the NEMD simulation system including the PA membrane model and two water reservoirs to simulate pressure-driven water flow along the $z+$ direction. The PA membrane shown by bonds in blue; the hydrogen atoms and oxygen atoms of water molecule showed by van der waals atoms in white and red, respectively. The external force (f) is applied on each water molecule of the two water control layers near the top and bottom boundaries along the $z+$ direction.

8.4. Results and Discussion

The membrane structure (membrane density, the fractional free volume (FFV), and free volume radius) of each cross-linked PA membrane is analyzed from the dry and hydrated PA membranes. Kruse^[22] introduced a method to analyze the free volume properties of a polymeric cell through the “accessible free volume”, which is determined by the unoccupied space of a polymeric cell and evaluated by using small standard spherical tracers to fill the unoccupied space. Based on the Kruse’s method,^[22] the authors^[16] evaluated the FFV, number average radius, and mean radius of an uncross-linked membrane by using water molecules as tracers. The mean radius is viewed as a more reasonable value than the average radius to represent the PA membrane, since the mean radius is evaluated from the membrane FFV with considering the relative contribution of pore sizes and pore numbers.^[16, 22] In this work, the tracers are water molecules with an accessible radius of 0.14 nm^[23] and Na⁺ ions with an accessible radius of 0.2 nm^[10] to evaluate the FFV and free volume radius (mean radius) of the cross-linked PA membrane. The detailed analysis of the cross-linked PA membrane structure is not explicated in this article. Note the free volume radius is measured from free volume holes in the membrane including closed holes and open holes (passing through the membrane), and only the open holes through the membrane are membrane pores which significantly affect the membrane transport properties. Here we use the free volume radius to represent the pore size of the membrane, as the free volume pore size is related to the free volume properties.

The water flux, defined as the number flow rate per membrane area, is analyzed from

the trajectory data of the NEMD simulation and is calculated in the units of both ‘molecules/(ns nm²)’ and ‘m³/(m²·s)’ or equivalently ‘m/s’. The flux calculation and the error evaluation are similar as in our previous work for studying water through CNT membranes.^[24] The water flux of each PA membrane at a certain pressure difference is averaged by the water fluxes of water flows along three axial directions (the $x+$, $y+$, or $z+$ directions), and the estimated error of the average flux is also averaged by the three errors of the water fluxes.

8.4.1. The effect of degree of cross-linking

The properties of the #1–4 membranes with different degrees of cross-linking are shown in Table 8.2, including the densities of the dry and hydrated membranes, FFV values, and free volume radii.

As the degree of cross-linking increases, the density of the dry membrane increases slightly, the density of the #4 membrane is about 5% higher than that of the #1 membrane (uncross-linked membrane). This slightly increasing density is caused by more cross-linkers added in the membrane model and the MPD molecule as the cross-linker of a lower molecular mass than the PA molecule. The density of the hydrated membrane depends on the number of water molecules filling the free volume of the membrane, so the hydrated membrane density is higher than the dry membrane density. The hydrated densities of the four membranes are almost the same, which indicates fewer water molecules fill the membrane with a higher degree of cross-linking. As expected, the cross-linked structure can reduce the free volume of the PA membrane. The free volume

properties are represented by the FFV value and the free volume radius, which both decrease with increasing the degree of cross-linking from 0 to 40%. Unlike the slightly increasing trend of the dry membrane density, the FFV and free volume radius of the #4 membrane decrease to about 70% and 60% of the values of the #1 membranes, respectively. Apparently, the FFV and the free volume radius of the PA membrane can better show the cross-linked structure than the membrane density.

Table 8.2 Properties of #1–4 membranes with different degrees of cross-linking.^{a,b}

PA membranes	Degree of cross-linking (%)	Membrane density (kg/m ³)		FFV (%)	Free volume radius, r_p (nm)
		Dry	Hydrated		
#1	0	1109	1409	9.18	0.41
#2	10	1123	1409	8.63	0.38
#3	25	1143	1407	7.89	0.33
#4	40	1163	1401	6.70	0.25

^aThe conditions are: T = 300 K, P = 0.1 MPa.

^bThe results are based on the whole 7.0 nm × 7.0 nm × 7.0 nm membrane.

For an amorphous polymeric membrane, the water transport properties are dominated by the free volume properties. Figure 8.5 shows the water flux as a function of the degree of cross-linking at each pressure difference, where the water flux decreases with increasing degree of cross-linking due to the decreasing free volume radius as shown in Table 8.2. As shown in Table 8.2, the free volume radii of the cross-linked membranes

are about 60% – 92% of the free volume radius of the uncross-linked membrane (#1), while the fluxes of the cross-linked membranes are about 5% – 40% of the flux of the #1 membrane as shown in Figure 8.5. As expected, the water flow is driven faster at a higher pressure difference; the fluxes of the four membranes are plotted as the water flux with respect to the pressure difference (from 1.0 MPa to 10 MPa) in Figure 8.6. As the pressure difference increases, the water flux increases proportionally for each membrane; the proportional relationship between the water flux and the pressure difference is shown by the linear trend line through the origin (as expected in Eqn. (8.1)). The water permeability coefficient of each membrane can be calculated by the slope of the linear trend line (through the origin) in Figure 8.6.

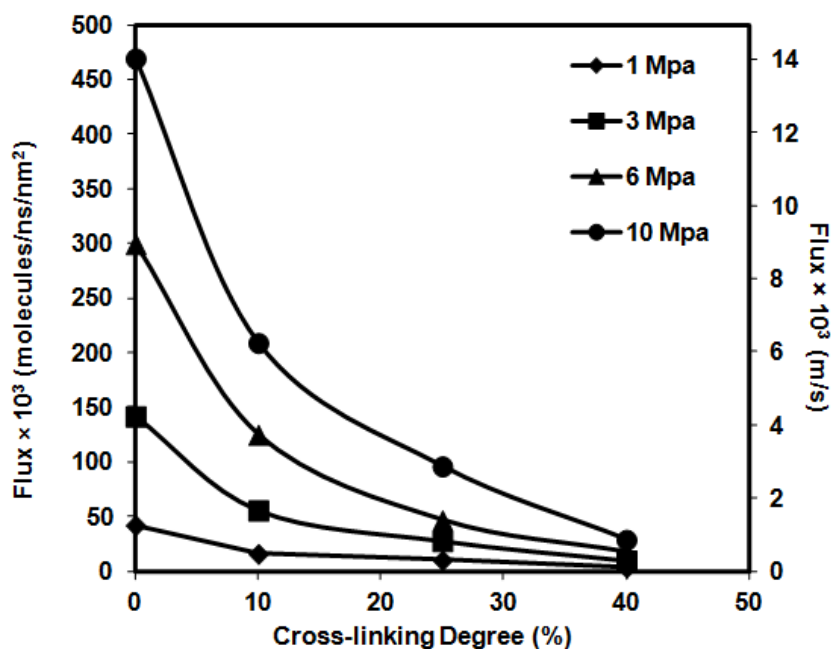


Figure 8.5 Flux (rate per membrane area) at each pressure difference, shown both as molecular flux and conventional flux (in m/s), as a function of the cross-linking degree. The statistical error for each data point is evaluated and less than 10%. The points are based on the NEMD simulations on the #1–4 membranes (Table 8.1): $L = 7.0$ nm; and $T = 300$ K. The solid curves are the trends based on the simulation results.

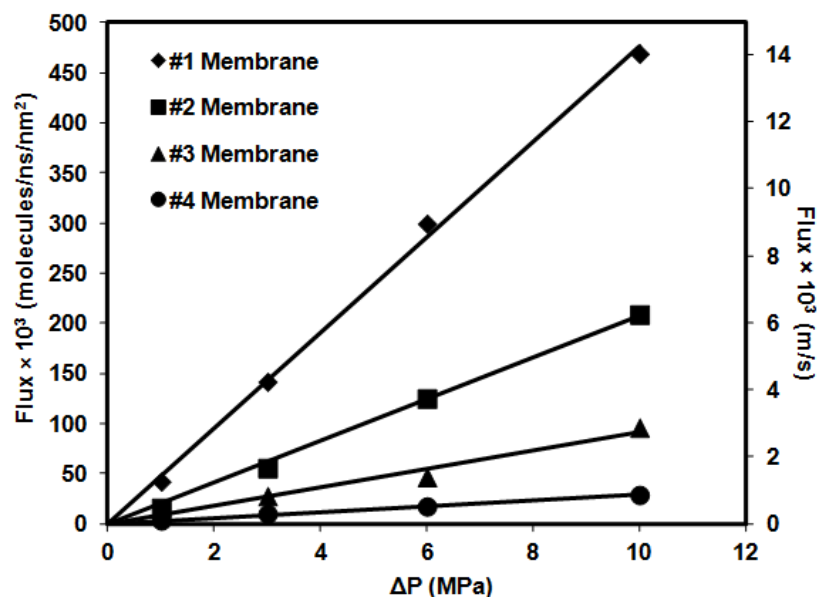


Figure 8.6 Flux (rate per membrane area) of each PA membrane, shown both as molecular flux and conventional flux (in m/s), as a function of the pressure difference. The statistical error for each data point is evaluated and less than 10%. The points are based on the NEMD simulations on the #1–4 membranes (Table 8.1): $L = 7.0$ nm; and $T = 300$ K. The solid lines are the linear trends through the origin based on the simulation results.

Figure 8.7 shows the water permeability coefficient as a function of the free volume radius (listed in Table 8.2), where the permeability coefficient decreases quickly with decreasing the free volume radius from 0.41 nm of the #1 membrane to 0.25 nm of the #4 membrane. The significant effect of free volume radius on the water permeability is caused by the small molecular size of water, 0.14 nm in the van der Waals molecular radius,^[23] which is a fractional value of the nanoscale membrane pore size. For example, the #1 membrane shows the highest permeability coefficient which is about 15 times of the #4 membrane, but the free volume radius of the #1 membrane is less than twice of the free volume radius of the #4 membrane. It can be imaged that the NF membrane with a larger free volume radius could exhibit a much faster pressure-driven water flow or the

water flow could be rejected by a NF membrane with a smaller free volume radius (a nonporous NF membrane).

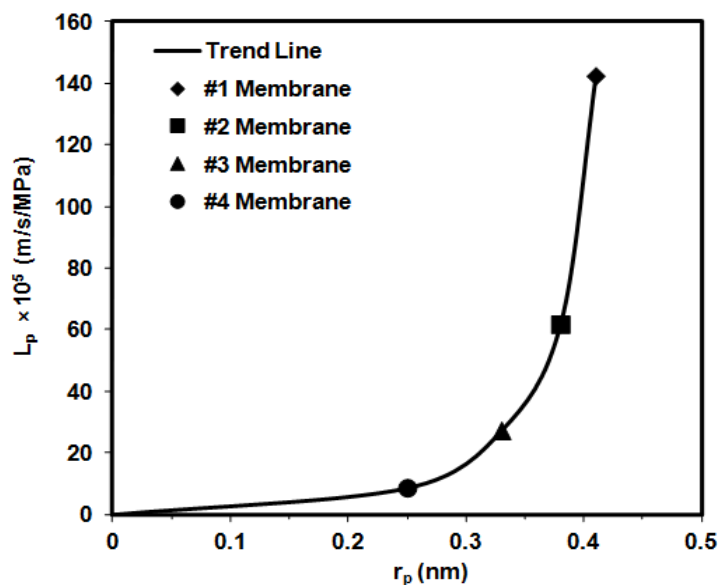


Figure 8.7 Water permeability coefficient as a function of the free volume radius. The solid curve is the trend through the origin based on the simulation results. The radii of the #1–4 PA membrane are shown in Table 8.2; and the standard error of each water permeability coefficient is evaluated from the linear regression of the linear trend (through the origin) in Figure 8.6 and is less than 10%.

To compare the #1–4 PA membranes with the real NF 90 membrane, the membrane properties (free volume radius, membrane thickness, and water permeability coefficient) of each membrane are shown in Table 8.3. The properties of the NF 90 membrane in Table 8.3 are measured and calculated by experimental approaches.^[25] The pore radius of the NF 90 membrane is close to the free volume radius of the #3 membrane (Table 8.2), while the water permeability coefficient of the NF 90 membrane is much lower than that of the #3 membrane (Table 8.3) due to the effect of membrane thickness. We cannot simply conclude that the #3 membrane has same membrane properties as the NF 90 membrane just because through the similar radii, since the two radii are measured based

on different methods/assumptions.

Table 8.3 Comparisons of the PA membranes and the NF 90 membrane.

PA membranes	Free volume radius ^a , r_p (nm)	Thickness, L (nm)	Water permeability coefficients ^b , $L_p \times 10^5$ (m/s/MPa)	$L \times L_p \times 10^{14}$ (m ² /s/MPa)
#1	0.33	7.0	142.5	997.5
#2	0.31	7.0	61.8	423.6
#3	0.27	7.0	27.3	191.1
#4	0.22	7.0	8.65	60.55
NF 90 ^[25]	0.34	174 ^b	1.78	309.72

^aThe free volume radius results are analyzed through water molecules located within the central 6.0 nm \times 6.0 nm \times 6.0 nm part of each hydrated PA membrane.

^bThe standard error of each water permeability coefficient is evaluated from the linear regression of the linear trend (through the origin) in Figure 8.6 and is less than 10%.

^cThe thickness of the NF 90 membrane is an average value of 134-214 nm.^[25]

The water permeability coefficient is inversely proportional to the membrane thickness, as described by the Hagen-Poiseuille equation.

$$J_w = L_p \Delta P = \frac{r_p^2}{8\eta\tau(L/A_K)} \Delta P \quad (8.1)$$

where L_p is the pure water permeability coefficient, r_p is the pore radius of the membrane, η is the viscosity of the liquid fluid at the operating temperature, τ is the pore tortuosity, L/A_K is the ratio of the membrane effective thickness to the surface porosity, and ΔP is the pressure difference. The Hagen-Poiseuille equation is usually used to predict the pure

water flux of a NF membrane.

A parameter calculated by the product of the permeability coefficient (L_p) and the membrane thickness (L) is shown in Table 8.3 to compare the real NF membrane with the modeled membranes. Unlike the similar radii of the NF 90 membrane and the #3 membrane in Table 8.2, the water transport property of the NF 90 membrane is between the properties of the #2 and #3 membranes based on the parameters (shown in the right column of the Table 8.3) with considering the effect of membrane thickness. While the water transport properties of the NF 90 and #3 membranes are on the same order of magnitude.

The deviation of the transport properties between the NF 90 and #3 membranes is probably caused by the modeled PA membrane without terminal amino groups and/or the uncertain physiochemical membrane structure of the NF 90 membrane characterized by experimental approaches. For example, the degree of cross-linking and pore radius of the NF 90 membrane are evaluated in different values from other experimental works,^[26-28] and the membrane thickness of the NF 90 membrane used in this work is an average value of a thickness range evaluated experimentally by Nghiem.^[25] In general, the simulation methods introduced in this work are feasible to model a PA membrane as the real NF 90 membrane and to study the membrane structure and water transport properties.

8.4.2. The effect of electrical charge

The membrane surface of the NF 90 membrane becomes negatively charged when the

membrane contacts with the feed solution of a pH value higher than 4, due to the deprotonated carboxylic acid groups. The surface charge density of the NF 90 membrane increases with increasing pH value of the solution.^[2, 25, 28] The content of the COO⁻ groups in the NF 90 membrane surface (within 5 nm) is about 33% higher than in the whole PA active layer of the NF 90 membrane (111 ± 56 nm).^[26, 27] The modeled membrane of a 7.0 nm thickness is much thinner than the PA active layer of the NF 90 membrane, thus the modeled PA membrane is viewed as the charged surface of the NF 90 membrane in this study. The negatively charged membranes (the #5 and #6 membranes in Table 8.1) both have much higher volume charge densities than the NF 90 membrane surface, in order to clearly show the effect of electrical charges on the membrane structure and pressure-driven water transport.

Table 8.4 shows the membrane structure properties of the neutral (#3) and negatively charged (#5 and #6) membranes, where the dry densities of the three membranes are similar but the hydrated densities increase with increasing negative charges of the membrane. In Figures 8.8 and 8.9 the water and ion distributions along the flow direction for the neutral and negatively charged membranes are illustrated. The equilibrated NEMD simulation system is used to show the water and ion distributions from the top reservoirs to the bottom reservoir (the flow direction), and the results of the three systems for the same PA membrane are averaged to represent the membrane properties. Each density profile in Figures 8.8 and 8.9 is the average for density profiles in each of the $x+$, $y+$, and $z+$ directions, and the water or ion density (kg of water or ions/(kg of wet membrane)) in the membrane is based on the volume of the thin cuboid

section (7.0 nm × 7.0 nm × 0.4 nm).

Table 8.4 Properties of the neutral and negatively charged membranes.^a

PA membranes	Neutral or Charged	Membrane density ^b (kg/m ³)		FFV ^c (%)	Free volume radius ^c , r_p (nm)
		Dry	Hydrated		
#3	Neutral	1143	1407	7.89	0.27
#5	Deprotonated half of the -COOH groups	1117	1483	13.6	0.35
#6	Deprotonated all the -COOH groups	1096	1524	18.5	0.37

^aThe conditions are: T = 300 K, P = 0.1 MPa.

^bThe results are based on the whole 7.0 nm × 7.0 nm × 7.0 nm membrane.

^cThe FFV and radius results are analyzed through water molecules located within the central 6.0 nm × 6.0 nm × 6.0 nm part of each hydrated PA membrane.

As shown in Figure 8.8, the nearly constant water density in the #5 or #6 membrane (shown by the dotted lines in Figure 8.8) is at least 1.3 times of that in the #3 membrane, which suggests that more water molecules are allowed to fill the charged membrane than the uncharged membrane. The ions distributions in Figure 8.9 shows that the ions density profile in the bulk solution is lower than in the membrane and the highest ions densities are near the membrane surfaces. It can be seen that the ion densities at the position within $\pm(4.5 - 5.5)$ nm are about 11% – 22% of the nearly constant densities in the membrane (shown by the dotted lines in Figure 8.9). The ions in the water solutions

are used to neutralize the simulation system for the charged membrane, so it is obvious that the number of ions is dependent on the number of charged groups in the membrane. Therefore, the ion densities in the #5 membrane are about half of the densities in the #6 membrane. However, for each charged membrane, most ions remain close to the charge groups, as the energy required to move an ion very far away from the balancing fixed charge are huge.

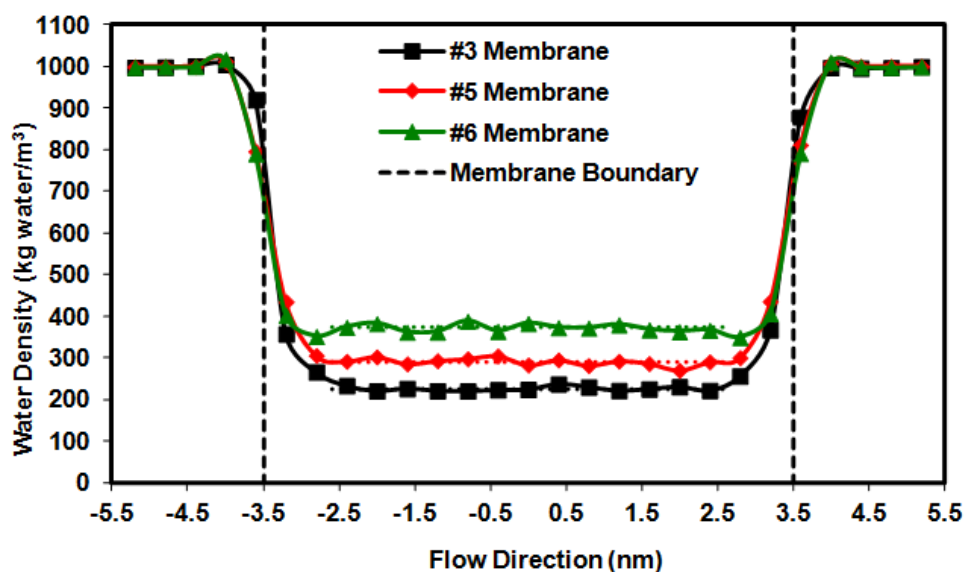


Figure 8.8 Average water density distributions along the $x+$, $y+$, and $z+$ directions for the #3, #5, and #6 PA membranes (see Table 8.1). The points of each membrane are based on the equilibrated status of the NEMD system at 300 K and 0.1 MPa. Each data point is the average of three density values from the cuboid sections at the same position along the $x+$, $y+$, and $z+$ directions; and the standard error of the three densities is less than 10% for most average density values. The solid lines are the trend curves based on the simulation results, and the dotted lines are the average densities from -2.6 nm to 2.6 nm. The dashed lines are the membrane boundaries along the flow direction separating the system in to three parts from left to right: the water reservoir at the high pressure side, the PA membrane, and the water reservoir at the low pressure side.

The hydrated membrane densities in Table 8.4 and the density profiles in Figures 8.8 and 8.9 show that there are more water molecules and Na^+ ions filling the membrane with

more negative charges, due to the increasing electrostatic interactions between water solution and the membrane. Consequently, an increasing FFV value is evaluated from the increasing number of water molecules and ions in the membrane, shown in Table 8.4. The carboxylate anion groups in the negatively charged membrane have a little smaller occupied volume than the carboxylic acid groups in the neutral membrane, which cannot significantly increase the FFV of the charged membrane. The negative charges in the membrane attract more water molecules and Na^+ ions located in the charged membrane, resulting in a higher FFV value of the charged membrane.

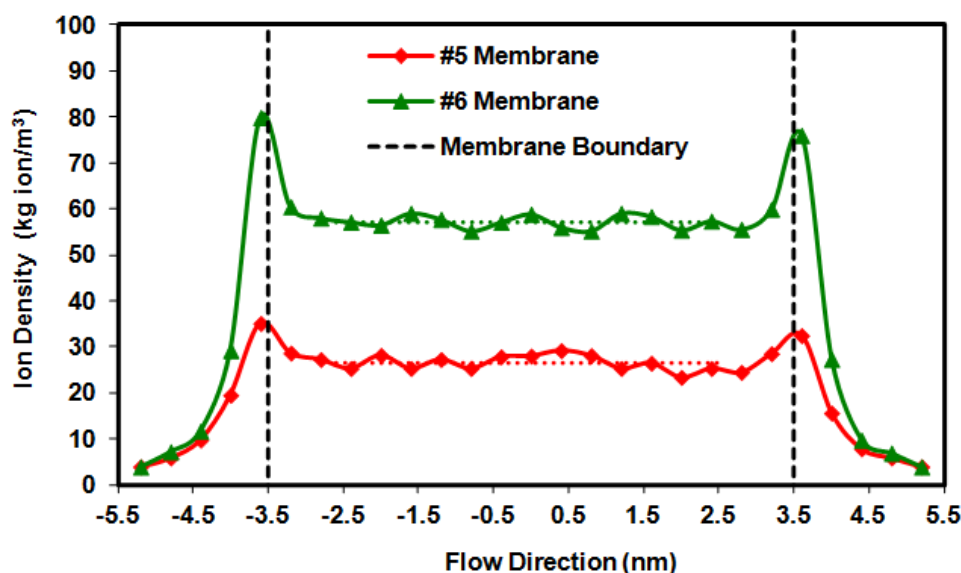


Figure 8.9 Average ion density distributions along the $x+$, $y+$, and $z+$ directions for the #3, #5, and #6 PA membranes (see Table 8.1). The points of each membrane are based on the equilibrated status of the NEMD system at 300 K and 0.1 MPa. Each data point is the average of three density values from the cuboid sections at the same position along the $x+$, $y+$, and $z+$ directions; and the standard error of the three densities is less than 10% for most average density values. The solid lines are the trend curves based on the simulation results, and the dotted lines are the average densities from -2.6 nm to 2.6 nm. The dashed lines are the membrane boundaries along the flow direction separating the system into three parts from left to right: the water reservoir at the high pressure side, the PA membrane, and the water reservoir at the low pressure side.

As shown in Table 8.4, the free volume radius, evaluated from the FFV, increases with

increasing negative charges of the membrane. The water molecules and ions in the hydrated membrane only exist in the free volume space, and more water and ions filling the free volume can inflate the free volume spaces in larger volumes. In addition, the repulsive electrostatic interaction between each pair of the carboxylate anion groups of the charged membrane replaces the hydrogen bond interaction between the corresponding pair of the carboxylic acid groups of the neutral membrane. The repulsive electrostatic interactions in the charged membrane may contribute to a larger distance between a pair of the carboxylate anion groups, resulting in larger free volume. Therefore, the larger free volume radius of the charged membrane is caused by more water/ion in the membrane interactions and/or the PA – PA electrostatic interactions.

The water fluxes of the neutral and negatively charged membranes at the pressure difference of 10 MPa are shown in Figure 8.10, where the water flux decreases with increasing negatively charges of the membrane. The ion fluxes of the charged membranes are quite lower than the water fluxes and not shown here. The decreasing water flux is also observed experimentally by Childress,^[29] who experimentally studied the commercial NF 55 membrane with a similar chemical structure of the NF 90 membrane. Childress^[29] found that the water flux of the NF 55 membrane decreases with increasing the pH value of the feed solution from 5 to 9 and concluded that the decreasing water flux is caused by the decreasing pore size. The electrostatic repulsion between the charged COO⁻ groups contributes to an extended chain configuration of polymer and then reduces the pore size.^[29] However, the simulation results in this work show the negatively charged membrane has a larger free volume radius but a lower water

flux. The PA membrane used in our simulation study is a nanoscale model composed of 20 PA polymers and several MPD monomers, while the real NF 90 membrane has a complicated configuration of polymers in the membrane due to the larger membrane area and thickness. Moreover, the number of charged COO⁻ groups in the #5 or #6 membrane is set as a limit value (50% or 100% of the remained carboxylic acid groups) in order to remarkably observed the effect of membrane charge. The carboxylic acid groups in the NF 90 membrane cannot be deprotonated fully in a solution to reach such a high charge density as modeled in the #5 or #6 membrane. The small simulation size and high charge density may cause that the reducing pore size due to the extended polymer chains is not observed in our simulation study here. A reducing pore size or closing pore in a charged membrane is as one might expect.

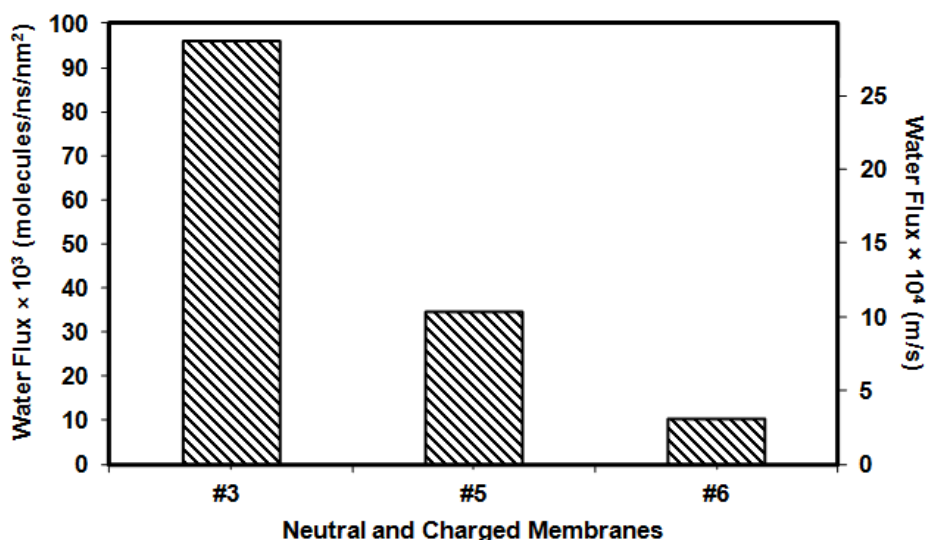


Figure 8.10 Bar chart of the water fluxes, shown both as molecular flux and conventional flux (in m/s), of the neutral (#3) and negatively charged membranes (#5, #6). The statistical error for each data point is evaluated and less than 10%. The results are based on the NEMD simulations: $L = 7.0$ nm; $T = 300$ K; and $\Delta P = 10$ MPa.

In this work, as the water solution passes through the negatively charged membrane,

the attractive forces applied on the water molecules in the charged membrane restrict the movement of the water solution to pass through the membrane. Moreover, the Na^+ ions remain close to the charge groups (stick on the membrane and pore surfaces), which blocks the effective space where the water solution passes through the membrane. Therefore, the lower water fluxes (in Figure 8.10) and negligible ion fluxes of the negatively charged membranes are observed, which is caused by a combination of the solution–membrane interactions and the reduced effective space in the membrane.

The effective space of the free volume pores for allowing the water solution to pass through the charged membrane can be view as the effective pore size. The effective pore size decreases with increasing negative charges of the membrane, contributing to the decreasing flux. The experimental pore size is usually evaluated from a series of retention experiments using uncharged organic solutes and calculated from an empirical mathematical modeling, like in Nghiem's work^[25]. The resulted pore size through an experimental measurement is the effective pore size of an amorphous polymeric membrane, which cannot show the real configuration of the free volume pores. While, the free volume radius is a mean value of all free volume holes including free volume pores, and the larger free volume radius of the charged membrane may imply larger free volume pores formed. The simulation study in this work provides a direct way to show the free volume properties and the water transport properties.

8.5. Conclusions

This study introduced MD/NEMD simulation approaches to model amorphous

cross-linked PA membranes as NF membranes and investigated pressure-driven water flows through the modeled PA membranes at low pressure differences.

Four neutral PA membranes are modeled to have different degrees of cross-linking from 0 to 40%. As the degree of cross-linking increases, the FFV and the free volume radius both decrease. The membrane with a higher degree of cross-linking shows a slower pressure-driven water flow due to the cross-linking structure of the membrane. For each neutral PA membrane, the water flux increases with increasing pressure difference and the water permeability coefficient decreases with increasing degree of cross-linking. For the modeled PA membrane with a similar degree of cross-linking to the real commercial NF 90 membrane, the simulation transport property is close to the experimental result with considering the effect of membrane thicknesses and the discrepancy between the simulation and experimental results is acceptable.

Two negatively charged PA membranes with different numbers of negative charges are modeled to investigate the effect of electrical charges on the membrane structure and pressure-driven water transport. The negatively charged PA membrane shows a larger free volume radius but a lower water flux than the neutral PA membrane. The larger free volume radius of the charged membrane is caused by more water/ion filling the free volume and/or the deformation of PA polymer chains. The ions sticking on the charged pore surfaces reduce the effective free volume space for water passing through the charged membrane, resulting in the lower water flux of the charged membrane. The reduced water transport of the charged membrane in this simulation study is similar to the experimental conclusion for a real PA NF membrane.

The MD/NEMD simulations to study pressure-driven water flows at NF operating conditions can give molecular scale results of the PA membrane morphologies and water transport properties. This simulation study shows the relationship between membrane structure and water transport, which can be expected to provide a deeper understanding of polymeric NF membranes and to improve NF membranes. The improvement of NF membranes will be helpful for achieving better NF performance, particularly for water treatment and environmental applications.

References

- [1] Y. Kwon, C. Y. Tang, and J. O. Leckie, *J. Appl. Polym. Sci.* **108** 2061 (2008).
- [2] C. Bellona and J. E. Drewes, *J. Membr. Sci.* **249** 227 (2005).
- [3] FILMTEC™ Reverse Osmosis Membranes Technical Manual, Dow Water & Process Solutions.
- [4] L. Fritz and D. Hofmann, *Polymer* **38** 1035 (1997).
- [5] S. K. Patel, A. Lavasanifar, P. Choi, *Biomaterials* **31** 345 (2010).
- [6] E. R. Cruz-Chu, T. Ritz, Z. S. Siwy, and K. Schulten, *Faraday Discuss.* **143** 47 (2009).
- [7] S. Neyertz and D. Brown, *Macromolecules* **37** 10109 (2004).
- [8] A. A. Gusev and U. W. Suter, *J. Chem. Phys.* **99** 2228 (1993).
- [9] J. R. Fried, M. Sadat-Akhavi, and J. E. Mark, *J. Membr. Sci.* **149** 115 (1998).
- [10] J. Pitera, T. Chen, Y. Na, R. Sooriyakumaran, A. Vora, and G. Dubois.

Computational modeling of reverse osmosis membrane active layers: structure and transport, (NAMS Annual Meeting, Las Vegas, USA, 2011).

- [11] R. Nadler and S. Srebnik, *J. Membr. Sci.* **315** 100 (2008).
- [12] E. Harder, D. E. Walters, Y. D. Bodnar, R. S. Faibish, and B. Roux, *J. Phys. Chem. B* **113** 10177 (2009).
- [13] Y. Luo, E. Harder, R. S. Faibish, B. Roux, *J. Membr. Sci.* **384** 1 (2011). [14] M. J. Kotelyanskii, N. J. Wagner, and M. E. Paulaitis, *Comput. Theor. Polym. Sci.* **9** 301 (1999).
- [15] Z. E. Hughes and J. D. Gale, *J. Mater. Chem.* **20** 7788 (2010).
- [16] L. Wang, R. S. Dumont, and J. M. Dickson, "Molecular dynamics simulations of pressure-driven water transport through polyamide membranes", to be submitted (2012).
- [17] W. Humphrey, A. Dalke, and K. Schulten, *J. Mol. Graphics* **14** 33 (1996).
- [18] J. Phillips, R. Braun, W. Wang, J. Gumbart, E. Tajkhorshid, E. Villa, C. Chipot, R. D. Skeel, L. Kalé and K. Schulten, *J. Comput. Chem.* **26** 1781 (2005).
- [19] K. Vanommeslaeghe, E. Hatcher, C. Acharya, S. Kundu, S. Zhong, J. Shim, E. Darian, O. Guvench, P. Lopes, I. Vorobyov, and A. D. Jr. MacKerell, *J. Comput. Chem.* **31** 671 (2010).
- [20] W. L. Jorgensen, J. Chandrasekhar, J. D. Madura, R. W. Impey, and M. L. Klein, *J. Chem. Phys.* **79** 926 (1983).
- [21] L. Wang, R. S. Dumont, and J. M. Dickson, "Comparison of two nonequilibrium

molecular dynamics simulation systems for the pressure-driven water permeation through carbon nanotube membrane”, submitted *Microfluid. Nanofluid.* (2012).

- [22] J. Kruse, J. Kanzow, K. Rätzke, F. Faupel, M. Heuchel, J. Frahn, and D. Hofmann, *Macromolecules* **38** 9638 (2005).
- [23] F. Franks, *Water: A Matrix of Life, (Second Edition)* (Royal Society of Chemistry, Cambridge, 2000).
- [24] L. Wang, R. S. Dumont, and J. M. Dickson, *J. Chem. Phys.* **134** 044102 (2012).
- [25] L. D. Nghiem, Removal of emerging trace organic contaminants by nanofiltration and reverse osmosis, (PhD thesis, School of Civil, Mining and Environmental Engineering, University of Wollongong, Wollongong, Australia, 2005).
- [26] O. Coronell, M. I. González, B. J. Mariñas, and D. G. Cahill, *Environ. Sci. Technol.* **44** 6808 (2010).
- [27] O. Coronell, B. J. Mariñas, and D. G. Cahill, *Environ. Sci. Technol.* **45** 4513 (2011).
- [28] G. Artug, I. Roosmasari, K. Richau, and J. Hapke, *Separ. Sci. Technol.* **42** 2947 (2007).
- [29] A. E. Childress and M. Elimelech. *Environ. Sci. Technol.* **345** 3710 (2000).

Chapter 9 General Conclusions, Contributions, and Future Work

9.1. General Conclusions

In the thesis, pressure-driven liquid flows passing through carbon nanotube (CNT) membranes and polyamide (PA) membranes at nanofiltration (NF) operating conditions are investigated by using nonequilibrium molecular dynamics (NEMD) simulations.

The NEMD simulation system proposed in Chapter 2 is to study the effects of CNT membrane structure (pore size and membrane thickness) on pressure-driven water transport. The results show that the continuum equations (the Navier-Stokes equations) are no longer valid for predicting transport properties of water flows passing through the CNT membranes driven by a low pressure difference. Due to a combination of the nanoscale pore size, the smooth pore surface of the CNT, and the weak water-CNT interactions, the pressure-driven water flow exhibits a much higher flux than the theoretical value from the Hagen-Poiseuille equation and a non-parabolic axial velocity distribution along the radial direction in the CNT. The extraordinary fast water flow through the CNT membrane increases with increasing membrane pore size or with decreasing membrane thickness. The water density distribution and the well-ordered configuration of water molecules in the CNT are strongly dependent on the pore size but not the membrane thickness.

The 2D PBC system (used in Chapter 2) and the 3D PBC system in Chapter 3 are used to simulate pure water flows passing through the same CNT membrane driven by different pressure differences. The two kinds of systems use different periodic boundary conditions (PBC) along the flow direction and difference methodology for producing the constant pressure difference across the membrane. The 2D PBC system can simulate high and low pressures on the two sides of the membrane, and the 3D PBC simulate a net pressure difference across the membrane. The two systems are both feasible to achieve steady pressure-driven water flows passing through the CNT membrane and exhibit similar transport phenomenon (an extraordinary fast flow and a non-parabolic velocity distribution). However, the comparisons between the two systems show that the 2D PBC system is a better system for studying the water transport and even has higher computational cost. The fast water flow cannot be described by the Navier-Stokes equations (as explained in Chapter 2), but becomes faster at a higher pressure difference, which is similar as the flux/velocity proportional to the pressure difference in the Navier-Stokes equations.

In Chapters 4 and 5, the 2D PBC system is used to simulate pressure-driven pure water flows passing through modified CNT membranes for investigating the effects of water–membrane interactions on water transport. For the CNT membranes with the same membrane structure, the increasing water–membrane interactions (the van der Waals interactions or the electrostatic interactions) can enhance the hydrophilic property of the hydrophobic CNT membrane but reduce the water flow. Moreover, the results of the charged CNT membranes in Chapter 5 illustrate that the charges on the pore surface

take a more significant effect on the reduced water transport than the charges on the membrane surface, and the charge type on the CNT membrane exhibits similar influences on water transport for the positive and negative charges. The reduced water flow passing through the modified CNT membrane is still at least 7 times as fast as expected from the Navier-Stokes equations, due to the unique transport properties of water through a CNT.

In Chapter 6, organic flows passing through CNT membranes are simulated driven by the same pressure difference by using the 2D PBC system, and the effects of liquid properties (molecular weight, viscosity, and molecular structure) and membrane pore size on liquid transport are investigated. Similar as the fast water flow observed in Chapters 2-5, most organic flows are faster than the theoretical values predicted by the Navier-Stokes equation due to the unique properties of the CNT membrane. However, the simulation benzene flux is close to the theoretical value, due to the hexagon ring structure of benzene and the benzene–CNT interactions. With increasing molecular weight or liquid viscosity, the steric hindrance effect and the resistance force on the flow increase resulting in a slow flow. For each liquid, the radial distribution and the liquid configuration in the CNT are dependent on the liquid molecular size and the pore size of the CNT membrane. With increasing membrane pore size, the liquid of a linear molecular structure exhibits a faster flow rate, while the benzene flow exhibits an irregular changing trend.

In Chapters 7 and 8, uncross-linked and cross-linked PA membranes are modeled by using MD simulations and the 3D PBC system is used to study pressure-driven water

transport by using NEMD simulations. The membrane structure (membrane density, fractional free volume, and free volume radius) of the amorphous PA membrane is analyzed and the effects of membrane structure and pressure difference on the transport properties (water flux and permeability coefficient) are investigated. The PA membrane composed of more PA polymers (in Chapter 7) or with a higher cross-linked degree (in Chapter 8) exhibits a smaller free volume radius, corresponding to a slower water flow through the membrane. For the negatively charged PA membrane (in Chapter 8), the membrane structure and water transport properties are both affected by the electrostatic interactions between the polymer chains in the membrane and by the water–membrane electrostatic interactions. With increasing negative charges of the PA membrane, the free volume radius increases, but the water flux decreases due to the decreasing effective pore size. The simulation results about the membrane structure and water transport correspond to the experimental results of the commercial NF 90 membrane.

The works in this thesis introduce feasible and reliable approaches to study pure liquid NF transport by using MD/NEMD simulations, and reveal some transport fundamentals on a molecular scale, especially about the relationship between the liquid–membrane interactions and the liquid transport properties.

9.2. Contributions

To our knowledge so far, little work has been reported to develop NEMD simulation methods for studying NF processes under the conditions of a real NF system, **a low pressure difference**. In particular, the works in this thesis are **novel and innovative**

and the major contributions are as follows:

1. To simulate pressure-driven flows at low pressure differences.

A NEMD simulation system, the 2D PBC system, is derived to study pure liquid transport at low pressure differences by using NEMD simulations. A constant high pressure and a constant low pressure on the two sides of a membrane are generated to drive a liquid flow passing through the membrane. This system can provide reliable simulation results of liquid transport and can be used to simulate a liquid flow of a large molecular size or a complicate molecular structure. Moreover, a 3D PBC system which is a comment method in previous published studies is compared with the 2D PBC system, and is used to study water transport through PA membranes at low pressure differences.

2. To model modified CNT membranes.

In addition to study the effects of pore size, membrane thickness, and pressure difference on water transport through unmodified CNT membranes, this thesis investigates the effect of water–membrane interactions. Different Lennard-Jones parameters are set on the unmodified membrane to alter the water–membrane van der Waals interactions, and atomic charges are set on the unmodified membrane to alter the water–membrane electrostatic interactions. The results provide a potential to control water flows passing through CNT membranes by modifying the membranes and to understand how the membrane characteristics affect membrane performance in NF processes.

3. To study organic liquid transport.

Organic flows passing through CNT membranes are simulated to investigate the effects of liquid physicochemical properties on pressure-driven transport. The organic flows have different molecular weights (molecular sizes), different viscosities, and different molecular structures (linear and ring structures). Through NEMD simulations, the transport properties of organic flows are evaluated and the distributions of the organic molecules in the CNTs are directly displayed. This work provides a fundamental understanding of organic flows through a nanoporous membrane and can help to improve membrane performance for separating organic solutes – water mixtures in a real NF process.

4. To model polymeric NF membranes.

Uncross-linked and cross-linked PA membranes are modeled as NF membranes, based on previous published works for modeling porous or RO polymeric membranes. The PA membranes are amorphous membranes having similar structures as the aromatic PA selective layer of a real commercial NF membrane, the FILMTEC™ NF 90 membrane. The numbers of PA polymers in the uncross-linked membranes, the degrees of cross-linking of the cross-linked membranes, or the numbers of charged carboxylates in the cross-linked membranes are set with different values, in order to model PA membranes with different membrane structures by using MD simulations. The free volume pore properties of the PA membranes are evaluated, and the effects of membrane structure and pressure difference on water transport are investigated through NEMD simulations.

The **expected significance** of the works in this thesis is to have a better understanding of some fundamentals about NF transport and ultimately improve the potential of NF membranes, particularly in water treatment and environmental applications. This thesis is not only meaningful for studying a NF transport process but for studying other transport processes, such as transport in biology, some novel nanoporous materials, and nanofluidic devices.

9.3. Future Work

The successful studies in this thesis suggest that NEMD simulations can be applied in some future works about NF transport:

- 1. To simulate other organic flows of long linear structures or complicated ring structures passing through a CNT membrane.**

In Chapter 6, the n-pentane and n-pentanol flows of a linear molecular structure formed by five carbon atoms are studied to show the transport properties of alkane or alcohol flows; and the benzene fluid is studied as an aromatic hydrocarbon. The simulation results show the transport properties and the liquid distribution in the nanoscale pore of the CNT membrane are dependent on the molecular structures and physical properties of the organic flows. It would be interesting to simulate other organic flows of linear structures longer than the five-carbon chain or of ring structures more complicated than the single six-carbon hexagon ring and then to investigate the pressure-driven transport of these organic flows.

- 2. To simulate organic flows passing through PA membranes.**

It has been proved that the commercial NF 90 membrane can be used to separate organic – water mixtures. The studies in Chapter 6 show the transport properties of five organic flows passing through CNT membranes with single straight cylindrical pores. It has not been well known how an organic flow passes through a polymeric membrane with free-volume pores. The simulation studies of organic flows passing through PA membranes can show the fluxes and liquid configurations in the free-volume pores, and investigate the effects of free volume pores on the organic flow, which could provide a more fundamental understanding of a real polymeric NF membrane and NF transport.

3. To simulate pressure-driven water transport through an asymmetry PA membrane.

The polymeric top layer of a real TFC NF membrane usually has an asymmetry structure, and becomes denser from the bottom to the top surface. A PA membrane can be modeled as an asymmetry membrane with an increasing mean pore size along flow direction to simulate pressure-driven water transport through the membrane, which means a water flow passes through the membrane from smaller pores to larger pore sizes. The simulation studies of asymmetry membranes may show different transport properties with a symmetry membrane (like the PA membranes in Chapters 7 and 8). This work would provide information about the effect of pore distribution on water transport.

The limitation of the works in this thesis is that the proposed 2D PBC NEMD simulation method is unseemly to simulating a separation process under a constant pressure difference and a constant concentration difference across the membrane. For

example, a NF separation process is a concentrated stream at high pressure side passing through a NF membrane to form a purified stream at low pressure side. During a NEMD simulation, the concentration difference across a membrane model is hard to be controlled at a constant value: the concentrations of the upper and lower solution reservoirs would keep changing, as the solute and solvent molecules pass through the membrane in different flow rates. Therefore, it is still a challenge to design a NEMD simulation methodology to simulate a liquid mixture rejected by a NF membrane, which can achieve the high and low pressures and the high and low concentrations on the two sides of the membrane.

In a real NF process, a high solute rejection is obtained for a concentrated feed solution with a low solute concentration at a low pressure difference. To simulate the very slow solute flow in NF transport, a huge computational capability/cost would be required even if there were possible simulation systems. It can be expected some further works could be developed for studying NF transport or other membrane separation processes through MD/NEMD simulations.